



UNIVERSITAT DE
BARCELONA

Electrocatalyst development for PEM water electrolysis and DMFC: towards the methanol economy

Radostina Vasileva Genova-Koleva

ADVERTIMENT. La consulta d'aquesta tesi queda condicionada a l'acceptació de les següents condicions d'ús: La difusió d'aquesta tesi per mitjà del servei TDX (www.tdx.cat) i a través del Dipòsit Digital de la UB (diposit.ub.edu) ha estat autoritzada pels titulars dels drets de propietat intel·lectual únicament per a usos privats emmarcats en activitats d'investigació i docència. No s'autoritza la seva reproducció amb finalitats de lucre ni la seva difusió i posada a disposició des d'un lloc aliè al servei TDX ni al Dipòsit Digital de la UB. No s'autoritza la presentació del seu contingut en una finestra o marc aliè a TDX o al Dipòsit Digital de la UB (framing). Aquesta reserva de drets afecta tant al resum de presentació de la tesi com als seus continguts. En la utilització o cita de parts de la tesi és obligat indicar el nom de la persona autora.

ADVERTENCIA. La consulta de esta tesis queda condicionada a la aceptación de las siguientes condiciones de uso: La difusión de esta tesis por medio del servicio TDR (www.tdx.cat) y a través del Repositorio Digital de la UB (diposit.ub.edu) ha sido autorizada por los titulares de los derechos de propiedad intelectual únicamente para usos privados enmarcados en actividades de investigación y docencia. No se autoriza su reproducción con finalidades de lucro ni su difusión y puesta a disposición desde un sitio ajeno al servicio TDR o al Repositorio Digital de la UB. No se autoriza la presentación de su contenido en una ventana o marco ajeno a TDR o al Repositorio Digital de la UB (framing). Esta reserva de derechos afecta tanto al resumen de presentación de la tesis como a sus contenidos. En la utilización o cita de partes de la tesis es obligado indicar el nombre de la persona autora.

WARNING. On having consulted this thesis you're accepting the following use conditions: Spreading this thesis by the TDX (www.tdx.cat) service and by the UB Digital Repository (diposit.ub.edu) has been authorized by the titular of the intellectual property rights only for private uses placed in investigation and teaching activities. Reproduction with lucrative aims is not authorized nor its spreading and availability from a site foreign to the TDX service or to the UB Digital Repository. Introducing its content in a window or frame foreign to the TDX service or to the UB Digital Repository is not authorized (framing). Those rights affect to the presentation summary of the thesis as well as to its contents. In the using or citation of parts of the thesis it's obliged to indicate the name of the author.



UNIVERSITAT DE
BARCELONA

IK4 CIDETEC
Research Alliance

Programa de Doctorat: ELECTROQUÍMICA. CIÈNCIA I TECNOLOGIA

Departament de Ciència de Materials i Química Física

Secció de Química Física

ELECTROCATALYST DEVELOPMENT FOR PEM WATER ELECTROLYSIS AND
DMFC: TOWARDS THE METHANOL ECONOMY

Tesi que presenta Radostina Vasileva Genova-Koleva
per optar al títol de Doctor per la Universitat de Barcelona

Directors de tesi:

Dr. Pere Lluís Cabot Julià
Catedràtic de Química Física
Universitat de Barcelona

Dr. Francisco Alcaide Monterrubio
Investigador Principal
Fundación CIDETEC

Tutor:

Dr. Enric Brillas Coso
Catedràtic de Química Física
Universitat de Barcelona



*Laboratori d'Electroquímica de
Materials i del Medi Ambient*

IK4 CIDETEC
Research Alliance

Dr. PERE-LLUÍS CABOT i JULIÀ, Catedràtic del Departament de Ciència de Materials i Química Física de la Facultat de Química de la Universitat de Barcelona i Dr. FRANCISCO ALCAIDE MONTEERRUBIO, Investigador Principal de la Divisió de Energía d'IK4-CIDETEC,

CERTIFIQUEN:

Que el present treball de recerca, que porta per títol “*Electrocatalyst development for PEM water electrolysis and DMFC: Towards the methanol economy*”, constitueix la memòria presentada per **Radostina Vasileva Genova-Koleva** per optar al grau de Doctor per la Universitat de Barcelona, i ha estat realitzat sota la nostra direcció en el marc del Programa de Doctorat “Electroquímica. Ciència i Tecnologia”, preferentment als laboratoris de Fundació CIDETEC, en col·laboració amb el Laboratori d'Electroquímica dels Materials i del Medi Ambient del Departament de Ciència de Materials i Química Física de la Universitat de Barcelona.

I per tal de deixar-ne constància, signem el present certificat a Barcelona, sis de juny de dos mil disset.

ACKNOWLEDGEMENTS

First of all I would like to acknowledge my supervisors, Prof. Pere Lluís Cabot and Dr. Francisco Alcaide Monterrubio for their enormous help, support and guidance during the entire process of research and administrative issues related to this PhD thesis.

My special thanks goes to my colleagues and my office-mates in IK4-CIDETEC Dr. Garbiñe Álvarez and Eng. Amaia Querejeta for their willing assisting me when help was needed, for their support, enthusiasm and useful discussions and advices, for helping with practical and administrative issues.

My thanks also go out to the support I received from the collaborative work at the ICGM-CNRS, University of Montpellier 2, to Prof. Deborah Jones for her invitation and supervision of my secondment and to Dr. Julia Savych for her help to measurements performed there.

I would like to thank to Initial Training Network, SUSHGEN, funded by the FP7 Marie Curie Actions of the European Commission (FP7-PEOPLE-ITN-2008-238678), for the financial support.

Finally, I would like to thank my family for their love and support.

Contents

Abstract	1
Resumen	7
1.Introduction	27
1.1. Water electrolysis	35
1.2 Basic principles of water electrolysis. Theory	39
1.2.1 Thermodynamics	39
1.2.2 Kinetics	42
1.3 Proton Exchange Membrane Water Electrolysis (PEMWE). Literature review	45
1.3.1 Bipolar Plates	45
1.3.2 Gas Diffusion Layer	47
1.3.3 Solid Polymer Electrolyte Membrane	49
1.3.4 Electrocatalysts for the hydrogen evolution reaction (HER)	51
1.3.5 Electrocatalysts for the oxygen evolution reaction (OER)	53
1.3.6 Supports for the hydrogen evolution (HER) and the oxygen evolution reaction (OER) catalysts	57
1.3.7 MEA formulation and performance	60
1.4 Basic principles of DMFC. Theory	67
1.4.1 Thermodynamics	67
1.4.2 Kinetics	69
1.5 DMFC catalysts. Literature review	73
1.5.1 Electrocatalysts for the oxygen reduction reaction (ORR)	75
1.5.2 Electrocatalysts for the methanol electrooxidation reaction (MOR)	76

1.5.3 Supports for the electrocatalysts in DMFC	77
1.5.4 MEAs for DMFC	79
2. Thesis objectives	83
3. Methodology	85
3.1 Synthesis of the materials	85
3.1.1 Synthesis of the TiO ₂ and Nb-doped TiO ₂ supports	85
3.1.2 Synthesis of the TNT and Nb-doped TNT supports	85
3.1.3 Synthesis of Pt catalysts	86
3.1.4 Synthesis of IrO ₂ and IrRuO _x catalysts	86
3.2 Physico-chemical characterization of the PEMWE materials	87
3.3 Electrochemical characterization of the PEMWE materials	91
3.3.1 Experimental setup	91
3.3.2 Electrode preparation and characterization of the HER catalysts	92
3.3.3 Electrode preparation and characterization of the OER catalysts	93
3.4 MEA preparation and characterization for PEMWE	94
3.4.1 Membrane pretreatment	94
3.4.2 Catalysts inks composition	94
3.4.3 MEA preparation	95
3.4.4 Cell design and electrochemical characterization	96
3.5 Physico-chemical characterization of the DMFC materials	97
3.6 Electrochemical characterization of the DMFC materials	98
3.6.1 Experimental setup	98
3.6.2 Preparation of the DMFC electrodes	98
3.6.3 Electrochemical characterization of DMFC electrodes	99
3.7 MEA preparation and characterization for DMFC	100

3.7.1 MEA preparation	100
3.7.2 Cell design and electrochemical characterization	100
4. Results and discussion	103
4.1 PEM water electrolysis	103
4.1.1 Supports characterization	103
4.1.1.1 Formation of TiO ₂ nanotubes	103
4.1.1.2 Physico-chemical characterization of the supports	105
4.1.2 Hydrogen evolution electrocatalysts	114
4.1.2.1 Physico-chemical characterization	114
4.1.2.2 Electrochemical characterization	120
4.1.2.3. PtPd deposited on Nb-doped TNT	129
4.1.3 Oxygen evolution electrocatalysts	133
4.1.3.1 Physico-chemical characterization	134
4.1.3.2 Electrochemical characterization	138
4.1.4 Membrane electrode assemblies (MEAs)	152
4.1.4.1 Electrochemical characterization	153
4.1.4.2 Cost estimation	161
4.2 DMFC	171
4.2.1 Methanol oxidation reaction electrocatalyst	171
4.2.1.1 Physico-chemical characterization	171
4.2.1.2 Electrochemical characterization	175
4.2.2 Membrane electrode assemblies (MEAs)	181
5. Conclusions	189
6. References	193

APPENDIX	223
List of symbols	225
List of acronyms	227
Curriculum vitae	231

ELECTROCATALYST DEVELOPMENT FOR PEM WATER ELECTROLYSIS AND DMFC: TOWARDS THE METHANOL ECONOMY

Abstract

The concept of the so-called “methanol economy” suggests the use of methanol for: (i) energy storage means; (ii) readily transportation and fuel dispensing, especially for DMFC; (iii) feedstock for a wide variety of products and chemicals.

The direct methanol fuel cell (DMFC) enables the direct conversion of the chemical energy stored in liquid methanol fuel to electrical energy, with water and carbon dioxide as by-products. They are very appropriate for portable applications. Compared to the more well-known hydrogen fueled polymer electrolyte membrane fuel cells (H₂-PEMFCs), DMFCs present several advantages mainly related to the use of liquid fuel. Methanol, as a liquid, is significantly safer and easier to handle, transport and store. In addition, it is available at low cost, as well as its higher energy density than H₂ (6 kWh kg⁻¹). At present, methanol it is mostly prepared from synthesis gas (syn-gas, CO and H₂ mixture), obtained mainly from the incomplete combustion of fossil fuels. It can be also produced by oxidative conversion of methane or by reductive conversion of CO₂ with H₂. The former could be obtained from industrial exhaust from fossil fuel power plants or captured from the atmosphere. The methanol production in this form can be conceived as storing hydrogen in liquid form, which is easier to manage. In addition, this would allow CO₂ recycling, which would help in the attempts for the climate change mitigations.

On the other hand, a variety of processes are available for H₂ production, like thermochemical, electrolytic, direct solar water splitting and biological, being the most important the reforming of natural gas. Polymer electrolyte membrane water electrolysis (PEMWE) undergoes significant interest within the last years. It has several advantages in comparison with the widely commercially used alkaline electrolysis, like lower

power consumption, more flexible operating conditions, smaller mass of the system, and higher purity of the evolved gases. The development of this technology demands new requirements for those active core materials, like catalysts and catalysts supports and membranes.

The main part of this thesis has been devoted to the development of electrocatalysts for the hydrogen evolution reaction and the oxygen evolution reaction, in response to the new challenges facing the development of PEM water electrolyzers. The second part of this thesis is dealing with the development of electrodes for direct methanol fuel cells (applying concepts of the so-called “electrode engineering”), their characterization and application in single DMFCs.

TiO₂ materials were developed as supports for electrocatalysts for hydrogen evolution reaction (HER) and oxygen evolution reaction (OER) in PEM water electrolyser to address the corrosion resistance, mechanical stability and durability required under the operating conditions of the PEMWE cell. TiO₂ and Nb-doped TiO₂ with different Nb-concentrations (3, 6 and 10 at.% Nb vs. Ti) were synthesized via sol-gel method and were characterized. In order to achieve higher specific surface area of the supported materials, TiO₂ nanotubes (TNT) and Nb-doped TiO₂ nanotubes (Nb-TNT) were prepared by hydrothermal method.

The outer diameter of the nanotubes was found to be about 10 nm and the length of 100-200 nm. The observed values of the specific surface area of the reported supports were in the range of 80 m² g⁻¹ for TiO₂ (anatase) to 100 m² g⁻¹ for 10Nb-TiO₂ and about 150 – 303 m² g⁻¹ for the nanotubes.

Electrical conductivity was measured at temperatures up to 250 °C. The results show that the highest values of the conductivity were observed at 80 °C and further

temperature increasing over 80 °C leads to a conductivity decrease, which can be assigned to the dehydration of the samples.

Hydrogen evolution reaction

As observed TiO₂, Nb-TiO₂, TNT, Nb-TNT, TNT-P and Nb-TNT-P were applied as catalysts supports for Pt toward hydrogen evolution reaction in PEM water electrolysis. By X-ray photoelectron spectroscopy (XPS) was found a local increase of the electron density on Pt when supported onto Nb-TNT which was considered the responsible for the strong metal-support interaction (SMSI) in the Pt-TiO₂ system, pointing out the effect of the substrate.

From the recorded *j-E* curves of Pt on (Nb)-TiO₂ and (Nb)-TNTs, it was found that the highest activity towards HER corresponds to Pt/3Nb-TNT catalyst. The performance of Pt/3Nb-TNT was found to be very close to that of the homemade prepared reference Pt/Vulcan XC72 in the entire range of current densities. Further comparison with other materials reported in the literature confirmed the good activity towards HER of Pt deposited on the TiO₂ and TNTs supports developed in this work.

Oxygen evolution reaction

As OER catalysts IrO₂ and IrRuO_x (atomic ratio Ir:Ru equal to 60:40) were synthesized via hydrolysis method and their further development was investigated by deposition onto TNT and 3 at. % Nb-TNT as supports.

From the recorded *j-E* curves of IrO₂ unsupported and supported on TNT and Nb-TNT catalysts, it was shown that IrO₂/Nb-TNT exhibits the highest HER activity. Better activity of the supported catalysts in comparison to unsupported was attributed mainly to the better dispersion onto the support surface. The lowest overpotentials were found for the catalysts supported onto Nb-doped TNT, which confirms the better sensitivity toward oxygen evolution reaction in presence of Nb as previously has been

reported in the literature.

Membrane electrode assembly (MEA)

MEAs of 5 cm² geometric area were prepared via a new low temperature decal method, developed in this work and optimized. On the anode side IrO₂, IrRuO_x and 50 wt. % IrO₂/Nb-TNT were applied as electrocatalysts and anode catalyst loading was optimized to 2.0 mg_{oxide} cm⁻². Pt loading on the cathode was optimized to 0.5 mg_{Pt} cm⁻² (Pt black and 20 wt. % Pt/Vulcan XC72 were used). After optimization of the electrode loadings and method of preparation, the best performance of the MEA for the low temperature electrolyser corresponded to cell voltages at 0.100 and 0.500 A cm⁻² of: 1.430 and 1.494 V at 80 °C; and 1.407 and 1.468 V at 90 °C (*IR*-drop not corrected) with 50 wt.% IrO₂/Nb-TNT on the anode and 20 wt. % Pt/Vulcan XC72 on the cathode.

After cost estimation of the materials was found that the cost of 50 wt.% IrO₂/3Nb-TNT was 49% lower in comparison to IrO₂ black. The final cost estimation of the MEA was found to be only 6 % higher when 50 wt. % IrO₂ / 3Nb-TNT was applied as anodic catalyst for the same oxide loadings on the anode in comparison to IrO₂ and for same MEA compositions. Similar values of cost growth were obtained and when on the cathode was used 20 wt. % Pt/Vulcan XC72 instead of Pt black (for equal anode catalysts and MEA composition).

DMFC electrodes

The complementary part of this thesis is devoted to the development and evaluation of DMFC anodes. Different solvents (n-butyl acetate (NBA) and 2-propanol (IPA)) with different polarity (dielectric constants $\epsilon_{\text{IPA}}=18.0$ and $\epsilon_{\text{NBA}} = 5.01$) were used in the catalyst inks as a pathway to tune the catalyst layer porosity. Commercially available Pt and PtRu blacks were used as catalysts.

To study the influence of the solvents in the catalyst ink on the morphology and textural properties of catalyst layers, first of all inks were characterized by light scattering experiments. The results indicate that the PtRu-Nafion[®] aggregates in the inks prepared with n-butyl acetate (NBA) are larger than those prepared with 2-propanol (IPA). SEM images of the samples show that both catalyst layers (CLs) have granular-shape morphology, but the CL prepared using IPA is more compact and less porous than that prepared using NBA. The lower polarity of the latter favours the aggregation of Nafion[®] and nanoparticles. The electron microscopy images and porosimetry measurements of the catalyst layers show that the secondary pore volume between the agglomerates is larger for NBA. The linear sweep voltammetry and electrochemical impedance spectroscopy (EIS) results for the methanol electrooxidation in the three-electrode cell denote the higher active surface area for NBA and comparable specific oxidation rates of the intermediates in both catalysts layers.

The activity of PtRu porous diffusion electrodes towards methanol oxidation was studied in three-electrode cell filled with 0.5 mol dm⁻³ H₂SO₄ + 2.0 mol dm⁻³ CH₃OH aqueous electrolyte. The oxidation current given by the CL formulated with NBA as solvent was larger than that corresponding to the CL formulated with IPA. The transport limitation was found to be more apparent for IPA and could be explained considering the size and porosity of the agglomerates formed by the ionomer and the catalyst nanoparticles in both solvents, which are smaller in IPA.

DMFCs Membrane electrode assembly

The polarization curves of MEAs in which the anode CLs were formulated with NBA and IPA were recorded in single DMFCs operating CH₃OH aqueous solutions at 60 °C. The cathode feed was synthetic air at atmospheric pressure. It was observed that the differences between the current densities delivered by both MEAs increased as the

cell voltage decreased (thus delivering more current). The curvature tending to a limiting current density for the MEA_{IPA} shows mass transport limitation for currents much smaller than those obtained for MEA_{NBA}.

The power density given by MEA prepared with NBA was about 74 % greater when compared to that prepared with IPA. The interpretation of the EIS results indicates that the proton resistance for NBA is significantly lower than for IPA, thus confirming that the greater number of accessible active sites for methanol oxidation in the former are well connected to the Nafion[®] ionomers and easier transported to the membrane.

DESARROLLO DE ELECTROCATALIZADORES PARA ELECTROLIZADORES DE AGUA PEM Y PILAS DMFC: HACIA LA ECONOMÍA DEL METANOL

Resumen

Las pilas de combustible son dispositivos que convierten la energía química liberada en reacciones electroquímicas directamente en energía eléctrica. El combustible utilizado es típicamente un hidrocarburo o una sustancia derivada de él o basado en él como, por ejemplo, hidrógeno o un alcohol. Las pilas de combustible se clasifican normalmente según el tipo de electrolito y su temperatura de funcionamiento. En las pilas de combustible de metanol directo (DMFCs) el reactivo anódico es comúnmente una mezcla de metanol y agua, mientras que en las denominadas pilas de combustible de membrana de electrolito polimérico (PEMFCs) es hidrógeno, siendo el oxígeno el reactivo catódico en ambos casos.

Cuando se utiliza hidrógeno puro directamente como combustible, sólo se genera agua y no se emiten contaminantes. Sin embargo, el hidrógeno no está disponible para su uso directo en la naturaleza y por lo tanto, debe producirse a partir de una variedad de fuentes. Al tratarse de un gas muy ligero y potencialmente explosivo, necesita condiciones especiales de almacenamiento (tanques criogénicos de alta presión, materiales especiales para minimizar la difusión y las fugas, etc.), sobre todo en aplicaciones de transporte, así como la estricta observancia de precauciones de seguridad, lo que hace que el hidrógeno sea más bien costoso. Por otra parte, el metanol, como líquido, es significativamente más seguro y fácil de almacenar y transportar. En la actualidad, se prepara en su mayor parte a partir de gas de síntesis (mezcla de CO y H₂), el cual se obtiene principalmente de la combustión incompleta de combustibles fósiles. Se puede obtener también por oxidación del metano o por reducción del CO₂ con H₂. El CO₂ podría capturarse de los gases residuales emitidos por las centrales eléctricas de

combustibles fósiles, o bien de la atmósfera. La producción de metanol en esta forma puede concebirse como almacenamiento de hidrógeno en forma líquida, que es más fácil de manejar. Además, se procede de esta forma a un reciclaje del CO₂, lo que ayudaría a mitigar el cambio climático.

El concepto de la denominada "economía del metanol" sugiere el uso de metanol como: (i) medio de almacenamiento de energía; (ii) combustible de fácil transporte y dispensación, especialmente para DMFC y (iii) materia prima de una amplia variedad de productos químicos.

Por otra parte, existen diferentes procesos para la producción de H₂. Uno de los más eficaces es la electrólisis de agua, ya que produce hidrógeno y oxígeno puros. La electrólisis mediante membranas de electrolito polimérico (PEMWE) es objeto de gran interés en los últimos años, apoyada en el aumento de la investigación y desarrollo en el campo de la tecnología de las pilas de combustible de membranas de electrolito polimérico (PEMFC). La PEMWE tiene varias ventajas en comparación con la electrólisis alcalina, ampliamente utilizada de forma comercial, por su respeto por el medio ambiente, menor consumo de energía, menor masa del sistema y mayor pureza de los gases producidos. Con el desarrollo de las PEMFC y la PEMWE, se exigen nuevos requisitos a los soportes de catalizador: resistencia a la corrosión, estabilidad mecánica y durabilidad en las condiciones de funcionamiento de la celda.

Electrolisis del agua mediante PEM

En esta tesis, en primer lugar, se han desarrollado soportes de TiO₂ para electrocatalizadores de la reacción de desprendimiento de hidrógeno (HER) y la reacción de desprendimiento de oxígeno (OER) y ser aplicados en dichos electrolizadores. Se han sintetizado soportes de TiO₂ y de TiO₂ dopado con Nb (concentraciones de Nb de 3, 6 y 10 at. % con respecto a Ti) mediante la técnica sol-gel

y se han caracterizado. Con el fin de lograr una mayor superficie específica de los materiales soporte, se han preparado nanotubos de TiO_2 (TNT) y de TiO_2 dopados con Nb (Nb-TNT) mediante el método hidrotérmico y se sometieron a tratamiento con $0,1 \text{ mol dm}^{-3}$ de HCl y $0,1 \text{ mol dm}^{-3}$ de H_3PO_4 (designados por Nb-TNT y Nb-TNT-P, respectivamente), como una forma simple de aumentar su conductividad eléctrica.

A partir de los resultados de las observaciones de microscopía electrónica de barrido (SEM) y microscopía electrónica de transmisión (TEM) se calculó que el diámetro exterior de los nanotubos (TNT) era de aproximadamente de 10 nm y su longitud de 100-200 nm. En cambio, los soportes TNT-P presentaban forma esférica (Fig. 1).

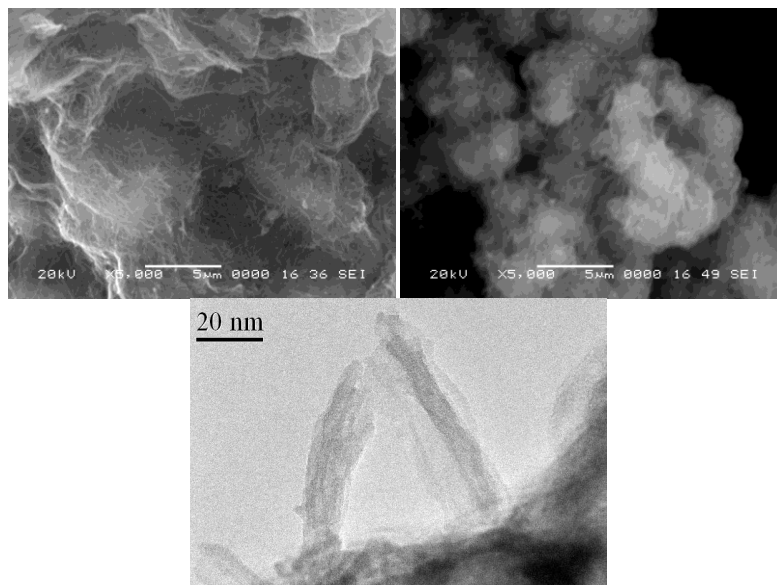


Figura 1 Imágenes SEM de los soportes: (a) 3 Nb-TNT y (b) 3Nb-TNT-P. La figura (c) es una imagen TEM del soporte 3Nb-TNT.

Los diagramas de difracción de rayos X (XRD) de los soportes de TiO_2 , TNT, TNT-P y de los mismos soportes dopados con Nb pusieron de manifiesto que la fase principal era anatasa. Con el aumento de la cantidad de Nb, la intensidad de los picos de anatasa disminuyeron y su anchura aumentó, lo cual sugiere que el tamaño cristalino del TiO_2 dopado con Nb era más pequeño que el no dopado. Adicionalmente, un ligero

desplazamiento hacia ángulos de difracción inferiores sugirió una expansión de la red debido a la incorporación de Nb^{5+} en la red cristalina (Fig. 2).

Los valores del área superficial específica de los soportes eran de unos $80 \text{ m}^2 \text{ g}^{-1}$ para TiO_2 (anatasa), $100 \text{ m}^2 \text{ g}^{-1}$ para 10Nb-TiO_2 y en el intervalo de 150 a $303 \text{ m}^2 \text{ g}^{-1}$ para los nanotubos. Se observa una distribución estrecha del tamaño de poro para los soportes de TiO_2 dentro del intervalo de $3,77$ a $7,08 \text{ nm}$, diámetros de poro ligeramente más grandes para los TNT, entre $6,5$ y $13,42 \text{ nm}$ y aún mayores para los TNT-P, entre $8,05$ y $16,18 \text{ nm}$. El tamaño de poro más pequeño de los soportes de TiO_2 es muy similar al tamaño de partícula típico de los electrocatalizadores de Pt, lo cual puede limitar su uso como soporte de catalizador, ya que las nanopartículas podrían quedar atrapadas dentro de los poros.

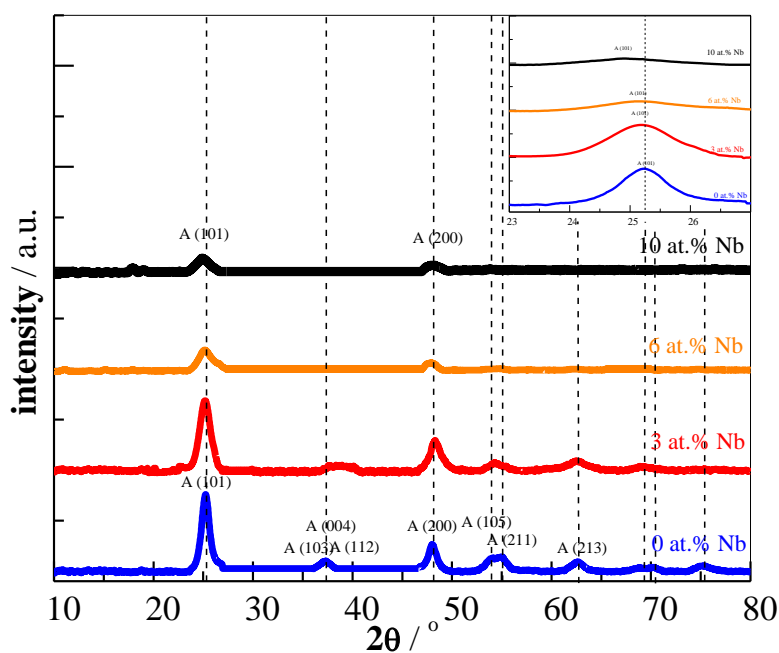


Figura 2 Difractograma de rayos X de los nanotubos de óxido de titanio (TNT) con diferente contenido de Nb: (a) 0, (b) 3, (c) 6 y (d) 10 at. %.

La conductividad del TiO₂ a temperatura ambiente estaba en el intervalo de 0,6 a 41 $\mu\text{S cm}^{-1}$ mientras que para los diferentes soportes de TNT estaba en el intervalo de 0,22 a 2,43 $\mu\text{S cm}^{-1}$. Estos resultados son comparables con los aportados anteriormente en la literatura por otros investigadores. Se midió la conductividad eléctrica a temperaturas elevadas de hasta 250 °C, de cara a considerar el uso de estos catalizadores en PEMWE de alta temperatura. Los resultados muestran los valores más altos de conductividad a 80 °C, disminuyendo después conforme seguía aumentando la temperatura, lo cual se puede asignar a la deshidratación de los soportes.

Reacción de desprendimiento de hidrógeno

Como se ha indicado anteriormente, se procedió a la aplicación de TiO₂, Nb-TiO₂, TNT, Nb-TNT, TNT-P y Nb-TNT-P como soportes de catalizadores de Pt para la reacción de desprendimiento de hidrógeno en la electrólisis del agua mediante PEM.

Se caracterizaron mediante espectroscopia fotoelectrónica de rayos X (XPS) los catalizadores de Pt/3Nb-TNT y de Pt/Vulcan XC72 con un 20 % en peso del metal, observándose para el primero de ellos un desplazamiento del pico Pt 4f de aproximadamente 0,3 eV hacia energías de enlace inferiores en comparación con el del catalizador de referencia Pt/Vulcan XC72. Esta diferencia sugiere un aumento local de la densidad electrónica sobre el Pt en el primero y se considera el responsable de la interacción fuerte entre el metal y el substrato (SMSI) en el sistema Pt-TiO₂, mostrando el efecto positivo de dicho substrato en las prestaciones del catalizador.

A partir de los difractogramas de XRD se calcularon tamaños medios cristalinos de Pt en el intervalo de 3,71 a 5,22 nm para el Pt soportado sobre los soportes estudiados. En el caso del negro de Pt fueron de 5,95 nm y en el de Pt/Vulcan XC72, de 2,38 nm. Las imágenes TEM mostraron una buena dispersión de Pt sobre la superficie de los nanotubos (Fig. 3).

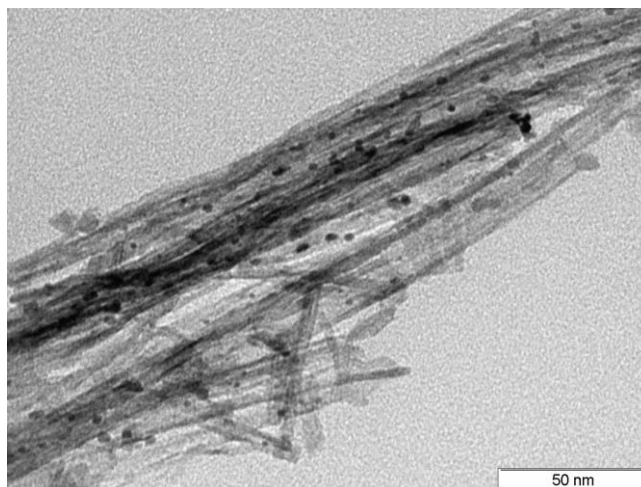


Figura 3 Imagen TEM del catalizador 20 wt. % Pt/3Nb-TNT

Se determinaron las prestaciones electroquímicas de los catalizadores de Pt soportados para la HER mediante voltamperometría cíclica (CV) y voltamperometría de barrido lineal (LSV) en $0,50 \text{ mol dm}^{-3} \text{ H}_2\text{SO}_4$. Se observaron pequeñas modificaciones en el voltamperograma cíclico de Pt en las muestras que contenían los soportes de TNT y de TNT dopados con Nb con respecto al Pt soportado sobre carbono. Se encontró también alguna contribución de los soportes de óxido, como se sugiere a partir de la ligera curvatura en la región de doble capa, siendo todo ello indicativo de una interacción diferente entre Pt y el soporte.

De acuerdo con las curvas $j-E$ obtenidas empleando los catalizadores de Pt/Nb- TiO_2 , es evidente que el de Pt/6Nb- TiO_2 es el que muestra una actividad frente a la reacción de desprendimiento de hidrógeno más alta, ya que presenta los potenciales más bajos en todo el intervalo de densidades de corriente. En cambio, de las curvas $j-E$ para el Pt depositado sobre los nanotubos dopados con Nb (Nb-TNTs), la actividad más alta para dicha reacción corresponde al catalizador Pt/3Nb-TNT. Las prestaciones de este último son muy cercanas a las del catalizador de referencia Pt/Vulcan XC72 en todo el

intervalo de densidades de corriente (Fig. 4). Una comparación posterior con otros catalizadores reportados en la literatura confirma la buena actividad frente a la HER de los catalizadores de Pt depositado sobre los soportes de TiO₂ y TNT desarrollados en este trabajo.

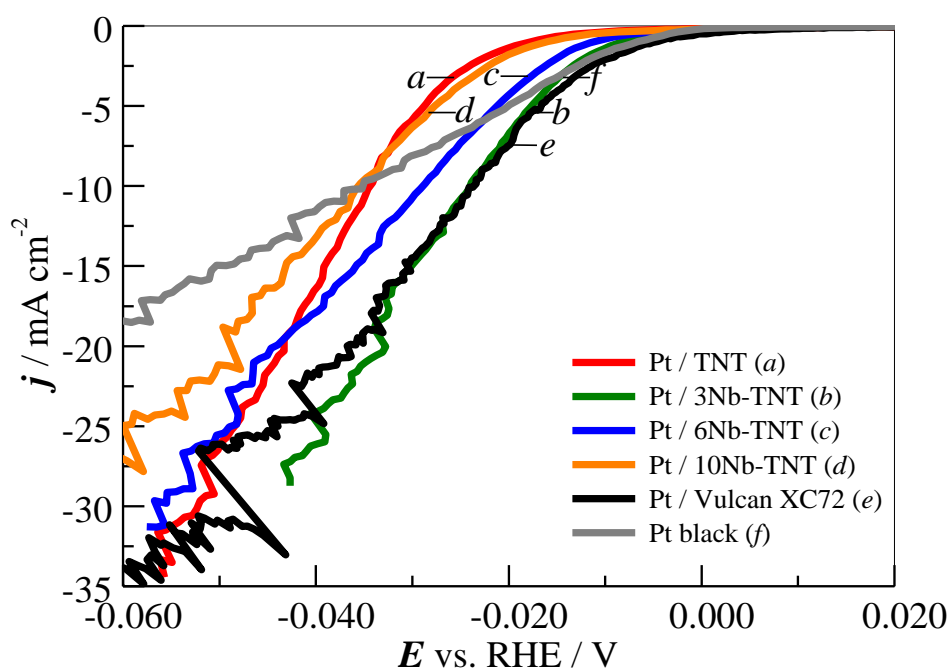


Figura 4 Curvas j - E correspondientes a la HER sobre (a) 20 wt. % Pt/TNT, (b) 20 wt. % Pt/3Nb-TNT, (c) 20 wt. % Pt/6Nb-TNT, (d) 20 wt. % Pt/10Nb-TNT, (e) 20 wt. % Pt/Vulcan XC72 y (f) negro de Pt en 0.50 mol dm⁻³ H₂SO₄. $T = 25.0$ °C. $s_r = 1$ mV s⁻¹. Densidad de corriente referida a la sección geométrica del electrodo. Caída óhmica corregida.

Reacción de desprendimiento de oxígeno

Los catalizadores para la reacción OER en el electrolizador PEMWE son típicamente no soportados debido a los altos potenciales aplicados en el ánodo, que hace imposible el uso de los soportes de carbón convencionales. En esta tesis se han sintetizado catalizadores de IrO₂ e IrRuO_x (relación atómica Ir:Ru de 60:40) por el método de hidrólisis, empleados sin soporte o bien soportados sobre TNTs y 3Nb-TNT.

A partir de los difractogramas de XRD se determinó el tamaño medio cristalino y los parámetros de red de los catalizadores. Los picos de IrRuO_x se desplazaron hacia ángulos más altos en comparación con los de IrO₂, lo cual indica la contracción de la red y la formación de solución sólida, tal como puede esperarse de la similitud en los radios iónicos del iridio y el rutenio (de 0,0625 y 0,062 nm para Ir⁴⁺ y Ru⁴⁺, respectivamente). De acuerdo con ello, los parámetros de red de IrRuO_x fueron menores que los de IrO₂. Se atribuyó el aumento del tamaño cristalino de IrRuO_x en comparación con IrO₂ a que la temperatura de cristalización de RuO₂ es menor que la de IrO₂. La deposición de los catalizadores sobre los soportes indicados conduce a un aumento de tamaño cristalino en comparación con los no soportados, lo cual se relacionó con los centros disponibles para la nucleación para una misma concentración de los precursores.

Se determinaron las prestaciones de los catalizadores de la reacción OER en disolución acuosa 0,50 mol dm⁻³ H₂SO₄ mediante CV y LSV, técnicas comunes para estudiar las propiedades electroquímicas superficiales de los electrodos de óxidos de metales nobles. La carga integrada de los voltamperogramas cíclicos proporciona información sobre los centros activos en la superficie del catalizador. Se encontró que las cargas anódicas y catódicas totales de los catalizadores soportados eran significativamente mayores que las del catalizador no soportado y, al mismo tiempo, el tamaño cristalino también era mayor. Como el mayor tamaño cristalino hace sospechar una menor área superficial electroquímica, se concluyó que los cristales de los catalizadores soportados están mejor dispersos debido a los mismos soportes, siendo su superficie de más fácil acceso en comparación con la de los cristales de los catalizadores no soportados, que debían presentar una aglomeración significativa.

Las curvas *j-E* obtenidas para el catalizador IrO₂ no soportado y soportado sobre TNTs y Nb-TNTs mostraron una mayor actividad catalítica para la reacción OER en el

caso de IrO₂/Nb-TNT, ya que presentaron los potenciales más bajos en todo el rango de densidades de corriente. Se obtuvieron resultados similares empleando IrRuO_x no soportado y soportado sobre TNTs y Nb-TNTs. Si se procede a la comparación del potencial de electrodo para una densidad de corriente baja y a otra alta, 1 y 18 mA cm⁻² respectivamente, se encuentran los potenciales más bajos para los catalizadores soportados sobre TNTs dopados con Nb, confirmando su mayor actividad frente a la OER frente a los no soportados.

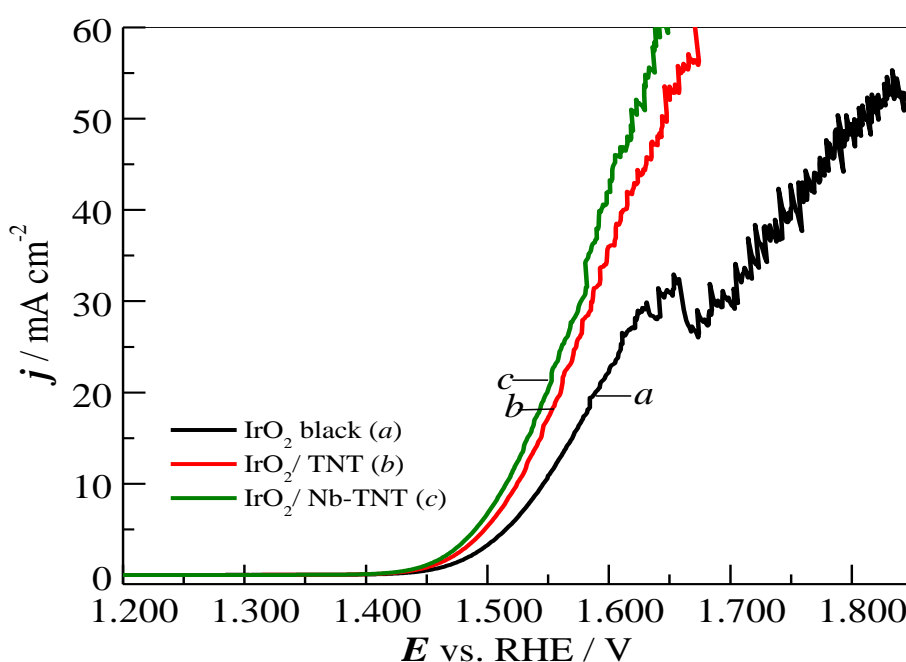


Figura 5 Curvas j - E correspondientes a la OER sobre (a) IrO₂, (b) 50 wt. % IrO₂/TNT, (c) 50 wt. % IrO₂/3Nb-TNT en 0,50 mol dm⁻³ H₂SO₄. $T = 25.0$ °C. $s_r = 1$ mV s⁻¹. Densidad de corriente referida a la sección geométrica del electrodo. Caída óhmica corregida.

Conjunto membrana-electrodo (MEA)

Se prepararon MEAs de 5 cm² de área geométrica y se ensayaron en un dispositivo de celda de electrólisis con un bloque anódico de canales de flujo hecho de titanio sinterizado poroso. Se registraron las curvas de polarización V - j a 80 °C y presión atmosférica antes y después de la sustitución de la placa final de carbón en el

ánodo por Ti sinterizado poroso. No se encontraron efectos significativos en las prestaciones del dispositivo.

Debido al mayor precio del titanio poroso utilizado como capa de difusión de gas (GDL) y su utilización durante un período más largo, el tipo preferido de MEA es el de membrana recubierta con catalizador (CCM), en lugar del de sustrato recubierto con catalizador (CCS) más utilizado en pilas de combustible. Para la fabricación de los MEAs se ha aplicado la técnica de calcomanía convencional “decal” (carga de catalizador sobre el sustrato de la calcomanía seguido de transferencia por presión sobre la membrana), optimizando las condiciones de prensado y la temperatura de transferencia del catalizador con el fin de observar la transferencia completa y un mejor contacto entre capa catalítica y membrana. El método convencional requiere temperaturas de aproximadamente 210 °C. Por esta razón se requiere el uso de la membrana de Nafion® en forma sódica. Sin embargo, esta temperatura podría afectar la estabilidad de la capa de catalizador y de la membrana. El esquema de la Fig.6 muestra la diferencia entre ambos.

Se consiguió la transferencia completa del catalizador bajo las condiciones de calcomanía a baja temperatura y se optimizaron las condiciones de prensado para un mejor contacto entre la capa de catalizador y la membrana. La carga de Pt sobre el cátodo se redujo de 1 a 0,5 mg_{Pt} cm⁻², reemplazando el negro de Pt por 20 wt. % Pt/Vulcan XC72. La carga del catalizador anódico se optimizó en 2,0 mg_{IrO₂} cm⁻².

Como catalizadores anódicos se emplearon IrO₂, IrRuO_x y 50 % en peso de IrO₂/Nb-TNT. Los resultados correspondientes se muestran en la Fig. 7. Como era de esperar, la MEA con 50 % en peso de IrO₂/Nb-TNT en el ánodo presentó las mejores prestaciones. En la Tabla 1 se muestran los voltajes de celda a 0,100 y a 0,500 A cm⁻² obtenidos con los diferentes catalizadores anódicos estudiados.

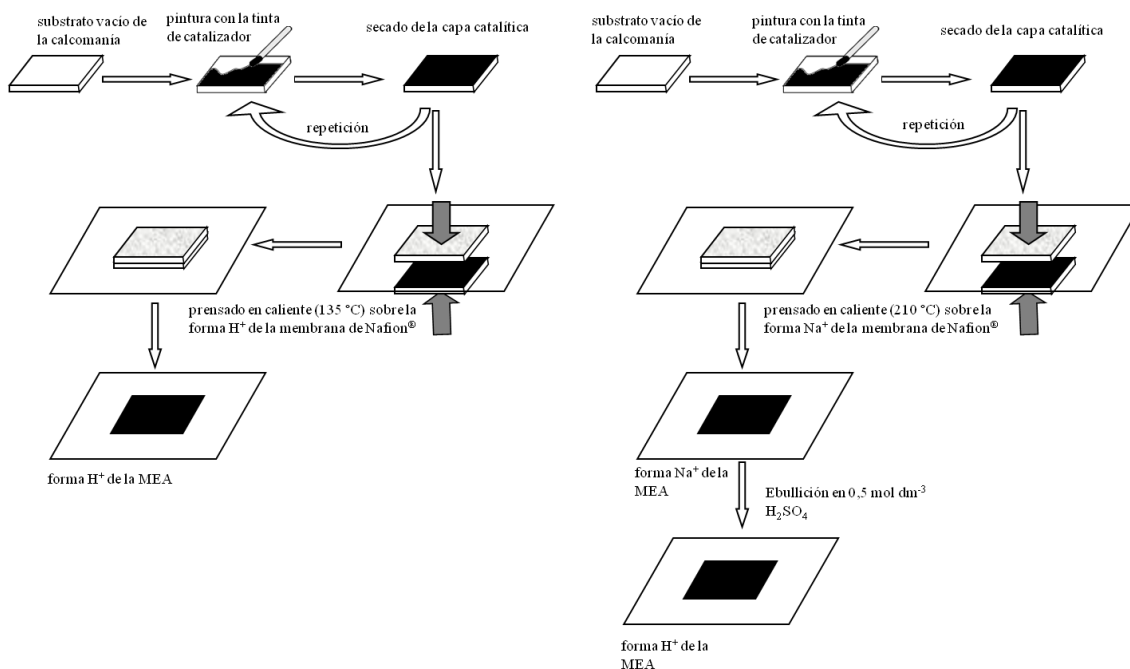


Figura 6 Método de la calcomanía convencional frente a la de baja temperatura para la preparación de los MEAs.

Se puede comprobar que los voltajes obtenidos para IrRuO_x e $\text{IrO}_2/3\text{Nb-TNT}$ son muy similares entre sí y mejores que para el negro de IrO_2 . Se obtuvieron resultados similares en las celdas de tres electrodos empleando $0,5 \text{ mol dm}^{-3}$ de H_2SO_4 . Después de la optimización de las cargas de los electrodos y del método de preparación, los resultados finales de V - j para el electrolizador de Nafion a 80 °C son $1,43 \text{ V}$ a $0,1 \text{ A cm}^{-2}$ y $1,49 \text{ V}$ a $0,5 \text{ A cm}^{-2}$, mientras que a 90 °C son $1,41 \text{ V}$ a $0,1 \text{ A cm}^{-2}$ y $1,47 \text{ V}$ a $0,5 \text{ A cm}^{-2}$. Los valores de potencial reportados en la literatura a $0,100 \text{ A cm}^{-2}$, medidos en condiciones similares, son mayores que los obtenidos en este trabajo, confirmando las buenas prestaciones de los electrocatalizadores seleccionados.

Un estudio de costes de material permitió estimar que el precio del catalizador 50 wt. % IrO_2 soportado en 3Nb-TNT era de un 49 % menor que el de negro de IrO_2 . No obstante, el coste final estimado de un MEA que incorporaba el catalizador 50 wt. % IrO_2 soportado en 3Nb-TNT era un 6 % mayor que el de un MEA de idénticas

características que incorporaba negro de IrO₂. Por otra parte, se encontró un aumento similar para un MEA con 20 wt. % Pt/Vulcan XC72 en lugar de negro de Pt (para el mismo ánodo y composición del MEA).

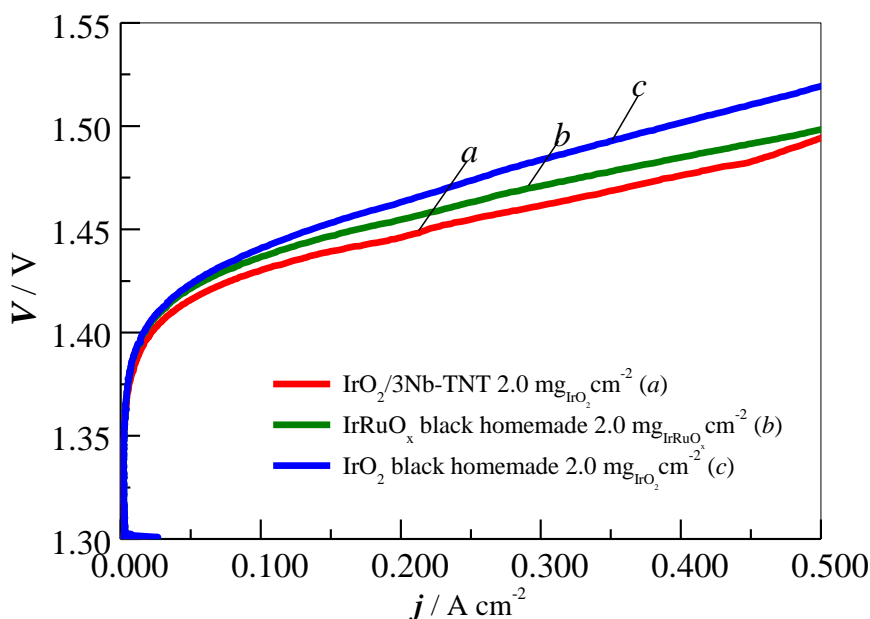


Figura 7 Curvas V - j correspondientes a los MEAs: (a) 20 wt. % Pt/Vulcan XC72 con $0.5 \text{ mg}_{\text{Pt}} \text{ cm}^{-2}$, IrO₂/3Nb-TNT con $2.0 \text{ mg}_{\text{IrO}_2} \text{ cm}^{-2}$; (b) 20 wt. % Pt/Vulcan XC72 con $0.5 \text{ mg}_{\text{Pt}} \text{ cm}^{-2}$, negro de IrRuO_x con $2.0 \text{ mg}_{\text{IrRuO}_x} \text{ cm}^{-2}$; y (c) 20 wt. % Pt/Vulcan XC72 con $0.5 \text{ mg}_{\text{Pt}} \text{ cm}^{-2}$, negro de IrO₂ con $2.0 \text{ mg}_{\text{IrO}_2} \text{ cm}^{-2}$. $T = 80 \text{ }^\circ\text{C}$.

Tabla 1 Prestaciones del electrolizador a 0,100 y a 0,500 A cm⁻² empleando diferentes catalizadores anódicos.

Catalizador	$T / ^\circ\text{C}$	$V(0,100 \text{ A cm}^{-2}) / \text{V}$	$V(0,500 \text{ A cm}^{-2}) / \text{V}$
Negro de IrO ₂	80	1,441	1,519
Negro de IrRuO _x	80	1,436	1,498
IrO ₂ /3Nb-TNT	80	1,430	1,493
IrO ₂ /3Nb-TNT	90	1,407	1,468

Ánodos de la DMFC

Por otra parte, en esta tesis también se ha abordado el desarrollo y evaluación de ánodos para DMFC. Se utilizaron diferentes disolventes, tales como acetato de n-butilo (NBA) y 2-propanol (IPA), con diferentes propiedades físicas, para preparar las tintas de catalizador como una vía para ajustar las propiedades de la capa catalítica (CL), como por ejemplo la porosidad. Los catalizadores de base fueron negro de Pt y negro de PtRu comerciales.

Para evaluar la influencia de los disolventes en la tinta del catalizador sobre la morfología y las propiedades texturales de las capas de catalizador, en primer lugar las tintas se caracterizaron mediante experimentos de dispersión de luz. La Fig. 8 muestra la distribución de tamaños de los aglomerados en las tintas de catalizador de PtRu que contienen NBA o IPA como disolventes orgánicos (véase la Tabla 2). Se observaron dos picos principales centrados alrededor de 1 y 10 μm en ambas tintas. Los picos en la región por debajo de 1 μm se atribuyeron a la distribución de tamaño de los aglomerados de ionómero de Nafion[®], que depende de la constante dieléctrica y la solubilidad de los disolventes en agua. El ionómero de Nafion[®] tiene partes polares y tiende a agregarse cuando la polaridad del disolvente disminuye. Esto explica por qué el pico de menos de 1 μm está centrado en un tamaño menor para IPA que para NBA, ya que este último disolvente tiene una polaridad inferior a la anterior. Por otro lado, los picos superiores a 1 μm pueden asignarse a distribuciones de tamaños de aglomerados de las nanopartículas de catalizador y Nafion[®]. Se puede observar que estos aglomerados son mayores cuando se usa NBA (pico a 26 μm). Esto también puede explicarse por la menor polaridad de la NBA, que favorece la agregación de nanopartículas y Nafion[®] de mayor tamaño.

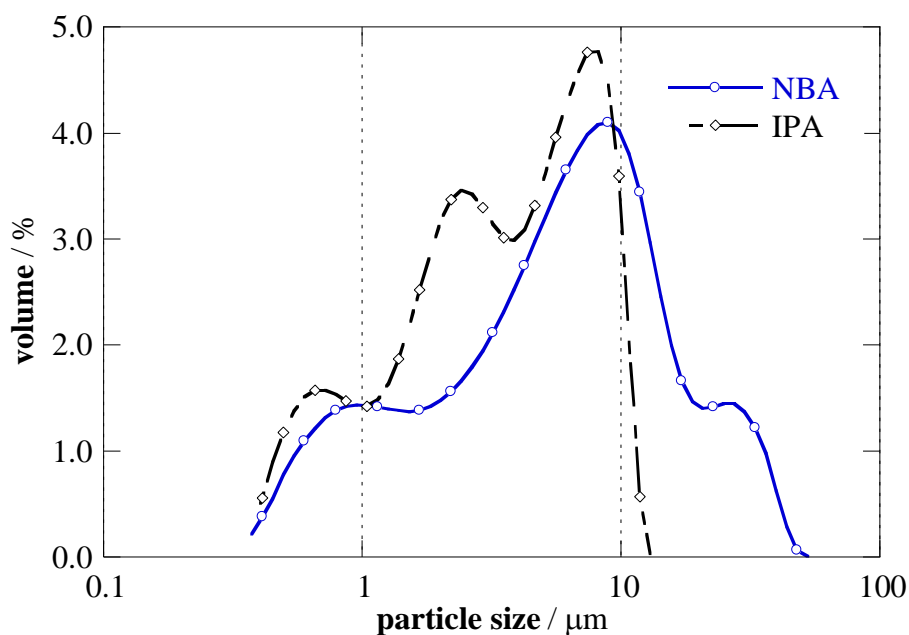


Figura 8 Distribución de tamaños de partícula en las tintas de los catalizadores de PtRu formuladas con diferentes disolventes orgánicos: (○) NBA e (◇) IPA.

Tabla 2 Propiedades físicas de los disolventes orgánicos utilizados para preparar las tintas de catalizador.

Disolvente	ϵ^a	P_v^b / hPa	T_b^c / °C
acetato de n-butilo (NBA)	5.01	13.0	126.5
2-propanol (IPA)	18.0	43.0	82.4

^aConstante dieléctrica a 25 °C

^bPresión de vapor a 20 °C

^cTemperatura de ebullición

Los cambios morfológicos de las capas de catalizador de PtRu se examinaron mediante microscopía electrónica de barrido (SEM). La Fig. 9 muestra las imágenes SEM correspondientes a las CL preparadas usando NBA e IPA, respectivamente. En esta figura se muestra que ambas CL tienen una morfología de forma granular, pero parece que la CL preparada usando IPA es más compacta y menos porosa que la preparada usando NBA. Las distribuciones de tamaño de poro correspondientes a las

capas de catalizador de PtRu preparadas usando NBA e IPA se muestran en la Fig. 10. Ambas curvas presentan una forma similar. Sin embargo, en la región entre 0.1-10 μm , el volumen específico de los poros fue mayor para NBA que para IPA. Tal como se ha encontrado previamente en la literatura, esta región corresponde a los poros secundarios, es decir, al espacio existente entre los aglomerados formados por las nanopartículas de catalizador y Nafion[®]. Por lo tanto, el volumen de poro secundario es mayor en aproximadamente 12% cuando se usa NBA como disolvente orgánico, lo cual se halla de acuerdo con la morfología de las capas de catalizador de la Fig. 9.

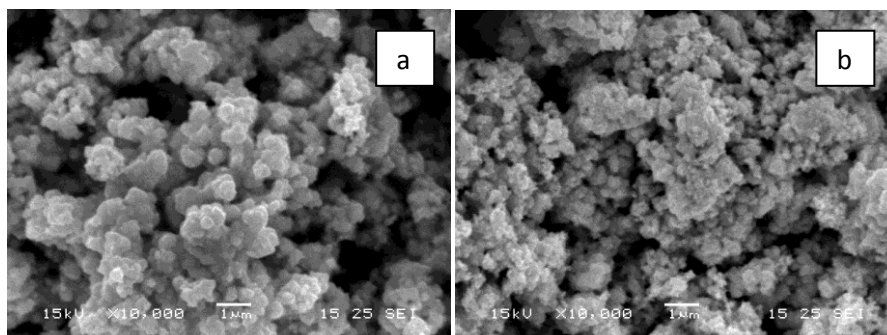


Figura 9 Imágenes SEM de capas de catalizador de PtRu preparadas utilizando: (a) NBA y (b) IPA como disolventes orgánicos.

Se estudió la actividad de los electrodos de PtRu frente a la oxidación del metanol en celdas de tres electrodos conteniendo $2,0 \text{ mol dm}^{-3} \text{ CH}_3\text{OH} + 0,5 \text{ mol dm}^{-3} \text{ H}_2\text{SO}_4$. La Fig. 11 muestra los voltamperogramas de barrido lineal correspondientes a la oxidación de metanol en capas de catalizador en contacto con el electrolito líquido, barriendo el potencial de 0,075 a 0,750 V. La corriente de oxidación dada por la CL formulada con NBA como disolvente era mayor que la correspondiente a la de la CL formulado con IPA.

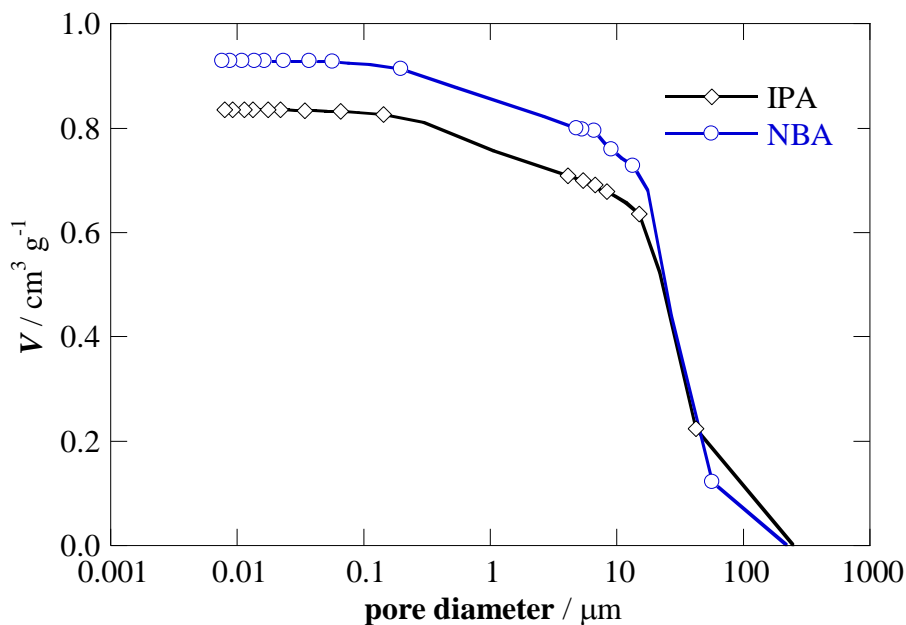


Figura 10 Volumen de poro acumulado (V) vs. diámetro de poro para las capas de catalizador preparadas a partir de tintas de catalizador de PtRu con (\circ) NBA e (\diamond) IPA como disolventes.

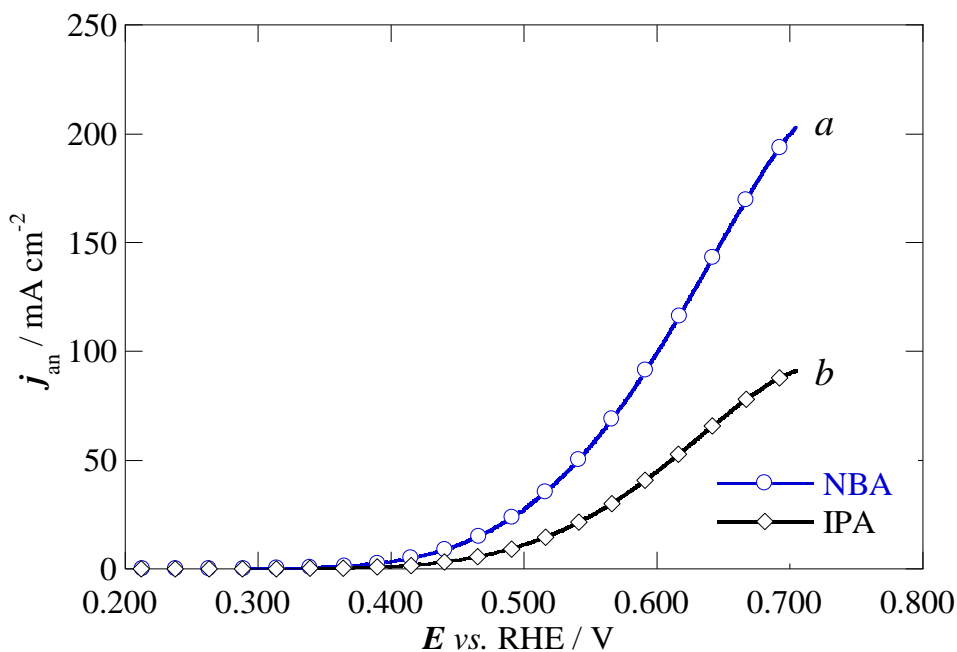


Figura 11 Curvas j - E correspondientes a la electrooxidación de metanol sobre electrodos de negro de PtRu manufacturados usando: (a) NBA y (b) IPA. Disolución $2.0 \text{ mol dm}^{-3} \text{CH}_3\text{OH} + 0.5 \text{ mol dm}^{-3} \text{H}_2\text{SO}_4$. $T = 20 \text{ }^\circ\text{C}$. Velocidad de barrido de $0,5 \text{ mV s}^{-1}$.

A densidades de corriente bajas, donde no se espera un efecto significativo del transporte de masa y caída óhmica, esto puede explicarse, al menos parcialmente, por las diferentes áreas de superficie activa de ambas capas de catalizador. Se determinó que las áreas electroquímicamente activas (ECSA) para la oxidación de CO eran de 52,4 y 47,3 $\text{m}^2 \text{g}^{-1}$, para las CL hechas con NBA e IPA, respectivamente, es decir, aproximadamente un 11% mayor en la primera. A mayores densidades de corriente estos valores son aún mayores. Esta diferencia y la desviación de la forma exponencial en el rango de potencial 0,55-0,70 V sugieren fuertemente que hay efectos de limitación de transporte. Dicha limitación es más evidente para IPA y podría explicarse considerando el tamaño y porosidad de los aglomerados formados por el ionómero y las nanopartículas de catalizador en ambos disolventes, que son menores en IPA (Fig. 1). La porosidad más pequeña puede limitar el transporte de masa a través de la capa de catalizador y, por tanto, se puede ralentizar la velocidad de la difusión de los reactivos a los centros activos del catalizador y la velocidad de eliminación de los productos de reacción a partir de los mismos.

Conjunto membrana-electrodo (MEA)

La Fig. 12 muestra las curvas de polarización de los MEAs en que las capas de catalizador de ánodo se formularon con NBA e IPA, denominadas MEA_{NBA} y MEA_{IPA} , respectivamente, en celda sencilla DMFC con soluciones acuosas de 2 mol dm^{-3} CH_3OH a $60 \text{ }^\circ\text{C}$. El cátodo se alimentó con aire sintético seco a presión atmosférica. Puede observarse como las diferencias entre las densidades de corriente suministradas por los MEAs aumentan a medida que disminuye el voltaje de la celda (proporcionando así más intensidad de corriente). La curvatura que tiende a una densidad de corriente límite para el MEA_{IPA} muestra dicho límite para valores mucho menores que los obtenidos para MEA_{NBA} .

Las densidades de corriente suministradas por los MEA preparados con NBA e IPA al voltaje de interés técnico de 0,400 V eran de 148 y 85 mA cm⁻², respectivamente, correspondientes a una densidad de potencia de 59 y 34 mW cm⁻², en ese orden. La densidad de potencia dada por el MEA preparada con NBA corresponde a una mejora de aproximadamente el 74 % en comparación con el MEA preparado con IPA. Esta diferencia en el rendimiento de la celda DMFC se debe únicamente a la capa de catalizador del ánodo en los MEA, ya que el resto de la celda era, por lo demás, la misma. La interpretación de los resultados de espectroscopia de impedancia electroquímica (EIS) indica que la resistencia protónica para el NBA es significativamente menor que para el IPA, lo que sugiere que el mayor número de centros activos accesibles para la oxidación de metanol en el primero están bien conectados con los ionómeros de Nafion[®] y son más fácilmente transportados hacia la membrana.

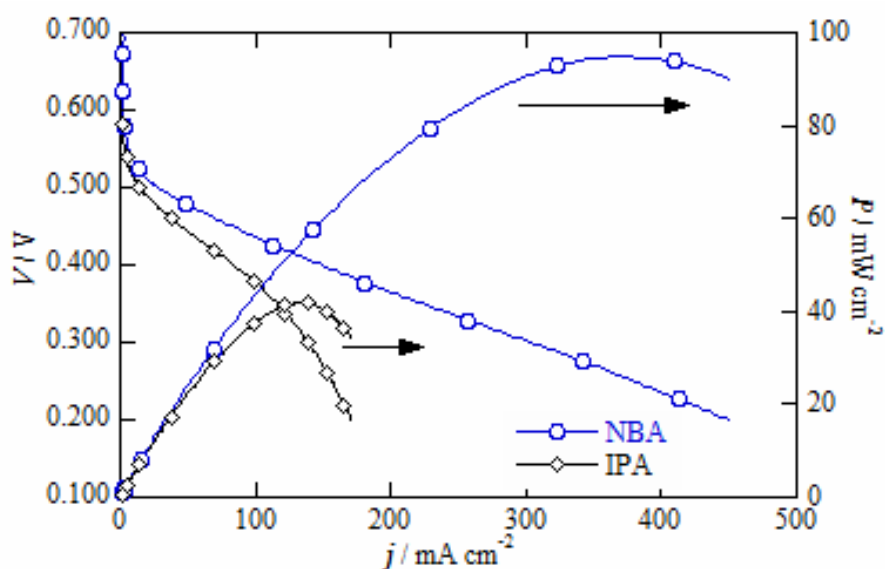


Figura 12 Curvas de polarización V - j y curvas P - j para la celda DMFC con ánodos de negro de PtRu formulados con diferentes tintas conteniendo: (○) NBA e (◇) IPA. Cátodos catalizados con negro de Pt. $T = 60$ °C; $[\text{CH}_3\text{OH}] = 2.0$ mol dm⁻³; flujo del combustible = 2 mL min⁻¹; flujo del aire = 100 mL min⁻¹.

Finalmente, con el fin de comprender si el tamaño de cristalito del catalizador podría contribuir a la diferencia observada en el rendimiento de la pila de combustible, se obtuvieron los espectros de difracción de rayos X de las capas de catalizador de PtRu preparadas usando NBA (PtRu-NBA) o IPA (PtRu-IPA) y negro de PtRu. En este sentido, no se encontró ninguna diferencia significativa entre los tamaños de cristalito de las tres muestras, lo que indicaría que se puede excluir este efecto como el causante de la diferencia de prestaciones observada en MEA, tanto en la preparación de la tinta de catalizador, como después de la preparación del MEA.

1. Introduction

Renewable sources for energy are getting significant attention within the recent years. Main reason is the increased global warming, caused by the combustion of fossil fuels. The utilization of fossil sources as fuels would release CO_x, carbon black, heavy metals, ash, tars and organic compounds. Today concerns about air pollution, energy security and climate change, leads to a search for new, environmentally friendly, economically attractive, and commonly accessible and renewable energy sources.

Fuel cells are electrochemical devices, which convert the chemical energy released in electrochemical reactions directly into electrical energy. The fuel used is typically a hydrocarbon or a substance derived from it or based on it, *e.g.* hydrogen or alcohol. The fuel cells are normally classified according to the type of electrolyte and operation temperature. The low temperature fuel cells are Alkaline Fuel Cell (AFC), Phosphoric Acid Fuel Cell (PAFC), Polymer Electrolyte Membrane Fuel Cell (PEMFC) and Direct Methanol Fuel Cell (DMFC). The DMFC differs from PEMFC by the anode reactant, which is commonly a liquid mixture of water and methanol instead of gaseous hydrogen in the PEMFC. The high temperature fuel cells are Solid Oxide Fuel Cell (SOFC) and Molten Carbonate Fuel Cell (MCFC) [1]. Overview of the different types of fuel cells is presented in Table 1.1. This thesis is dealing with DMFC.

Table 1.1 Comparison between different fuel cell technologies.

	PEMFC	DMFC	AFC	PAFC	MCFC	SOFC
Transportation application	Automotive power	APU ¹ bicycles, Automotive power	Space vehicles, Apollo. Shuttle	Large vehicle power	Ship service and auxiliary power units	Vehicle auxiliary power, heavy vehicle propulsion
Other applications	Portable power, small-scale stationary UPS ² (uninterruptible	Portable power, electronic device	Portable power source	On-site cogeneration, electrical power	On-site cogeneration, electrical power generation,	On-site cogeneration, stationary power

	power supplies)			generation (200 kW)	subMW to multi-MW	generation, 2kW to 100 kW, portable military applications
Electrolyte	Polymer (plastic) membrane (Nafion/Dow) protons mobile, electrolyte immobile (hydrated membrane as the electrolyte)	Polymer (plastic) membrane (Nafion/Dow/Gore) protons mobile, electrolyte immobile (hydrated membrane as the electrolyte)	Solution of concentrated (30%-50%) KOH in water	Liquid concentrated phosphoric acid retained in a matrix of silicon carbide particles held by PTFE	Liquid molten carbonate (Li ₂ CO ₃ /K ₂ CO ₃ or Li ₂ CO ₃ /Na ₂ CO ₃) retained in ceramic matrix of LiAlO ₂	Solid oxide ceramic: yttrium-stabilized zirconium dioxide (ZrO ₂ /Y ₂ O ₃)
Operating temperature	50-100 °C	25-90 °C	50-200 °C	150-220 °C	600-700 °C	600-1000 °C
Charge carrier through electrolyte	H ⁺	H ⁺	OH ⁻	H ⁺	CO ₃ ²⁻	O ²⁻
Prime cell components	Carbon-based	Carbon-based	Carbon-based	Graphite-based	Metal and ceramics	Ceramic
Catalyst	Platinum (Pt, PtRu)	Pt/Ru on anode, Pt on cathode	Platinum	Platinum	Nickel	Nickel perovskites
Primary Fuel	H ₂	CH ₃ OH	H ₂	H ₂	H ₂ , CO, CH ₄	H ₂ , CO, CH ₄
Product water management	Evaporative, diffusive	Evaporative, diffusive, recycled	Evaporative	Evaporative	Gaseous product	Gaseous product
Product thermal management	Process gas + independent cooling medium	Process streams/natural breathing + independent cooling medium	Process gas + electrolyte circulation	Process gas + independent cooling medium	Internal reforming and/or + process gas	Internal reforming and/or + process gas
Startup time (from STP ³)	Seconds-minutes	Seconds-minutes		Hours	Hours	Hours
Power density [kW m ⁻² of active cell area]	3.8-6.5	0.4-0.6 at ambient (10 times higher at 90 °C, but not robust, complex)	~1	0.8-1.9	1.0-2.0	2.0-7.0
Fuel cell efficiency	50-60%	20-30%	50-60%	55%	55-65%	60-65%
Reformer	External	N/A	External	External	Internal or external	Internal or external
Status of development	Demonstration systems up to 50 kW. 250 kW units expected	Demonstration up to 100 kW	Due to CO ₂ poisoning, there is	Most commercial systems operating at	Commercial, pre-commercial units available in 250 kW, 1 MW and 3	Demonstration systems up to 300 kW

	in next few years		very little development going on	200 kW, an 11 MW model has been tested	MW modules	
Technical challenges	Lower cost of catalyst and membranes, improve performance/long term durability of MEAs, develop high temperature MEAs, extend high current density, improve sensitivity to fuel contaminants (CO, sulfur, higher hydrocarbons)	Lower cost of catalyst, reduce methanol crossover, need higher power output, increase fuel utilization, develop advanced high temperature membrane, develop integrated sensors and controls	Lower cost, CO ₂ removal both from the H ₂ and air streams	Lower cost of catalyst and bipolar plate, improve performance and high power density, corrosion resistant materials	Lower cost of stack with acceptable life, balance of power plant cost reduction, increased manufacturing volume	Improve performance, electrolyte leakage, structural stability and composition, increase sulfur tolerance, reduce bipolar plate corrosion and improve durability (continuous operation and thermal cycling), reduce startup time for automotive applications

¹ APU Automotive power unit

² UPS Uninterruptible power supplies

³ STP Standard temperature pressure (standard conditions)

When pure hydrogen is used directly as a fuel, only water is generated and no pollutants are emitted. However, hydrogen is not available for direct use in the nature and therefore, hydrogen fuel must be produced from a variety of sources. Its lightness appears to be a problem for its storage, transportation and use in its gaseous form. The small H₂ molecule can also diffuse through most materials. It can be condensed at very low temperature of -253 °C. Hydrogen can also ignite or explode in contact with air and should be stored with a substantial care, mainly for transport applications. The handling of volatile and potentially explosive hydrogen gas needs special conditions (high pressure, cryogenic tanks, special materials to minimize diffusion and leakage, etc.) as well as strict adherence to extensive safety precautions, all of which make hydrogen rather costly as a fuel. On the other hand methanol, as a liquid, is significantly safer and easier to store and to transport. At present it is mostly prepared from synthesis gas (syn-

gas, CO and H₂ mixture), obtained mainly from the incomplete combustion of fossil fuels. Methanol can also be obtained from biomass, but this method plays a minor role in the methanol production methods. The production of methanol is also possible by the oxidative conversion of methane or by reductive conversion of CO₂ with H₂. The former could be obtained from industrial exhaust from fossil fuel power plants or captured from the atmosphere. The methanol production in this form can be conceived as storing hydrogen in liquid form, which is easier to manage. In addition, this would allow CO₂ recycling, which would help in the attempts for the climate change mitigations [2].

Besides its application as a fuel and energy storage, methanol also is an important starting material for wide range of chemicals such as formaldehyde, acetic acid, a variety of products like polymers, paints and pharmaceuticals. The concept of the so-called “methanol economy” [2] suggests the use of methanol for: (i) energy storage means; (ii) readily transportation and fuel dispensing, especially for DMFC, and (iii) feedstock for a wide variety of products and chemicals.

To deal with small CO₂ emitters and to avoid the need to constructing huge CO₂ collecting infrastructure, CO₂ can be captured from the atmosphere directly, independently of the CO₂ source. This can be done by the use of absorbents such as calcium hydroxide or potassium hydroxide, both reacting with CO₂ to produce carbonates. CO₂ extraction facilities can be placed anywhere but for further methanol synthesis it is more useful if they are placed close to the place for H₂ production. CO₂ can be released by heating, by the effect of vacuum or by electrochemical means.

The removal of significant share of CO₂ from industrial emissions and CO₂ capture from the atmosphere could release a significant amount of available CO₂. This

CO₂ could be recycled by its utilization in methanol synthesis. The methanol recycling cycle in the nature is shown in Fig. 1.1.

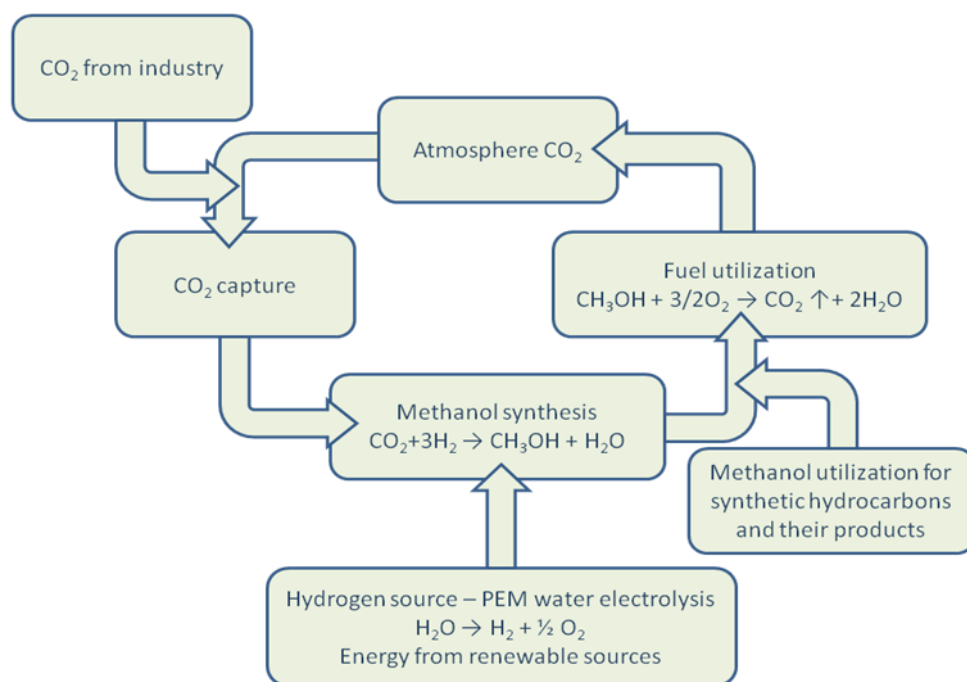


Figure 1.1 CO₂ recycling cycle in the nature [2].

The recycling of CO₂ includes its chemical reduction with H₂ to methanol, its further utilization as a fuel or for the production of hydrocarbons and their products, releasing of CO₂ in the atmosphere due to combustion processes of methanol or hydrocarbons, CO₂ capture and further release for the purposes of methanol synthesis. Hydrogen required for the methanol production could be obtained by water electrolysis or other hydrogen production method (Table 1.2) [3], but a carbon neutral cycle regarding CO₂, requires obtaining H₂ from a renewable sources, by electrolysis.

A variety of processes are available for H₂ production which can be divided into two groups according to the raw materials: conventional and renewable technologies. The first group includes the methods of hydrocarbon reforming and pyrolysis of fossil fuels. In hydrocarbon reforming process, the participating chemical techniques are

steam reforming, partial oxidation and autothermal steam reforming. The second group includes the methods which produce hydrogen from renewable resources, either from biomass or water. The methods utilizing biomass as a feedstock can be subdivided into two general subgroups namely thermochemical and biological processes. The second class of renewable technologies regards the methods, which can produce H₂ through water-splitting processes such as electrolysis, thermolysis and photo-electrolysis, utilizing water as the only raw material. Major advantages and disadvantages of the different methods are summarized in Table 1.2 [3]. This thesis focuses on electrolysis, specifically on polymer electrolyte membrane water electrolysis (PEMWE) technology.

Table 1.2 Comparison of the different hydrogen production methods.

Process	Efficiency (%)	Major advantages	Major disadvantages
SR ¹	74-85	Most developed technology, existing infrastructure	CO ₂ byproduct, dependence on fossil fuels
POX ²	60-75	Proven technology, existing infrastructure	CO ₂ byproduct, dependence on fossil fuels
ATR ³	60-75	Proven technology, existing infrastructure	CO ₂ byproduct, dependence on fossil fuels
CHs pyrolysis	-	Emission-free, reduced-step procedure	Carbon byproduct, dependence on fossil fuels
Biomass pyrolysis	35-50	CO ₂ -neutral, abundant and cheap feedstock	Tar formation, varying H ₂ content due to seasonal availability and feedstock impurities
Biomass gasification	-	CO ₂ -neutral, abundant and cheap feedstock	Tar formation, varying H ₂ content due to seasonal availability and feedstock impurities
Bio-photolysis	10	CO ₂ -consumed, O ₂ is the only byproduct, operation under mild conditions	Requires sunlight, low H ₂ rates and yields, requirement of large reactor volume, O ₂ sensitivity, high raw material cost
Dark fermentation	60-80	CO ₂ -neutral, simple, can produce H ₂ without light, contributes to waste	Fatty acids removal, low H ₂ rates and yields, low conversion efficiency,

		recycling, no O ₂ limitation	requirement of large reactor volume
Photofermentation	0.1	CO ₂ -neutral, contributes to waste recycling, can use different organic wastes and wastewaters	Requires sunlight, low H ₂ rates and yields, low conversion efficiency, requirement of large reactor volume, O ₂ sensitivity
Electrolysis	40-60	No pollution with renewable sources, proven technology, existing infrastructure, abundant feedstock, O ₂ is the only byproduct, contributes to RES integration as an electricity storage option	Low overall efficiency, high capital cost
Thermolysis	20-45	Clean and sustainable, abundant feedstock, O ₂ is the only byproduct	Elements toxicity, corrosive problems, high capital costs
Photo-electrolysis	0.06	Emission-free, abundant feedstock, O ₂ is the only byproduct	Requires sunlight, low conversion efficiency, non-effective photocatalytic material

¹ SR - Steam reforming

² POX - Partial oxidation

³ ATR - Autothermal steam reforming

1.1 Water electrolysis

Water electrolysis offers a practical route for sustainable hydrogen production by utilizing a renewable electrical energy source for water splitting. The reaction, however, is very endothermic thus the required energy input is provided by electricity. A typical electrolysis unit consists of a cathode and an anode immersed in an electrolyte, and generally when electrical current is applied water splits and hydrogen is produced at the cathode and oxygen is evolved on the anode side, according to the following reaction [3,4]:



which is endothermic (the backward reaction is that occurring in the hydrogen fuel cell). At room temperature the splitting of water is very small, approximately 10^{-7} moles per liter due to the poor electric conductivity of water. Therefore, acid or base is added to improve it. The solution splits into ions and these ions readily conduct electricity in a water solution by flowing between the electrodes.

Depending on the electrolyte used in the electrolysis cell, three different electrolyzers for electrochemical water splitting are available: alkaline water electrolyser, solid-polymer electrolyte (SPE) water electrolyser (WE), which can also be called polymer-electrolyte membrane (PEM) WE, and solid oxide electrolyte cell (SOEC). Major differences in the three technologies are shown in Table 1.3.

Table 1.3 Differences between Alkaline, PEM and Solid oxide water electrolysis.

Technology	Operating temperature	Cathode reaction (HER)	Anode reaction (OER)	Charge carrier
Alkaline electrolyser	40 – 90°C	$2H_2O + 2e^- \rightarrow H_2 + 2OH^-$	$2OH^- \rightarrow \frac{1}{2} O_2 + H_2O + 2e^-$	OH^-
PEMWE	20 – 100°C	$2H^+ + 2e^- \rightarrow H_2$	$2H_2O \rightarrow \frac{1}{2} O_2 + 2H^+ + 2e^-$	H^+
SOEC	700 – 1000°C	$H_2O + 2e^- \rightarrow H_2 + O^{2-}$	$O^{2-} \rightarrow \frac{1}{2} O_2 + 2e^-$	O^{2-}

As a well-established technology alkaline water electrolysis is the dominating technology due to the lower cost of production. Typically, alkaline units are operated at temperatures around 80 °C. PEM water electrolysis, on the other hand, may offer advantages like improved energy efficiency, higher production rate, purer hydrogen, and a more compact design [1,5-9]. PEM technology is also usually employed at around 80 °C. SOEC technology operates at high temperatures such as 800 °C, and offers a significant reduction in consumption of electrical energy, but usually requires a source of high-temperature heat.

The main features of the design and components of the PEM electrolyser offer several advantages over other electrolysis technologies [10]:

- The membrane as a solid electrolyte is very thin, which allows shorter proton transport and therefore, lower ohmic loss.
- High efficiencies and faster kinetics are allowed by the electrocatalysts that are platinum group metals.
- Since the electrode is coated as a thin layer onto the membrane, the proton transfer from the reaction sites to the solid electrolyte surface is facilitated, which minimize the mass transport limitation.
- The electrolyte is immobilized in the membrane and cannot be leached out of the membrane to contaminate the produced gases.
- The membrane provides high gas tightness.
- The cell design is very compact resulting in low thermal masses and fast heat-up and cooling-off times and in combination with the fast kinetics of the electrocatalysts, in a very fast response time even at ambient conditions.
- Only pure water is fed to the cell that entails a simple system design.

The main disadvantages of PEMWE can be summarized as follows:

- The membrane as a solid electrolyte is more expensive than the liquid electrolyte in the alkaline electrolyser.
- The membrane is very thin foil and can be easily damaged by an inappropriate cell design and operation.
- The corrosive nature of the membrane requires more expensive metal components.
- Chemical degradation may occur depending on the used materials.
- The electrodes are mostly catalysts systems with structures at the nanoscale that requires a comprehensive understanding for a high electrochemical durability.

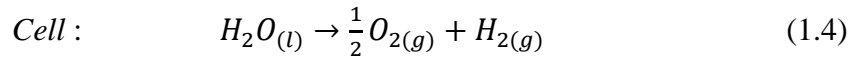
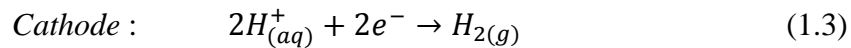
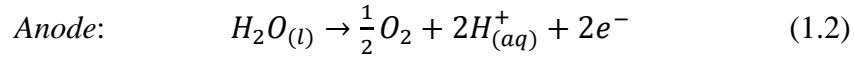
Higher cost of the components and the acidic corrosive environment are the main challenges and represent a major scientific interest toward better durability and commercialization of the PEM technology.

Table 1.4 Advantages and disadvantages of Alkaline electrolysers, PEMWE and SOEC [3].

Technology	Advantages	Disadvantages
Alkaline electrolyser	Well established technology Non noble catalysts Long term stability Relative low cost	Low current densities Crossover of gases (low degree of purity) Low partial load range Low dynamics Low operational pressures Corrosive liquid electrolyte
PEMWE	High current densities High voltage efficiency Good partial load range Rapid system response Compact system design High gas purity Dynamic operation	High cost of components Acidic corrosive environment Possibly low durability Commercialization Stack below MW range
SOEC	Efficiency up 100% Thermoneutral efficiency >100% w/hot steam Non noble catalyst High pressure operation	Laboratory stage Bulky system design Durability (brittle ceramics) No dependable cost information

1.2 Basic principles of water electrolysis. Theory

Water electrolysis is the electrochemical splitting of water into the gases hydrogen and oxygen. An electrical power source is connected to two electrodes, the anode and the cathode which are usually placed in water containing an electrolyte. Hydrogen evolves on the cathode (negative) and oxygen releases on the anode (positive electrode). In PEM water electrolysis, the electrodes are attached to the membrane, which conducts ions, typically protons, between the electrodes. The electrons are transported by the external circuit. In the PEMWE cathode the electrons and protons are recombined to form hydrogen. The electrode and total reactions are given by reactions 1.2-1.4:



1.2.1 Thermodynamics

The nature of the electrochemical equilibria of water with molecular hydrogen and oxygen provides a useful system in which energy can be stored with water electrolysis or released with fuel cells [11,12]. The two half-reactions that describe electrochemical water splitting are given by reactions 1.2 and 1.3 and the net reaction is given by reaction 1.4. The Gibbs energy change of reaction 1.4, ΔG , is given by Eq. 1.5:

$$\Delta G = \mu_{H_{2(g)}} + \frac{1}{2}\mu_{O_{2(g)}} - \mu_{H_2O_{(l)}} = \Delta G^0 + RT \ln(p_{H_2} p_{O_2}^{1/2}) \quad (1.5)$$

where the terms μ_i are the chemical potentials of the indicated species and ΔG^0 is the standard Gibbs energy of that reaction. The activity of water is assumed to be unity. The energy balance of reaction 1.4 can be written as:

$$\Delta H = \Delta G + T\Delta S \quad (1.6)$$

where ΔH is the enthalpy and ΔS is the entropy of reaction 1.4.

The enthalpy of the reaction consists of two parts. ΔG corresponds to the minimum share of ΔH that has to be applied as work, for example as electricity. The term $T\Delta S$ represent the maximum share of ΔH which can be applied as thermal energy to the process. Under standard conditions the enthalpy of reaction 1.4 is $\Delta H^0 = 286 \text{ kJ mol}^{-1}$ (note that it is for liquid water).

Under reversible conditions (no losses in the process), the difference between the electrode potentials is the reversible cell potential E'_{rev} given by the Nernst equation:

$$E'_{rev} = -\frac{\Delta G^0}{nF} - \frac{RT}{nF} \ln(p_{H_2} p_{O_2}^{1/2}) \quad (1.7)$$

$$E'_{rev} = E'_{rev}{}^0 - \frac{RT}{nF} \ln(p_{H_2} p_{O_2}^{1/2}) \quad (1.8)$$

where n is the number of electrons transferred per molecule of produced hydrogen according to reaction 1.4, F is the Faraday constant and $E'_{rev}{}^0$ is the standard cell potential. Note that negative values for E'_{rev} and $E'_{rev}{}^0$ result from Eqs. 1.7 and 1.8, since we are taking into account the reaction opposite to that occurring in a spontaneous hydrogen fuel cell. Therefore, a cell potential of $E_{rev} = -E'_{rev}$ is theoretically the lowest potential at given conditions which must be applied between the electrodes for reaction 1.4 to proceed to the right.

At 298 K and atmospheric pressure, $\Delta G^0 = 237 \text{ kJ mol}^{-1}$ the standard reversible cell voltage E_{rev}^0 for the decomposition of liquid water can be calculated as:

$$E_{rev}^0 = \frac{\Delta G^0}{nF} = \frac{237 \text{ kJ mol}^{-1}}{2 \times 96485 \text{ C mol}^{-1}} = 1.23 \text{ V} \quad (1.9)$$

E_{rev} is the minimum cell voltage that is required for the decomposition of liquid water as long as heat corresponding to $T\Delta S$ can be integrated into the process. However, PEM water electrolysis is a low-temperature process and thermal energy cannot be added from the surroundings. In this limiting case, the missing energy has also to be supplied as electricity. Therefore, the minimum cell voltage under ideal conditions,

which is called thermoneutral cell voltage, E_{th} , for liquid water with the reaction in standard conditions, can be calculated as follows:

$$E_{th}^0 = \frac{\Delta H^0}{nF} = \frac{286 \text{ kJmol}^{-1}}{2 \times 96485 \text{ Cmol}^{-1}} = 1.48 \text{ V} \quad (1.10)$$

A voltage term $T\Delta S^0/nF = 0.25 \text{ V}$ must be added to the thermodynamic voltage E_{rev}^0 to provide the heat required by reaction 1.1. It should be noted that splitting of water vapour in place of liquid water requires less energy, the difference being the enthalpy change associated with water vaporisation. This is referred to the literature as low and high heating values (LHV and HHV, respectively) of H_2 formation [13,18].

When the cell potential equals to the thermoneutral voltage no net heat exchange from environment takes place. At $E_{cell} < E_{th}$, the cell absorbs heat from outside, and when $E_{cell} > E_{th}$, than the cell release heat and needs to be cooled.

Table 1.5 Thermodynamic quantities for reaction 1.4 [14, 15].

T / K	$\frac{\Delta H^0}{nF} / V$	$\frac{\Delta G^0}{nF} / V$	$\frac{T\Delta S^0}{nF} / V$
298	1.481	1.229	0.2521
373	2.469	1.167	0.3018

From the thermodynamic point of view, high-temperature water electrolysis is preferred as ΔG^0 decreases when the temperature increases and the splitting of water requires then less electricity. According to Eq. 1.9, the values of E_{rev}^0 are consequently reduced with the temperature increase. However, ΔH^0 and thus E_{th}^0 , remain nearly constant with temperature, resulting in a higher demand for heat $T\Delta S^0$ (Fig. 1.2).

As PEM water electrolysis is roughly limited to the temperature range from room temperature to 373 K, only slight changes in ΔH° and ΔG° , and therefore in E_{th}^0 and E_{rev}^0 , can be observed (Table 1.5).

The thermal energy efficiency can be defined as:

$$\varepsilon_{\Delta H} = \frac{E_{th}}{E_{cell}} \quad (1.11)$$

whereas the energy efficiency in terms of Gibbs energy can be defined as:

$$\varepsilon_{\Delta G} = \frac{E_{rev}}{E_{cell}} \quad (1.12)$$

In an electrochemical process the energy efficiency is better expressed by $\varepsilon_{\Delta G}$, which represents the efficiency in terms of the available work [15].

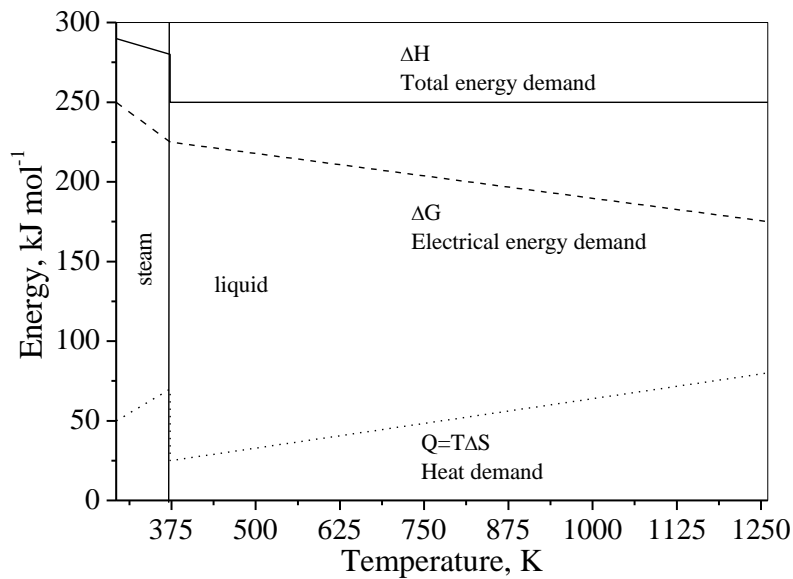


Figure 1.2 Energy required for water electrolysis. Increasing the temperature above 100 °C (373K) increases the heat demand but reduces the electrical energy required. The total energy required is lower at high temperature, but it does not include the heat required to raise the temperature in the incoming water.

1.2.2 Kinetics

The cell voltage, E_{cell} , of an operating electrolysis cell is significantly higher than the theoretical reversible cell voltage, E_{rev} , derived from Thermodynamics. Some extra

voltage is needed to overcome the irreversibilities resulting from reactant products, transportation, charge transfer and resistance of electrolyte and electrodes in the electrolysis process.

The resistance due to membrane, electrolyte, bubbles, and circuit also contribute to the high energy consumption and are called ohmic voltage drop (R_{total}). The real cell voltage E_{real} can be expressed as a sum of the reversible cell voltage E_{rev} , voltage drop $i \times R_{total}$ when a current i circulates through the cell, and the overpotentials at the anode and at the cathode (oxygen overpotential and hydrogen over potential, respectively). Due to the more complex oxidation at the anode (the OER contains an overall transfer of 4 electrons), the overpotential at this electrode is dominant [1,16,17].

$$E_{real} = E_{rev} + |\eta_a| + |\eta_c| + i \times R_{total} \quad (1.13)$$

For an electron charge transfer between oxidized (O) and reduced (R) species



under activation conditions, the relation between the overpotential η and current density j is expressed by the Butler-Volmer equation:

$$j = j_0 \left\{ \exp\left(\frac{\alpha_a n F}{RT} \eta\right) - \exp\left(\frac{\alpha_c n F}{RT} \eta\right) \right\} \quad (1.15)$$

where j_0 is the exchange current density, α_a and α_c are the corresponding anodic and cathodic transfer coefficients. When reaction 1.14 is driven sufficiently to the anodic or to the cathodic direction, the respective cathodic or anodic terms are negligible and η can be solved to give the anodic or cathodic Tafel equations:

$$\eta_a = b_a \cdot \log \frac{j}{j_0} \quad (1.16)$$

$$\eta_c = b_c \cdot \log \frac{|j|}{j_0} \quad (1.17)$$

where b_a and b_c are anodic and cathodic Tafel slopes, respectively, which depend on the nature of the electrode and can be expressed by the equations:

$$b_a = \frac{RT \times 2.303}{\alpha_a n F} \quad (1.18)$$

$$b_c = -\frac{RT \times 2.303}{\alpha_c n F} \quad (1.19)$$

In the case when n is equal to one, the α values are usually close to 0.5 and they are related with the activation barrier of the charge transfer step. In addition, when $\alpha=0$ the reaction is spontaneous from the left to the right, and for $\alpha=1$, the spontaneous reaction is the reverse one. For a proposed reaction mechanism with $n>1$, the rate determining step can be ascertained from the values of b_a and b_c . For a given electrocatalytic reaction the exchange current density depends on the nature of the electrocatalyst. The values of the exchange current density and Tafel slopes strongly indicate the performance of an electrocatalyst. The best electrocatalysts have the highest values of j_0 .

1.3 Proton Exchange Membrane Water Electrolysis (PEMWE).

Literature review

Typical design of a PEM water electrolysis cell is shown below. The components are membrane electrode assembly (MEA, includes membrane, anode and cathode electrodes), gas diffusion layer (GDL, current collector), gaskets, bipolar plates. The core component is the MEA. GDL and gaskets are used to enable an electric current to flow between the bipolar plates and the electrodes. The bipolar plates are electrically conductive and support the water transport to the electrodes and hydrogen and oxygen out of the cell.

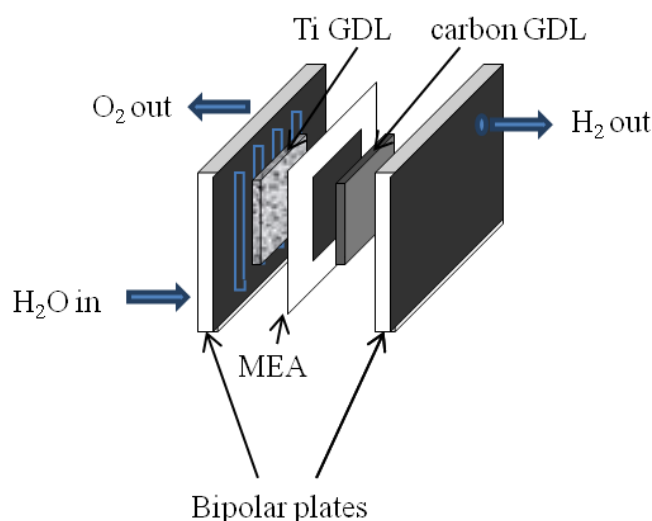


Figure 1.3 Typical design of a PEM electrolysis cell-

1.3.1 Bipolar Plates

Bipolar plates and current collectors together represent 48% of the PEMWE stack cost [4]. They contribute linearly to the ohmic losses within the cell. At high current densities the internal ohmic resistance and mass transport become the dominating sources of irreversibility. The combination of low ohmic resistance, good mass transport and cost of the material determine the bipolar plates for PEM water electrolysis.

The most common bipolar plates are made from titanium, graphite and coated stainless steel [4,18,19]. Titanium offers excellent strength, low initial resistivity, high initial thermal conductivity and low permeability. However, under aggressive environment on the anode side Ti corrodes until a passive oxide layer is formed, which affects the thermal conductivity and the contact resistivity [18,19]. For this reason, typically gold coating is used to protect the surface of the bipolar plate from corrosion.

Graphite is widely used in PEM fuel cells due to its high conductivity. However, its low mechanical strength makes it difficult for manufacturing. Additionally it corrodes very fast under the higher potentials applied at the anode.

Stainless steel is one of the less expensive alternatives that offers a good mechanical properties to facilitate the manufacturing of the bipolar plates and very good conductivity. However it corrodes very quickly in acidic environment, so protective coating is required [4,18,20,21]

Main functions of bipolar plates are [22, 23]:

- (i) to separate the individual cells in the stack
- (ii) to carry current away from the cell
- (iii) to remove heat from the active areas
- (iv) to prevent leakage of reactants
- (v) to facilitate water management within the cell
- (vi) to distribute the fuel and oxidant within the cell.

Therefore, the material for bipolar plates should meet the following criteria [22,24]: electrical conductivity, plate resistance, thermal conductivity, hydrogen/gas permeability, corrosion resistance, compressive strength and density.

The flow of the water can be controlled by employing different patterns in the bipolar plates. The bipolar plates have different designs to improve a gas flow by

avoiding the trapping of bubbles in the channels which reduce the overall active area. Many electrolyser designs, mainly those used in early development and testing, have been borrowed directly from PEM fuel cells. Different geometries and shapes of the channels have been investigated [25-27]. In [26], serpentine and parallel flow channels, together with current density distribution, have been compared. The current density in the middle region is near zero for the bipolar plates with parallel flow channel, which renders lower cell performance. Additionally the performance of the serpentine flow channel is insensitive to the different depths of the flow channel design [26], such as geometry, shape and direction of the fuel feed into the channels.

1.3.2 Gas Diffusion Layer

Typically the water travels via the channels on the bipolar plates and then diffuses through the current collectors. The water reaches the anode catalyst and water splitting takes place into electrons, protons and oxygen. Oxygen is released from the catalyst layer through the gas diffusion layer to the bipolar plate and out of the cell. Released electrons travel from the catalytic layer through gas diffusion layer (current collector), bipolar plates and then go to the cathode side. The protons go to the cathode side through the ionomer and crossing the membrane. On the cathode they combine with the electrons and hydrogen is evolved through the current collector to the bipolar plates and out of the cell. The main requirements to the current collectors can be summarized as follows [4,28]:

- (i) Due to the aggressive environment (high overpotential, acidic environment from the solid electrolyte, presence of oxygen) the current collectors must be corrosion resistant;
- (ii) To have very good electrical conductivity;

- (iii) Must provide mechanical support to the membrane, specially under higher pressure operating conditions;
- (iv) The gases evolution and removal out of the cell and water distribution must be facilitated, especially at higher current densities, where the mass transport is a limiting factor for the cell performance.

From a qualitative point of view, current collectors of large porosity will facilitate gas removal from the interfaces. However, they will also increase the ohmic resistance of the plates and introduce additional parasitic ohmic losses at contact points between current collector and catalytic layers, and between current collector and channels. Therefore the optimization of the geometry of the pore structure is required in terms of overall porosity and pore size distribution. For practical applications, a porosity of 30% is recommended as a minimum value. Concerning the upper limit, a value of 50% is a threshold above which mechanical strength of the porous plates becomes a limiting factor. Thus the recommended porosity is in the range 30–50% [19]. Current collectors with different porosities (25–40%) and different mean pore size values (8–100 μm) were tested. The optimum values for the pore diameter were found to be in the range 12–21 μm [19]. These observations correspond to atmospheric pressure, for current densities 0–2 A cm^{-2} .

The GDL is fabricated by either porous carbon materials (e.g., carbon cloth or carbon fiber paper or their modification) [29-31], or metals (e.g. Ti) [32] or gold plated porous titanium sinters [33].

Carbon materials like Toray Paper, Sigracet, and Freudenberg gas diffusion layer are lightweight, cheap, and have a small volume. However, at high temperatures or potentials they react easily with active oxygen species. The anode will then corrode due to the formation of carbon monoxide or carbon dioxide. The anode GDL should be

electronically conductive, corrosion resistant, non-ion leaching and allow easy transport of water to the membrane and active sites and simple gas release from the electrode structure.

Metallic diffusion layers have a high resistance toward corrosion. However, they would still form oxidized layers at their surfaces, and these will increase the resistance of the metallic diffusion layer during water electrolysis. To avoid this oxidation, thin layers of platinum or gold are used to protect the surface. Titanium properties have been discussed above in terms of the bipolar plates requirements. Typically for the purposes of anode current collectors, porous sintered titanium powder or fibers are used [8,13,19,34-38]. Grid and mesh were used as other, simpler for manufacturing, form of titanium [39-43] and Ti foil with small holes of 1.5 mm in diameter [44]. Ti foil can be protected with $0.5 \text{ mg}_{\text{Ir}} \text{ cm}^{-2}$. Other option for small lab scale PEMWEs and relatively fast experiments is carbon cloth or paper covered with Ti (Toray+50 nm sputtered Ti) [45].

1.3.3 Solid Polymer Electrolyte Membrane

Main requirements to the membrane are:

- (i) To exhibit high proton conductivity for the transport of the ions from the anode to the cathode;
- (ii) Low permeability of gases, in order to prevent mixing of the produced gases;
- (iii) An electric insulator to prevent short-circuits within the cell;
- (iv) Ionomer must have high chemical and mechanical stability to withstand the harsh conditions in a PEM electrolysis cell.

Perfluorosulfonic acid polymers (PFSA) membranes are used such as Nafion[®], Flemion[®], Fumapem[®] and Aciplex[®]. The thickness of these membranes is in the range of 50 to approximately 200 μm . These membranes are known with their high oxidative

stability, high strength, high efficiency [1,4,46]. However, they have to be used at temperatures below 373 K, since dehydration of the ionomer takes place at higher temperatures, thus resulting in a loss of mechanical stability and proton conductivity. The hydration state of the membrane in the electrolyser is different from that of the fuel cells [4]. During fuel cell operation, the membrane is humidified from the humidified gases while in PEM water electrolyser the membrane is exposed to the liquid water and is fully hydrated [4,47]. Despite these different boundary conditions the water uptake and performance may or may not be affected [4,48,49].

Second type of solid polymer electrolyte at low temperature is SPEEK, sulfonated polyetherketone. Sulfonated aromatic high performance polymers exhibit similar domain formation and proton conductivity as Nafion[®] at high levels of hydration [46].

The operating temperature of the above mentioned membranes can be increased if materials such as inorganic oxides (i.e. SiO₂ [50-52], TiO₂ [52-54], ZrO₂ [50,52,55], CeO₂ [56,57]) are used as fillers to improve the water retention inside a PSFA membrane, which allows operation temperatures above 100 °C.

For higher temperatures the alternative membrane is poly[2,2'-(m-phenylene)-5,5'-bibenzimidazole] (PBI), which has a high-proton conductivity and excellent mechanical properties. However, PBI membranes need to be doped with highly concentrated phosphoric acid to achieve a sufficient conductivity. High conductivity, good mechanical properties and thermal stability have been reported at temperatures up to 200 °C under ambient pressure. Chemically, PBI is a basic polymer and can readily react with a strong acid. Phosphoric acid is of special interest because of its high proton conductivity, also in dry conditions, as well as its excellent thermal stability and very low vapour pressure at high temperatures [58-61].

Alternatively, pyridine containing poly (ether sulfone) [63], which has a high molecular weight, excellent mechanical properties as well as thermal and oxide stability [64], and PTFE [59], as support materials for Nafion[®] [51,52,56] or PBI [58] were applied in high temperature fuel cells and might find application in PEM water electrolysis as well.

A compromise between the properties (i)-(iv) reported above needs to be achieved regarding membrane thickness. Thinner membrane will have higher conductivity and will positively affect the performance of the MEA, but such a thin membrane cannot withstand the operating conditions of PEMWE such as pressure and high currents. Thicker membrane will result in MEA performance losses due to higher resistance. For this reason the thickness of the membrane is very important and needs to be optimized. Nafion[®] 115 (127 μm) is one of the mostly used membranes [8,36,38,40,43-46], and another one is Nafion[®]117 (178 μm) [13,34,35,37,42].

1.3.4 Electrocatalysts for the hydrogen evolution reaction (HER)

The standard potential of H₂ is zero by convention. As a first approximation the electrochemical activity of HER on different metals can be compared by the so-called "Vulcano-plot", where $\log(j_0)$ is related to the bond energy of atomic H chemisorbed on the metal [65]. A "Vulcano-plot" is shown in Fig. 1.4 where it can be seen that the metals of intermediate bond-strength energy, represented by the noble metals, are the most active towards the HER [65]. For the metals having low bond-strength (left-hand side of the curve), discharge of H becomes the rate determining step, whereas for the metals with high bond-strength (right-hand side), the H desorption step becomes rate determining [66]. The noble metals are of particular interest here due to their corrosion resistance in acidic solution. The reaction of HER together with the Tafel slopes of the rate determining steps are given in Table 1.6.

Pt is known as the most active catalyst for the HER and is commonly used in fuel cells as hydrogen oxidation and oxygen reduction catalyst. However, its high cost is a drawback to be used in large-scale applications. There are several ways of decreasing the Pt loading in proton exchange membrane fuel cells (PEMFCs) and PEMWEs [5,8,67-77]: (i) finding cheaper non noble catalysts or (ii) use of specific supports to achieve better dispersion and higher catalytic surface. Due to the extensive research in the field of fuel cells, commercially available Pt and Pd catalysts, unsupported or supported on carbon, from different manufacturers (EOTEK/BASF, Tanaka, and Johnson & Matthey), have been widely used. However, these catalysts represent a significant part of the PEM electrolyser corrosion due to corrosion of the carbon support [78,79].

Pt and Pd nanoparticles unsupported or supported on carbon blacks with high surface area have been compared in [8]. It has been shown that the performance of a single electrolysis cell at 90 °C with a Pd cathode is comparable to that using Pt. Replacement of Vulcan-XC-72 with carbon nanotubes (CNTs) results in improved behaviour toward HER [69]. Non-noble materials as cobalt and nickel glyoximes have been tested toward electro-reduction of protons. However, the main requirements in this field are improving the surface area of the electrodes and optimising their ability to reduce protons to molecular hydrogen [70].

MoS₂ is another compound studied as an alternative catalyst for the HER [71,72]. It was supported either on graphite [71] or on reduced graphene oxide (rGO) [72]. It exhibited significantly lower performance in comparison to conventional Pt cathodes. The MoS₂/rGO hybrid exhibited improved behaviour with respect to MoS₂ catalysts, but still they were not comparable to Pt. MoO₃ nanowires [73], Cu_{1-x}Ni_xWO₄ [74], heteropolyanions of tungstophosphoric acid (PWA) hybridized with CNTs [75], WO₃

nanorods [76,77] have been tested for HER. However, the results for these catalysts are not comparable to the conventional Pt catalysts.

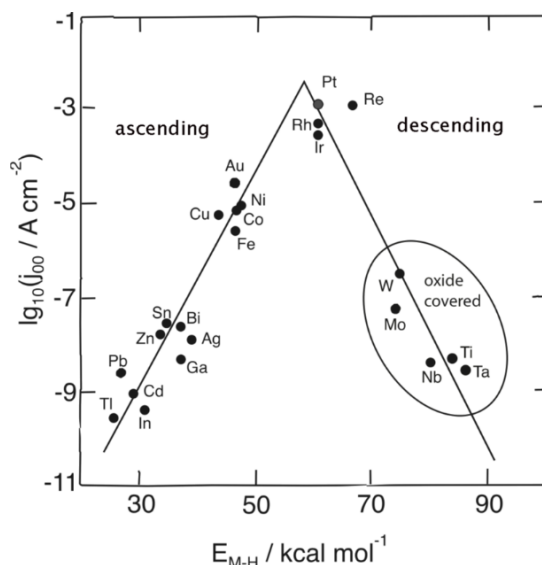


Figure 1.4 Volcano-plot of HER on different metals [65]

Table 1.6 Reaction steps and Tafel slopes of HER [80].

Rate determining step (rds)		$b_a / \text{mV dec}^{-1}$		
		low η	high η	
$M + H_3O^+ + e^- \rightleftharpoons M-H_{ads} + H_2O$	(1.20)	120	120	Tafel
$M-H_{ads} + H_3O^+ + e^- \rightleftharpoons M + H_{2(g)} + H_2O$	(1.21)	40	120	Heyrovsky
$2M-H_{ads} \rightleftharpoons 2M + H_{2(g)}$	(1.22)	30	∞	Tafel

1.3.5 Electrocatalysts for the oxygen evolution reaction (OER)

Oxygen evolution is more complex reaction than HER. It includes oxide generation on the metal surface by breaking of chemical bonds and formation of new bonds between the oxygenated species and the metal ions on the surface during the anodic reaction. Volcano plots for the OER shows the relation of the catalytic activity (η or $\log(j)$) depending on the enthalpy of transition from a lower oxidation state oxide to

a higher oxidation state oxide (representing the binding energy of adsorbents) [81]. IrO₂ and RuO₂ are situated near the peak of the volcano plot, thus indicating the highest catalytic activity of Ru and Ir oxides towards OER.

Metal oxides react with water and become covered by H or OH groups, depending on pH. Water molecules are adsorbed onto the surface metal cation while a proton from a water molecule becomes transferred to a neighboring oxygen atom in the oxide lattice [81].

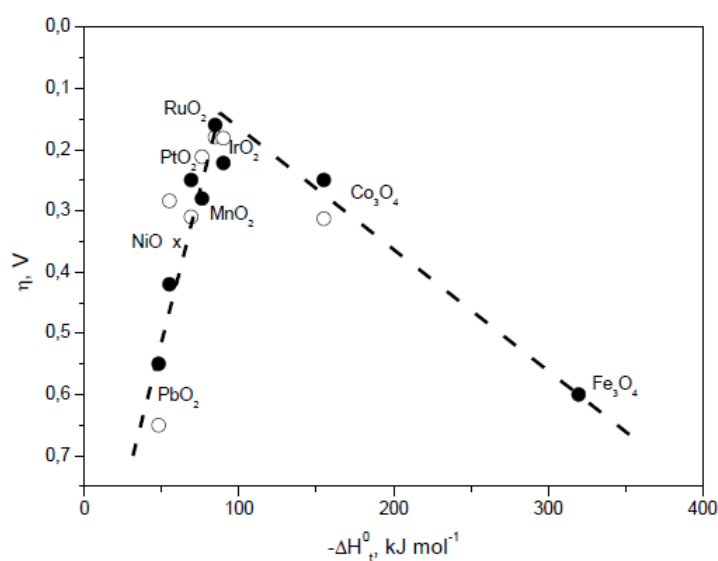


Figure 1.5 Electrocatalytic activity towards OER of various oxides as a function of the enthalpy of transition of lower to higher oxidation state oxide in acid (○) and in alkaline (●) solution [81].

Table 1.7 lists the generally proposed rate determining steps in the reaction mechanism of the oxygen evolution reaction on active oxide electrodes in acidic media together with the corresponding Tafel slopes for low and high overpotentials.

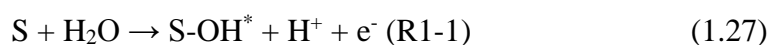
It is known that the rate determining step (rds) is related with the value of the Tafel slope. If the observed Tafel slope is of 120 mV dec⁻¹, the rds would be the first electron transfer R1 (Eq. 1.23). The Tafel slope of 40 mV dec⁻¹ indicates R2 (Eq. 1.24) as the rds (dissociation of the O–H bond in the S–OH group). Similarly, Tafel slopes of

30 and 15 mV dec⁻¹ indicate that the *rds* would be the recombination of S-OH, R2' (reaction (1.25)) and that of S-O, R3 (reaction (1.26)).

Table 1.7 Reaction steps and Tafel slopes for OER [82, 83], where S represents the active sites on the oxide surface (Ir and Ru).

Rate determining step (rds)		b_a / mV dec⁻¹ low η	b_a / mV dec⁻¹ high η
S + H ₂ O → S-OH* + H ⁺ + e ⁻ (R1)	(1.23)	120	120
S-OH → S-O + H ⁺ + e ⁻ (R2)	(1.24)	40	120
S-OH+S-OH →S-O+S+H ₂ O (R2')	(1.25)	30	∞
S-O + S-O →O ₂ + 2 S (R3)	(1.26)	15	∞

On the other hand, Tafel slopes of 60 - 120 mV dec⁻¹ were reported in the literature [83-88]. Faria et al. [83] proposed slightly changed mechanism of step R1 (reaction (1.23)). It is possible that the intermediate S–OH is first formed as an unstable species (S–OH*). Thus, R1 could be replaced by the following two steps:



The mixed kinetic control of those two steps gave a Tafel slope of 60–120 mV dec⁻¹ [83].

Reactions R2 and R2', (1.24) and (1.25), respectively, occur in parallel and the main process is determined by the adsorption coverage of the S–OH group [83,84]. At high surface density of adsorbed OH, neighbouring S–OH groups would easily combine so R2' (reaction (1.25)), would be relatively enhanced. Conversely, if the surface density of adsorbed OH is small R2 (reaction (1.24)), would be dominant. As already observed in [84] the density of adsorbed OH groups on the amorphous surfaces is much

larger than that on the crystalline surfaces. Thus, R2 (reaction (1.24) can be expected to be the *rds* at low current densities.

For the oxygen evolution reaction the electrocatalysts are typically unsupported due to the high potentials applied on the anode and the impossible application of the conventional carbon supports. Ru and RuO₂ are proved to be the best electrocatalysts for the oxygen evolution reaction [84] However, they have a serious problem of stability. The use of Ir black under the operating conditions of the anode leads to surface oxidation of the catalyst to iridium oxides [39]. IrO₂ has been shown to be the most stable and very active anodic electrocatalyst. It has been widely used for MEA preparation, optimization and evaluation [32,40,43,45,89]. Typical loads of the electrocatalyst are 2-4 mg cm⁻², and the main target is to be decreased by searching more active catalysts or by increasing the active area of IrO₂ using suitable supports. Some attempts to stabilize the active but less stable RuO₂ either by means of using different supports or forming mixed oxides with IrO₂ have been performed [36,37,38,41,42]. In order to achieve higher electrocatalytic performance for IrO₂, it has been synthesized as mixed oxide with several other oxides such as Ta₂O₅ [36,42] and SnO₂ [90,91], and by formation of RuIrCoO_x [92], Ru_xNb_{1-x}O₂ [93] and IrNbO_x [94]. Slightly better performance of MEAs prepared with Ir-Ta oxide in comparison to IrO₂-Pt and IrO₂-RuO₂ at lower current densities has been observed in [42], while at higher current densities it results in a lower performance. No beneficial effect other than dilution of IrO₂ has been found in the case of mixed oxide formation with SnO₂. Mixed oxides containing up to 20 mol % of SnO₂ has not lead to significant change in the active area [90,91]. RuIrCoO_x prepared by chemical reduction showed better activity toward OER when compared to commercial IrRuO_x [92]. The stability of RuO₂ was improved by the addition of Nb forming mixed Ru_xNb_{1-x}O₂ oxide [93]. Furthermore, the

addition of Nb to IrO₂ inhibited the catalytic activity at room temperature [94]. However, small concentrations of Nb increased the catalytic activity at elevated temperatures.

Significant improvement in the anodic kinetics of water electrolysis at 80 and 130°C for IrO₂ supported on Sb-doped SnO₂ and tin pyrophosphate was reported [90,91]. Indium tin oxide (ITO) has been reported as a support for IrO₂ catalyst in the oxygen evolution reaction [95]. The MEA performance prepared with the supported IrO₂ has been very similar to the one prepared with unsupported IrO₂.

Supporting IrO₂ onto TiO₂ and Nb-doped TiO₂ has resulted in an improvement in the electrocatalytic activity towards OER despite the lower conductivity of TiO₂ [96]. Supporting IrO₂ onto Nb-doped TiO₂ has been reported in [97] and better stability in comparison to unsupported IrO₂ has been observed.

1.3.6 Supports for the hydrogen evolution (HER) and the oxygen evolution reaction (OER) catalysts

As mentioned in 1.3.4 and 1.3.5, there are two main ways to improve catalytic performance either towards HER, either towards OER: (i) formation of alloys (for Pt, HER) or mixed oxides (OER) by addition of new elements to the main compound and improving in this way the activity of the catalyst; or (ii) by the use of supports, in order to achieve better dispersion and higher catalytic surface area. The materials reported in the literature as supports for the HER or the OER catalysts have been indicated in sections 1.3.4 and 1.3.5, respectively. In this section, the review will be focused on the properties of the materials selected as supports in this thesis.

TiO₂ is well known with its thermal stability and chemical resistance and widely investigated in the fields of electrochemistry and photoelectrochemistry [98,99]. Anatase form has been proved to have better catalytic activity than rutile and brookite

due to its higher surface area. In order to increase its conductivity, two different ways could be followed toward the creation of Ti^{3+} ions [100-102]: either reducing TiO_2 in H_2 atmosphere at elevated temperatures to achieve suboxides with general formula $\text{Ti}_n\text{O}_{2n-1}$ ($4 < n < 10$), known as Magneli phases; either by introducing donor agents (*e.g.*, Nb, F). The similarity of atomic radii suggests that solubility of Nb in TiO_2 phases will mainly depend on the charge compensation mechanism rather than on the induced stress (the atomic radius of Nb^{5+} is 0.70 Å, whereas that of Ti^{4+} is 0.68 Å) [100,101,103-105]. The higher positive charge of Nb leads to creation of Ti cation vacancies.

New properties, not expected for the bulk phase, led to an increased interest and intensive research of one-dimensional nanostructures such as nanotubes, nanorods and nanowires, which have high specific surface area and a wide range of applications [98,99,106]. Various methods for synthesis of titania nanotubes have been described in the literature [107-109] like anodization and template-assisted sol-gel method. However simple and cost-effective hydrothermal method has been developed by Kasuga et al. [110,111], suitable for large scale production of pure titania nanotubes with small diameters. However the crystallinity, purity, properties like conductivity and surface area (up to $400 \text{ m}^2\text{g}^{-1}$) [111,112] and the yield of the final product depend on different parameters like vessel filling [113], temperature of the synthesis [112], chemical post-treatment [111,112] and of the annealing time and temperature [114].

Kasuga reported in [111] the dependence of the electric conductivity on the chemical post-treatment with different acids. He prepared nanotubes of titania (TNTs) containing oxoacid molecules using phosphoric, sulphuric and perchloric acids (denoted respectively by P-TNTs, S-TNTs and C-TNTs) followed by heat-treatment at 500°C . The conductivity of the oxoacid treated nanotubes under 100% relative humidity (RH) was about two orders of magnitude higher than that obtained using the hydrochloric

acid treatment (TNTs— $1.6 \times 10^{-4} \text{ S cm}^{-1}$; P-TNTs— $1.4 \times 10^{-2} \text{ S cm}^{-1}$; S-TNTs— $8 \times 10^{-3} \text{ S cm}^{-1}$; C-TNTs— $1.6 \times 10^{-2} \text{ S cm}^{-1}$). Additionally when C-TNTs were heated to 300°C instead to 500°C their conductivity increased to $5 \times 10^{-2} \text{ S cm}^{-1}$. He suggested that protons on the surface of TNTs were involved in conduction and the oxoacid ions adsorbed on the surface increased the proton concentration and then, their conductivity. Tighineanu et al. [114] investigated the influence of annealing time and temperature on the conductivity of TiO_2 nanotubes. Their results showed that nanotubes annealed for short time (2.5 h) at temperatures in the range $350\text{--}400^\circ\text{C}$ had lower resistance when compared to longer annealing times (20 h) and lower or higher annealing temperatures.

Platinum has been investigated for the purposes of fuel cells application and has been proved its higher durability and stability in comparison to carbon supported electrocatalysts. Additionally, the use of metal oxides as supports led to enhanced catalytic activity of platinum due to a strong metal-support interaction (SMSI). Shim et al. [115] investigated the electrochemical properties of Pt- WO_3/C and Pt- TiO_2/C toward oxygen reduction in fuel cells. They observed lower adsorption strength of hydrogen and oxygen onto the Pt surface in comparison to pure platinum catalyst. The increased electrochemically active surface area and improved cell performance were attributed to synergistic effects due to the formation of an interface between Pt and the oxide material and the surface diffusion of intermediates. In [116], the enhanced catalytic activity of Pt/ TiO_2/C has been explained by the increased electrochemically active surface area and the modification of the surface electronic properties of Pt. Gustavsson et al. [117] attributed the better catalytic activity of Pt/ TiO_2 in comparison to Pt-black, to the better dispersion of Pt onto the oxide surface and to the substantial proton conduction of TiO_2 when a thin layer was placed between the Nafion membrane and Pt. In [118] Lewera performed a detailed analysis of the metal support interaction between

Pt and TiO₂ and WO₃ by the use of X-ray photoelectron spectroscopy. The lower intensity of the 4f binding energy signal of Pt supported on metal oxide than in the case of Pt/C and the changes in the symmetry of the signal suggested an increased electron density on Pt. The authors concluded that the observed shifts in the binding energy were due to a SMSI, which resulted in the superposition of two effects: (i) changes in the lattice energy due to alloy formation between Pt and the oxide on the surface and (ii) partial charge transfer from the oxide to Pt, which could be assigned and to the reported enhanced electrocatalytic activity toward ORR.

The use of non-conductive metal oxides for support of IrO₂ has been reported as well [96]. TiO₂ offers very high stability and resistance under the conditions of the anode. However, its low conductivity remains a problem [98,99]. It has been found that IrO₂-supported on TiO₂ shows better electrocatalytic activity toward oxygen evolution in comparison to unsupported catalyst. The main explanation given by the authors was that with high IrO₂ loadings, the non-conductive surface of the support with low specific surface area of 10 m² g⁻¹, was covered with a thin conducting layer of IrO₂. The conductivity of the final product was of 55.7 S cm⁻¹ in comparison to 64.2 S cm⁻¹ for unsupported IrO₂. For high specific surface area supports of 90 m² g⁻¹, the conductivity of the IrO₂-supported material was 0.7 S cm⁻¹ [96]. Nb-doped TiO₂ has been reported in [97] as support for IrO₂. In this case, a beneficial effect of the support in terms of better mass normalized activity and better stability in comparison to unsupported IrO₂ was found.

1.3.7 MEA formulation and performance

Main consideration within the MEA preparation methods is that conventional carbon based current collectors used in PEMFC technology cannot be applied on the anode side of the PEM water electrolyser, due to carbon oxidation (see chapters 1.3.1

and 1.3.2) and they are replaced by more expensive titanium materials. Two main types of MEAs depending on their preparation can be considered: catalyst-coated membrane (CCM) type and catalyst-coated substrate (CCS) type. In the latter, MEAs are prepared by depositing the catalyst ink onto the GDL (painting or spraying) and the resulting electrodes are hot-pressed on both sides of the membrane. This method is typically used to obtain MEAs for fuel cells, where cheaper carbon-based GDL are utilized. Larger electrodes can be prepared and cut into smaller electrodes at later stage. In PEM water electrolysis the anode catalyst ink needs to be deposited onto other gas diffusion layers, or either directly onto the current collectors, made by stainless steel, Ni or Ti with defined porosity [19]. Due to the higher price of porous titanium used as GDL and its utilization for longer period, the preferred type of MEAs in water electrolysis are CCM [35]

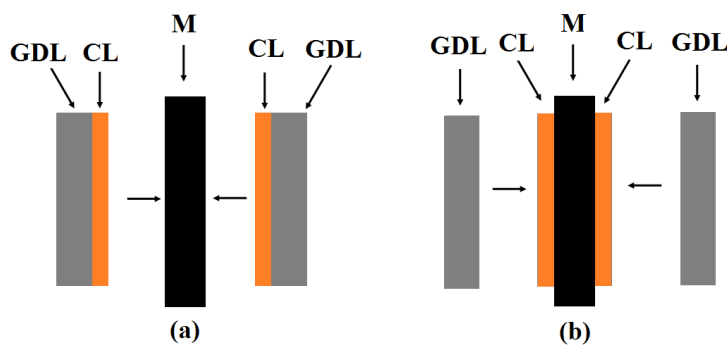


Figure 1.6 Difference between CCS (a) and CCM (b) type membranes.

On Fig. 1.6 is visualized the main difference between CCS and CCM type membranes. As it can be seen on Figure 1.6 b, GDL can be added at later stage to the MEA which is very useful for more expensive materials as GDL like porous sintered Ti.

The main preparation technique of CCM type MEAs is based on the conventional decal method: catalyst loading on decal substrate followed by its transfer when pressing onto the membrane. Another option is the direct spray of the catalyst ink onto the membrane. This method is not suitable for scaling-up because it is impossible to prepare

larger electrodes that later should be cut into smaller ones before pressing onto MEAs, what means that MEAs should be prepared one by one, thus taking longer time for the preparation of more than one MEA. By the application of the decal substrate, the catalyst loading surface can vary. Therefore, larger decal substrate can be firstly loaded with catalyst ink and later cut into smaller parts before transferring to the membrane surface by pressing. The main difficulty of the application of decal method is the high temperature (210 °C) of the decal transfer process. For this reason the use of the Na⁺ form of the Nafion[®] membrane is required due to its high stability at higher temperatures. In this way, it is necessary the transformation of the H⁺ form to the Na⁺ form of the Nafion[®] membrane before pressing and afterwards, boiling the complete MEA in sulphuric acid solution in order to protonate again the membrane. Within the last year this method has been developed and its low temperature version can be applied, which does not require high temperature transfer conditions. The transfer of the catalyst layer from the decal substrate to the membrane can be done and at 130°C, and the H⁺ form of the Nafion[®] membrane can be used [119,120].

Here will be paid attention to the MEA composition and performance for PEM water electrolysis at temperatures lower than 100 °C. For better visualization, this information is summarized in Table 1.8.

Table 1.8 MEA composition and performance details

Ref No	Cathode catalyst/loading (mg cm ⁻²)	GDL, Cathode	Anode catalyst/loading (mg cm ⁻²)	GDL, Anode	Membrane (thickness μm)	Exp. T °C/ CCS or CCM	E _{cell} at 0.1A cm ⁻² / 1A cm ⁻² (V)
[8]	40 wt.%Pt /C 0.70	porous Ti sheets	Ir 2.40	porous Ti sheets	Nafion [®] 115 (125)	90	1.48/ 1.7
	40 wt.% Pd /C 0.70	Porosity 45%		Porosity 45%		CCS	1.48/ 1.68
[13]	40 wt.% Pt/C 0.70	Ti, porosity 45%	Ir black 2.00	Ti, porosity 45%	Nafion [®] 117 (178)	90	1.5/ 1.7
	40 wt.% Pd/C 0.70					CCS	

[34]	Pt black 0.35	Ti, porosity 45%	Ir black IrO ₂ 2.00	Ti, porosity 45%	Nafion® 117 (178)	90 CCM, direct spraying	1.45/ 1.75
		Ti mesh		Ti mesh			1.48/ 1.7
[35]	Pt black 5.00	Sintered Ti powder mat	IrO ₂ 4.50	Sintered Ti powder mat	Nafion® 117 (178)	80	1.48/ 1.8
		Sintered Ti fiber mat		Sintered Ti fiber mat			1.48/ 1.8
			IrO ₂ 2.00				1.47/ 1.64
[36]	20 wt.% Pt/C 0.40	Porous Ti sheets Porosity 50%	Ir _{0.6} Ru _{0.2} Ta _{0.2} O ₂ 2.00 Ir _{0.8} Ru _{0.2} O ₂ 2.00	porous Ti sheets Porosity 50%	Nafion® 115 (125)	80 CCM	1.45/ 1.6 1.44/ 1.6
			Ir _{0.6} Ru _{0.4} O ₂ 2.00				1.42/ 1.56
[39]	Pt black 2.30	Toray	Ir black 3.80	40 mesh Ti-net	Nafion® 112 (50)	60 CCM decal	1.5/ 1.9
[40]	30 wt.% Pt /C 0.60	Carbon paper ELAT (E TEK)	IrO ₂ 3.00	Ti mesh	Nafion® 115 (125)	80°C	1.43/ 1.72
[42]	30 wt.% Pt /C 1.00	Carbon paper ELAT (E TEK)	IrO ₂ /RuO ₂ (Ir:Ru=50:50) 6.00	Ti-grid	Nafion® 117 (178)	80 60 CCM direct spraying	1.5/ 1.67 1.55/ 1.73
[42]	30 wt.% Pt /C 1.00	Carbon paper ELAT (E TEK)	IrO ₂ /RuO ₂ (Ir:Ru=50:50) 6.00 IrO ₂ /Pt (Ir:Pt=50:50) 6.00 IrO ₂ /Ta ₂ O ₅ (Ir:Ta=70:30) 6.00	Ti-grid	Nafion® 117 (178)	80 CCM direct spraying	1.6/ N/A
[43]	30 wt.% Pt /C 0.60	Carbon paper ELAT (E TEK)	IrO ₂ 3.00 Calcined at 200°C 300°C 400°C 500°C	Ti/Pt (95:5)- grid	Nafion® 115 (125)	80 CCM direct spraying	1.5/ 1.85 1.5/ 1.76 1.45/ 1.71 1.45/ 1.74
[44]	Pt black 1.00	Toray 60	Ir black 1.00 1.50 2.00 2.50 3.50	Ti-foil	Nafion® 1135 (88)	30 CCM	1.57/ 2.0 1.57/ 2.0 1.57/ 1.97 1.55/ 1.95 1.55/ 1.95
[44]	Pt black 1.00 10% Nafion 20% Nafion 30% Nafion 40% Nafion	Toray 60	Ir black 1.50 10% Nafion 20% Nafion 30% Nafion 40% Nafion	Ti-foil	Nafion® 1135 (88)	30 CCM	1.53/ 1.85 1.55/ 1.9 1.57/ 1.95 1.63/ N/A
[44]	Pt black 1.00	Toray 60	Ir black 1.50	Ti-foil	Nafion® 112 (50) Nafion® 1135	30	1.55/ 1.87 1.58/ 1.97

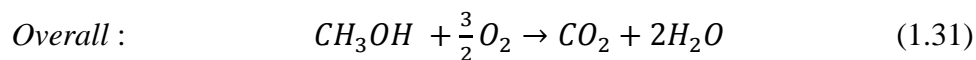
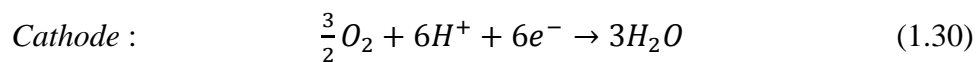
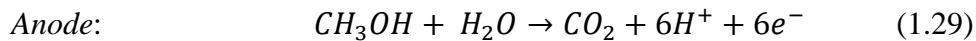
					(88) Nafion® 115 (125)		1.62/ N/A
[44]	Pt black 1.00	Toray 60	Ir black 1.50	Ti-foil	Nafion® 112 (50)	30 40 60 75 80	1.58/ 1.88 1.50/ 1.8 1.50/ 1.75 1.43/ 1.72 1.43/ 1.7
[44]	Pt black 1.00	Toray 60	Ir black 1.50	Ti-foil + Ir black	Nafion® 112 (50)	80	1.42/ 1.77
[44]	Pt black 1.00	Toray 60	Ir black 0.30 Ir/TiC (20% Ir) 1.50	Ti-foil with 1.5 mm diameter holes	Nafion® 112 (50)	80	1.55/1.94 1.55/1.9
[45]	Ir black sputtered	Toray + 50 nm sputtered Ti	Ir black sputtered	Toray + 50 nm sputtered Ti	Nafion® 115 (125)	Steam feed 30 60 80 Condensed water feed (t°C water=100) 35 60 80 90	1.8/ N/A 1.6/ N/A 1.5/ N/A 1.6/ N/A 1.55/ N/A 1.48/ N/A 1.48/ 1.8
[46]	20 wt.% Pt /C 0.30	N/A	Ir black 5.00	N/A	Nafion® 115 (125) 30 PES/SPEEK	80 CCM decal	1.42/ 1.67 1.5/ 1.8
[89]	28 wt.% Pt/C 0.50	Toray	IrO ₂ 3.00	Toray	Nafion® 112 (50)	80	N/A/ 1.63
[121]	60 wt.% Pt/C 0.50	Vulcan- XC72+PTF E	IrO ₂ 3.00	Ti fibre 60% porosity	Nafion® 115 (125) Nafion® 212 (51)	80	N/A/ 1.56 N/A/ 1.53
[122]	46.7 wt% Pt/C 0.35	Toray	IrO ₂ /TiO ₂ (75 wt% iridium) 2.00	Sintered Ti	Nafion® 212 (51)	80 CCM, decal	N/A/ 1.57

Up to our knowledge, best performance of PEM water electrolysis single cell has been reported in [121]. Nafion® membranes with different thickness have been tested. The use of different nominal content of Pt-catalyst (Pt-black, 20 wt. % Pt/C, 40 wt. % Pt/C, 60 wt. % Pt/C) has been studied as well. Catalyst loadings of 0.5 mg_{Pt} cm⁻² and 3 mg_{IrO₂} cm⁻² have been used. Best reported performance has been observed when 60 wt. % Pt/C has been used as cathode catalyst. When Nafion® 212 is used, the achieved cell voltage is 1.53 V at 1 A cm⁻², whereas for Nafion® 115 it is of 1.59 V at 1 A cm⁻² at 80 °C. Similar results with Nafion® 212 and 0.35 mg_{Pt} cm⁻² have been obtained in [122].

The content of Nafion[®] ionomer in the MEAs has been optimized to 25 % for the anode and 20 % for the cathode in [123].

1.4 Basic principles of Direct methanol fuel cells (DMFC). Theory

The basic DMFC is comprised by two electrodes, anode and cathode, and a solid electrolyte in between. At the anode, methanol and water are supplied and converted to carbon dioxide, protons and electrons. Currently most of the systems described in the open literature involve a liquid methanol-water feed, although in some platforms the methanol is supplied to the DMFC anode as vapor. The produced electrons from the anode reaction are subsequently transferred via the external circuit (which includes a load), where they can perform electric work. On the other hand, protons are transported to the cathode side through the PEM. At the cathode, the protons and electrons reduce oxygen (from air) to form water. Thermodynamic characteristics are similar to the hydrogen reaction, especially in terms of reversible oxidation potential. The methanol electro-oxidation reaction is a slow process, as it involves the transfer of six electrons to the electrode for complete oxidation to carbon dioxide:



1.4.1 Thermodynamics

The energy balance of reaction (1.31) can be written as:

$$\Delta H = \Delta G + T\Delta S \quad (1.32)$$

where ΔH is the enthalpy and ΔS is the entropy of reaction (1.31).

Under reversible conditions, the difference between the electrode potentials is the reversible cell potential E_{rev} given by the Nernst equation [124]:

$$E_{rev} = E_{rev}^0 - \frac{RT}{nF} \ln \left(\frac{p_{CO_2} (a_{H_2O})^2}{a_{CH_3OH} (p_{O_2})^{1.5}} \right) \quad (1.33)$$

where E_{rev}^0 is the reversible cell potential at standard conditions; p_{CO_2} and p_{O_2} are the CO_2 and the O_2 partial pressures, respectively; a_{H_2O} and a_{CH_3OH} the activities of water and methanol, also respectively; n represents the number of electrons involved in the electrochemical reaction (6 electrons for the DMFC); F is the Faraday constant (96484.6 C mol⁻¹); R is the gas constant and T is the thermodynamic temperature.

In an electrochemical cell, operating at isothermal conditions, if the enthalpy energy of both anode and cathode reactions could be fully converted into electric work, the enthalpic cell voltage, $E_{\Delta H}^0$, obtained under standard conditions would be:

$$E_{\Delta H}^0 = - \frac{\Delta H^0}{nF} \quad (1.34)$$

ΔH^0 is the overall reaction enthalpy at standard conditions (Table 1.9). However, according to the second law of thermodynamics, if an electrochemical cell operates reversibly (concerning the energy conversion) [125], there will be a variation of the system entropy (released heat). Thus, the maximal electric work of an electrochemical cell is obtained from the standard Gibb's energy variation, ΔG^0 , and the maximal fuel cell voltage at standard conditions, E_{rev}^0 is obtained as follows:

$$E_{rev}^0 = - \frac{\Delta G^0}{nF} = - \frac{\Delta H^0 - T\Delta S^0}{nF} \quad (1.35)$$

where ΔS^0 is the variation of the standard entropy of the system (Table 1.9).

Since not all the fuel chemical energy in a DMFC is converted into electric work, the thermodynamic fuel cell efficiency is limited by the fuel intrinsic properties. Therefore the maximum thermodynamic efficiency that can be achieved by a DMFC electrochemical cell can be obtained by the following equation:

$$\varepsilon = \frac{E_{rev}^0}{E_{\Delta H}^0} = \frac{\Delta G^0}{\Delta H^0} \quad (1.36)$$

Table 1.9 Thermodynamic data and overall enthalpic and reversible potential for the DMFC reactions at standard conditions, with $P = 1$ atm and $T = 298.15$ K. Anode: methanol oxidation reaction; cathode: oxygen reduction reaction) [126].

Reaction	$\Delta H^0 / \text{kJ mol}^{-1}$	$\Delta S^0 / \text{J mol}^{-1}$	$\Delta G^0 / \text{kJ mol}^{-1}$	$E_{\Delta H}^0 / \text{V}$	E_{rev}^0 / V
Methanol oxidation	110.69	-79.11	134.28	-0.19	-0.23
Oxygen reduction	-857.49	-97.98	-828.28	1.48	1.43
Overall cell	-746.80	-177.09	-694.00	1.29	1.20

From the data presented in Table 1.9, the maximal thermodynamic efficiency of 92.9% for the DMFC (at standard conditions) can be calculated.

1.4.2 Kinetics

The real electrode reactions differ from the theoretical ones and this decreases the overall cell performance and efficiency. The actual DMFC open circuit voltage (OCV) is less than the theoretical cell voltage predicted by Eq. (1.33) because of different losses. In addition, when the cell is producing energy, a current circulates through the external circuit and the cell separates from the OCV. The discharge voltage of the cell is then given by [127]:

$$E_{\text{real}} = E_{\text{rev}} - (\eta_{\text{act}} + \eta_{\text{ohmic}} + \eta_{\text{conc}}) \quad (1.37)$$

where E_{rev} is the reversible cell voltage, η_{act} the activation overpotential (summation of the anode and the cathode contributions, $\eta_{\text{act,a}}$ and $\eta_{\text{act,c}}$, respectively); η_{ohmic} (IR drop) the resistive losses (ohmic drop through the electrolyte); and η_{conc} the concentration (or mass transport) overpotential (summation of the anode and the cathode contributions, $\eta_{\text{conc,a}}$ and $\eta_{\text{conc,c}}$, respectively). The total overpotential η is the sum of these three later terms.

At low current densities, the DMFC performance is mostly limited by the electron transfer (at one or both electrodes) and this loss mechanism is called activation overpotential η_{act} . At medium current densities, the ohmic overpotential η_{ohmic} is a limiting factor representing the total cell resistance R of the DMFC, which is a sum of electronic, ionic and contact resistances. At high current densities, the electrode reactions proceed much faster than mass transport of the reacting species and the products generated, thus appearing concentration gradients with a limiting current density.

The activation and concentration overpotentials, which exist at both electrodes, allows writing the respective total overpotential at the anode and at the cathode by Eqs. (1.38) and (1.39).

$$\eta_a = \eta_{act,a} + \eta_{conc,a} \quad (1.38)$$

$$\eta_c = \eta_{act,c} + \eta_{conc,c} \quad (1.39)$$

The activation current density j at each electrode follow the Butler-Volmer equation:

$$j = j_0 \left\{ \exp\left(\frac{\alpha_a F}{RT} \eta\right) - \exp\left(-\frac{\alpha_c F}{RT} \eta\right) \right\} \quad (1.40)$$

When assuming high overpotentials, which correspond to a relatively slow rate at one electrode compared to the other, the first or second term in Eq. (1.40) can be neglected. Thus, a net cathodic current density is obtained for high negative overpotentials, and a net anodic current density is obtained for high positive overpotentials, which can be written from Eq. (1.40) neglecting the anodic and the cathodic part, respectively:

$$j = -j_0 \exp\left(-\frac{\alpha_c F}{RT} \eta\right) \quad (1.41)$$

$$j = j_0 \exp\left(\frac{\alpha_a F}{RT} \eta\right) \quad (1.42)$$

These equations hold for each one of both electrodes composing the cell and, normally, for low temperature fuel cells such as DMFC, when the cell operates giving current to the external circuit, the anode proceeds with high anodic overpotential and the cathode with high negative overpotential.

1.5 DMFC catalysts. Literature review

Typical design of a direct methanol fuel cell (DMFC) is shown below in Fig. 1.7. The components are the MEA (which includes membrane, anode and cathode), GDLs, current collectors, gaskets, bipolar plates. The core component is the MEA. GDLs and gaskets are used to enable an electric current to flow between the bipolar plates and the electrodes. The bipolar plates are electrically conductive and support the transport of the fuel to the electrodes and the transport of the reaction products out of the cell.

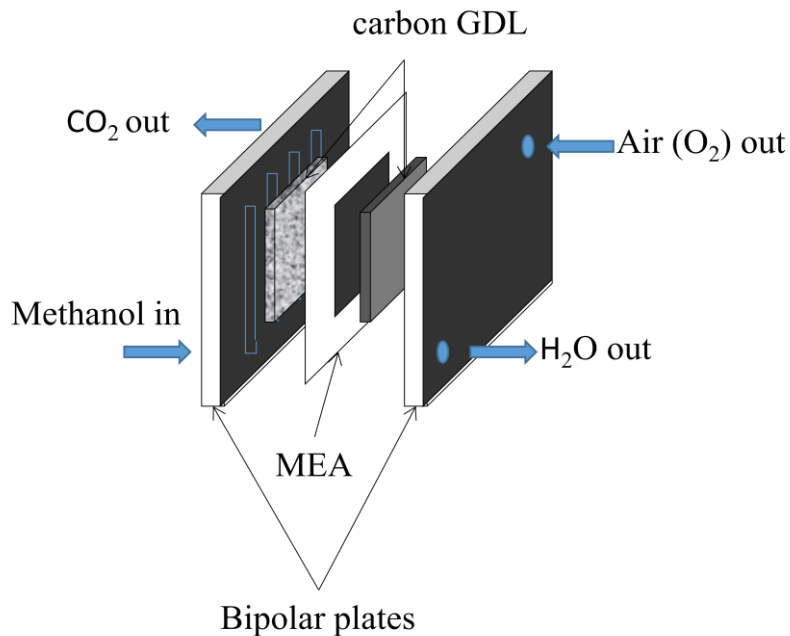


Figure 1.7 Typical design of a DMFC

The typical design of a DMFC is very similar to that shown in Fig. 1.3 for a PEMWE cell. The requirements to the GDL, current collectors, bipolar plates are similar and the main difference originates from the operating mode.

The purpose of GDLs is to form a thermal and electronic contact between the electrodes and flow field plates which are used as transport path for the reactants. They

have high electrical and thermal conductivity, good chemical and mechanical properties with high porosity. Generally GDLs material is carbon based papers which have a macroporous backing layer and a microporous diffusion layer on one or both sides of the backing layers [128,129].

The solid polymer electrolyte is used to provide ionic conductivity and avoid the flow of electrons, thus acting as a barrier between the reactants to maintain mechanical and chemical stability. The thickness of the membrane is in the range of 30-200 μ m. Different solid electrolyte membranes with their properties are reported in section 1.3.3.

MEA electrodes generally consist of expensive noble metal catalyst used to achieve sufficient rate of reaction at low temperature. Normally Pt is used at the cathode and a PtRu alloy at the anode for DMFC [128,129].

In order to proceed to review of the catalysts used in DMFC, here should be noted the main disadvantage of DMFC, which is the slow electrooxidation kinetics of methanol.

During methanol electrooxidation process various surface intermediates are formed. Methanol is mainly decomposed to CO which is then further oxidized to CO₂. Other by-products are formaldehyde and formic acid. Some of the intermediates cannot be fully oxidized and remain strongly adsorbed to the catalyst surface. In such a way they block the catalyst surface for new fresh methanol molecules adsorption and undergoing further reaction. Thus the electrooxidation of intermediates is the rate limiting step. This poisoning of the catalyst surface seriously slows down the oxidation reaction. Thus, a main challenge is to develop new electrocatalysts that provide complete oxidation of the intermediates to CO₂ and thus inhibit the poisoning and increase the rate of the reaction [128-130].

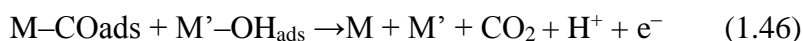
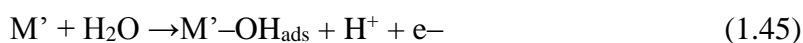
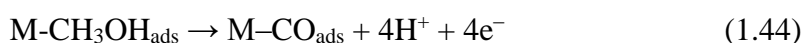
Other challenge is the methanol crossover. In DMFC the fuel diffuses through the Nafion[®] membrane. Due to the hydroxyl groups and their hydrophilic properties, methanol interacts with the ion exchange sites and it is dragged by hydronium ions in addition to diffusion as a result of a concentration gradient between the anode and the cathode. Methanol that crosses over is oxidized at the cathode, thus resulting in a current loss. Besides, the cathode catalyst, which is pure platinum, is blocked by the methanol oxidation intermediates, similarly to those in the anode [128-130].

1.5.1 Electrocatalysts for the oxygen reduction reaction (ORR)

To improve the kinetics of the ORR and the tolerance against methanol oxidation intermediates due to crossover, a variety of Pt alloys have been developed for the cathode (where second metal is Fe, Au, Pd, Cr or Rh) and these alloys show improved performance in DMFCs in comparison to pure Pt catalysts [129, 131-136]. It has been proposed that the formation of Pt-based alloys slightly decreases the Pt–Pt interatomic distance, facilitating the break of the strong O=O bond of oxygen and to achieve the complete oxygen reduction [135]. The stability of the PtCr and PtFe alloys has been studied in PEMFC cathodes [137,138] and the findings suggest that the stability of these alloys depends on the degree of alloying as well as the catalyst particle size [139]. In order to decrease the cost, the catalysts have been typically supported onto different materials. The mostly used material is carbon, due to its high electric conductivity and surface area, which provides better utilization and dispersion of the catalyst [131-135]. More attention to the supports will be paid later. Other attempts to lower the catalyst cost are performed towards developing new non-noble metal alternatives to Pt-based catalysts. Potential alternatives include pyrolysed Fe porphyrins and Ru-based chalcogenides, which show decent ORR performance (although still not competitive with Pt) and excellent methanol tolerance [129,140,141].

1.5.2 Electrocatalysts for the methanol electrooxidation reaction (MOR)

Typical catalysts used in the anode are alloys of PtRu, mainly in atomic ratio 1:1, which is considered to be the best ratio for CO oxidation. In these catalysts, Ru forms oxygenated species at lower potentials than Pt and promotes the oxidation of adsorbed CO molecules on platinum to CO₂, thus increasing the CO tolerance of the catalyst [142,143].



This mechanism of methanol oxidation intermediates by adsorbed OH is called bifunctional mechanism. Another mechanism involved in the oxidation of intermediates also mitigating their effect is the so-called ligand effect. The ligand effect involves a decrease in the adsorption energy of adsorbed species (like CO and CHO) on Pt due to alloying with the second metal, thereby facilitating the oxidation of these poisonous species at relatively lower anodic potential. The ligand mechanism in the addition of Ru reduces the strength of the Pt-CO bond, which facilitates the CO oxidation [144,145]. As second metals in the Pt-M alloys have been investigated Ru, Sn, Mo, Co, Ni, Rh, Pd, W [146-150] and it has been shown that the PtRu catalysts exhibit the highest MOR activity. The PtRh and PtRu nanowires have been compared in [146]. It has been found that the alloys with 1:1 atomic ratio resulted in the higher catalytic mass activity for the methanol electrooxidation than those with different atomic ratios. The mass activity of PtRu (1:1) nanowires (NWs) was superior to other NWs and even better than the commercial catalyst with highly dispersed PtRu 1:1 nanoparticles on carbon [146]. A comparison between trimetallic and bimetallic Pt alloys has been done in [147]. It has

been found that the Pt/Rh (2:1) and Pt/Ru/Rh (5:4:1) alloy catalysts showed better catalytic activities for methanol electrooxidation than Pt or Pt/Ru (1:1), respectively. Amongst other metals suitable to improve the Pt activity is Sn. Its main advantage is the low potential at which Sn is covered by OH species. The OH adsorbed species are required for the CO oxidation to CO₂. However, it appears that it is difficult to maintain Sn in the metallic state. Trimetallic Pt/Ru/Sn catalysts showed a slightly improved activity in comparison to PtRu [151]. However their preparation is more difficult.

Since PtRu has been proved to be the best catalyst towards MOR, a new problem related to it appears. Another process that can take place on the anode is Ru dissolution under particular conditions. Ruthenium dissolution can occur during the normal DMFC operation, where the anode potentials are as low as 0.3–0.5 V vs. DHE, even though the thermodynamic reversible potential for Ru oxidation is significantly higher (E° for Ru/Ru(OH)₃ and Ru(OH)₃/RuO₂·H₂O are 0.74 and 0.94 V vs. RHE, respectively). Although ruthenium has a relatively high thermodynamic reversible oxidation potential, the observed ruthenium dissolution in the lower potential region (0.3–0.5 V vs. DHE) of the anode is often attributed to the low Ru(OH)₃ activity in the catalyst layer and the relatively high operating temperature of the cell [129]. In order to improve the catalyst stability and its performance, different types of supports have been investigated [98].

1.5.3 Supports for the electrocatalysts in DMFC

Main requirements for the catalyst supports were discussed in section 1.3.6. However, the anode potentials in DMFC are lower than those in PEMWE and more materials can withstand the conditions, *e.g.* carbon-based materials [98]. As mentioned above, the main reason of the use of supports is the improved catalytic surface, which allows decreasing the catalyst loading of the electrode and therefore, its cost. Another reason is the stabilizing effect that the support provides to the catalyst and mitigate its

degradation. Typical supports used in DMFC are carbon blacks due to their high conductivity and high specific surface area. However, it appeared that they cannot remain stable for long time under the conditions of the fuel cell operation and suffer degradation [152]. Further attempts have been done to modify carbon blacks by the addition of doping elements or modifying their surface in order to improve their stability and the corresponding catalyst durability [153-156]. Enhanced catalytic activity and durability of Pt and Pt-alloys via nitrogen functionalization of the carbon supports has been achieved in [153,155]. To improve DMFC catalyst performance and stability, various types of carbon supports have been explored, *e.g.* nanotubes, nanofibers, graphene materials, which show better performance and stability in comparison to the use of conventional carbon blacks [157-159].

Other types of supports are non-carbon based materials, *e.g.* TiO₂, WO₃, SnO₂, CeO₂, SiO₂, WC, usually doped with Nb, In, Sb. [98,156]. Typically, the effect of such supports is related to a significant increase in the durability of the catalyst. Additionally, metal-support interactions between the support and Pt appear in such materials and result in an increase in the catalyst activity [98,115-118]. Most of the materials were discussed in section 1.3.6. Conducting polymers have been used as supports in DMFC alone or as a pathway to improve carbon support stability by covering its surface. Such conducting polymers were polyaniline (PANI), poly (3,4-ethylenedioxythiophene) (PEDOT) and others. The PANI coating prevented aggregation and the loss of particles and showed improved long-term stability [160]. Measurements with freshly prepared Pt-PEDOT/C electrodes showed poor activity for methanol oxidation in a half-cell and a DMFC. A substantial enhancement in that activity was evident after either electrochemical over-oxidation of PEDOT or long-time storage of the Pt-PEDOT/C gas diffusion electrode (GDE) in air. Both procedures led to a reorganization and increase in

porosity of the reaction layer, which obviously contributed to better methanol accessibility to Pt catalyst active centers [161].

1.5.4 MEAs for DMFC

Different types of MEAs (Fig. 1.6) and the methods for preparation were already discussed in section 1.3.7. The MEAs in DMFCs are typically CCS-type, which is facilitated by the use of lower cost carbon GDLs. However, since CCM type MEAs provide improved contact between the CL and the membrane, it is preferred when high performance is required. In fact, the reported low temperature decal method has been firstly optimized for DMFCs in [119,120].

At high concentrations, CO₂ can remain trapped inside the catalyst layer and therefore, mass transport limitations can appear. The use of unsupported catalysts facilitates the CO₂ transport because thinner active layers can be obtained in comparison to supported catalysts with similar catalysts loadings [142,143]. Furthermore, regarding durability issues, the use of unsupported catalysts avoids the problem of carbon corrosion [162,163].

One of the main challenges in the research field of DMFC is the optimization of the electrode composition and morphology in order to improve the fuel cell performance and durability. In H₂-fueled PEMFCs more attention has been paid in the literature to supported catalysts for increasing the active surface area and to obtain better cell performance [164-176]. In contrast, the use of unsupported catalysts is more extended in DMFCs. Unsupported catalysts or metal blacks are mainly utilized in systems operating in passive mode, that is, without any air blowers or fuel circulating pumps, such as in portable electronic applications [177-181]. In this sense, it has been reported that the best compromise between power density (21 mW cm⁻²) and fuel efficiency (63 %) for a passive single DMFC containing PtRu and Pt blacks is achieved with a

methanol feed concentration of 2 mol dm⁻³ operating at room temperature [182]. With regard to DMFC systems operating in active mode, the performance depends largely on the experimental operating conditions (Table 1.10).

The technical interest in unsupported PtRu alloy catalysts is based on the fact that, in practical applications, it is expected that catalyst layers with reduced thickness show better performance, due to the improved mass transport and the decrease of the inner electrical resistance [188]. It is known that the performance of a catalyst layer depends on the catalyst ink composition, the ink preparation procedure, and the application method onto a substrate to fabricate the MEA. Uchida and col. [167] reported the changes of the Nafion[®] layout in various kinds of organic media, depending on their dielectric constant. Thus, in organic solvents with $\epsilon > 10$, a solution is formed; when $3 < \epsilon < 10$, a colloidal solution results; and with $\epsilon < 3$, precipitation occurs [164,167,189].

Table 1.10 Performance and durability of single DMFCs.

Ref.	Methanol concentration / mol dm ⁻³	Oxidant	Anode catalyst loading / mg cm ⁻²	Cathode catalyst loading / mg cm ⁻²	Membrane	T / °C	Power density / mW cm ⁻²
[136]	2	O ₂	PtRu/5.00	PtRu (1:1)/5 PtRh (2:1)/5 Pt/5	Nafion [®] 117	30	40 60 45
[136]	2	O ₂	PtRu/5.00	PtRu (1:1)/5 PtRh (2:1)/5 Pt/5	Nafion [®] 117	70	165 185 180
[147]	2	O ₂	Pt PtRh PtRu PtRuRh	Pt	Nafion [®] 117	70	49 135 169 197
[160]	1	-	PtRu/PANI-C/2.50 PtRu/C/2.50	Pt/C/4.00	Nafion [®] 117	70	21 17
[183]	1	O ₂	PtRu/2.20	Pt/2.30	Nafion [®] 112	130	390
[184]	2	Air	PtRu/C/5.00	Pt/5.00	Nafion [®] 117	100	120

[185]	1	O ₂	PtRu/C/2.00	Pt/C/1.00	Nafion® 115	75	65
[186]	1	Air	PtRu/4.00	Pt/4.00	Nafion® 115	60	70
[187]	1	O ₂	PtRuMo PtRu	Pt	Nafion® 117	80	220 192.5

In the first case, it is considered that the ionomer can cover the surface of the carbon and, as the ionomer is an electron insulator, the Pt utilization decreases and thus resulting in a low fuel cell performance. In the second case, the ionomer colloids adsorb the catalyst powder and the size of the agglomerate of catalyst powder increases. Then, the electrode porosity increases, and the mass transfer is facilitated. A continuous network of ionomer throughout the catalytic layer can be built up, thus improving the proton conduction from the electrode to the membrane and resulting in a better fuel cell performance [164,189]. It has been reported that the electrode prepared by colloid formation shows an increase of about 30 % in the electrochemical reaction area and, therefore, a significant improvement in the cell performance compared to the solution method. Another point is that when colloid is formed, the ionomers can easily penetrate into the large pores and the small pores below 0.07 μm are not blocked. Conversely, all pores below 0.07 μm are blocked by ionomers in the case of the solution method [164].

An additional condition for producing a stable cast ionomer is related to the higher boiling point of the solvent with respect to water [189]. Even if ϵ of an organic solvent is larger than 10 and the perfluorosulfonated ionomer dissolves in the catalyst ink solution, the pore size can be tuned during the evaporation process of the catalyst ink, highly dependent on the viscosity and boiling point of the solvent [170-172]. It is worth mentioning that, in the best of the authors' knowledge, the influence of the ink composition on the catalytic layer properties for PEMFCs has only been studied when using carbon supported catalysts. The study of the effect of the catalyst ink composition

for unsupported catalysts would be also of interest since they are frequently used in DMFCs. Thus, this part of the thesis deals with the effect of different solvents used in the catalyst ink on the catalyst layer morphology for DMFC applications.

2. Thesis objectives

This thesis is devoted to two energy conversion technologies. One is the direct methanol fuel cell (DMFC) technology where methanol as a fuel is converted to electricity, and the other is polymer electrolyte membrane water electrolyser (PEMWE) as a technology for hydrogen production, which further can be applied together with captured CO₂ to synthesize methanol.

2.1 PEM water electrolysis objectives:

The main objective of this part of the research is to reduce the electrical energy requirements and electrolyser costs and increase the durability of the system, by development of the known materials for electrodes in PEM water electrolyzers. This objective can be split in the following ones:

Synthesis and development of TiO₂ as support for hydrogen and oxygen evolution reactions in PEM water electrolyzers.

Investigation of the use of Pt supported on TiO₂ materials to achieve better performance towards hydrogen evolution reaction (HER), than conventional Pt electrocatalyst.

Investigation of the effect of TiO₂ materials as supports on the development of IrO₂ and IrRuO_x as catalysts towards oxygen evolution reaction (OER), to reduce the loading by improving the activity and to improve the durability of IrO₂ and IrRuO_x.

Development of the preparation procedure of the MEAs and optimization of electrode loadings. Electrochemical characterization of the cell under the operating conditions of a PEM water electrolyser and cost estimation.

2.2 DMFCs objectives

This part of the thesis mainly aims to develop anode catalyst layers for DMFCs, with improved performance and mass transfer for the methanol oxidation.

Investigation of the influence of different solvents in the anode catalyst ink, on the catalyst layer properties and their electrochemical performance in three-electrode cell and in a single DMFC.

3. Methodology

3.1 Synthesis of the materials

3.1.1 Synthesis of the TiO₂ and Nb-doped TiO₂ supports

Sol-gel technique was applied for the synthesis of TiO₂ and Nb-doped TiO₂ (3 at.%, 6 at.% and 10 at.%). Titanium (IV) n-butoxide (98 %, Alfa Aesar) and niobium (V) ethoxide (99,999 %, Alfa Aesar) were mixed in absolute ethanol media in appropriate ratio (3 at.%, 6 at.% and 10 at.% of Nb toward Ti), then hydrochloric acid (37 %, Scharlau) and ultrapure water (resistivity of 18.2 MΩ cm, Millipore Corp.) were added and the mixture was vigorously stirred at room temperature for 1 h. At the end, the gellification of the sol was achieved by adding 1.0 mol dm⁻³ ammonium carbonate (aqueous solution) [101,103]. The final product was filtered, washed and dried at 60 °C for 10 h and after that annealed at 350 °C in air atmosphere [114].

Additional details:

Molar ratio (HCl)/(Ti+Nb)=1/1;

Molar ratio (H₂O)/(Ti+Nb)=50/1;

Niobium (V) ethoxide was used as 0.20 mol dm⁻³ solution in absolute ethanol.

3.1.2 Synthesis of the TNT and Nb-doped TNT supports

Modified hydrothermal method, described by Kasuga [110,111,190] was applied for the synthesis of the titania and niobium-doped titania nanotubes (TNT and Nb-TNT). The amount of about 1 g of the as synthesized TiO₂ or Nb-doped TiO₂ was dispersed in 100 mL of 10.0 mol dm⁻³ NaOH and placed in a Teflon vessel. The mixture was ultrasonicated for 2 h and then, it was placed for 72 h at 130 °C. The product was washed either with 0.1 mol dm⁻³ hydrochloric acid or with 0.1 mol dm⁻³ phosphoric acid (TNT and TNT-P samples, respectively, and the corresponding Nb-TNT and Nb-TNT-P

ones) [111,191] and with ultrapure water. Finally the nanotubes were annealed at 350°C [114].

The main steps in the synthesis of the nanotubes can be summarized as follows [106]:

- i) Dissolution of TiO_2 in NaOH (10 mol dm^{-3}) and formation of layered sodium titanates (general formula $\text{Na}_2\text{Ti}_x\text{O}_{2x+1}$);
- ii) Washing the sodium titanates with 0.10 mol dm^{-3} HCl (or 0.10 mol dm^{-3} H_3PO_4) and formation of protonated tubular titanates (with general formula $\text{H}_2\text{Ti}_x\text{O}_{2x+1}$);
- iii) Calcination of the protonated titanates to anatase nanotubes.

3.1.3 Synthesis of Pt catalysts

Pt supporting on the reported materials was performed by means of the borohydride reduction method with addition of sodium citrate as a stabilizing agent [192]. The support was dispersed in ultrapure water by ultrasonication for 30 min. (the supports used here were all materials obtained as indicated in sections 3.1.1 and 3.1.2), followed by the addition of the appropriate amount of $\text{H}_2\text{PtCl}_6 \cdot 6\text{H}_2\text{O}$ (99.9 %, Alfa Aesar) and sodium citrate (Sigma Aldrich). The pH was adjusted to 7 and the suspension was stirred for 10 h at 50 °C before adding sodium borohydride (Sigma Aldrich). Finally the suspension was filtered and washed with ultrapure water and dried at 60 °C. Using the same methodology and for comparison purposes, the reference catalyst 20 wt.% Pt/Vulcan XC-72 was prepared, using carbon Vulcan XC-72 (Cabot Corp.) as the support.

3.1.4 Synthesis of IrO_2 and IrRuO_x catalysts

Supported (50 wt. %) and unsupported IrO_2 and IrRuO_x catalysts, were synthesized by hydrolysis of their chlorides in alkaline media [43,94,193]. In 150 mL of

ultrapure water, 150 g of support (TNT and 3 at.% Nb-TNT) were dispersed. Here should be noted that the support was protonated titanate, *i.e.* it was not calcined at 350 °C for 2.5 h previously to the synthesis of the OER catalysts (the synthesis was stopped after step 2 in section 3.1.2). Required amounts of IrCl₃·xH₂O (99.9 %, Alfa Aesar) and support were dispersed in 150 mL of ultrapure water and placed in an ultrasonic bath for 30 min. (150 mL water per each 100 mg of support). The pH was adjusted to 12 with 1.0 mol dm⁻³ NaOH and the mixture was stirred at 80 °C for 2 h. At the end the pH was adjusted to 8 with 0.10 mol dm⁻³ HNO₃ (ultrapure, Scharlab) and kept for additional 30 min. stirring. The product was filtered and washed with ultrapure water and dried for 12 h at 80°C followed by calcination at 350°C for 2.5 h. For the synthesis of IrRuO_x, IrCl₃·xH₂O (99.9%, Alfa Aesar) and RuCl₃·xH₂O (99.9%, Alfa Aesar) in atomic ratio Ir:Ru 60:40 were used. Calcination times and temperatures are the same as for supported IrO₂. Unsupported IrO₂ and IrRuO_x black were prepared by the same method and calcined at 350°C for 2.5 h.

3.2 Physico-chemical characterization of the PEMWE materials

X-ray diffraction (XRD). The XRD technique was used to characterize the crystal structure and the average crystallite size of the catalysts. The XRD diffractograms were obtained by a Bruker D8 Advance diffractometer operating with Cu K α radiation ($\lambda=1.5406 \text{ \AA}$) and a 2θ scan from 5 to 80° (at 0.01° min.⁻¹). Diffraction peaks were assigned according to the International Centre for Diffraction Data (ICDD) cards in PDF-2 database. The XRD data were used to determine the lattice parameters, using Bragg's law:

$$2d \sin \theta = n\lambda \quad (3.1)$$

where, λ is the wave length of the incident X-ray, n is an integer called order of diffraction, θ is the glancing angle, d is the interplanar spacing and $2d \sin \theta$ is the path difference for rays from adjacent planes.

The value of d for planes in the set (hkl) may be found by the following equations, depending on the symmetry of the crystal system:

$$\text{Cubic: } \frac{1}{d^2} = \frac{h^2+k^2+l^2}{a^2} \quad (3.2)$$

$$\text{Tetragonal: } \frac{1}{d^2} = \frac{h^2+k^2}{a^2} + \frac{l^2}{c^2} \quad (3.3)$$

The average crystallite sizes were calculated by using the Scherrer equation:

$$B(2\theta) = \frac{K\lambda}{L \cos \theta} \quad (3.4)$$

Where $K = 0.9$, B is the peak width and L is the crystallite size.

X-ray photoelectron spectroscopy (XPS). XPS was used in order to get information on the chemical state and concentration of the surface species. The experiments were performed in a SPECS Sage HR 100 spectrometer with a non-monochromatic X-ray Mg source with a K_{α} line of 1253.6 eV energy and 250 W. The samples were placed perpendicular to the analyzer axis and calibrated using the $3d_{5/2}$ line of Ag with a full width at half maximum (FWHM) of 1.1 eV. The selected resolution for the high resolution spectra was 15 eV of Pass Energy and 0.15 eVstep⁻¹. Measurements were made in an ultra-high vacuum (UHV) chamber at a pressure around $8 \cdot 10^{-8}$ mbar. An electron flood gun was used to neutralize for charging. In the asymmetric fitting, Gaussian-Lorentzian functions were used (after a Shirley background correction), where the FWHM of all the peaks were constrained and the peak positions and areas were set free.

Scanning electron microscopy (SEM). The mass ratio of the catalyst to the support and the atomic ratios Nb:Ti and Ir:Ru were determined by means of energy dispersive

X-ray (EDX) spectroscopy. The EDX measurements were performed by means of an INCA-300 energy analyzer coupled to a JSM5910-LV JEOL scanning electron microscope.

Transmission electron microscopy (TEM). A JEOL JEM-1400PLUS transmission electron microscope operating at 120 kV equipped with a GATAN US1000 CCD camera (2k x 2k) was applied to analyse the nanotube morphology and catalyst dispersion. The samples were suspended in ethanol and ultrasonicated before deposition onto carbon coated copper grids for TEM analyses.

Pore size and volume analyses. Nitrogen adsorption/desorption isotherms of the supports were determined at 77 K by means of a Micromeritics ASAP 2020 equipment after outgassing for 10 h at 150 °C under vacuum (10^{-5} torr). The specific surface area (S_{BET}) was obtained using the Brunauer-Emmett-Teller (BET) equation and taking 0.162 nm^2 as the cross-sectional area of the N_2 molecule. The pore volumes and pore size distribution were determined from the desorption branches of the isotherms using the Barrett-Joyner-Halenda (BJH) model.

Electrical conductivity measurements of the supports.

An in-house developed conductivity cell consists of a Teflon body, ceramic heating element and four small area electrodes positioned, as shown in Fig. 3.1. The temperature was controlled using a thermocouple. The four electrodes (A, B, C and D) were coated with Pt and placed on the boundary of the pellet. A current was passed through two electrodes (for instance, I_{AB}) and the voltage was measured through the other two electrodes (for instance, U_{CD}). The resistance can be calculated using Ohm's law:

$$R_{\text{AB,CD}} = \frac{U_{\text{CD}}}{I_{\text{AB}}} \quad (3.5)$$

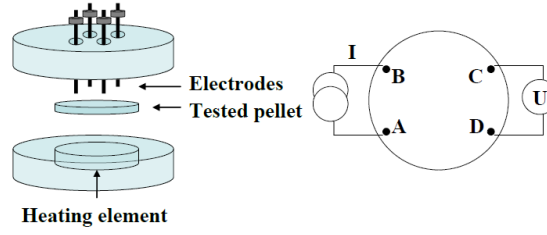


Figure 3.1: Scheme of the in-house developed conductivity cell.

Van der Pauw showed that the sheet resistance can be measured from these two resistances using the equation (3.6) [194]:

$$e^{-\pi t \frac{R_{AB,CD}}{\rho}} + e^{-\pi t \frac{R_{AC,BD}}{\rho}} = 1 \quad (3.6)$$

where t is the thickness of the sample and ρ is the specific resistance of the material. This equation can be solved for ρ . If the sample has an axis of symmetry ($R_{AB,CD} = R_{AC,BD}$) the sheet resistance can be calculated as:

$$\rho = \pi t \frac{R_{AB,CD}}{\ln 2} \quad (3.7)$$

Conductivity measurements at different temperatures in the range 25 to 250 °C were conducted. Different TiO₂-based samples were tested: Nb-doped TiO₂ (Nb-TiO₂), Nb-doped titania nanotubes (Nb-TNT) and Nb-doped titania nanotubes immersed in phosphoric acid (Nb-TNT-P), with different niobium content (0, 3, 6 and 10 at.%). An amount of 0.5 g of each material was grinded with mortar and pestle, and then pressed in a 13 mm pellet dye at 10 tons (880 MPa) for 10 min. The conductivity of each pellet (thickness 1.1±0.1 mm) was measured by the four-probe method described above at temperatures up to 250°C. After stabilizing the temperature for 10 min., 10 measurements were performed at each temperature, taking the average value. The selected temperatures were: 25, 50, 75, 80, 100, 125, 150, 175, 200, 225, and 250 °C.

After cooling down, the measurement at 25 °C was repeated in order to detect any possible differences in the conductivity due to heating to 250 °C.

3.3 Electrochemical characterization of the PEMWE materials

3.3.1 Experimental setup

The electrochemical measurements were conducted using a potentiostat PARSTAT 2273 (Ametek, Inc.) controlled by the PowerSuite 2.58 software in a three-electrode glass cell with the catalyst-covered glassy carbon (GC) working electrode (when studying HER) or the catalyst-covered gold working electrode (OER) both having 3 mm in diameter (0.0707 cm² in section). The reference electrode was the mercurous sulfate electrode (MSE) Hg|Hg₂SO₄,K₂SO_{4(sat)} (Radiometer Analytical). All the potentials reported in this work are expressed versus the reversible hydrogen electrode (RHE). A Pt wire was used as the auxiliary electrode. The electrolyte was an aqueous solution 0.50 mol dm⁻³ H₂SO₄ (prepared from Merck Suprapure), deaerated by purging with N₂ (Air Liquide, purity ≥ 99.995 %) for 20 min. The electrolyte temperature was maintained at 25 °C. Fig. 3.2 shows the experimental setup (on the left) and the GC working electrode (on the right).

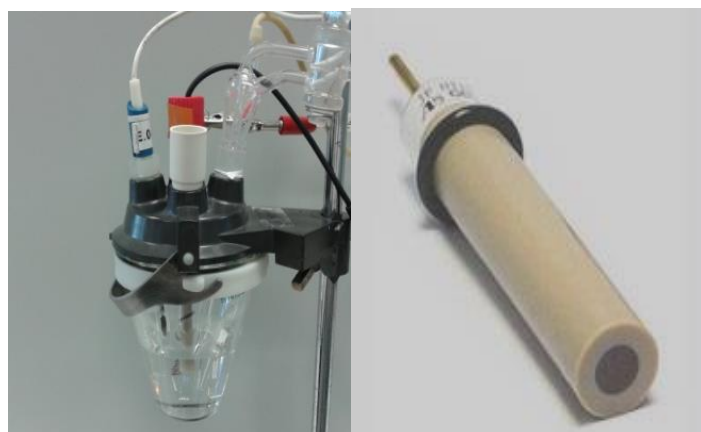


Figure 3.2 Three-electrode glass cell with 0.50 mol dm⁻³ H₂SO₄ as electrolyte (left hand side). An image of the GC working electrode, is shown on the right.

Before each analysis, the tip of the GC disk or the gold disk electrode was polished to a mirror finish using alumina powder suspensions (0.3 μm and 0.05 μm , Buehler), followed by sonication in ultrapure water.

The IR -drop in the solution was measured using electrochemical impedance spectroscopy (EIS). The impedance spectra were collected at open circuit potential (OCP) from 100 kHz to 0.1 Hz at ac amplitude of 5 mV. All j - E curves are corrected by the uncompensated resistance.

3.3.2 Electrode preparation and characterization of the HER catalysts

A quantity of 10 mg of the catalyst was dispersed in 0.50 ml mixture of isopropanol and ultrapure water, and ultrasonically treated for 30 min. The required amount of this suspension was placed by means of a micropipette onto the surface of the GC disk electrode to achieve a Pt loading of 14 $\mu\text{g}_{\text{Pt}} \text{cm}^{-2}$, and dried under a slow nitrogen flow (Air Liquide, purity $\geq 99.995\%$). It was then covered with 5 μl of a 0.05 % Nafion[®] solution in ethanol and dried again under nitrogen.

Cyclic voltammetry experiments were performed in the potential window 0.050 – 1.200 V at a scan rate of 100 mV s^{-1} until reproducible cyclic voltammograms were obtained. The hydrogen evolution reaction was studied by potentiodynamic scans in the range of 0.200 to -0.100 V in the negative direction, with a scan rate of 1 mVs^{-1} .

The electrochemical active surface area (ECSA) of Pt was estimated from the net charge for hydrogen adsorption in cyclic voltammograms recorded at scan rate 20 mV s^{-1} under N_2 inert atmosphere. It was calculated from the integrated charge of the hydrogen desorption peak areas and it was obtained from the following equation:

$$\text{ECSA} = \frac{Q_{\text{H}}}{0.21 \text{ mPt}} \quad (3.8)$$

where m_{Pt} is the platinum loading in the electrode, Q_H the charge for hydrogen desorption (mC) and assuming that 0.210 mC cm^{-2} was needed to produce a monolayer of adsorbed H on polycrystalline platinum [195].

3.3.3 Electrode preparation and characterization of the OER catalysts

An amount of 10 mg of the catalyst were dispersed in 0.50 mL mixture of isopropanol and ultrapure water, and ultrasonically treated for 30 min. The required amount of this suspension was placed by means of a micropipette onto the surface of the gold disk electrode to achieve an IrO_2 loading of $35.28 \mu\text{g}_{\text{IrO}_2} \text{ cm}^{-2}$ (or the same amount of IrRuO_x), and dried under a slow nitrogen flow (Air Liquide, purity $\geq 99.995 \%$). It was then covered with $5 \mu\text{l}$ of a 0.05% Nafion[®] solution in ethanol and dried again under nitrogen.

Cyclic voltammetry was performed in the potential window $0.100 \text{ V} - 1.400 \text{ V}$ at a scan rate of 100 mV s^{-1} until a reproducible cyclic voltammogram was obtained. For the purpose of calculating the redox charge, cyclic voltammograms were recorded after that in the same potential range at scan rates of 200, 100, 50 and 20 mV s^{-1} . Linear sweep voltammetry was performed in the range $1.20 \text{ V} - 2.00 \text{ V}$ with a scan rate of 1 mV s^{-1} . The overall voltammetric charge was calculated from the area under the anodic sweep. However, the cathodic charge was taken into account to evaluate the quantity of the catalysts. The total voltammetric charge can be divided into a fast charge, due to the charging of the outer surface area of the electrode and shows more accessible active sites on the catalyst surface at high scan rates, and a slow charge, representing the total active sites and respectively less accessible surface regions at lower scan rates. In this way it is possible to find the so-called redox, double-layer and total charge of the electrode. At high scan rates, the double-layer (outer) charging (q_{dl} , q_{outer}) dominates while at low scan rates redox region (inner) is also accessible. The proton exchange

between surface OH groups and the acidic electrolyte is considered to be rapid at “easily accessible” regions, whereas this exchange has some diffusion limitations within the inner regions. Quantitatively the double-layer charge can be found by plotting the integrated total charge q^* vs. the inverse of the square root of the scan rate $v^{-1/2}$ (Eq. (3.9)). Extrapolating the curve to zero ($v \rightarrow \infty$) gives the double-layer (outer) charge (q_{dl}). Similarly, Eq. (3.10) allows finding the total charge. As the total charge consists of the double-layer charge and redox charge, the redox charge can be easily calculated (Eq. 3.11) [37,196]:

$$q = q_{outer} + const (v^{-1/2}) \quad (3.9)$$

$$q^{-1} = q^{-1}_{total} + const (v^{1/2}) \quad (3.10)$$

$$q = q_{outer} + q_{inner} \quad (3.11)$$

3.4 MEA preparation and characterization for PEMWE

3.4.1 Membrane pretreatment

As purchased membrane Nafion[®] 115 (thickness ~127 μm , Du Pont, USA) was boiled in 3 % water solution of H_2O_2 for 1 h and then it was boiled in 0.50 mol dm^{-3} H_2SO_4 for 2 h to ensure its full protonation. At the end the membrane was rinsed with and boiled in ultrapure water for 2 h with the water being changed after every 30 min to remove any remaining acid. The cleaned membrane was stored in ultrapure water and dried before use.

When the sodium form of the membrane had to be used, the clean membrane was boiled for 1 h in 1.0 mol dm^{-3} NaOH and afterwards, in ultrapure water for 1 h.

3.4.2 Catalysts inks composition

For X g of catalyst (total mass support + catalyst)

8.57 X g of 5 wt. % Nafion ethanol dispersion (Aldrich)

8 X g of glycerol (Panreac, RG).

0.4 X g of tetrabutylammonium hydroxide (Sigma Aldrich, RG)

3.4.3 MEA preparation

CCM type MEAs with 5 cm² geometric area (4.84 cm² square shape active area) were prepared using the decal method modified for low temperature applications reported in [119]. Catalyst ink for each one of the electrodes was prepared by mechanical stirring of the supported catalyst, appropriate amounts of 5 wt. % Nafion[®] dispersion, tetrabutylammonium hydroxide, and glycerol. The inks were painted onto clean fiberglass-reinforced Teflon decal substrates and put it in a drying oven. The procedure was repeated until the desired catalyst loading was achieved: 0.50 mg_{Pt} cm⁻² for the cathodes and 2.50 mg_{IrO₂} cm⁻² for the anodes [13,32,34,121]. The Nafion[®] content was adjusted to 30 wt. % (dry weight) in all electrodes (see ink composition in section 3.4.2). Then, the painted sides of two decals were placed facing each other on each side of a previously cleaned Nafion 115[®] membrane (see section 3.4.1). The MEA was pressed at 135 °C and 80 bar (optimized within this work) for 120 s. After hot-pressing, the decal substrates were peeled off from the membrane. Similar electrode loadings and membranes were used before in the literature [13,32,34,119]. Here, the reported values of the catalyst loadings were adjusted and optimized for our system.

The procedure of MEA preparation by conventional decal method is the same as that described above. The membrane was used in its Na⁺ (“sodium”) form. Both decal substrates loaded with the catalysts and the Na⁺ form of the Nafion 115[®] membrane were pressed at 210 °C and 50 bars for 120 s.

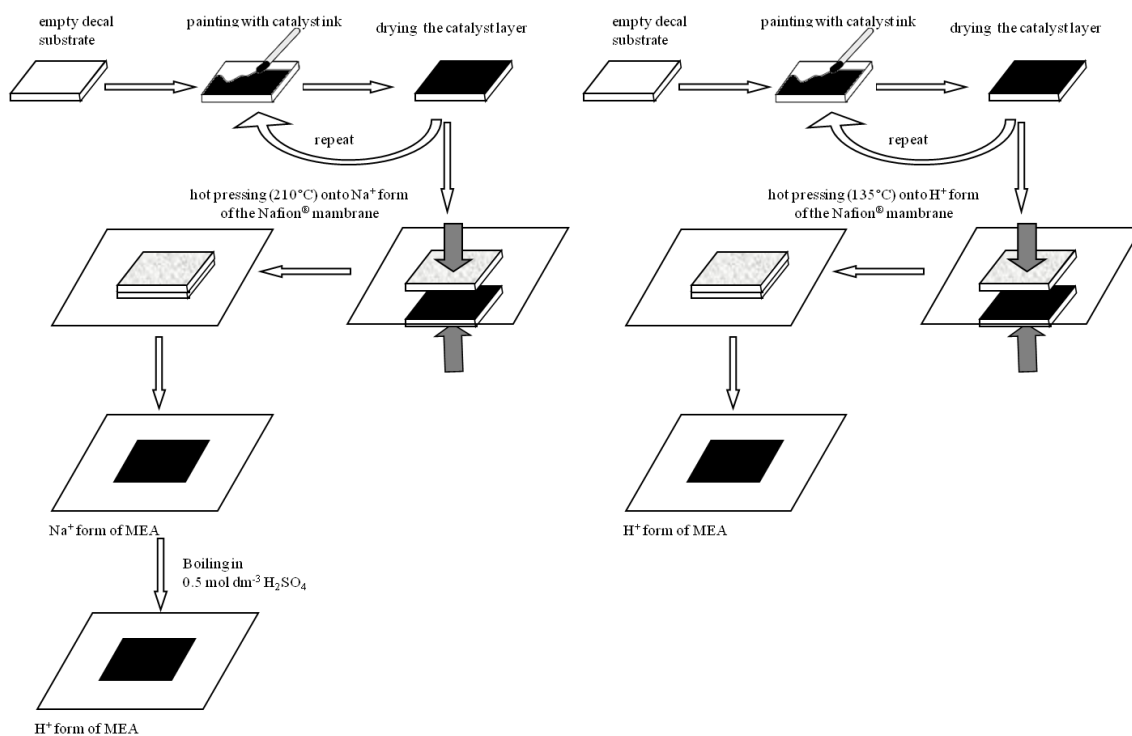


Figure 3.3 Conventional vs. low temperature decal method for the MEA preparation

3.4.4 Cell design and electrochemical characterization

The MEAs were tested in a typical electrolyser cell fixture (5 cm² geometric area, Fuel Cell Technologies, Inc.). On the anodic side the flow field channel block was replaced by a titanium block made of porous sintered titanium plates (SIKA-T3, 30% porosity, GKN Sinter Metals) [8,13,19,34,197] with serpentine flow fields. A set of retaining bolts was positioned around the periphery of the cell and a uniform clamping torque of 5 N m was applied.

The scheme of the cell is shown in Fig. 1.3. PTFE-pretreated Toray-060 carbon paper (Toray, Japan) was used in the cathode as the GDL. Anode GDL was porous sintered titanium (SIKA-T10, thickness 1.4 mm, 45 % porosity, GKN Sinter Metals). Ultrapure water was fed by a peristaltic pump to both, anode and cathode with a flow rate in the range from 0.2 to 10 mL min.⁻¹.

The MEA performance was evaluated by the use of Potentiostat SI 1287 Electrochemical Interface (Solartron Analytical) with frequency response analyzer 1255B (Solartron Analytical) controlled by Software Corware 3.3b and Zplot 3.3b. Measurements were done at atmospheric pressure and 80 °C. Cyclic voltammetry was performed at 100 mV s⁻¹ until reproducible voltammograms were obtained. Then, a cyclic voltammogram at 20 mV s⁻¹ was recorded. Cell polarization curves were recorded potentiodynamically between 1.300 and 1.800 V with a scan rate of 0.1 mV s⁻¹ at different water flow rates.

The *IR*-drop was measured using EIS. The impedance spectra were collected at open circuit potential (OCP) from 100 kHz to 0.1 Hz at *ac* amplitude of 5 mV. All the *j*-*E* curves were corrected by the uncompensated resistance.

3.5 Physico-chemical characterization of the DMFC materials

The XRD technique was used to characterize commercial PtRu and Pt black catalysts. The XRD diffractograms for bulk materials and electrodes were obtained by a Bruker D8 Advance diffractometer operating with Cu K α radiation ($\lambda = 1.5406 \text{ \AA}$) and a 2θ scan from 30 to 100° (at 0.02° min⁻¹). Diffraction peaks were assigned according to the International Centre for Diffraction Data (ICDD) cards in PDF-2 database. The XRD data were used to determine the lattice parameter (from the interplanar distances) and the average crystallite size by using Bragg's law (Eq. 3.1) and Scherrer equation (Eq. 3.4).

SEM images of the anode catalyst layers were taken using a JSM5910-LV JEOL microscope. The mass ratio of Pt to Ru was analysed by EDX. The EDX measurements were performed with an INCA-300 energy analyser coupled to the SEM. The PtRu bulk composition was determined from the average of five different measurements on the same sample with relative errors less than 1%.

The particle size distribution in the catalyst inks was measured by laser diffraction using a LS 13 320 (Beckman Coulter) particle size analyser. The pore size distributions in the anodes were determined by a mercury porosimeter (Quantachrome Pore Master).

3.6 Electrochemical characterization of the DMFC materials

3.6.1 Experimental setup

Methanol electrooxidation measurements were carried out in a thermostated two-compartment electrochemical glass cell. A N₂-purged solution of 2.0 mol dm⁻³ CH₃OH + 0.5 mol dm⁻³ H₂SO₄ was used as electrolyte. The working electrode, prepared according subsection 3.6.2, was placed inside a holder, being 0.79 cm² the geometric area exposed to the solution. A gold mesh was used as the current collector. The reference electrode was Hg|Hg₂SO₄, K₂SO_{4sat} (0.700 ± 0.003 V vs. RHE in 0.5 mol dm⁻³ H₂SO₄), separated from the main solution compartment by a tube ended in a Luggin-Haber capillary, but potentials in this work are quoted against the reversible hydrogen electrode (RHE). The auxiliary electrode consisted of a Pt wire separated from the main solution by a fritted glass.

3.6.2 Preparation of the DMFC electrodes

Porous diffusion anodes consisted of a GDL and a catalyst layer (CL). The former was a thin layer made of Vulcan XC-72 (Cabot Corp.) carbon black and polytetrafluoroethylene deposited on the top of hydrofobized Toray carbon paper (TGPH-090, 20 % wet proofing, E-TEK Inc.). A catalyst ink was prepared using the following procedure based on the “dropping process” reported by Uchida *et al.* for Proton Exchange Membrane Fuel Cell (PEMFC) electrodes [165]. First, the PtRu black catalyst (Pt:Ru; 50:50 at. %, HISPECTM 6000, Alfa Aesar[®]) was wetted with ultrapure water ($\kappa \leq 0.054 \mu\text{S cm}^{-1}$, obtained from a Millipore Milli-Q System), and mixed with

an organic solvent (see Table 1 for more details) under ultrasonic stirring for 30 min. Next, an appropriate amount of Nafion[®] dispersion (5 wt. %, Aldrich) was dropped into the catalyst solution while stirring to achieve a dry ionomer composition of 15 wt. % in the catalyst layer. Ultrasonic stirring was applied for another 2 h at room temperature to obtain a uniform dispersion. Afterwards, the catalyst ink was sprayed onto the GDL by an air-gun feed with pure nitrogen (99.999 %, Praxair) and dried at 60 °C in an oven. The PtRu black loading was adjusted to 4.0 mg cm⁻².

The gas diffusion cathode consisted of an ELAT[®] V2.1 (E-TEK, Inc.) gas diffusion layer and a catalyst layer made of Pt black (HSA, Premetek Co.) at a loading of 4.0 mg cm⁻² and Nafion[®] ionomer with a 10 wt. % by dry weight content. The catalyst layer was prepared following the same technique as for the anode, but the catalyst ink contained n-butyl acetate as organic solvent.

3.6.3 Electrochemical characterization of the DMFC electrodes

The electrochemical measurements were performed with a potentiostat PGSTAT 30 (Eco Chemie) driven by the GPES software. Before these measurements, the surface of the PtRu catalysed electrodes was cleaned by CV between 0.075 and 0.750 V at 0.100 V s⁻¹ in N₂-purged 0.5 mol dm⁻³ H₂SO₄ (Merck Suprapure) solution until observing a steady voltammogram (usually 25 cycles). Linear sweep voltammetry was performed between 0.075 and 0.750 V to avoid Ru dissolution.

The electrochemical active surface areas (ECSAs) were estimated from CO stripping voltammetry. Before stripping, CO was first adsorbed onto the electrode surface at 0.100 V for 30 min and subsequently the electrolyte was purged by N₂ bubbling for 20 min.

The EIS measurements were carried out in the potentiostatic mode using a 1255 FRA combined with a 1287A potentiostat (both Solartron Analytical, Inc.), commanded

by the CorrWare Electrochemical/Corrosion and Z-Plot impedance software. Impedance spectra were collected applying a potential of 0.400 V. The *ac* amplitude was 5 mV and the frequency ranged between 10 kHz and 0.010 Hz, with 10 steps dec^{-1} . The integration time was 10 s.

3.7 MEA preparation and characterization for DMFC

3.7.1 MEA preparation

CCS type MEAs with 5 cm^2 geometric area (4.84 cm^2 square shape active area) were prepared using the hot press method [198]. Nafion[®] 115 membranes (DuPont) were cleaned following the procedure described in section 3.4.1 and stored in ultrapure water and dried before use. Each MEA was assembled by hot-pressing the anode and cathode on either side of the pretreated membrane at 50 bar and 130 °C for 3 min. Previously, additional ionomer solution was sprayed onto the catalyst layer of each electrode at a loading of 0.80 mg cm^{-2} (dry basis).

3.7.2 Cell design and electrochemical characterization

On the other hand, each type of MEA was manufactured and tested by triplicate. Testing in single DMFC was performed using MEAs of 5 cm^2 in active area section, coupled to commercial fuel cell hardware (Fuel Cell Technologies, Inc.). The MEA, flanked by the two graphite current collectors with serpentine flow fields, was held between two gold-plated stainless-steel contact plates using a set of retaining bolts positioned around the periphery of the cell. A uniform clamping torque of 5 N m was applied. The anodic compartment of the cell was fed with 2.0 mol dm^{-3} aqueous methanol solution preheated at 60 °C, keeping the flow rate at 2.0 mL min^{-1} . Dry high purity synthetic air (Praxair, 99.999 %) at fixed flow rate of 100 mL min^{-1} and atmospheric pressure, was fed through the cathodic compartment. The cell temperature

was set at 60.0 °C. Steady-state V - j polarization curves were recorded from the open circuit voltage down to 0.1 V at scan rate of 1 mV s⁻¹ by a 1287A potentiostat (Solartron Analytical, Inc.). Polarization curves with an error less than 5 % in the overall current density range were obtained. To carry out in situ EIS measurements and CO stripping, the MEA was operated in driven cell mode, *i.e.* the anode was the working electrode and the cathode was feed with hydrogen, acting as a counter and reference electrode (dynamic reference electrode, DHE). CO voltammetry stripping experiments were carried out at $T_{\text{cell}} = 25$ °C, feeding the anode with a mixture of 0.1% CO in N₂ at 250 cm³ min⁻¹ at atmospheric pressure for 50 min, while holding the electrode potential at 0.100 V vs. DHE. After adsorption, the gas was switched to N₂ for 20 min at 250 mL min⁻¹ at the admission potential, to remove any CO from the single cell. The cathode was fed with humidified hydrogen at 200 mL min⁻¹. All gases were humidified at T_{cell} . Two CO stripping voltammograms were then recorded in the positive direction at 20 mV s⁻¹ [199].

4. Results and discussion

4.1 PEM water electrolysis

4.1.1 Supports characterization

4.1.1.1 Formation of TiO_2 nanotubes

In section 3.1.2 the synthesis of TNT in 10 mol dm^{-3} NaOH via alkaline hydrothermal method is described. The mechanism of formation of TNT includes dissolving of TiO_2 in NaOH and formation of layered sodium titanates. After that scrolling of the layered titanates into nanotubes. However, it is not clear whether TNT are formed before or after the acidic treatment.

The purpose of the acid treatment was to remove the Na^+ ions from the samples and to form new Ti-O-Ti bonds that would improve photocatalytic activity of the titania nanotubes [200]. The Na^+ ions were displaced by H^+ ions to form Ti-OH bonds in the washing process and further dehydration of Ti-OH bonds produced Ti-O-Ti bonds or Ti-O---H-O-Ti hydrogen bonds. The bond distance between one Ti and another on the surface consequently decreased, facilitating the sheet folding process [200,201]. Kasuga et al. [200] concluded that washing with acid and with deionized water were two principal crucial steps to produce high activity of titania nanotubes [200,202].

In [203] Yuan and Su proposed a mechanism for the fabrication of titanate nanotubes that was similar to Kasuga's. They postulated that the crystalline structure of TiO_2 was represented as TiO_6 octahedral in the three-dimensional nanosheets. The Ti-O-Ti bonds were broken in the alkaline media and titanate sheets were then peeled off into nanosheets and subsequently folded into nanotubes. The Na^+ ions were exchanged and eliminated after washing with acid and then with deionized water.

For our purposes titanate nanotubes were acid treated in order to obtain their protonated form and further were calcined to anatase phase to compare both materials before and after nanotube formation.

X-ray diffractograms of the samples before calcination are shown on Fig. 4.1. Main titanate phases indicated in the XRD patterns were monoclinic $\text{H}_2\text{Ti}_3\text{O}_7$ ($a=1.926\text{nm}$, $b=0.378\text{ nm}$, $c=0.300\text{ nm}$ and $\beta=101.45^\circ$) and $\text{H}_2\text{Ti}_4\text{O}_9$ ($a=1.877\text{nm}$, $b=0.375\text{ nm}$, $c=1.162\text{ nm}$ and $\beta=104.6^\circ$).

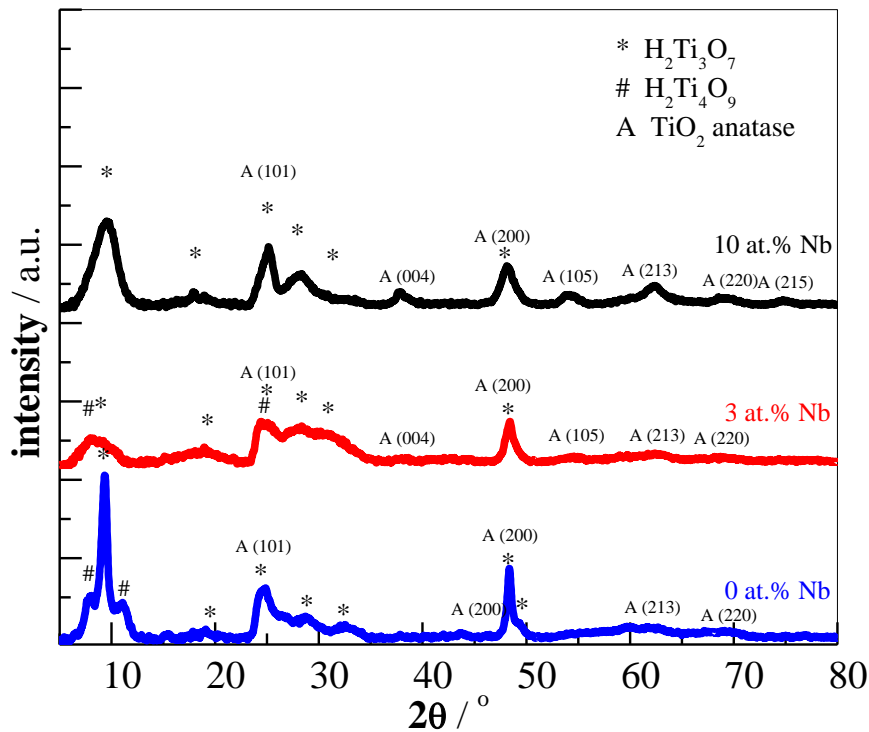


Figure 4.1 X-ray diffractograms of titanates obtained from TiO_2 with different content of Nb (0 at.%, 3 at.% and 10 at.%).

Anatase peaks, marked with the symbol A in Fig. 4.1, can also be found with increasing Nb-concentration, which is in agreement with the previously reported stabilizing effect of Nb on the anatase phase [103]. The characteristic peak at around $2\theta = 10^\circ$ for all XRD patterns indicates that the samples are composed of a layered titanate.

Moreover, the peak shifts gradually to higher angles which means the decrease of the interlayer spacing due to incorporation of Nb in the titanate phase [112].

4.1.1.2 Physico-chemical characterization of the supports

SEM and TEM images of TiO₂ and titania nanotubes are shown in Figs. 4.2 and 4.3 are shown. The TEM images display the nanotubes formed after chemical post-treatment with 0.1 mol dm⁻³ HCl (Figs. 4.2b and 4.3). When immersed in 0.1 mol dm⁻³ H₃PO₄ the nanotubes formed ball-shaped structures (Fig. 4.2c). The outer diameter of the nanotubes was calculated to be about 10 nm and the length of 100-200 nm.

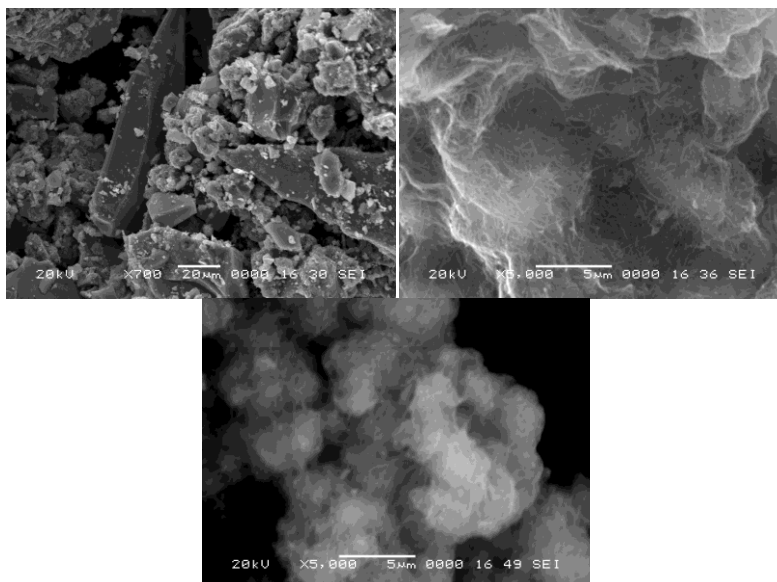


Figure 4.2 SEM images of (a) 3 Nb-TiO₂, (b) 3Nb-TNT and (c) 3Nb-TNT-P

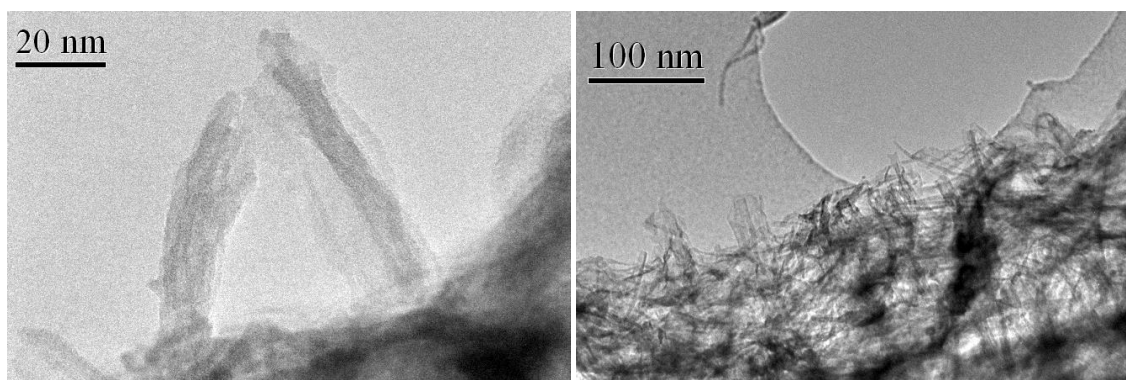


Figure 4.3 TEM images of 3Nb-TNT at different resolutions-

X-ray diffraction

X-ray diffractograms of TiO₂, TNT and TNT-P materials are presented in Figs. 4.4, 4.5 and 4.6, respectively. Typical peaks can be found for the anatase phase of TiO₂ (peaks A in such figures). With the nanotube formation, the intensity of the peaks decreases. With increasing the amount of Nb, the intensity of anatase peaks decrease and they become wider, thus suggesting smaller crystallite size of the doped TiO₂ in comparison to the non-doped one. This is in agreement with previously reported grain growth inhibition by the Nb-dopant [103,204]. Additionally, slightly shift to lower angles suggests lattice expansion due to the incorporation of Nb⁵⁺ into the crystal lattice [205]. Crystallite size and lattice parameters were calculated by the use of Bragg's law, Eq. (3.1), and the Scherrer equation, Eq. (3.4).

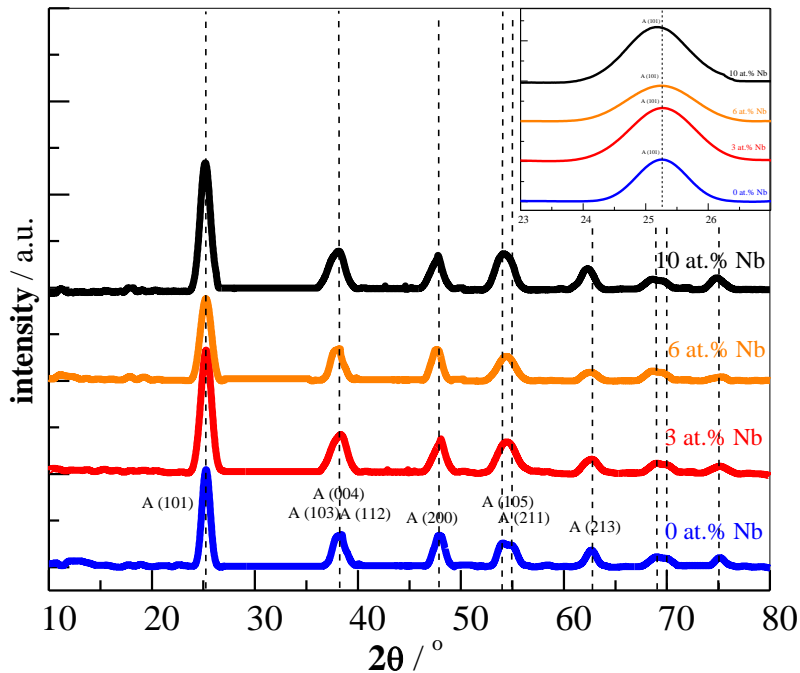


Figure 4.4 X-ray diffractogram of titania dioxide (A=anatase) with different content of Nb (a) 0 at.%, (b) 3 at.%, (c) 6 at.% and (d) 10 at.%.

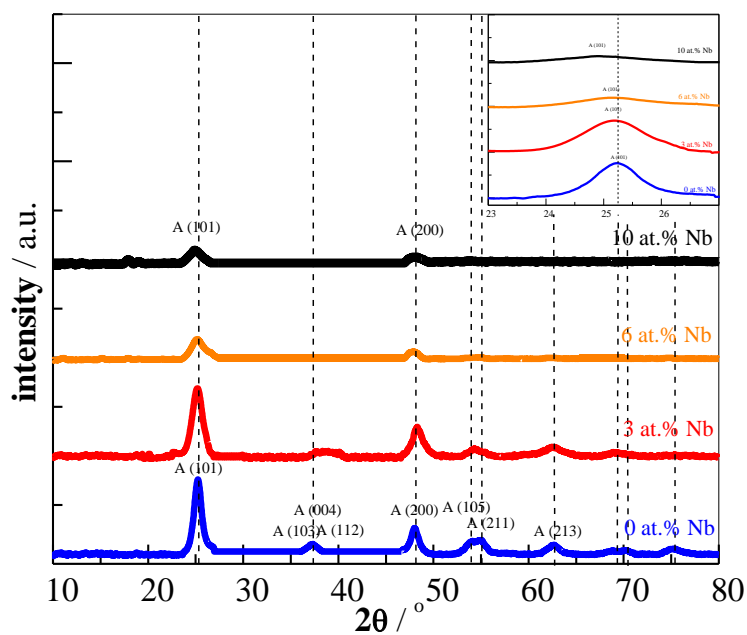


Figure 4.5 X-ray diffractogram of titania nanotubes (TNT) with different content of Nb (a) 0 at.%, (b) 3 at.%, (c) 6 at.% and (d) 10 at.%.

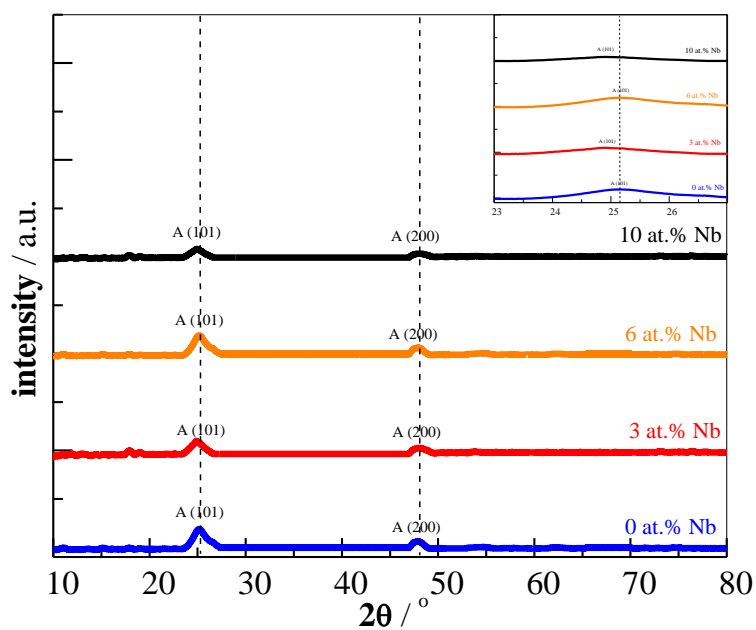


Figure 4.6 X-ray diffractograms of titania nanotubes immersed in phosphoric acid (TNT-P) with different content of Nb (a) 0 at.%, (b) 3 at.%, (c) 6 at.% and (d) 10 at.%.

The corresponding results are listed in Table 4.1, in which the decrease in the crystallite size and the increase of the lattice parameter with Nb doping is confirmed. For TiO₂ samples, the calculated particle sizes are in the range 6.4 to 8.7 nm for the different values of Nb-content. In the case of the TNT samples these values are in the range 6.0 to 8.8 nm for the different Nb-concentrations, whereas for TNT-P, the range of crystallite size is 4 to 6.3 nm.

BET surface area and porosimetry

The morphology of the nanotubes is very sensitive to the conditions of their preparation. In [112,206] the effect of the synthesis temperature on the specific surface area and pore size distribution is analysed. The effect of the concentration of the washing acid is other important factor [111,112]. The observed values of the specific surface area of the reported supports are in the range of 80 m²g⁻¹ for TiO₂ (anatase) to 100 m²g⁻¹ for 10Nb-TiO₂ and typical specific surface area of about 150 – 250 m² g⁻¹ for nanotubes and up to 303 m² g⁻¹ for 10 Nb-TNT (see Table 4.1). For comparison, Vulcan-XC72 (Cabot Corp.) has a specific surface area of about 250 m²g⁻¹. Narrow pore size distribution is observed for TiO₂ supports within the range 3.77 to 7.08 nm and slightly wider pore diameters for the TNT supports between 6.5 nm and 13.42 nm and larger between 8.05 to 16.18 nm for TNT-P. Smaller pore size of TiO₂ supports is very similar to the typical particle size of Pt electrocatalysts, which may limit their use as catalyst support. Metallic nanoparticles could be trapped inside the pores and therefore, become inaccessible to the reactants of the electrochemical reaction.

Table 4.1 Textural properties from BET analysis and crystallite size and lattice parameters from XRD and electrical conductivity at room temperature of the supports with different Nb content.

	Pore volume/ cm³ g⁻¹	Pore diameter/ nm	BET area/ m² g⁻¹	Crystallite size/ nm	Lattice parameter/ Å	Conductivity/ μS cm⁻¹
TiO ₂	0.202	7.08	80	8.7	4.9782	16.61
3Nb-TiO ₂	0.178	6.05	87	6.4	4.9860	42.62
6Nb- TiO ₂	0.165	4.87	93	6.5	4.9865	6.67
10Nb- TiO ₂	0.126	3.77	100	7.3	4.9978	20.92
TNT	0.581	13.42	145	8.8	4.9865	0.35
3Nb-TNT	0.769	9.33	260	6.5	5.0007	2.02
6Nb-TNT	0.317	6.45	148	6.0	5.0049	2.43
10Nb-TNT	0.861	9.13	303	7.8	5.0544	0.31
TNT-P	0.494	16.18	104	6.0	4.9865	0.90
3Nb-TNT-P	0.669	11.96	162	4.0	5.0077	0.44
6Nb-TNT-P	0.198	8.67	58	6.3	4.9964	0.22
10Nb-TNT-P	0.681	8.05	265	4.0	5.0106	2.09

Conductivity measurements

The conductivity at elevated temperatures of TiO₂ with 0 to 10 at. % Nb as a dopant is shown in Fig. 4.7. In the temperature range 50-80 °C the highest value of the conductivity is observed for 3 at. % Nb, followed by 10 at. % Nb. At temperatures higher than 80 °C the conductivity is decreasing rapidly. After heating to 250 °C and then cooling slowly down to 30 °C, the conductivity of the samples cannot be recovered. This may suggest dehydration during heating, which strongly affects the conductivity.

The TiO₂ conductivity at room temperature is in the range 0.6 to 41 μS cm⁻¹. These values are very similar to those reported by Rau in [207] of 10⁻⁵ S cm⁻¹ and Chhina et al. [205] for the same compound (10 at.% Nb-TiO₂) calcined at 500 °C for 6 h and then reduced at 500 °C and at 600 °C, with conductivities of 0.12-0.14 μS cm⁻¹ and 1.06-1.29 μS cm⁻¹, respectively, depending on the reduction conditions (Table 4.2).

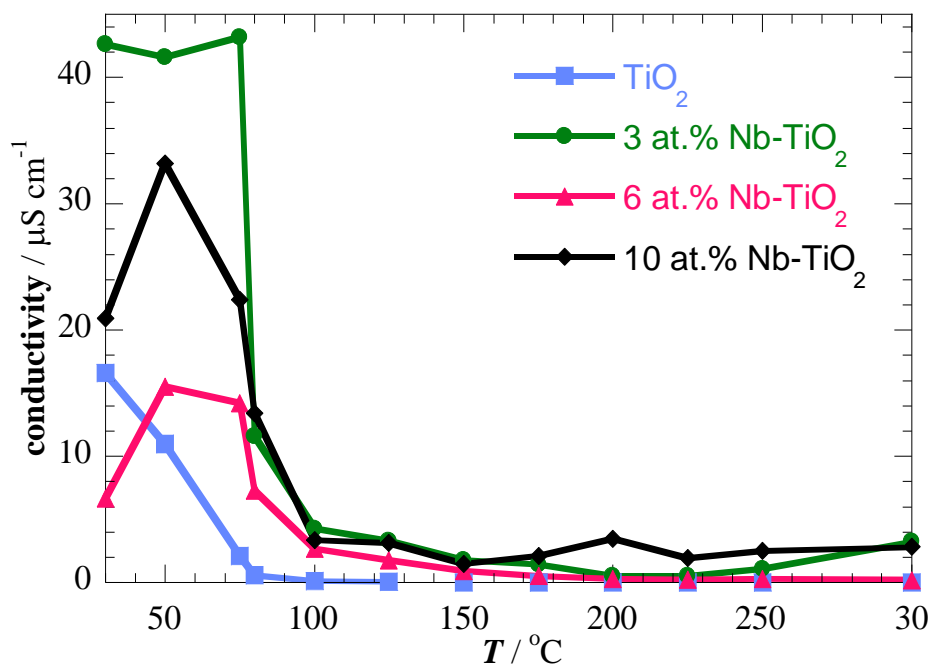


Figure 4.7 Conductivity at different temperatures in the range 30-250 °C of TiO₂ and Nb-doped-TiO₂ with 3, 6 and 10 at. % Nb.

Table 4.2 Conductivity of Nb₁₀-TiO₂ calcined at 500 °C for 6 h, reported by Chhina [205].

Reduction temperature / °C	Conductivity / μS cm ⁻¹	
	Calcined then reduced	Reduced directly
500	0.12	0.14
600	1.06	1.29
700*	610*	511
900*	1400*	1640

*At temperatures higher than 700 °C there is rutile phase which has a better conductivity but a lower specific surface area.

In [208] the room temperature electronic conductivity increased from 1×10^{-8} S cm⁻¹ for the non-doped titania microspheres to 1×10^{-4} S cm⁻¹ for 5 at % Nb-doped TiO₂, which is a larger range of conductivities in comparison to those reported in [207] and [205] and to our results. The instrumentation and the pellets pressing conditions we

used in our measurements are the same as those reported in these later works. However, the difference is that in these previous works, the catalyst supports were mixed with a Nafion ionomer dispersion in isopropanol (20 % in vol.), added as a binder when pressed into pellets at 880 MPa (10 t).

Fig. 4.8 shows the conductivity of titania nanotubes (denoted by TNT) with 0 to 10 at. % Nb as a dopant. In the temperature range 50-200 °C the highest value of the conductivity is observed for 6 at. % Nb, followed by 3 at.% Nb. At temperatures higher than 75 °C the conductivity is decreasing, but not so sharply as in the case of TiO₂.

The conductivity at different temperatures of titania nanotubes immersed in phosphoric acid (denoted by TNT-P) with 0 to 10 at. % Nb as a dopant is shown on Fig. 4.9. In the temperature range 50-200 °C the highest value of the conductivity is observed for 10 at. % Nb, followed by non-doped TNT-P. At temperatures higher than 75-80 °C the conductivity is decreasing slowly as in the case of TNTs.

Kasuga reported in [111] the dependence of the electric conductivity on the chemical post-treatment with different acids. He prepared nanotubes containing oxoacid molecules using phosphoric, sulfuric and perchloric acids (denoted respectively by P-TNTs, S-TNTs and C-TNTs) followed by heat-treatment at 500 °C. The conductivity under 100 % relative humidity (RH) of the oxoacid-treated nanotubes was of about two orders of magnitude higher than that corresponding to the hydrochloric acid-treated (TNTs) (TNTs– 1.6×10^{-4} S cm⁻¹; P-TNTs– 1.4×10^{-2} S cm⁻¹; S-TNTs– 8×10^{-3} S cm⁻¹; C-TNTs– 1.6×10^{-2} S cm⁻¹). Additionally, when C-TNTs were heated at 300°C instead of 500°C, their conductivity increased to 5×10^{-2} S cm⁻¹. He suggested that protons on the surface of TNTs were involved in conduction and as long as the oxoacid ions adsorbed on the surface increase the proton concentration, the conductivity increases. In [114] Tighineanu *et al.* investigated the influence of annealing time and temperature on the

conductivity of TiO₂ nanotubes. Their results showed that nanotubes annealed for short time (2.5 h) at temperatures in the range 350-400 °C had lower resistance of about one order of magnitude, compared to longer annealing times (20 h) and up to 4 orders of

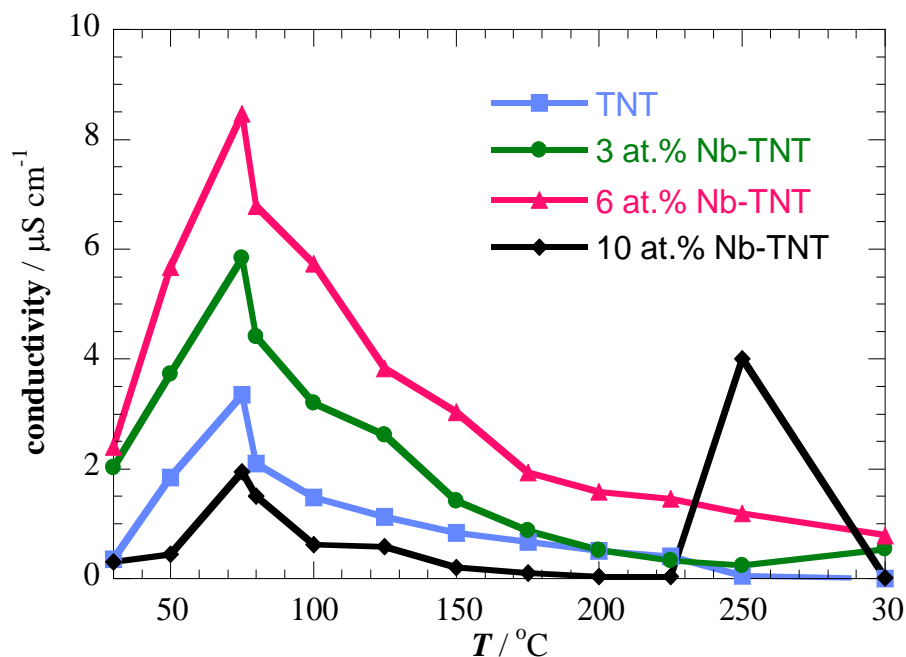


Figure 4.8 Conductivity at different temperatures in the range 30°C to 250°C of titania nanotubes and Nb-doped-titania nanotubes with 3, 6 and 10 at. % Nb.

magnitude in comparison to lower or higher annealing temperatures. However, Ref. [114] refers to several micrometer long nanotubes grown by anodization, not to powder sample pressed to a pellet as in our case. Therefore, these results cannot be easily compared with ours. The conductivity decrease after increasing the temperature over 80 °C in the samples studied here can be explained by dehydration. Kasuga's work [111] reported higher conductivity values probably because the RH was kept at 100% during the measurements, which can compensate samples dehydration during the heat treatment at 300 °C or 500 °C.

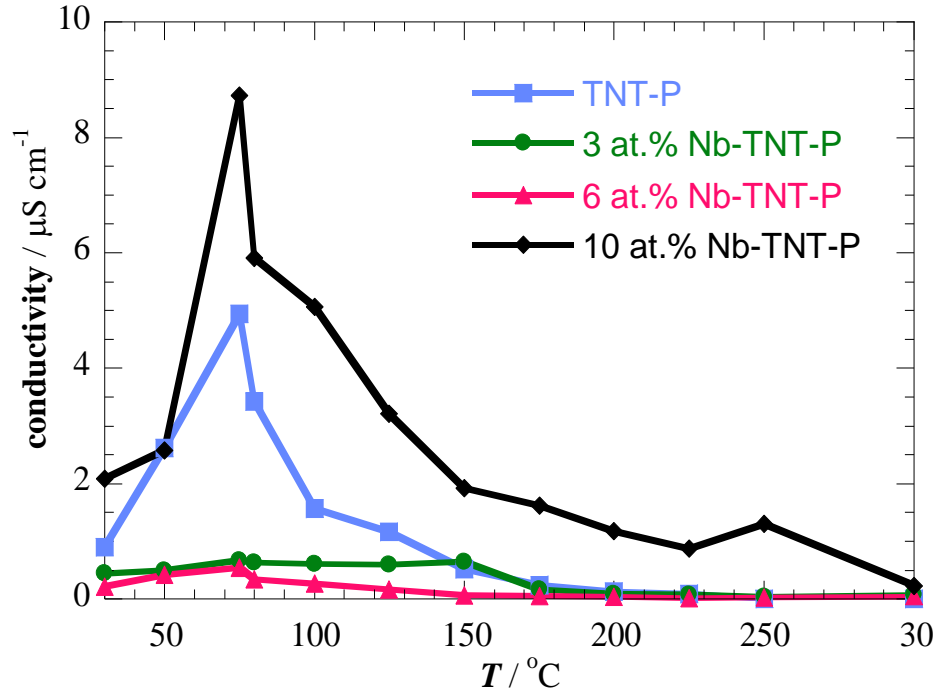


Figure 4.9 Conductivity at different temperatures in the range 30 °C to 250 °C of titania nanotubes and Nb-doped-titania nanotubes with 3, 6 and 10 at. % Nb immersed in H₃PO₄.

When TNT and 10 at. % Nb-TNT were immersed in phosphoric acid (see Fig. 4.9), the conductivity was slightly higher than that of the samples prepared with hydrochloric acid (see Fig. 4.8). Anyway, this difference cannot be seen in the other Nb-doping levels, so such an effect cannot be confirmed under the conditions of the measurements.

TiO₂ supports show one order of magnitude higher conductivity of 10 to 40 μS cm⁻¹ (Fig. 4.7) comparing to the nanotubes with typical conductivity in the range 1 to 10 μS cm⁻¹ (Figs. 4.8 and 4.9). In all our cases, the temperature increase over 80°C leads to a conductivity decrease, which can be assigned to the dehydration of the samples suggested above, when considering the mechanism of the conductivity of titania nanotubes described by Kasuga et al. [111] and the use of a RH of 100 % during the measurements.

4.1.2 Hydrogen evolution electrocatalysts

4.1.2.1 Physico-chemical characterization

In this section the results related to the structural characterization of the supported Pt catalysts for hydrogen evolution are reported. TiO₂ and Nb-doped TiO₂, TNTs, and Nb-doped TNTs and TNTs-P and Nb-doped TNTs-P were used as supports. The morphological and compositional properties have been determined using SEM, TEM, EDX, XRD and XPS.

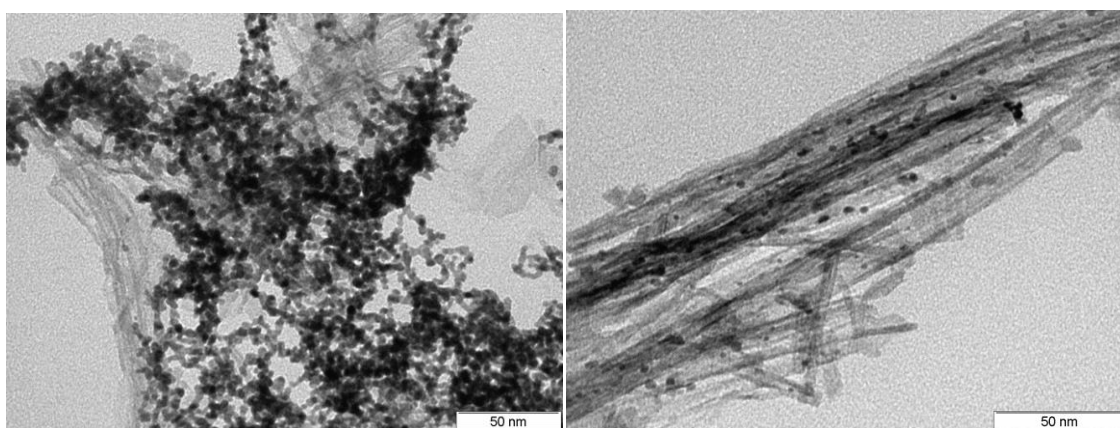


Figure 4.10 TEM images of the 20 wt. % Pt/3Nb-TNT at different magnification.

In general terms, the deposited Pt shows homogeneous distribution on the different supports studied. Thus, Fig. 4.10 shows as an example the TEM images of the 20 wt.% Pt/3Nb-TNT catalyst. It is clearly observed that the Pt nanoparticles have been deposited homogeneously along the titania nanotubes.

The diffractograms corresponding to Pt supported on TiO₂, TNTs and on TNTs-P for different Nb contents are depicted in Figs. 4.11-4.13, respectively. Typical peaks for (111), (200) and (220) planes, characteristic of the face-centred cubic (*fcc*) lattice structure of platinum, which appear at 2θ values of around 39.7, 46.2 and 67.6, respectively, are indicated. In all cases, it is shown that Pt peaks are superimposed to the anatase ones shown in section 4.1.1.2. From Scherrer equation and Bragg's law, the

corresponding crystallite sizes and lattice parameters were determined for all the

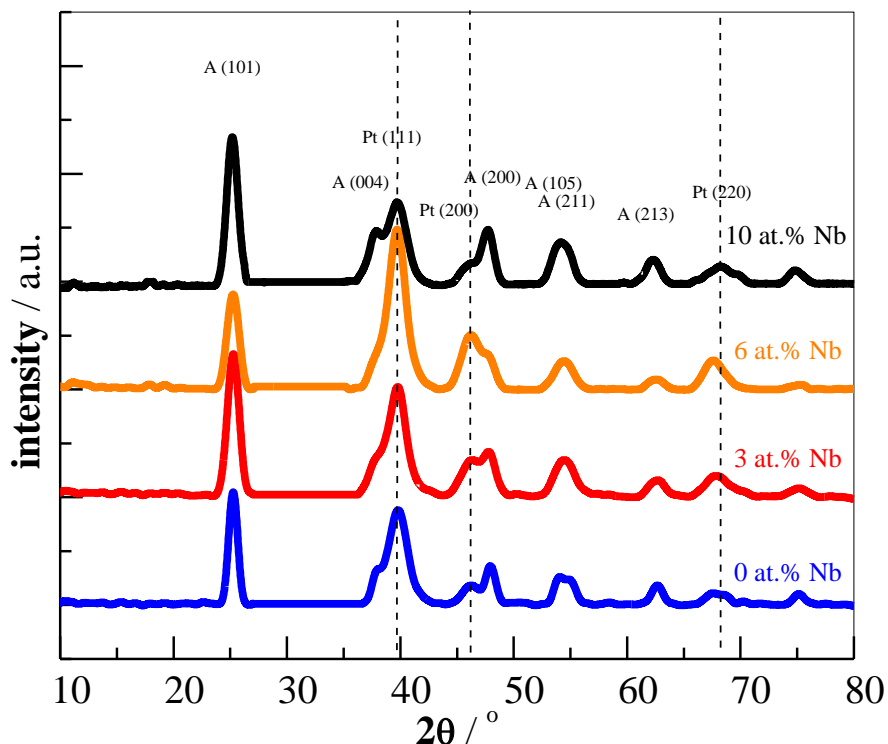


Figure 4.11 X-ray diffraction patterns of Pt deposited onto titanium dioxide (Nb-TiO₂) with different content of Nb (a) 0 at.%; (b) 3 at.%; (c) 6 at.%; (d) 10 at.% (in parenthesis, planes corresponding to characteristic diffraction signals of anatase, A, and *fcc* Pt).

specimens (see Table 4.3). The lattice parameters were always found to be close to $a = 3.922 \text{ \AA}$, confirming that the nanoparticles consisted of pure Pt. The crystallite size, however, calculated from (111) Pt plane, depended essentially on the type of support. Values in the range 4.1-5.2 \AA were obtained for the Pt nanoparticles supported on TiO₂, whereas they were in the range 3.9-4.9 \AA for TNTs and in the range 3.7-4.3 \AA for TNTs-P. This difference is not considered very significant, but it seems that there is some dependence on the titania support morphology.

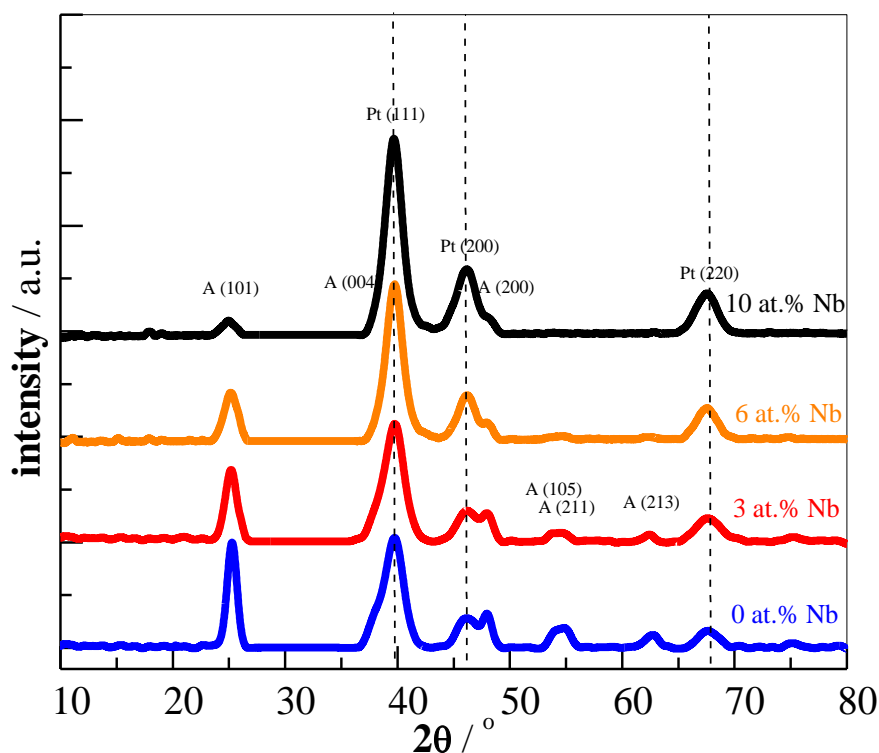


Figure 4.12 X-ray diffraction patterns of Pt deposited onto titania nanotubes (Nb-TNT) with different content of Nb (a) 0 at.%; (b) 3 at.%; (c) 6 at.%; (d) 10 at.% (in parenthesis, planes corresponding to characteristic diffraction signals of anatase, A, and *fcc* Pt).

Figs. 4.14 a and b show the Pt 4f XPS spectra of 20 wt.% Pt/3Nb-TNT and of 20 wt.% Pt/Vulcan XC72 for comparison, respectively. As shown in Fig. 4.14 a, the main Pt 4f_{7/2} and Pt 4f_{5/2} peaks of 20 wt.% Pt/3Nb-TNT are located at about 71.3 and 74.4 eV, respectively, and can be mainly assigned to Pt(0) [209]. Similar results have been obtained for 20 wt.% Pt/Vulcan XC72. Fig. 4.14 b shows the respective Pt 4f_{7/2} and Pt 4f_{5/2} peaks located at about 71.4 and 74.7 eV, which can also be assigned to Pt(0) [209]. However, there is a shift of the Pt 4f signal of about 0.3 eV for Pt/3Nb-TNT to lower binding energies in comparison to the Pt/Vulcan XC72 reference catalyst. This difference suggests a local increase of the electron density on Pt in the former and it is

considered the responsible for the SMSI in the Pt-TiO₂ system [115-117], pointing out the effect of the substrate.

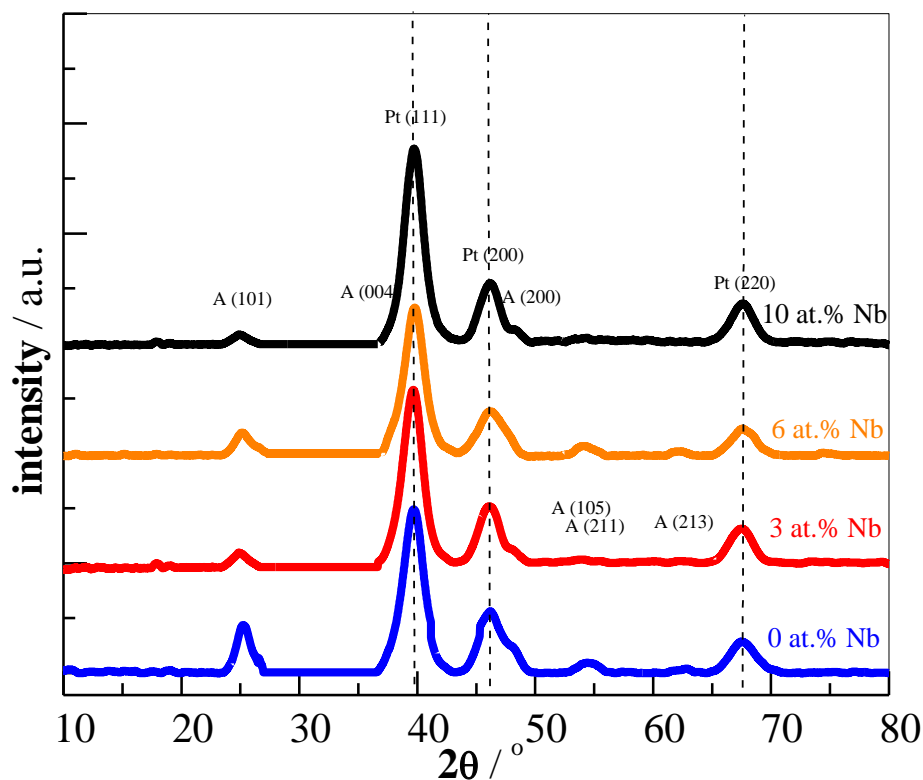


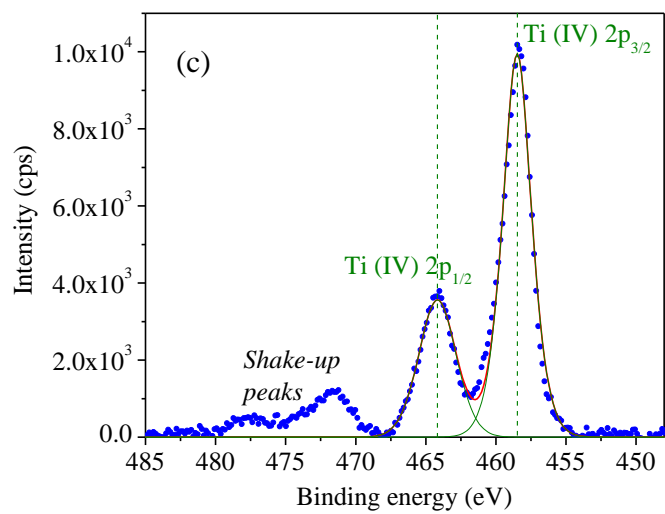
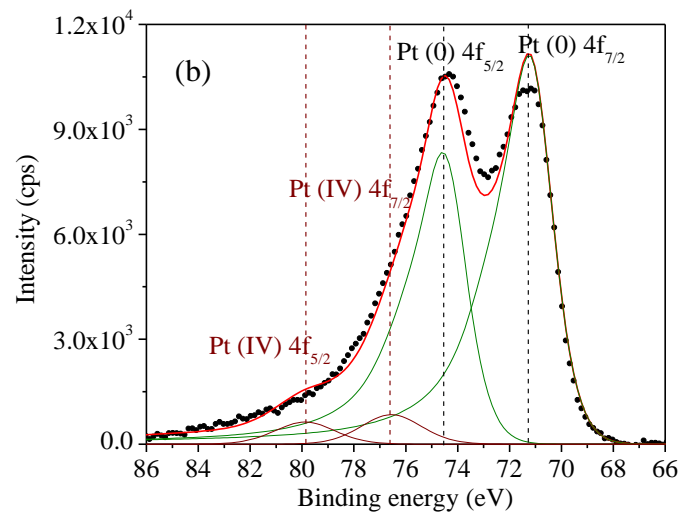
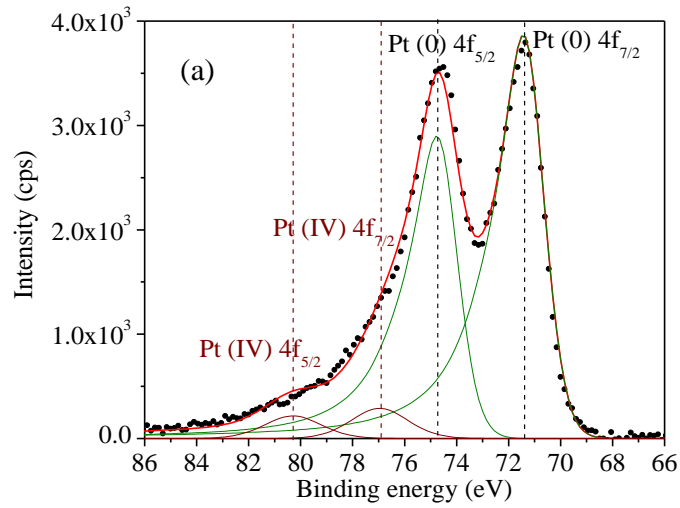
Figure 4.13 X-ray diffractogram of Pt deposited onto titania nanotubes treated with phosphoric acid (Nb-TNT-P) with different content of Nb (a) 0 at.%; (b) 3 at.%; (c) 6 at.%; (d) 10 at.% (in parenthesis, planes corresponding to characteristic diffraction signals of anatase, A, and *fcc* Pt).

With regard to the peaks deconvolution, also shown in Figs. 4.14 a and b, the Pt(0) and Pt(IV) signals have been considered. Note that the Pt(0) component was fitted to an asymmetric shape, which is characteristic of conductive materials. The deconvolutions depicted in Figs. 4.14 a and b clearly show that the main contribution are due to Pt(0). The Pt(IV) contributions are minor and the Pt 4f_{7/2} peaks of 20 wt.% Pt/3 Nb-TNT and 20 wt.% Pt/Vulcan XC72 are located at about 76.6 and 77.0 eV, respectively, the bonding energy shift being also in agreement with the different chemical nature of both supports.

Table 4.3. Selected structural, compositional and electrochemical characteristics of Pt on different titania based supports.

Composition	Crystallite size / nm	Lattice parameter / Å	Pt content / wt. %	ECSA (CV) / m ² g ⁻¹
20 wt.%Pt/TiO ₂	4.91	3.92	20.71	11.89
20 wt.%Pt/3NbTiO ₂	4.14	3.92	18.81	14.09
20 wt.%Pt/6NbTiO ₂	4.63	3.93	19.16	10.35
20 wt.%Pt/10NbTiO ₂	5.22	3.92	18.07	12.26
20 wt.%Pt/TNT	4.42	3.93	19.59	13.72
20 wt.%Pt/3NbTNT	3.93	3.92	20.73	11.13
20 wt.%Pt/6NbTNT	4.88	3.92	18.81	12.94
20 wt.%Pt/10NbTNT	4.48	3.93	17.58	10.53
20 wt.%Pt/TNT-P	3.71	3.93	19.52	5.24
20 wt.%Pt/3NbTNT-P	4.15	3.93	20.23	6.81
20 wt.%Pt/6NbTNT-P	4.31	3.92	19.36	4.68
20 wt.%Pt/10NbTNT-P	4.27	3.92	18.26	6.31
20 wt.%Pt/VulcanXC72	2.38	3.95	21.23	42.09
Pt black	5.95	3.93	-	10.87

The bonding XPS energy regions of Ti, O and Nb for 20 wt. % Pt/3Nb-TNT are depicted in Figs. 4.14 c, d and e, respectively. In Fig. 4.14 c, the main Ti 2p_{3/2} peak is located at about 458.5 eV, which corresponds to the titanium bond with oxygen in TiO₂ [209]. The characteristic shake-up peaks of TiO₂ are also observed. The fitting of the O1s spectrum revealed the presence of two components (see Fig. 4.14 d); the main one at around 529.9 eV can be attributed to metal-oxygen bonds, while the smaller one at around 531.9 eV can be assigned to metal-OH bonds [209]. According to Fig. 4.14 e,



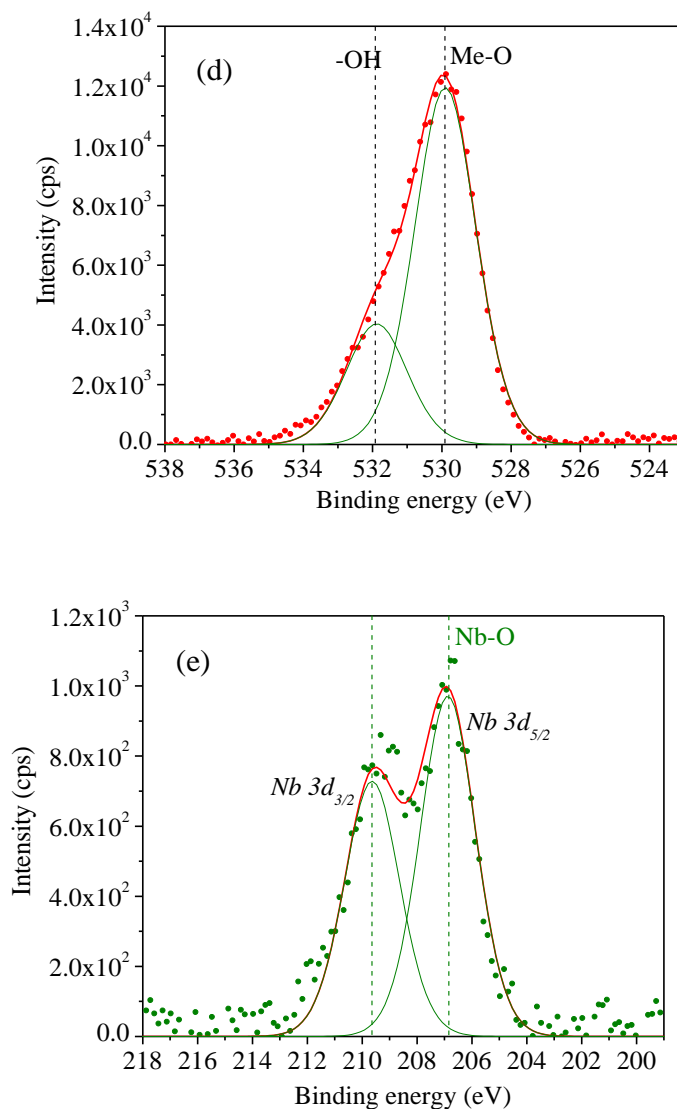


Figure 4.14. XPS spectra of 20 wt. % Pt/3 Nb-TNT in the different binding energy regions: (a) Pt 4f, (c) Ti 2p, (d) O 1s and (e) Nb 3d. The Pt 4f XPS spectra of 20 wt. % Pt/Vulcan XC72 (b) has been included for comparison.

the main Nb 3d_{5/2} peak is located at around 206.8 eV and can be attributed to Nb-O bonds in NbO₂ or Nb₂O₅ [209].

4.1.2.2 Electrochemical characterization

The electrochemical performance of the supported Pt catalysts were evaluated for the HER in acidic media by means of cyclic voltammetry (CV) and linear sweep

voltammetry (LSV). The catalytic properties have been compared to those of some commercially and home-made available Pt supported catalysts.

Cyclic voltammetry

Figs. 4.15-4.17 show cyclic voltammograms corresponding to Pt supported on TiO_2 and TNTs in deaerated $0.50 \text{ mol dm}^{-3} \text{ H}_2\text{SO}_4$ aqueous solution. The cyclic voltammograms corresponding to the Pt-black and Pt/Vulcan/XC72 are shown for comparison. Typical features for polycrystalline platinum can be seen [210]. Small modifications can be noticed in the samples containing TNT and Nb-doped TNT (respectively TNT-P and Nb-TNT-P) as well as in the case of the carbon supported material which indicate interaction between the catalyst and the support. However, it can be seen that the hydrogen adsorption/desorption peaks are well resolved. There is

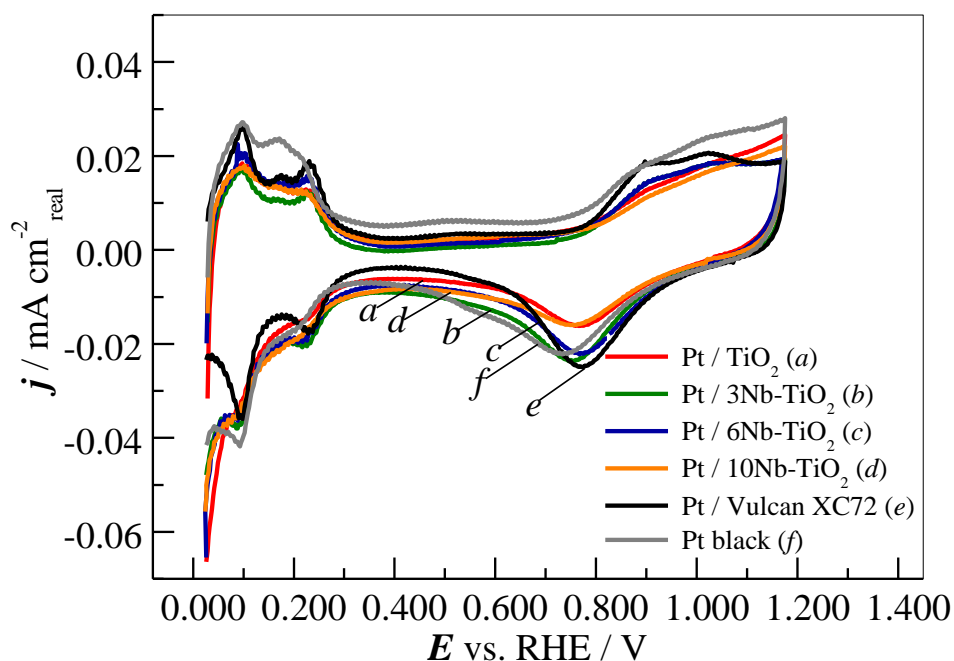


Figure 4.15. Cyclic voltammograms for (a) 20 wt. % Pt/ TiO_2 , (b) 20 wt. % Pt/3Nb- TiO_2 , (c) 20 wt. % Pt/6Nb- TiO_2 , (d) 20 wt. % Pt/10Nb- TiO_2 , (e) 20 wt. % Pt/Vulcan XC72 and (f) Pt black, recorded at 20 mV s^{-1} and $25.0 \text{ }^\circ\text{C}$ in deaerated $0.50 \text{ mol dm}^{-3} \text{ H}_2\text{SO}_4$ aqueous solution. *IR*-drop corrected.

also some contribution of the TiO₂ and TNTs supports, as suggested by the slight curvature in the double layer region, more evident for the latter, thus indicating a different interaction between Pt and the support.

Cyclic voltammograms were used for calculation of the ECSA of the different catalysts (Table 4.3). The Pt electrochemical surface area was calculated from the integrated charge of the hydrogen desorption peak. areas and it was obtained from the following equation:

$$\text{ECSA} = \frac{Q_{\text{H}}}{0.21 m_{\text{Pt}}} \quad (4.1)$$

where m_{Pt} is the platinum loading in the electrode, Q_{H} the charge for hydrogen desorption (mC cm⁻²) and 0.21 (mC cm⁻²) represent the charge required to oxidize a monolayer of H₂ on smooth Pt surface.

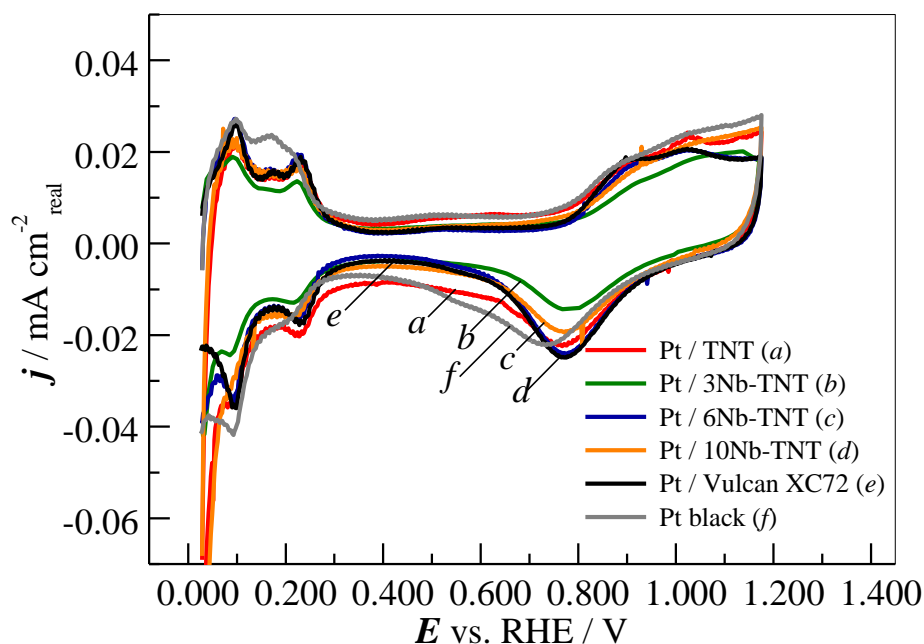


Figure 4.16 Cyclic voltammograms for (a) 20 wt.% Pt/TNT, (b) 20 wt.% Pt/3Nb-TNT, (c) 20 wt.% Pt/6Nb-TNT, (d) 20 wt.% Pt/10Nb-TNT, (e) 20 wt.% Pt/Vulcan XC72 and (f) Pt black recorded at 20 mVs⁻¹ and $T = 25.0$ °C in deaerated 0.50 mol dm⁻³ H₂SO₄ aqueous solution. IR-drop corrected.

Figs. 4.18-4.20 show the linear sweep voltammograms corresponding to the HER in deaerated $0.50 \text{ mol dm}^{-3} \text{ H}_2\text{SO}_4$ aqueous solution on the catalysts based on the TiO_2 , TNTs and TNTs-P supports, respectively. Note that in Figs 4.18-4.20A the current densities are given with respect to the geometric electrode area and in Fig. 4.18-4.20B currents are normalized to the ECSA. The scans were initiated at 0.200 V towards negative potentials. Around -0.060 V the effect of hydrogen bubbles evolved from the working electrode is evident on the shape of j - E curves shown in both figures. From the j - E curves depicted in Fig. 4.18A for Pt on (Nb)- TiO_2 catalysts, it is apparent that Pt/6Nb- TiO_2 exhibits the highest HER activity, because it shows lower potentials in the entire range of current densities. By contrast, from the j - E curves shown in Fig. 4.19A

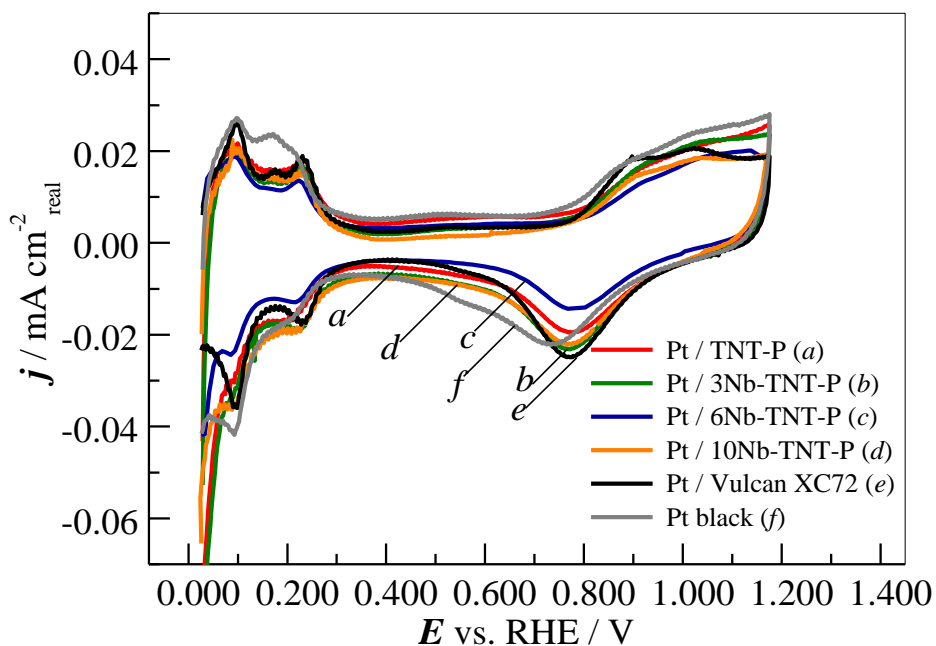


Figure 4.17 Cyclic voltammograms for (a) 20 wt.% Pt/TNT-P, (b) 20 wt.% Pt/3Nb-TNT-P, (c) 20 wt.% Pt/6Nb-TNT-P, (d) 20 wt.% Pt/10Nb-TNT-P, (e) 20 wt.% Pt/Vulcan XC72 and (f) Pt black, recorded at 20 mVs^{-1} and $T = 25.0$ in deaerated $0.50 \text{ mol dm}^{-3} \text{ H}_2\text{SO}_4$ aqueous solution. IR -drop corrected.

for Pt on (Nb)-TNTs, the highest activity towards HER corresponds to Pt/3Nb-TNT catalyst. Comparison of the curves in Fig. 4.20A shows that at lower current densities

Pt/6Nb-TNT-P exhibits best performance while at higher current densities Pt/10Nb-TNT-P is better. The lowest onset potential is given by Pt/6Nb-TNT-P. In all these figures, the curves obtained for the catalysts prepared using the titania supports are compared with those corresponding to Pt black and Pt/Vulcan XC72. It can be seen that on Fig. 4.19a the performance of Pt/3Nb-TNT is very close to that of the homemade prepared reference Pt/Vulcan XC72. Comparison of the catalytic activity when current is normalized to the real surface area of the catalyst shows that Pt/3Nb-TNT and Pt/6Nb-TNT-P are better than Pt/Vulcan XC72. From a quantitative point of view, it is more useful to provide some characteristic parameters used to evaluate the HER performance of the different catalysts, like the onset potential and the potential required to achieve a current density relevant for the electrolyser design [211-213].

In Table 4.4 it has been compared the onset potential and the potential required to achieve a $j = -0.010 \text{ A cm}^{-2}$ for the catalysts in Figs. 4.18-4.20. The values confirm that Pt/6Nb-TiO₂, Pt/3Nb-TNT and Pt/6Nb-TNT-P catalysts show the best performance towards HER. Additionally the performance of Pt/6Nb-TNT is very close to the performance of Pt/3Nb-TNT (table 4.4 and Fig. 4.19A). These two supports were characterized with the highest specific surface area and with highest conductivity (table 4.1) in comparison to the other (Nb)-TNTs. However the better performance of Pt/3Nb-TNT in comparison to Pt/6Nb-TNT, mainly in terms of the onset potential, can be attributed to the higher Pt content (table 4.3). The fact that both curves remain parallel in the entire range of potentials of the measurement is due to their similar textural properties and electrical conductivities. Similar is the situation of Pt/6Nb-TNT-P and Pt/10Nb-TNT-P. Despite the better textural characteristics and electrical conductivity of 10Nb-TNT-P (table 4.1) in comparison to the other (Nb)-TNT-P materials, Pt/6Nb-TNT-P shows better onset potential due to the higher Pt content (table 4.3). At higher

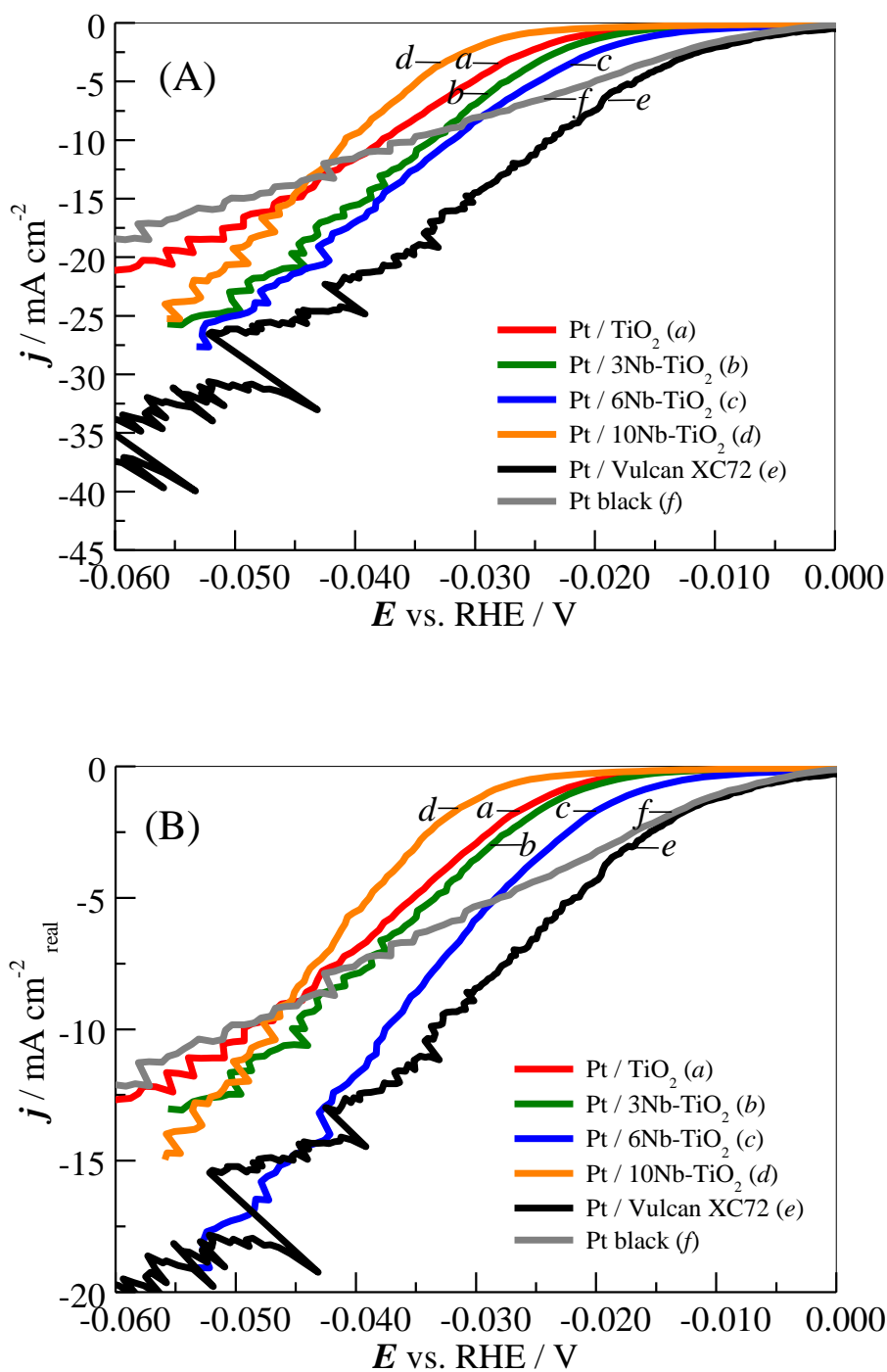


Figure 4.18 j - E curves corresponding to the HER on (a) 20 wt.% Pt/TiO₂, (b) 20 wt.% Pt/3Nb-TiO₂, (c) 20 wt.% Pt/6Nb-TiO₂, (d) 20 wt.% Pt/10Nb-TiO₂, (e) 20 wt.% Pt/Vulcan XC72 and (f) Pt black catalysts in 0.50 mol dm⁻³ H₂SO₄ aqueous solution. $T = 25.0$ °C. $s_r = 1$ mV s⁻¹. Current density referred to the electrode geometric area (A) and to the ECSA (B). IR -drop corrected.

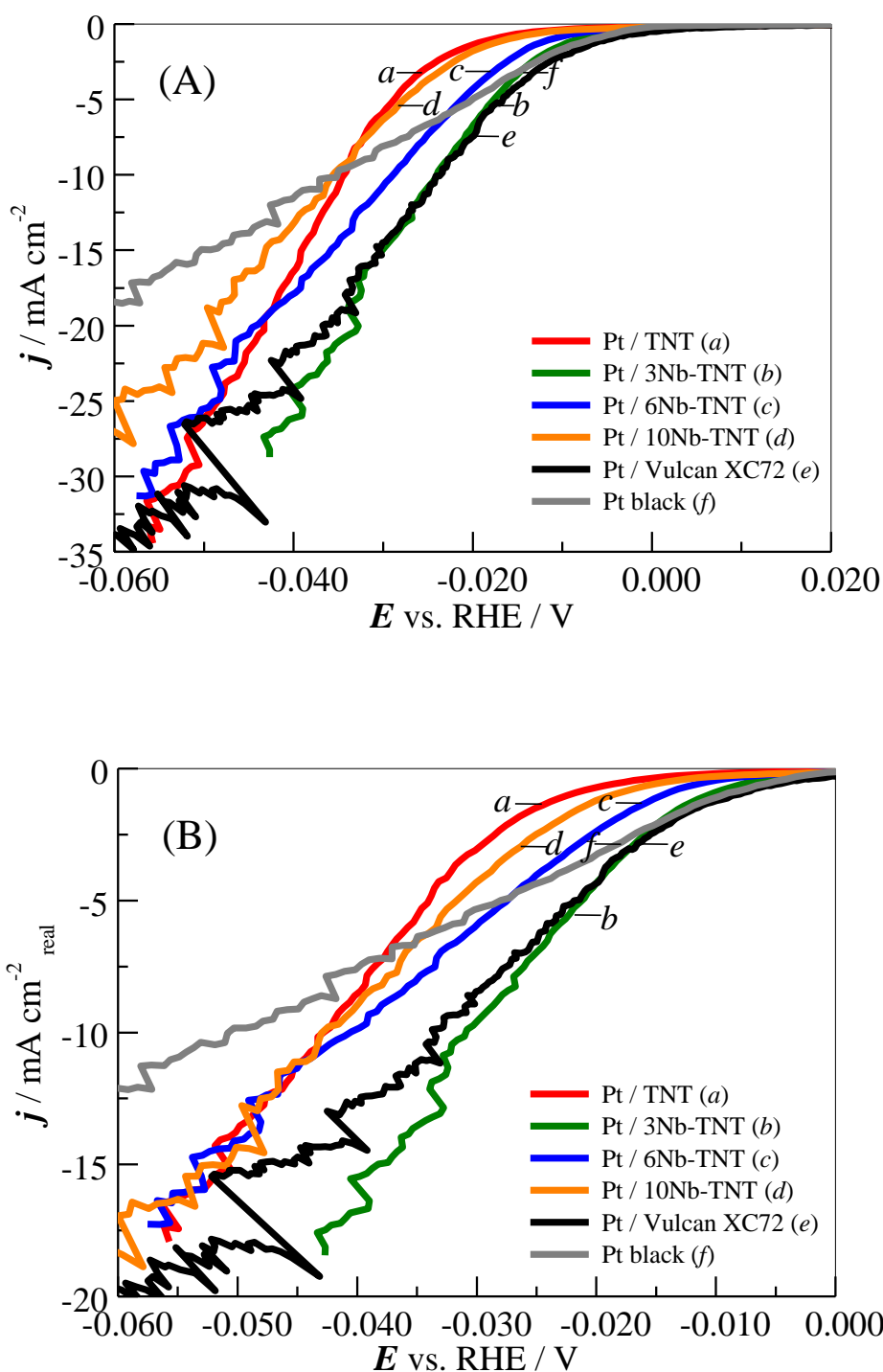


Figure 4.19 j - E curves corresponding to the HER on (a) 20 wt.% Pt/TNT, (b) 20 wt.% Pt/3Nb-TNT, (c) 20 wt.% Pt/6Nb-TNT, (d) 20 wt.% Pt/10Nb-TNT, (e) 20 wt.% Pt/Vulcan XC72 and (f) Pt black catalysts in 0.50 mol dm⁻³ H₂SO₄ aqueous solution. $T = 25.0$ °C. $s_r = 1$ mV s⁻¹. Current density referred to the electrode geometric area (A) and to the ECSA (B). IR -drop corrected.

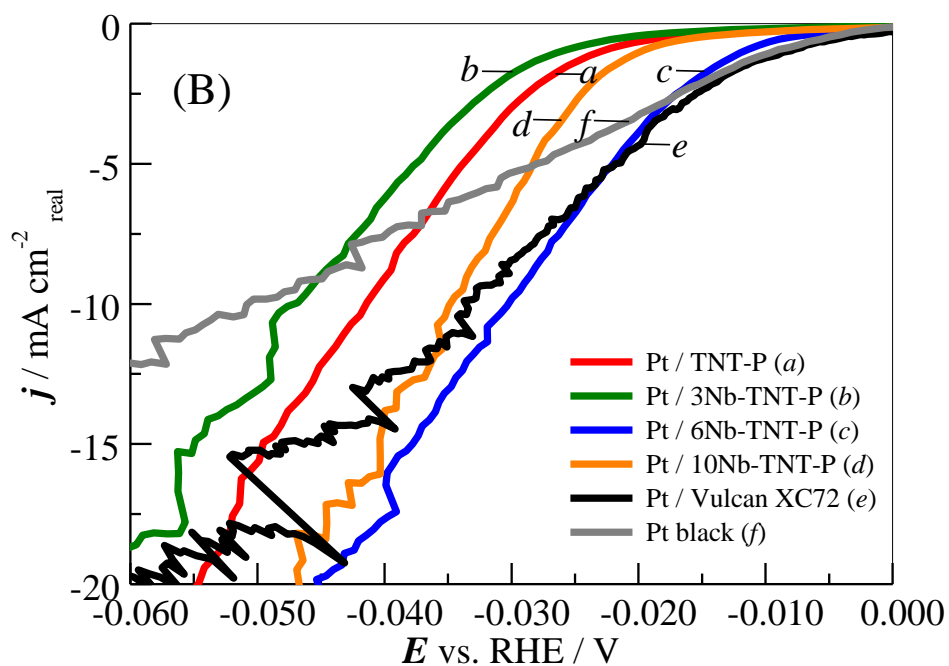
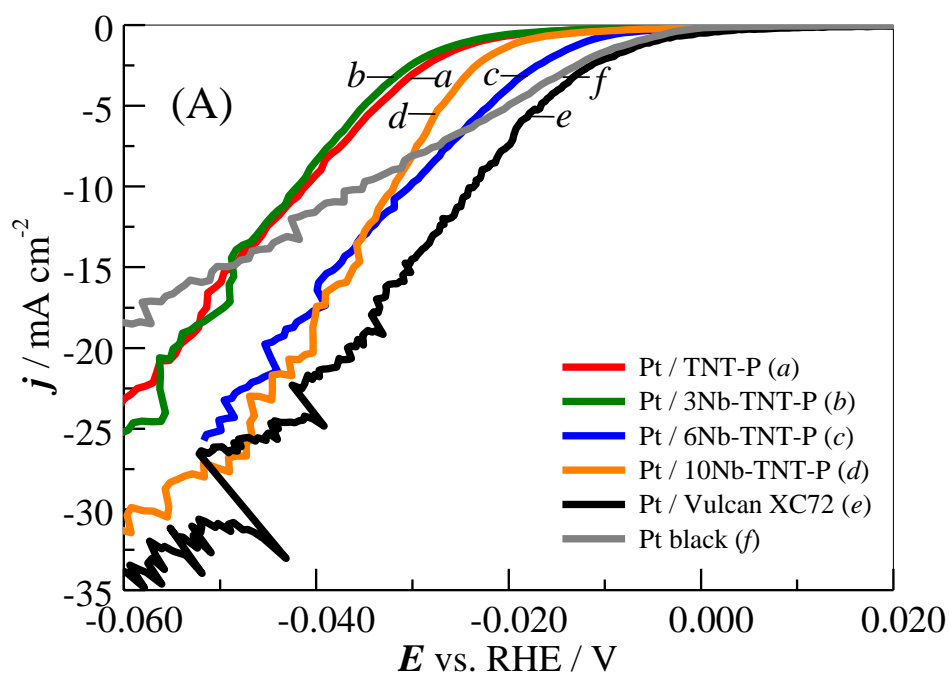


Figure 4.20 j - E curves corresponding to the HER on (a) 20 wt.% Pt/TNT-P, (b) 20 wt.% Pt/3Nb-TNT-P, (c) 20 wt.% Pt/6Nb-TNT-P, (d) 20 wt.% Pt/10Nb-TNT-P, (e) 20 wt.% Pt/Vulcan XC72 and (f) Pt black catalysts in $0.50 \text{ mol dm}^{-3} \text{ H}_2\text{SO}_4$ aqueous solution. $T = 25.0 \text{ }^\circ\text{C}$. $s_r = 1 \text{ mV s}^{-1}$. Current density referred to the electrode geometric area (A) and to the ECSA (B). IR -drop corrected.

current densities the performance of Pt/10Nb-TNT-P is better than that of Pt/6Nb-TNT-P which can be attributed to the better textural properties and electrical conductivity.

In any case, Nb doping of TiO₂, TNTs and TNTs-P generally leads to better electrocatalyst activity, as shown in Figs. 4.18-4.20 and Table 4.4. This can be explained by the local increase of the electron density on Pt due to the SMSI discussed above, favoured with the Nb doping, in particular for the TNTs.

Table 4.4 HER parameters of Pt on different titania based supports in 0.50 mol dm⁻³ H₂SO₄

Electrocatalyst	Onset potential^a / V	<i>E</i>₁₀ (<i>E</i> at -10 mA cm⁻²) / V
20 wt. % Pt/TiO ₂	-0.0169	-0.0378
20 wt. % Pt/3Nb-TiO ₂	-0.0149	-0.0336
20 wt. % Pt/6Nb-TiO ₂	-0.0098	-0.0318
20 wt. % Pt/10Nb-TiO ₂	-0.0212	-0.0408
20 wt. % Pt/TNT	-0.0127	-0.0342
20 wt. % Pt/3Nb-TNT	-0.0049	-0.0241
20 wt. % Pt/6Nb-TNT	-0.0069	-0.0289
20 wt. % Pt/10Nb-TNT	-0.0114	-0.0355
20 wt. % Pt/TNT-P	-0.0177	-0.0417
20 wt. % Pt/3Nb-TNT-P	-0.0186	-0.0420
20 wt. % Pt/6Nb-TNT-P	-0.0083	-0.0305
20 wt. % Pt/10Nb-TNT-P	-0.0133	-0.0319
20 wt. % Pt/Vulcan XC72	-0.0002	-0.0237
Pt black	-0.0034	-0.0351

^aDefined as the potential at $j = -0.5 \text{ mA cm}^{-2}$

On the other hand, it is interesting to compare the performance of the catalysts developed through this work with published data related to home-made and commercial Pt supported catalysts, but it is not easy due to the variety of Pt loadings and

experimental conditions used to assess the HER catalyst activity. However, some comparisons can be established in terms of the potential at which $j = -0.010 \text{ A cm}^{-2}$ (E_{10}). Thus, Zhang and col. [214] developed a Pt/WS₂ catalyst for enhanced hydrogen evolution reaction. In N₂-saturated 0.50 mol dm⁻³ H₂SO₄, the E_{10} was about -0.080 V vs. RHE, according the experimental data. Wang and col. [215] reported monodisperse 20 wt. % Pt on N-doped black TiO₂ as high performance bifunctional catalyst. The E_{10} for the HER was about -0.047 V vs. RHE in 0.10 mol dm⁻³ H₂SO₄. Yang and col. [216] developed PtCo alloy nanoparticles encapsulated in carbon nanofibers for electrochemical hydrogen generation. From the reported j - E curves for HER in 0.50 mol dm⁻³ H₂SO₄, PtCo/CNFs (with Pt content 5 wt. %) shows an E_{10} about -0.068 V vs. RHE. In the same work it was reported that commercial 20 wt. % Pt/C (Johnson-Matthey) showed an E_{10} about -0.056 V vs. RHE. Bhowmik and col. [211] reported the HER on Pd-CN_x and commercial 10 wt. % Pt/C in 0.50 mol dm⁻³ H₂SO₄. The E_{10} of the latter was about -0.068 V vs. RHE. These data confirm the good activity towards HER of Pt deposited on the TiO₂ and TNTs supports developed in this work.

4.1.2.3 PtPd deposited on Nb-doped TNT

Within this section the reduction of Pt loading by replacing it partially with Pd is discussed. As Pd precursor was used PdCl₂ dissolved in 1 mol dm⁻³ HCl. The procedure is the same as reported in section 3.1.3. The corresponding results are compared with those obtained using 20 wt.% Pt/3Nb-TNT, which has been considered as the best catalyst within the previous section.

The diffractograms corresponding to PtPd₂ supported on 3Nb-TNTs is shown in Fig. 4.21. Typical characteristic peaks of the face-centered cubic (*fcc*) lattice structure of platinum are observed. Since Pd has the same crystal structure, it can be expected

that they can form alloys. This can be indicated by a contraction in the crystal lattice which is confirmed by the decrease in the crystal lattice parameters reported in Table 4.5 and by a shift toward higher angles of the corresponding peaks. Peaks of PtPd₂/3Nb-TNT are sharper and narrower, which justify the bigger crystallite size reported in Table 4.5.

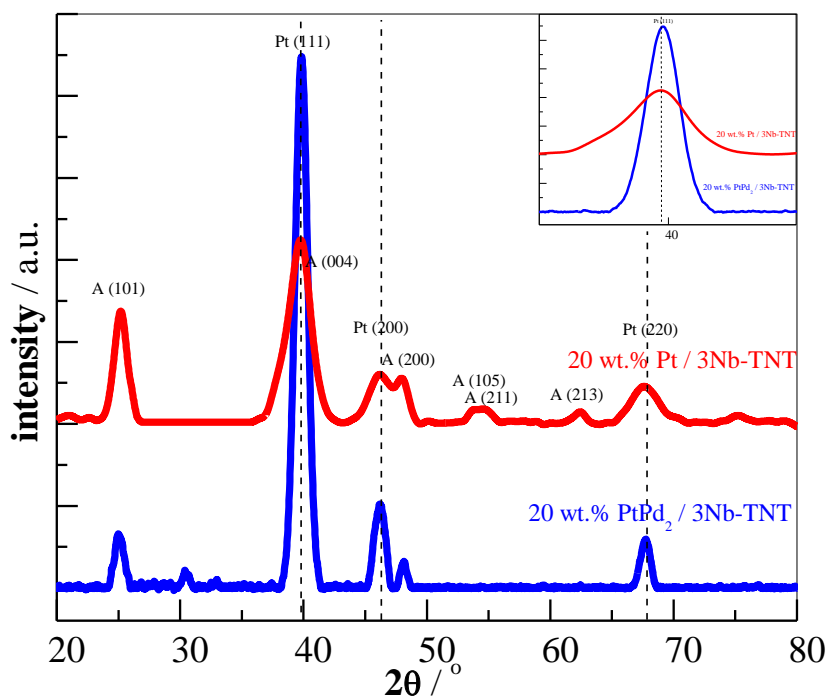


Figure 4.21 X-ray diffraction patterns of Pt and PtPd₂ deposited onto 3Nb-TNT (in parenthesis, planes corresponding to characteristic diffraction signals of anatase, A, and *fcc* Pt).

Table 4.5. Selected structural and electrochemical characteristics of Pt and PtPd₂ on 3Nb-TNT.

Composition	Crystallite size / nm	Lattice parameter / Å	ECSA (CV) / m ² g ⁻¹
20 wt.%Pt/3NbTNT	3.93	3.92	11.13
20 wt.%PtPd ₂ /3Nb-TNT	6.98	3.91	6.74

The cyclic voltammograms of PtPd₂/3Nb-TNT and Pt/3Nb-TNT are shown in Fig. 4.22. It can be seen small shift toward lower potentials of the reduction peak of chemisorbed oxygen in the CV results of PtPd₂/3Nb-TNT in comparison to Pt/3Nb-TNT [8]. The ECSA of PtPd₂/3Nb-TNT was estimated from the net charge for hydrogen adsorption in cyclic voltammograms as described above in section 4.1.2.2. Results were compared and with ECSA estimated from the charge of the reduction peak of chemisorbed oxygen taken into account that the specific amount of electricity corresponding to the full coverage of the Pd surface by one monolayer of oxygen is 0.42 mC cm⁻² [8].

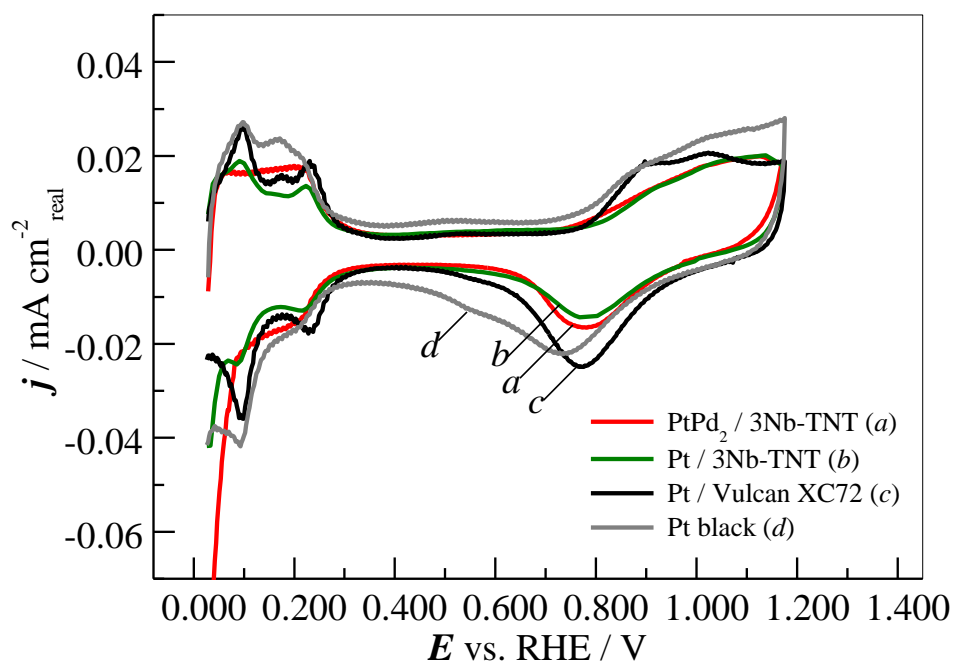


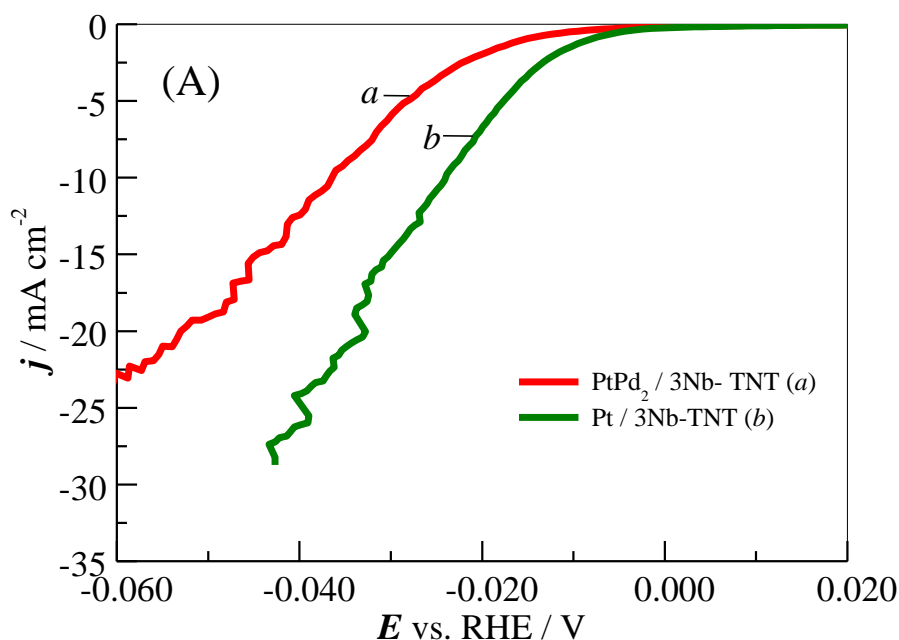
Figure 4.22 Cyclic voltammograms of (a) 20 wt.% PtPd₂/3Nb-TNT and (b) 20 wt.% Pt/3Nb-TNT, (c) 20 wt.% Pt/VulcanXC72 and (d) Pt black, recorded at 20 mVs⁻¹ and $T = 25.0$ °C in deaerated 0.50 mol dm⁻³ H₂SO₄ aqueous solution. *IR*-drop corrected.

The polarization curves of Pt/3Nb-TNT and PtPd₂/3Nb-TNT are plotted in Fig. 4.23. As expected, the performance of the PtPd₂/3Nb-TNT is lower in comparison to Pt/3Nb-TNT due to the lower activity of Pd and the lower ECSA of PtPd₂/3Nb-TNT.

Table 4.6 HER parameters of Pt on different titania based supports in 0.50 mol dm⁻³ H₂SO₄

Electrocatalyst	Onset potential ^a / V	<i>E</i> ₁₀ (<i>E</i> at -10 mA cm ⁻²) / V
20 wt. % Pt/3Nb-TNT	-0.0049	-0.0241
20 wt. % PtPd ₂ /3Nb-TNT	-0.0962	-0.0364

As it can be seen in Table 4.6 that the main difference between PtPd₂/3Nb-TNT and Pt/3Nb-TNT is in the onset potential values. Comparing the potential at $j = -0.010$ A cm⁻² (*E*₁₀) of PtPd₂/3Nb-TNT with other reported in the previous section [211, 214-216] confirm its good catalytic activity toward HER.



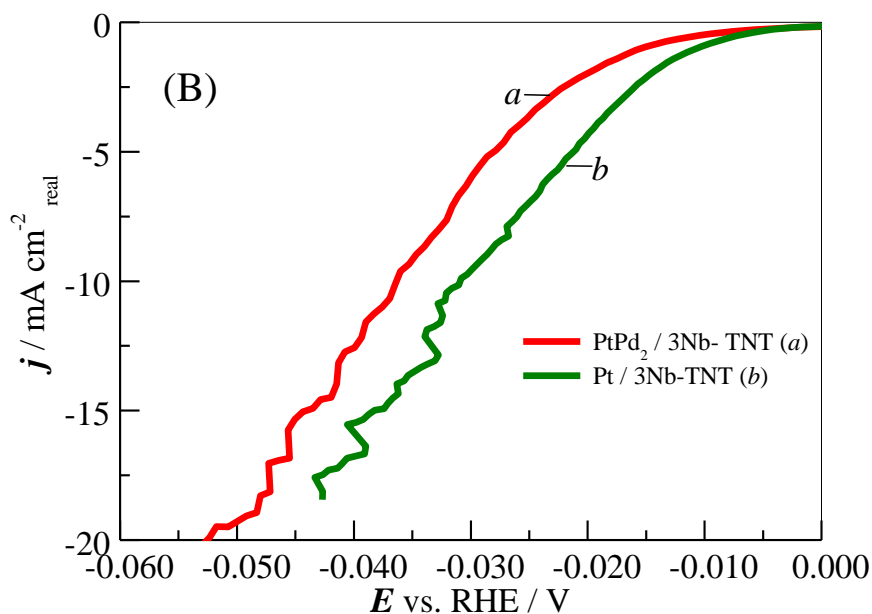


Figure 4.23 j - E curves corresponding to the HER on (a) 20 wt. % PtPd₂/3Nb-TNT, (b) 20 wt. % Pt/3Nb-TNT, (c) 20 wt.% Pt/Vulcan XC72 and (d) Pt black catalysts in 0.50 mol dm⁻³ H₂SO₄ aqueous solution. $T = 25.0$ °C. $s_r = 1$ mV s⁻¹. Current density referred to the electrode geometric area (A) and to the ECSA (B). IR -drop corrected.

4.1.3 Oxygen evolution

For the oxygen evolution reaction (OER) typically the electrocatalysts are unsupported due to the high potentials applied to the anode and the impossibility of the application of conventional carbon supports, which become easily oxidized under these conditions. The main target of this work is supporting OER electrocatalysts on TiO₂ nanotubes for PEM water electrolysis in order to achieve better durability and performance. For this purpose IrO₂ and IrRuO_x were synthesized and deposited onto TNTs and Nb-doped TNTs (3 at.% Nb) and electrochemically tested as catalysts toward oxygen evolution in 0.50 mol dm⁻³ H₂SO₄.

4.1.3.1 Physico-chemical characterization

The mass ratio of the catalyst to the support and the atomic ratio between Ir and Ru in the electrocatalysts was analyzed by EDX. The Ir:Ru atomic ratio was kept close to 60:40 and the results of the corresponding analyses are given in Table 4.7.

Table 4.7 Ir:Ru atomic ratio measured by EDX

Composition	Ir / at. %	Ru / at. %
IrRuO _x	58.74	41.26
IrRuO _x /TNT	57.82	42.18
IrRuO _x /Nb-TNT	56.62	43.38

TEM images of 50 wt.% IrO₂/Nb-TNT are shown in Fig. 4.24, taken in different parts of the sample, where the dispersion of the catalyst (Fig. 4.24a and b) and the presence of TNTs (Fig. 4.24b and c) are shown.

X-ray diffraction

Tetragonal space group (136) of rutile type crystal lattice of IrO₂ and IrRuO_x are identified in the X-ray diffraction patterns (Fig. 4.25). Peaks located at 10.5, 18, 29 and 32° correspond to the reflections (200), (400), (600) and (001) of monoclinic titanates H₂Ti₃O₇ (the original phase of the support before IrO₂ and IrRuO_x deposition and calcination) [112]. The characteristic peaks at around $2\theta = 10^\circ$ indicates the presence of a layered titanate. Detailed analysis of the X-ray diffraction patterns of titanates was done in section 4.1.1.

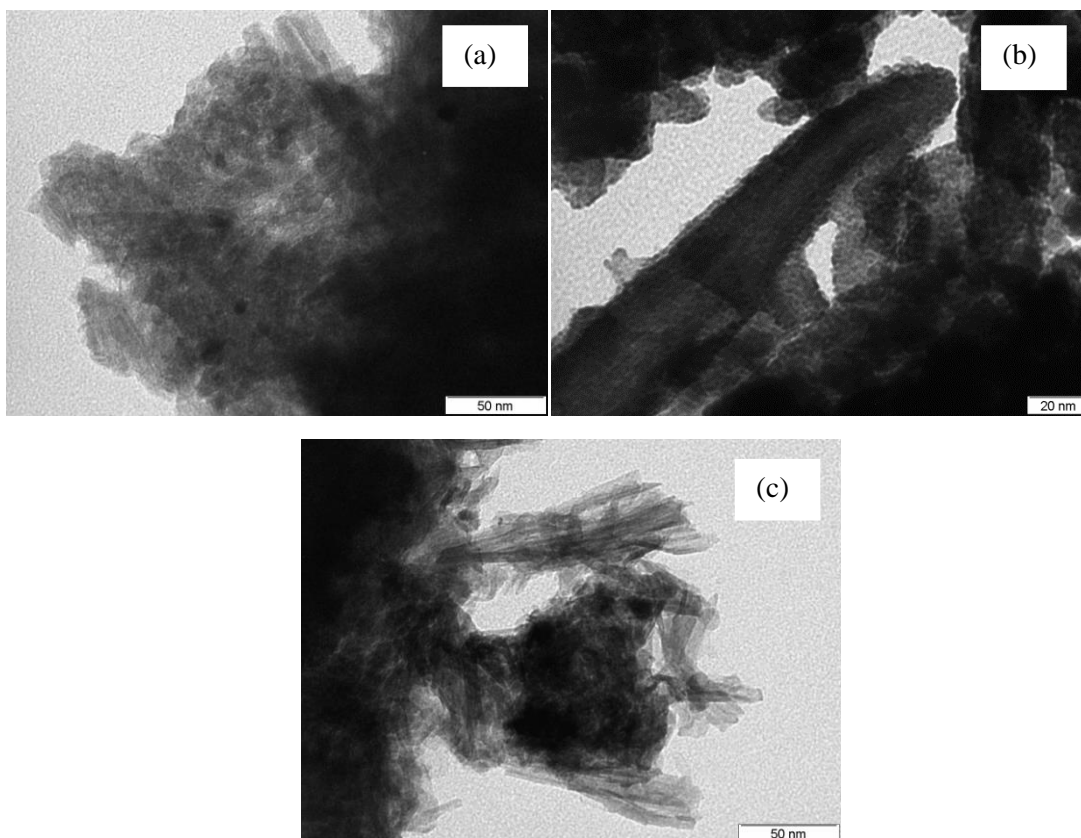


Figure 4.24 TEM micrographs of IrO₂/Nb-TNT at different sample regions: (a) focused on catalyst dispersion, (b) catalyst coverage onto Nb-TNT and (c) on the presence of Nb-TNT.

IrO₂ and RuO₂ have similar structure and lattice parameters since the ionic radii of Ir⁴⁺ and Ru⁴⁺ are 0.0625 and 0.0620 nm, respectively, and therefore, it is expected that they can coexist in the same solid solution. Peaks of IrO₂ are shifted toward higher angles after introducing Ru, which indicates lattice contraction and formation of solid solution [38,217]. The corresponding lattice parameters calculated from the main peaks (110) and (101) by Bragg's law (Eq. 3.1, section 3.2) are given in Table 4.8, where the decrease in the lattice parameters of IrRuOx in comparison to IrO₂ is observed.

Average crystallite sizes given in Table 4.8 were calculated from Scherrer equation (Eq. 3.4, section 3.2) [95] applied also to the main peaks (110) and (101). Increased crystallite size of IrRuOx in comparison to IrO₂ can be attributed to the lower crystallization temperature of RuO₂ than that of IrO₂ [38,217]. Catalyst deposition onto

supports leads to an increase in the crystallite size of the catalysts when compared to the unsupported samples. In addition, an increase in the crystallite size of the catalysts after Nb-doping of the TNTs is observed. This effect can be attributed to the formation of smaller number of larger crystals on the support surface in contrast to the bigger number of smaller crystals of the unsupported catalyst [95]. Similar effect has been reported before in the literature [96]. The main reason is related to the nucleation sites available for crystal formation at one and the same concentration of the precursors. The crystallites of pure IrO₂ and IrRuO_x are formed from the homogenous phase, which need to overcome a significant energy barrier in comparison to the supported catalyst, in which as heterogeneous system, the energy barrier is lower and crystal formation is easier [95,96].

Table 4.8 Average crystallite size and lattice parameters of IrO₂, IrRuO_x and supported IrO₂ and IrRuO_x.

catalyst	(110) peak / degree	(101) peak / degree	crystallite size	lattice parameter a=b	lattice parameter c
IrO ₂ black	27.91	34.79	7.38	4.517	3.152
IrO ₂ /TNT	28.03	34.87	9.78	4.496	3.131
IrO ₂ /Nb-TNT	28.03	34.94	10.67	4.493	3.118
IrRuO _x black	28.01	35.00	8.96	4.501	3.119
IrRuO _x /TNT	28.09	35.06	14.00	4.489	3.115
IrRuO _x /Nb-TNT	28.05	35.07	14.37	4.492	3.105

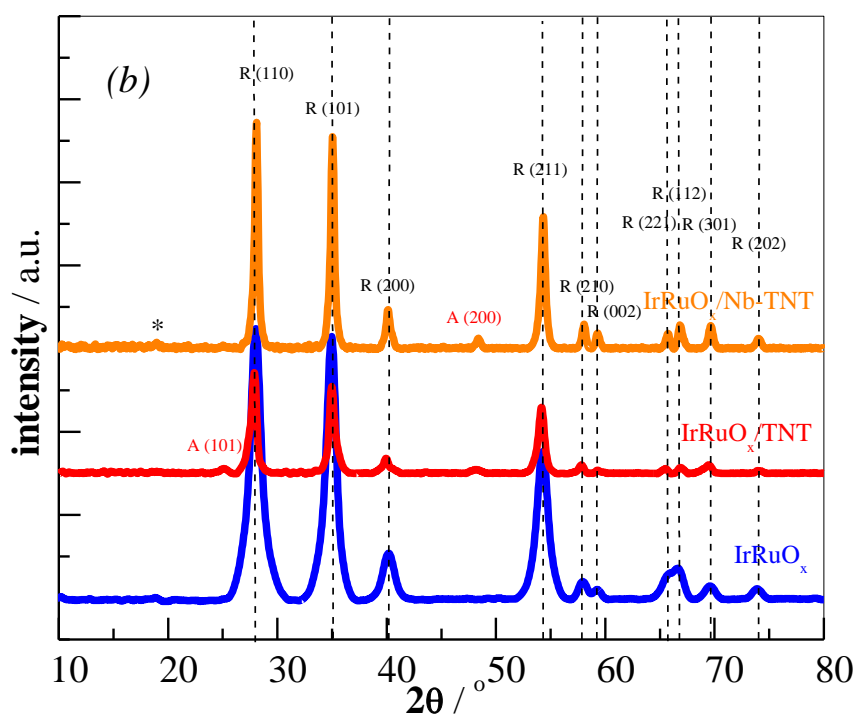
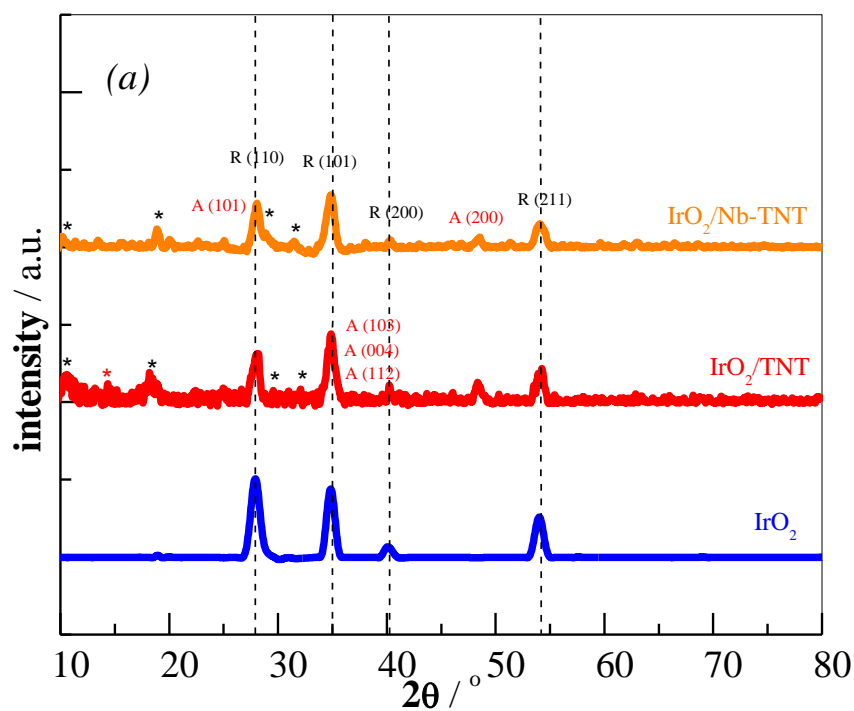


Figure 4.25 X-ray diffractogram of IrO₂ (a) and IrRuO_x (b) unsupported and supported onto TNT and Nb-TNT. Rutile phase of IrO₂ is denoted with R and anatase phase of TNT with A (*Titanate peaks of the support).

4.1.3.2 Electrochemical characterization

Cyclic voltammetry of noble metal oxide electrodes is a common method of evaluation their electrochemical surface properties. The peaks found in the voltammograms of iridium oxide in H_2SO_4 0.50 mol dm^{-3} are located around 0.800-0.900 and 1.300-1.400 V both in positive and negative going direction and correspond to the redox transitions of $\text{Ir}^{3+}/\text{Ir}^{4+}$ and $\text{Ir}^{4+}/\text{Ir}^{6+}$ respectively (Fig. 4.26). The peaks found in the voltammograms of IrRuO_x in H_2SO_4 0.50 mol dm^{-3} are located in the same region and also correspond to the redox transitions of $\text{Ir}^{3+}/\text{Ir}^{4+}$ and $\text{Ir}^{4+}/\text{Ir}^{6+}$ (Fig. 4.27), whereas redox transitions $\text{Ru}^{3+}/\text{Ru}^{4+}$ and $\text{Ru}^{4+} / \text{Ru}^{6+}$ peaks can be observed near 0.580 and 0.720 V vs. RHE, respectively, and overlap with Ir-peaks [37,85,97,219]. Hydrogen region, where underpotential deposition (UPD) and desorption of H takes place, is located at potentials below 0.400 V vs. RHE.

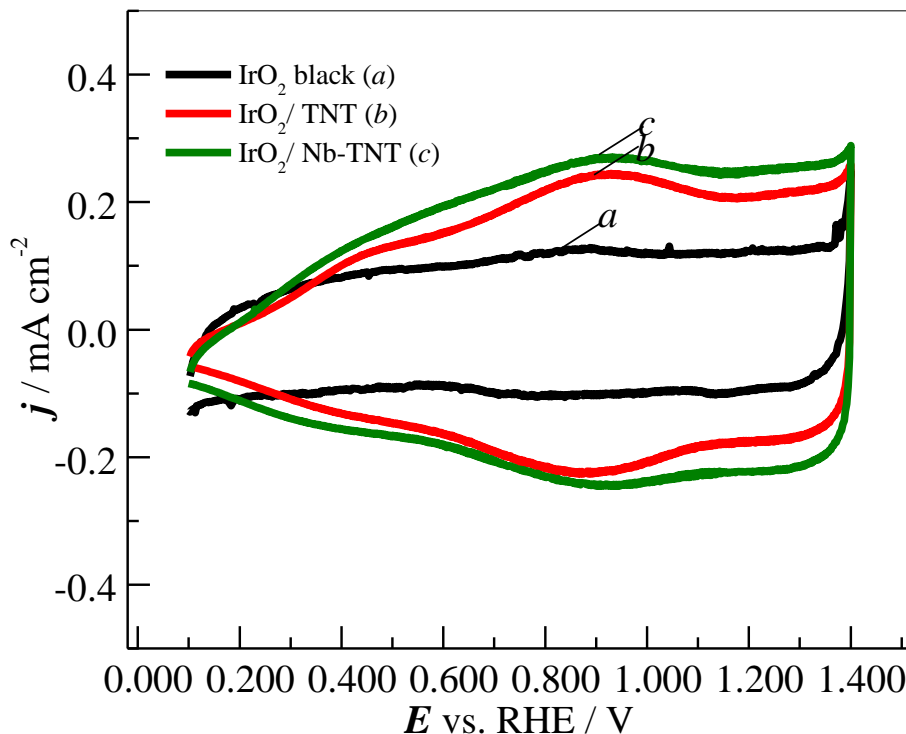


Figure 4.26 Cyclic voltammograms of the different IrO_2 catalysts, registered in $0.5 \text{ mol dm}^{-3} \text{ H}_2\text{SO}_4$ at $T = 25.0 \text{ }^\circ\text{C}$. $s_r = 20 \text{ mV s}^{-1}$.

Series of cyclic voltammograms at different scan rates were recorded and typical pseudocapacitive behaviour of IrO₂ and RuO₂ electrocatalysts was observed (Figs. 4.26 and 4.27). The areas under the anodic and over the cathodic current peaks of these voltammograms were determined to correlate the respective anodic and cathodic charges to the quantity of active sites or specific surface area of the different catalysts. The overall voltammetric charge (q_{total}) can be divided into a fast charge (q_{outer}), due to the charging of the outer surface area of the electrode, which shows more accessible active sites on the catalyst surface at higher scan rates, and a slow charge (q_{inner}), representing the total active sites which are placed in less accessible surface regions at lower scan rates. In this way it is possible to find the so-called redox, double-layer and total charge of the electrode. At high scan rates, the double-layer (outer) charging (q_{dl} , q_{outer}) dominates while at low scan rates redox region (inner) is also accessible. The proton exchange between surface oxide-OH groups and the acid electrolyte is considered to be rapid at “easily accessible” regions, whereas this exchange has some diffusion limitations within the inner regions. Quantitative calculations of q_{total} , q_{inner} and q_{outer} were done by the procedure described in section 3.3.3 and the corresponding results are reported in Table 4.9. Since the calculated total charges of the supported materials are significantly higher in comparison to the unsupported catalyst and at the same time their crystallites are larger (which indicated lower electrochemical surface area) in comparison to the unsupported black materials, it can be concluded that the bigger crystallites of the supported catalysts are better dispersed and easier to access on the support surface in comparison to the smaller size of the agglomerated unsupported materials.

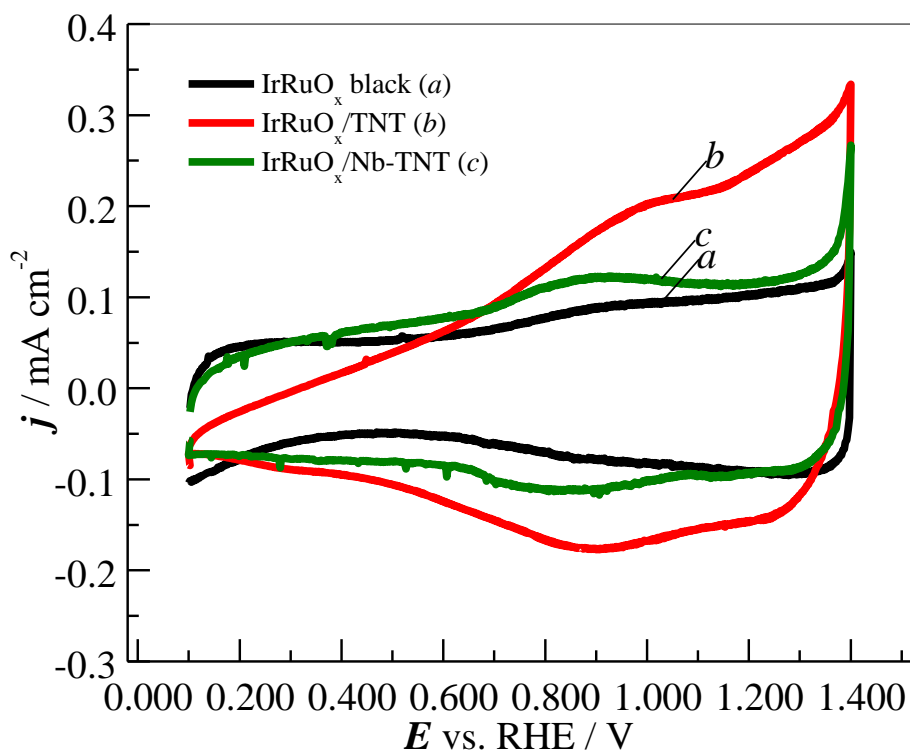


Figure 4.27 Cyclic voltammograms of the different IrRuO_x catalysts, registered in 0.5 mol dm⁻³ H₂SO₄ at $T = 25.0$ °C. $s_r = 20$ mV s⁻¹.

Table 4.9 Calculated from cyclic voltammogram inner, outer and total charges of IrO₂ and IrRuO_x catalysts before recording polarization curves.

Catalyst	outer charge (q^*_{outer}) / mC	inner charge (q^*_{inner}) / mC	anodic total charge (q^*_A) / mC	cathodic total charge (q^*_C) / mC	q^*_A / q^*_C	accessibility $q^*_{\text{outer}}/q^*_{\text{total}}$
IrO ₂	272	265	538	503	1.07	0.50
IrO ₂ /TNT	543	239	781	794	0.98	0.69
IrO ₂ /Nb-TNT	602	360	961	962	1.00	0.63
IrRuO _x	270	88.3	358	347	1.03	0.75

IrRuO _x /TNT	149	713	862	847	1.02	0.17
IrRuO _x / Nb-TNT	279	176	455	442	1.03	0.61

The reversibility of the redox transitions of Ir³⁺/Ir⁴⁺ and Ir⁴⁺/Ir⁶⁺ and Ru³⁺/Ru⁴⁺ and Ru⁴⁺ / Ru⁶⁺ can be understood from the respective voltammograms by the symmetry of the anodic and cathodic peaks. For reversible surface process (fast process), the obtained cyclic voltammogram shows horizontal symmetry. On the contrary, for an irreversible surface process (slow process), the obtained voltammograms are asymmetric.

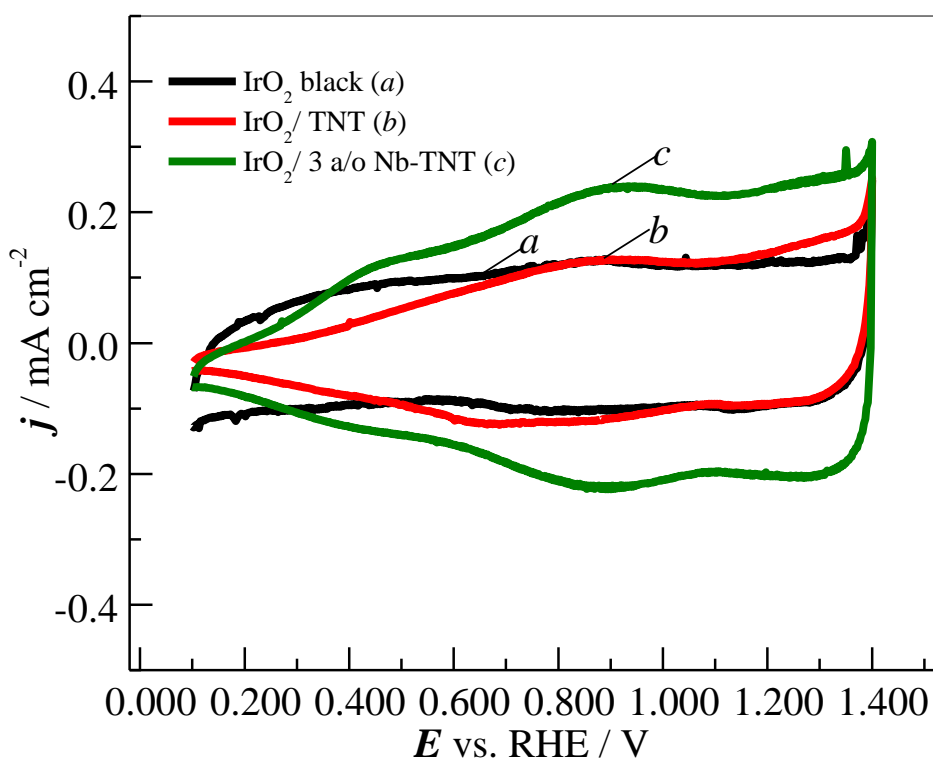


Figure 4.28 Cyclic voltammograms after recording polarization curves of different IrO₂ catalysts, registered in 0.5 mol dm⁻³ H₂SO₄ at $T = 25.0$ °C. $s_r = 20$ mV s⁻¹.

Utilization of the cyclic voltammetry results to identify the quality of the electrocatalyst surface, in terms of its similarity to the bulk IrO₂ properties, is based on an evaluation of the ratio of anodic-to-cathodic charge passed during the cyclic voltammogram (q^*_A/q^*_C). If the ratio is close to the unity, the system behaves reversibly as bulk IrO₂ [96,218]. The results obtained for IrO₂ and IrRuOx unsupported and supported on TNT and Nb-TNT are also summarized in Table 4.9. The q^*_A/q^*_C ratio attained a value of almost 1 for all samples. The values remain independent of the support. These results indicate that all samples exhibit almost ideal behaviour and the solid state surface redox transition is reversible for all catalysts. The fact that the ratio between the anodic and cathodic charges is close to unity for all scan rates (see Table 4.9), indicates that the large cathodic current is completely regained over the whole anodic range during the anodic sweep [37,96,97,217-220].

The values of q^*_{out}/q^*_{tot} , which is a measurement of the catalyst accessibility, are also listed in Table 4.9. When IrO₂ is supported on TNT and Nb-TNT, the ratio q^*_{outer}/q^*_{total} is slightly increased, thus indicating an increase in the amount of easier access active sites due to a better distribution onto the support surface. When IrRuOx is deposited onto the Nb-TNT support, there is a decrease in the accessibility, but still keeping relatively high values of about 60 %. On the contrary, IrRuOx deposited onto TNT shows a very low accessibility of 17%, which could be associated to a thicker catalyst layer, resulting in a bigger part of the catalyst active sites accessible only at lower scan rates. This is confirmed by the form of the cyclic voltammograms of

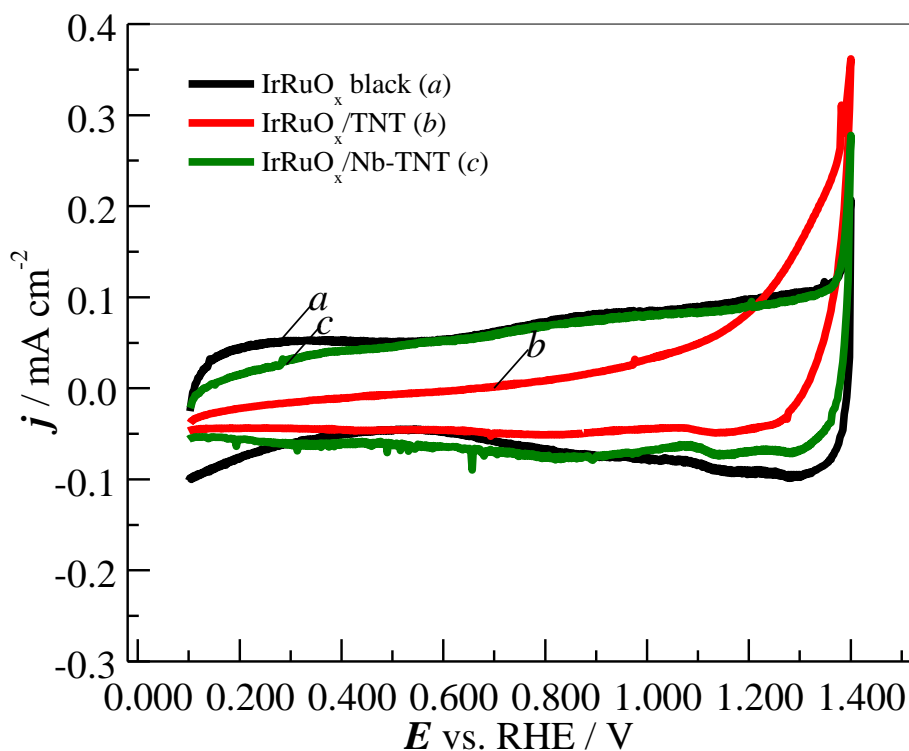


Figure 4.29 Cyclic voltammograms after recording polarization curves of different IrRuO_x catalysts, registered in 0.5 mol dm⁻³ H₂SO₄ at $T = 25.0$ °C. $s_r = 20$ mV s⁻¹.

IrRuO_x/TNT, which is relatively different in comparison to the voltammograms of the other catalysts. The form of the cyclic voltammograms of IrO₂ and IrO₂ supported onto TNT and Nb-TNT and IrRuO_x and IrRuO_x supported onto Nb-TNT are nearly symmetric with approximately equal reduction and oxidation peak heights, characteristic of thin layers.

The cyclic voltammograms of the catalysts after recording several polarization curves in order to determine possible changes in the catalysts during the OER are shown in Figs 4.28 and 4.29. The corresponding charges are collected in Table 4.10 and the ratio between the charges before and after oxygen evolution are shown in Table 4.11. As it can be seen in Table 4.11, the ratio of q^*_{inner} before and after polarization curves for some catalysts shows an increase in the inner active surface and a decrease in the

outer active surface, which means that part of the outer (more accessible) surface is transformed into a less accessible inner surface. When IrO₂ is supported onto TNTs, its total surface area is increased in comparison to unsupported IrO₂. However this support has not a stabilizing effect and the total surface active area has decreased by 66 %. Comparing the total charges of IrRuO_x catalysts before and after oxygen evolution shows that similar destabilization can be seen when IrRuO_x is deposited onto the TNTs. The effect is even stronger since only 30 % of the total charge remains. When IrRuO_x is deposited onto Nb-TNT, the destabilization is lower and 62 % of the total catalyst active sites were still active after recording oxygen evolution polarization curves. Except for the catalysts deposited onto the TNTs, the change in the outer surface charge is not more than 16 %.

Table 4.10 Inner, outer and total charges of IrO₂ and IrRuO_x catalysts after recording the polarization curves.

Catalyst	outer charge (q^{*}_{outer}) / mC	inner charge (q^{*}_{inner}) / mC	anodic total charge (q^{*}_A) / mC	cathodic total charge (q^{*}_C) / mC	q^{*}_A / q^{*}_C	accessibility, $q^{*}_{outer} / q^{*}_{total}$
IrO ₂	229	220	448	455	0.98	0.51
IrO ₂ /TNT	195	323	518	543	0.95	0.38
IrO ₂ /Nb-TNT	538	295	833	826	1.01	0.65
IrRuO _x	252	92.5	345	346	1.00	0.73
IrRuO _x /TNT	61.7	201	262	455	0.57	0.24
IrRuO _x / Nb-TNT	243	40.7	284	355	0.80	0.86

The recorded polarization curves of IrO₂ and IrRuO_x catalysts are shown in Figs 4.30 - 4.31. The Tafel slope data were subject to IR-drop correction. The Tafel plots corresponding to the oxygen evolution reaction are shown in the insets of the figures. Two Tafel slopes have been identified for the oxygen evolution process and the corresponding kinetic parameters are given in Table 4.12. At low current densities (below 1.0 mA cm⁻²) the Tafel slopes for the IrO₂ samples are in the range from 0.049 to 0.054 V dec⁻¹ whereas for the IrRuO_x samples, in the range from 0.050 to 0.065 V dec⁻¹. At high current densities (over 10 mA cm⁻²), the Tafel slopes for the IrO₂ samples range from 0.108 to 0.144 V dec⁻¹, whereas for the IrRuO_x samples, from 0.122 to 0.150 V dec⁻¹. These values are similar to those already reported in the literature of 0.060 and 0.120 V dec⁻¹ in the low and high overpotential current densities range, respectively [83,85,92]. Four possibilities were presented to explain the change in the anodic Tafel slope: 1) two different reaction pathways; 2) change in the electrode substrate; 3) change in the rate-controlling step; and 4) influence of potential controlled conditions.

Table 4.11 Inner, outer and total charges ratios before and after recording the polarization curves for the IrO₂ and IrRuO_x catalysts.

Catalyst	$q^{*}_{\text{outer after}}/q^{*}_{\text{outer before}}$	$q^{*}_{\text{inner after}}/q^{*}_{\text{inner before}}$	$q^{*}_{\text{A total after}}/q^{*}_{\text{A total before}}$
IrO ₂	0.84	0.83	0.83
IrO ₂ /TNT	0.36	1.35	0.66
IrO ₂ /Nb-TNT	0.89	0.82	0.87
IrRuO _x	0.93	1.05	0.96
IrRuO _x /TNT	0.41	0.28	0.30
IrRuO _x / Nb-TNT	0.87	0.23	0.63

The details of the mechanism of oxygen evolution on the oxide catalyst surface in acidic media were discussed in section 1.3.5, Table 1.6 and Eqs. (1.23)-(1.28). According to our results R2 (OH dissociation in S-OH) is identified as the *rds* at low current densities, whereas R1 is identified to be the *rds* at high current densities (see Table 1.6).

The Tafel slope for unsupported IrO₂ is slightly higher, but only of a few mV dec⁻¹ (see Table 4.12) than that for supported IrO₂, but it is not very different from 40 and 120 mV dec⁻¹ and therefore, R2 appears to be the *rds*. The crystallite sizes of unsupported and supported IrO₂ are not very different (Table 4.8), but the much higher surface area of the supported catalysts (Table 4.9) suggests a bigger amount of active sites for OH adsorption, with the corresponding higher density of surface S-OH groups. For unsupported IrO₂, the smaller crystallites are expected to provide more active sites in comparison to the supported samples. However, the supported samples have a better dispersion, thus providing advantage toward bigger number of active sites for S-OH formation on the surface.

Two slope regions of IrRuOx catalysts can be attributed to the corresponding changes in the reaction mechanisms. Replacing partially Ir with Ru in the unsupported samples leads to reducing the Tafel slope as expected and reported previously in [38]. When titania nanotubes were added as support, Tafel slopes did not change significantly and instead, they even slightly increased. The addition of Nb as a dopant to the support results in a reduction of the catalytic activity of IrRuOx in comparison to IrRuOx/TNT (Fig. 4.31B). Because of the change in the obtained Tafel slopes, a direct comparison of the exchange current densities (j_0) as a measure of electrocatalytic activity is not very useful [92]. Furthermore, the exchange current density is usually based on the geometric surface area and the roughness factor is not taken into account. The potential (E) for

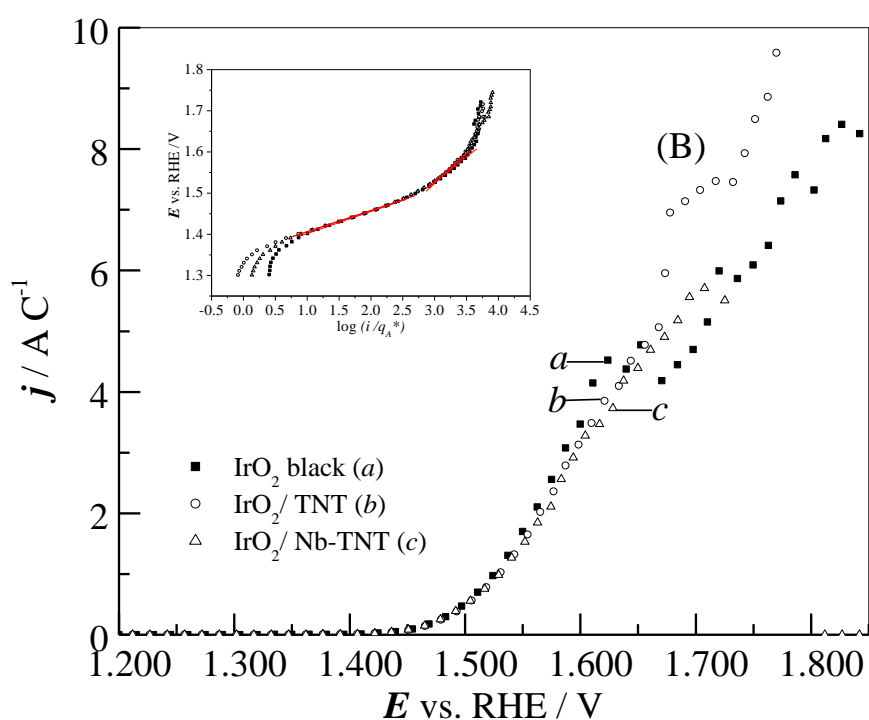
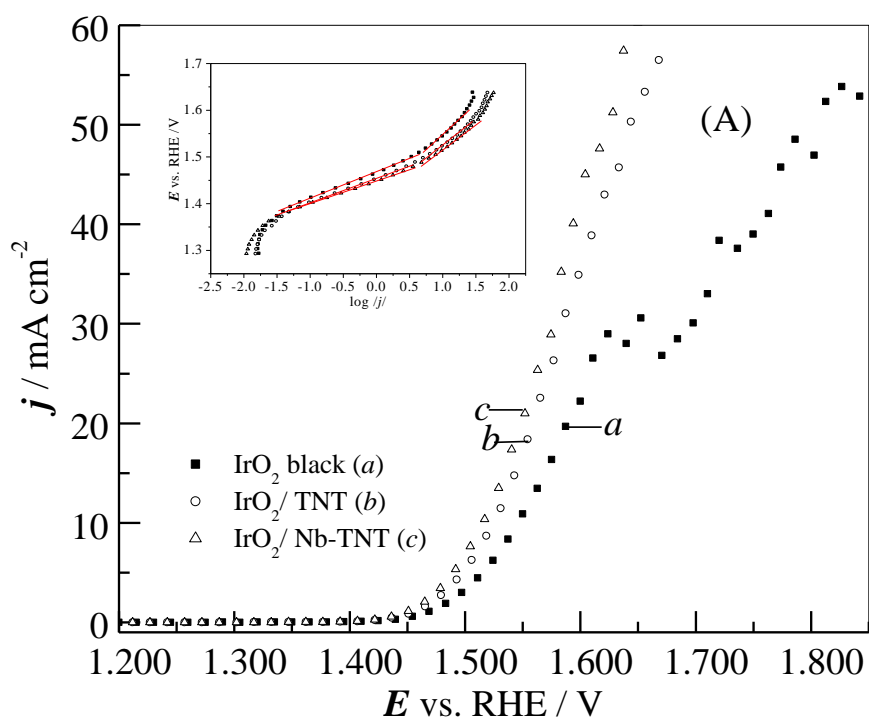


Figure 4.30 j - E curves corresponding to the OER on (a) IrO_2 , (b) 50 wt.% IrO_2/TNT , (c) 50 wt.% $\text{IrO}_2/3\text{Nb-TNT}$ catalysts in $0.50 \text{ mol dm}^{-3} \text{ H}_2\text{SO}_4$ aqueous solution. $T = 25.0 \text{ }^\circ\text{C}$. $s_r = 1 \text{ mV s}^{-1}$. Current density referred to the electrode geometric area (A) and to the total charge (B). IR -drop corrected.

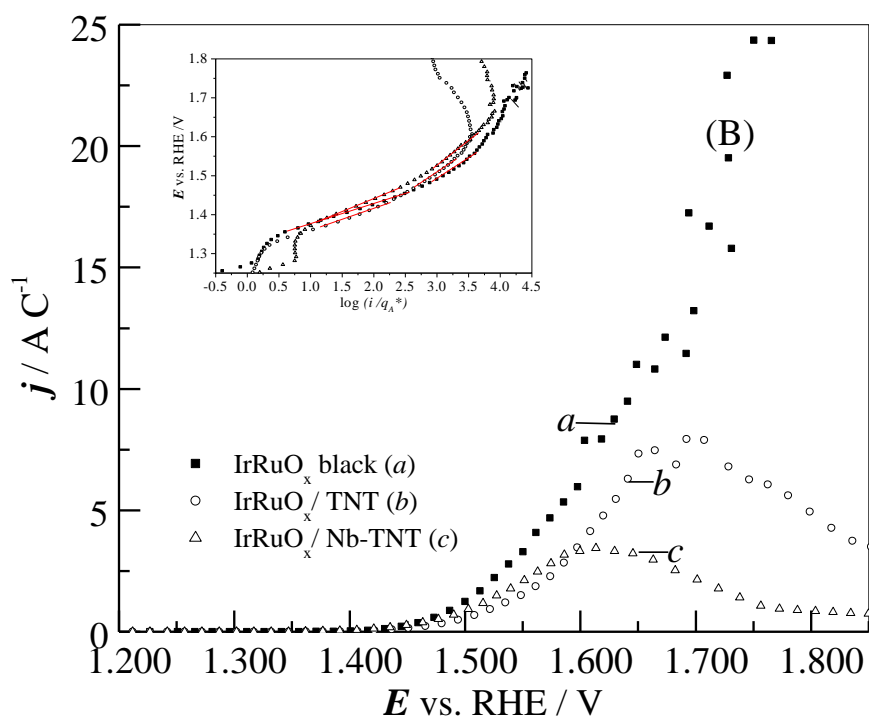
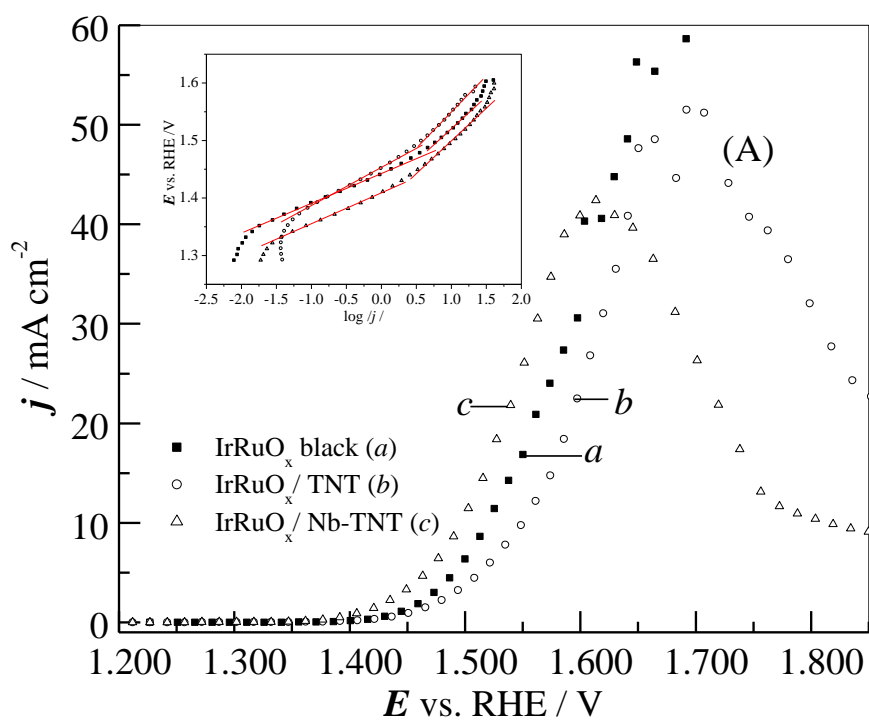


Figure 4.31 j - E curves corresponding to the OER on (a) IrRuO_x, (b) 50 wt.% IrRuO_x/TNT, (c) 50 wt.% IrRuO_x/3Nb-TNT catalysts in 0.50 mol dm⁻³ H₂SO₄ aqueous solution. $T = 25.0$ °C. $s_r = 1$ mV s⁻¹. Current density referred to the electrode geometric area (A) and to the total charge (B). IR -drop corrected.

oxygen evolution at a specific current density (E at 18 mA cm^{-2}) was proposed for a practical comparison of the electrocatalytic activity in [92]. However, comparing the potential at low and at high current densities (at 1 and at 18 mA cm^{-2}) shows the results corresponding to the low current density region, which in the case of the catalyst supported onto Nb-doped TNT, indicated a better sensitivity toward the OER of these catalysts in the presence of Nb [103].

Table 4.12 Kinetic parameters corresponding to the polarization curves calculated from Tafel plots (E - $\log j$) of IrO_2 and IrRuOx samples.

catalyst	Low current density region			High current density region		
	E at	b	j_0	E at	b	j_0
	$1 \text{ mA cm}^{-2} /$ V	$/ \text{ V dec}^{-1}$	$/ \text{ nA cm}^{-2}$	$18 \text{ mA cm}^{-2} /$ V	$/ \text{ V dec}^{-1}$	$/ \text{ nA cm}^{-2}$
IrO_2	1.467	0.054	42.4	1.584	0.144	64.1
IrO_2/TNT	1.455	0.052	45.5	1.553	0.108	26.6
$\text{IrO}_2/\text{Nb-TNT}$	1.449	0.049	33.4	1.543	0.114	31.4
IrRuOx	1.442	0.050	62.8	1.554	0.136	76.3
IrRuOx/TNT	1.452	0.065	375	1.586	0.150	74.1
$\text{IrRuOx}/\text{Nb-TNT}$	1.408	0.054	487	1.526	0.122	65.6

Better performance of the catalysts deposited onto lower surface area non-conductive supports is reported in [96]. 60 wt. % IrO_2 was deposited onto TiO_2 non-conductive supports with different surface areas. The authors covered the support with a thin conductive layer of IrO_2 , thus increasing the conductivity of the final catalyst. In

this work, an opposite trend is found, the better performance being observed when IrO₂ is deposited onto a higher surface area support of Nb-TNT (260 m² g⁻¹). Since the present supports have a significantly higher surface area than that reported in [96], we can attribute the better performance to a better dispersion onto the surface of the support, as evidenced by the higher values of the anodic total charge determined from the CV experiments.

The catalytic activity of the different catalysts has been compared in Figs 4.30B-4.31B. The polarization curves were normalized to the total number of active sites on the catalytic surface, because the total charge refers to the total amount of active catalyst sites which are accessible for oxygen evolution. After normalization, it can be seen that the three curves of IrO₂ materials are fully comparable (Fig. 4.30B).

Table 4.13 Kinetic parameters corresponding to the polarization curves calculated from Tafel plots ($E - \log i/q^*$) of IrO₂ and IrRuO_x samples.

Sample	Low current densities region			High current densities region	
	E at 1 mA C ⁻¹ / V	b / V dec ⁻¹	j_0 / μ A C ⁻¹	b / V dec ⁻¹	j_0 / mA C ⁻¹
IrO ₂	1.3507	0.0525	5.0372	0.1330	6.6050
IrO ₂ /TNT	1.3551	0.0508	3.4382	0.1408	8.2372
IrO ₂ /Nb-TNT	1.3568	0.0492	2.6574	0.1706	20.4381
IrRuO _x	1.3282	0.0492	10.1318	0.1070	3.8276
IrRuO _x /TNT	1.3103	0.0649	57.7569	0.1471	10.3715
IrRuO _x /Nb-TNT	1.2916	0.0624	103.3364	0.1522	16.5022

The performance of the catalysts studied in this work has been compared to that for different catalysts reported in the literature. Here should be noted that such a

comparison is not easy due to the variety of catalyst loadings and experimental conditions. However, the comparison can be done in terms of the potential at which $j = 0.001 \text{ A cm}^{-2}$ and $j = 0.018 \text{ A cm}^{-2}$ (see Table 4.14).

Starting with the catalyst taken as the reference unsupported IrO_2 , in [222] the value of E at 1 mA cm^{-2} is 1.475 V , in [97] it is 1.480 V and in this work it is 1.467 V , then slightly better than those reported before in the literature. Other direct comparison can be done between almost equal materials, *i.e.* $\text{IrO}_2/3\text{Nb-TNT}$ developed in this work and $\text{IrO}_2/\text{Nb}_{0.05}\text{Ti}_{0.95}\text{O}_2$ (33 wt. %) reported in the literature [97]. In this later work, with increasing the catalyst loading, the potential at 1 mA cm^{-2} is decreasing and reaching a minimum value of 1.430 V at 33 wt. % load. Lower loadings result in a potential higher than 1.50 V . In this work, the potential measured at 1 mA cm^{-2} $\text{IrO}_2/3\text{Nb-TNT}$ ($\text{IrO}_2/\text{Nb}_{0.05}\text{Ti}_{0.95}\text{O}_2$ (50 wt. %)) is 1.449 V . In the higher current density region, *i.e.* over 10 mA cm^{-2} , the comparison is difficult to be done due to changes in the shape of the polarization curves (not linear), resulting from the oxygen evolution. However, these data are also included in Table 4.14. Note, however, that for the same catalysts, the potentials corresponding to a given current density reported in this work are always smaller than those previously reported in the literature.

Table 4.14 Comparison of the performance of the catalysts studied in this work and that of similar catalysts reported in the literature.

Oxide loading / mg cm^{-2}	E at 1 mA cm^{-2} / V	E at 18 mA cm^{-2} / V	Catalyst	Reference
0.16	1.488		20 wt% IrO_2 on ATO	[221]
0.16	1.461		20 wt% $\text{Ir}_{0.5}\text{Ru}_{0.5}\text{O}_2$ on ATO	[221]
0.16	1.427		20 wt% RuO_2 on ATO	[221]
0.78	1.500		$\text{Ir}_{0.7}\text{Sn}_{0.3}\text{O}_2$ particles	[91]
0.70	1.488		$\text{Ir}_{0.7}\text{Ta}_{0.3}\text{O}_2$ particles	[222]

1.00	1.475		IrO ₂ particles	[222]
1.00	1.463		Ir _{0.6} Ru _{0.4} O ₂ particles	[222]
0.064*	1.53	1.64	RuIrCoOx powder	[92]
0.064*	1.52	1.66	RuIrOx powder	[92]
0.255	1.53		IrO ₂ /Nb _{0.05} Ti _{0.95} O ₂ (17 wt%)	[97]
0.255	1.52		IrO ₂ /Nb _{0.05} Ti _{0.95} O ₂ (18 wt%)	[97]
0.255	1.51		IrO ₂ /Nb _{0.05} Ti _{0.95} O ₂ (22 wt%)	[97]
0.255	1.50		IrO ₂ /Nb _{0.05} Ti _{0.95} O ₂ (26 wt%)	[97]
0.255	1.43		IrO ₂ /Nb _{0.05} Ti _{0.95} O ₂ (33 wt%)	[97]
0.255	1.48		Unsupported IrO ₂	[97]
0.035	1.467	1.584	Unsupported IrO ₂	this work
0.035	1.455	1.553	IrO ₂ /TNT	this work
0.035	1.449	1.543	IrO ₂ /3Nb-TNT (IrO ₂ /Nb _{0.03} Ti _{0.97} O ₂ (50 wt%))	this work
0.035	1.442	1.554	IrRuOx	this work
0.035	1.452	1.586	IrRuOx/TNT	this work
0.035	1.400	1.526	IrRuOx/3Nb-TNT (IrRuO _x /Nb _{0.03} Ti _{0.97} O ₂ (50 wt%))	this work

*Reported values are in mg. In ref [92] is not mentioned the GC electrode area, however is reported the amount of catalyst deposited onto it.

4.1.4 Membrane electrode assemblies (MEAs)

MEAs for low temperature electrolysis were prepared using conventional high and low temperature decalcomania methods (“decal”), with the following materials:

- Cathode: commercial Pt-black and Pt/C.
- Anode: RuO₂; commercial IrO₂ and RuO₂:IrO₂ physical mixture with atomic ratio Ru:Ir equal to 1:1, and homemade IrRuO_x, IrO₂ and IrO₂/3Nb-TNT catalysts.
- Polymer electrolyte membrane: Nafion[®] 115 (127μm).

Single Electrolysis Cell Modifications

The experiments were performed in a typical 5 cm² single electrolysis cell test fixture (4.84 cm² active area), as indicated in the experimental part. The graphite end plate on the anode side was coated with a thin Au layer and as GDL Teflon[®] coated carbon paper Toray 060 was used. Another end plate and GDL for the anode were made of titanium (porous sintered Ti, respectively SIKA-T3 at the end plate and SIKA-T10 as GDL, as described in section 3.4.4). On the cathode side a Teflon[®] coated carbon paper Toray 060 and standard carbon end plate were used.

The difference of the performance of both cells can be seen in Fig. 4.32. *V-j* curves were recorded at 80 °C and atmospheric pressure. It can be seen that the replacement of the anodic carbon current collector by porous Ti, which is more stable under OER conditions, does not significantly affect the performance of the cell. The cell voltage at 400 mA cm⁻² was of 1.53 V for carbon end plates and Toray as GDL on the anode, whereas it was of 1.60 V for the porous Ti GDL and end plate on the anode.

4.1.4.1 Electrochemical characterization

MEAs were of CCM type and they were prepared by the conventional decal method described in section 3.4.3. In order to establish a benchmark, the MEAs were prepared with commercial catalysts and their performance was recorded. IrO₂, RuO₂ (purchased from Alfa Aesar) and a physical mixture of both (atomic ratio Ir:Ru equal to 1:1) were applied as catalysts for the OER. The corresponding results are shown in Fig. 4.33.

The cell voltages at 0.400 A cm⁻² when using the purchased catalyst anodes RuO₂ and IrO₂, and the RuO₂:IrO₂ physical mixture were, respectively, 1.53, 1.98 and 2.21 V. The best performance was then obtained for RuO₂, as expected, since it has been recognized to be the most active catalyst. However, as mentioned before in section

1.3.5, RuO₂ is not very stable under these anodic conditions of and suffers oxidation. Due to the lower cost of RuO₂ in comparison to IrO₂, it was used as the anodic catalyst for the optimization of the MEA preparation and the optimization of the catalyst loading on the cathode.

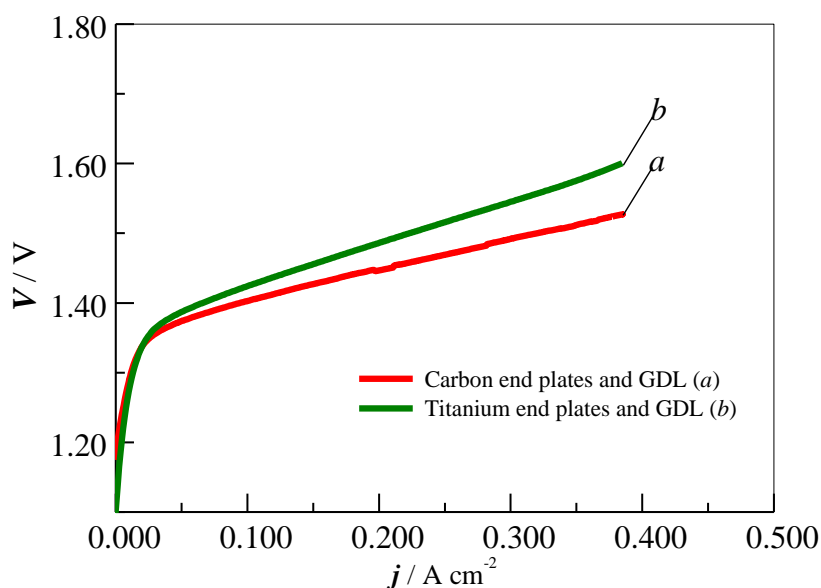


Figure 4.32 V - j curves of the MEAs tested in the modified fixture: (a) with carbon end plates and (b) with titanium current collector and gas diffusion layer. $T = 80\text{ }^{\circ}\text{C}$ and atmospheric pressure.

Optimization of the MEA preparation

As indicated before, the conventional decal method requires very high temperature ($210\text{ }^{\circ}\text{C}$) for catalyst layer transfer from the decal substrate to the membrane. The transformation of the Nafion[®] membrane from its H⁺-form to its Na⁺-form is needed and additionally, these high temperatures could cause cracks in the catalyst layer. We have developed the method at low temperature ($135\text{ }^{\circ}\text{C}$) transfer conditions where: (i) the H⁺-form of the membrane can be used, thus eliminating one step in the MEA preparation procedure; and (ii) the risk of cracks in the catalyst layer is

lowered. Results for MEAs prepared using both methods with different pressing conditions are presented in Fig. 4.34. At low temperatures, it seems that the pressing pressure of 50 bar (curve *a*) was not sufficient to achieve a good contact between the membrane and the electrodes. For this reason, the pressure was increased to 80 bar (curve *b*). The results are compared with the conditions of the high temperature decal (curve *c*) which provides good contact and performance. As shown in this figure, the cell voltages at 0.400 A cm^{-2} with the MEA prepared by the high temperature decal method was of 1.53 V, whereas for the low temperature one, it was of 1.59 V.

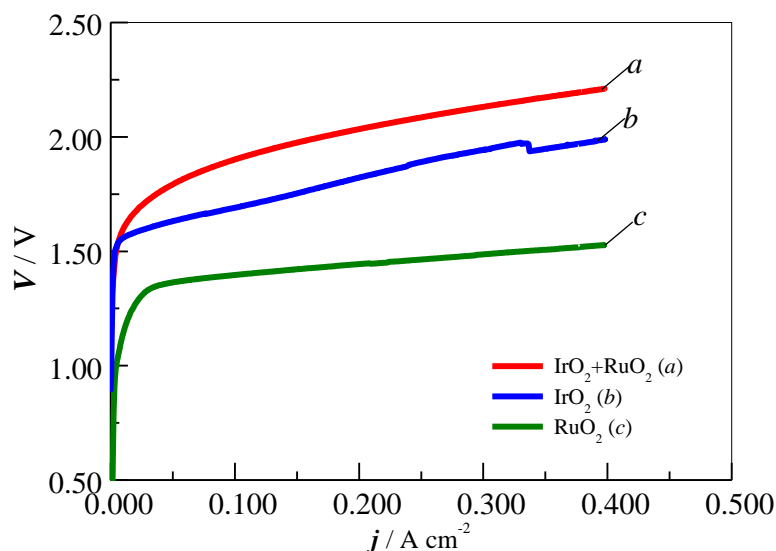


Figure 4.33 *V-j* curves corresponding to MEAs: (a) Pt black $1.0 \text{ mg}_{\text{Pt}} \text{ cm}^{-2}$, $\text{RuO}_2 + \text{IrO}_2$ (Ru:Ir=1:1) $2.0 \text{ mg}_{\text{oxides}} \text{ cm}^{-2}$; (b) Pt black $1.0 \text{ mg}_{\text{Pt}} \text{ cm}^{-2}$, IrO_2 $2.0 \text{ mg}_{\text{IrO}_2} \text{ cm}^{-2}$; (c) Pt black $1.0 \text{ mg}_{\text{Pt}} \text{ cm}^{-2}$, RuO_2 black $2.0 \text{ mg}_{\text{RuO}_2} \text{ cm}^{-2}$. $T = 80 \text{ }^\circ\text{C}$ and atmospheric pressure. High T decal method.

Cathode catalyst loading optimization

The results of Pt optimization are presented in Fig. 4.35, where the use of 20 wt.% Pt/Vulcan-XC72 and Pt black commercial catalysts was done. A loading of 0.5 $\text{mg}_{\text{Pt}} \text{ cm}^{-2}$ for 20 wt.% Pt/Vulcan shows same performance as with $1 \text{ mg}_{\text{Pt}} \text{ cm}^{-2}$ loading of

Pt black. The cell voltages at a current density of 0.400 A cm^{-2} were 1.53 V for $20 \text{ wt.\%Pt/Vulcan XC72}$ ($0.5 \text{ mg}_{\text{Pt}}\text{cm}^{-2}$) and 1.52 V for Pt black XC72 ($1.0 \text{ mg}_{\text{Pt}}\text{cm}^{-2}$).

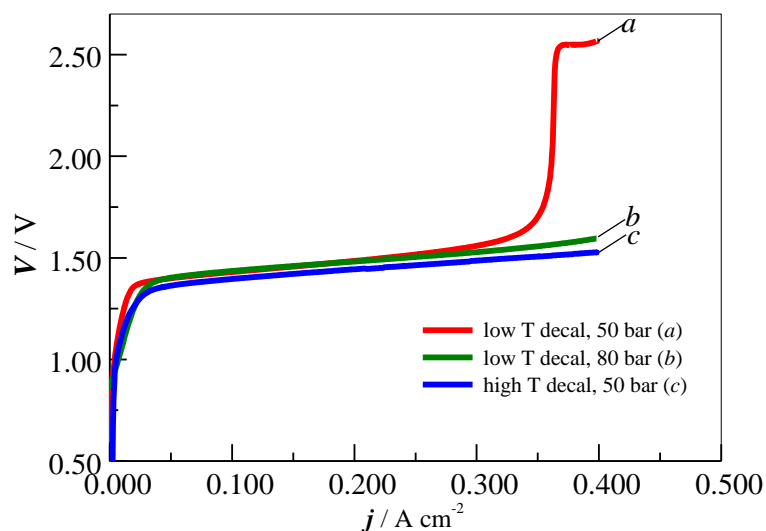


Figure 4.34 V - j curves showing the performance of MEA prepared with Pt black ($1.0 \text{ mg}_{\text{Pt}} \text{ cm}^{-2}$) on the cathode side and RuO_2 black ($2.0 \text{ mg}_{\text{RuO}_2} \text{ cm}^{-2}$) on the anode side: (a) $135 \text{ }^\circ\text{C}$, 50 bar ; (b) $135 \text{ }^\circ\text{C}$, 80 bar ; and (c) $210 \text{ }^\circ\text{C}$, 50 bar . $T = 80 \text{ }^\circ\text{C}$ and atmospheric pressure.

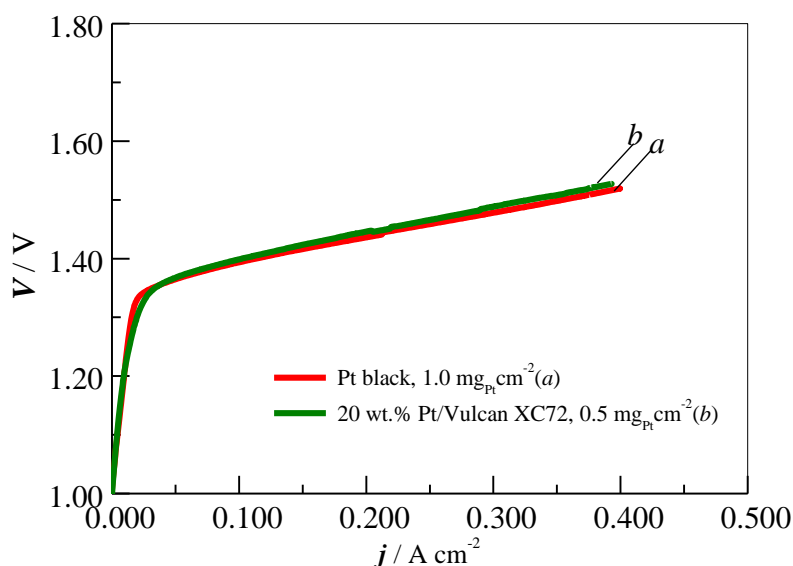


Figure 4.35 V - j curves showing the performance of the MEAs prepared by the low T decal method ($135 \text{ }^\circ\text{C}$, 80 bar), with RuO_2 black ($2.0 \text{ mg}_{\text{RuO}_2} \text{ cm}^{-2}$) on the anode side and, in the cathode side: (a) Pt black $1.0 \text{ mg}_{\text{Pt}} \text{ cm}^{-2}$ and (b) $20 \text{ wt. \% Pt/Vulcan}$ $0.5 \text{ mg}_{\text{Pt}} \text{ cm}^{-2}$. $T = 80 \text{ }^\circ\text{C}$ and atmospheric pressure.

Anode catalyst loading optimization

Homemade IrO₂ black, more stable than RuO₂ for OER, was used to optimize the anode catalyst loading. Loadings of 1.5, 2.0 and 3.0 mg_{IrO₂} cm⁻² were used. The corresponding results are shown in Fig. 4.36. From the *V-j* curves it is apparent that an IrO₂ loading of 1.5 mg cm⁻² was relatively sufficient to provide a good MEA performance. The difference in cell voltages at 500 mA cm⁻² is only of 9 mV when compared to 2.0 mg cm⁻² (1.519 and 1.528 V, respectively). It seems that loadings of 3.0 mg cm⁻² are too high, with mass transport problems at high current densities (note the cell voltage increase in the high current density region).

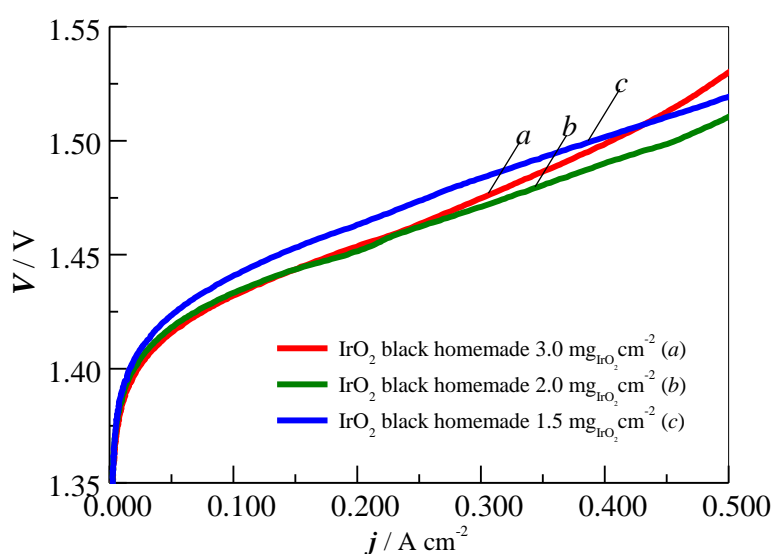


Figure 4.36 *V-j* curves showing the performance of the MEA prepared by the low *T* decal method, using 20 wt. % Pt/Vulcan XC72 with a loading of 0.5 mg_{Pt} cm⁻² as the cathode, the anode catalyst being homemade IrO₂ black with different loadings: (a) 3.0, (b) 2.0 and (c) 1.5 mg_{IrO₂} cm⁻². *T* = 80 °C. and atmospheric pressure.

Fig. 4.37 shows the performance as anodic OER catalyst of homemade IrO₂ and IrRuO_x blacks, and 50 wt. % IrO₂/3Nb-TNT, which were the subjects of investigation

(see section 4.3.2). As expected, the best performance was found for the MEA with 50 wt. % IrO₂/3Nb-TNT. The corresponding results are listed in Table 4.17.

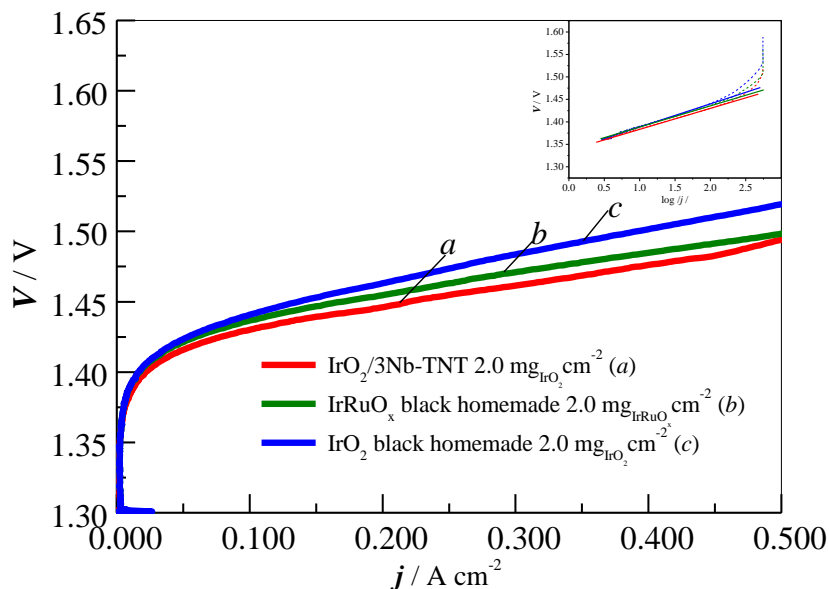


Figure 4.37 V - j curves showing the performance of the MEAs, prepared by the low T decal method, using 20 wt. % Pt/Vulcan XC72 with a loading of 0.5 mg_{Pt} cm⁻² as the cathode, the anode catalyst being: (a), IrO₂/3Nb-TNT, 2.0 mg_{IrO₂} cm⁻²; (b) homemade IrRuO_x black, 2.0 mg_{IrRuO_x} cm⁻² and (c) homemade IrO₂ black, 2.0 mg_{IrO₂} cm⁻². $T = 80$ °C and atmospheric pressure.

The working temperature dependence is shown in Fig. 4.38, where the V - j curves were recorded at 80 and at 90 °C. The difference in the cell voltages with increasing the temperature is practically constant and about 20 mV in the entire current density range of measurement, with a better performance at 90 °C.

The dependence on the water feeding flow rate is given on Fig. 4.39. It is obvious that there is no significant difference in the V - j curves under equal conditions of measurement and MEA composition.

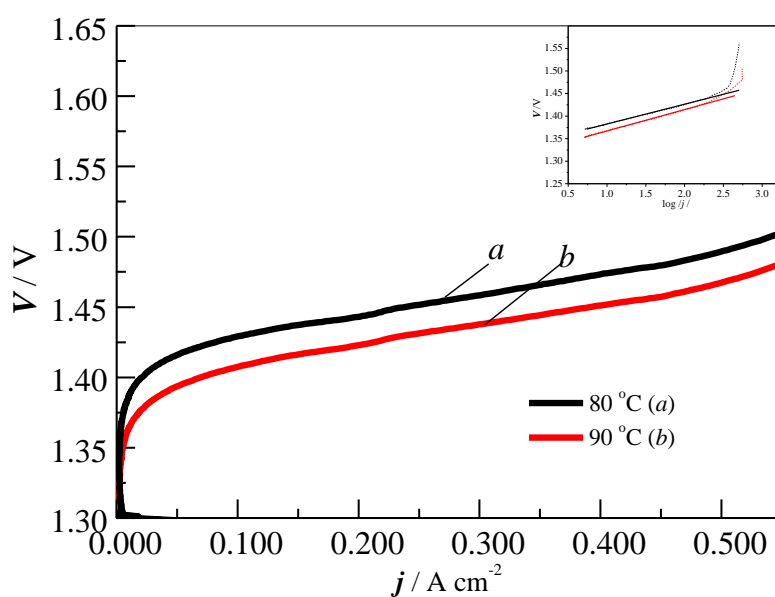


Figure 4.38 V - j curves showing the performance of the MEAs, prepared by the low T decal method, with 20 wt. % Pt/Vulcan XC72 $0.5 \text{ mg}_{\text{Pt}} \text{ cm}^{-2}$ as the cathode and $\text{IrO}_2/3\text{Nb-TNT}$ $2.0 \text{ mg}_{\text{IrO}_2} \text{ cm}^{-2}$ as the anode: (a) $80 \text{ }^\circ\text{C}$ and (b) $90 \text{ }^\circ\text{C}$. Atmospheric pressure.

Table 4.15 Cell performance at 0.100 and 0.500 A cm^{-2} with different anode catalysts.

Catalyst	$T / ^\circ\text{C}$	$b / \text{V dec}^{-1}$	V at	V at	V at
			1 mA cm^{-2}	0.100 A cm^{-2}	0.500 A cm^{-2}
			/ V	/ V	/ V
homemade IrO_2 black	80	0.048	1.341	1.441	1.519
homemade IrRuO_x black	80	0.046	1.343	1.436	1.498
$\text{IrO}_2/3\text{Nb-TNT}$	80	0.046	1.339	1.430	1.494
$\text{IrO}_2/3\text{Nb-TNT}$	90	0.044	1.320	1.407	1.468

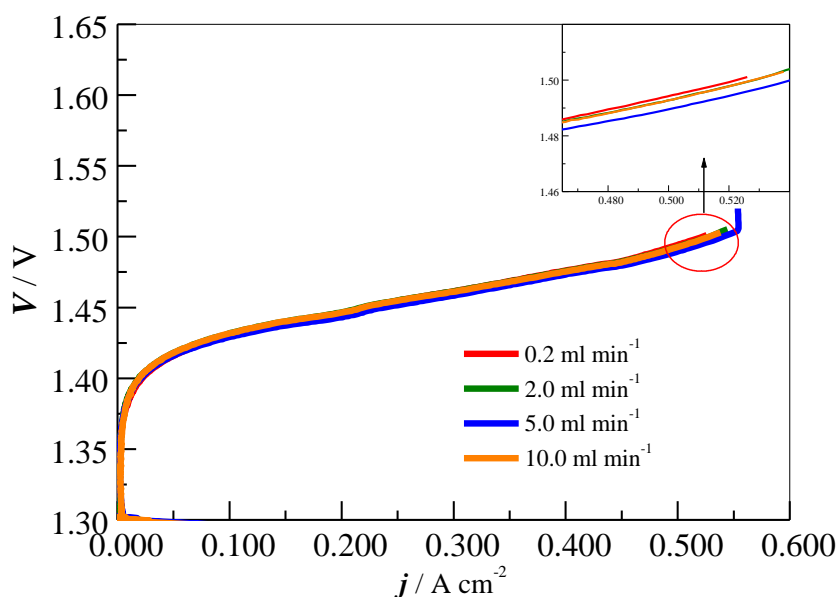


Figure 4.39 V - j curves showing the performance of the MEAs, prepared by the low T decal method using 20 wt. % Pt/Vulcan XC72, $0.5 \text{ mg}_{\text{Pt}} \text{ cm}^{-2}$ as the cathode, $\text{IrO}_2/3\text{Nb-TNT}$, $2.0 \text{ mg}_{\text{IrO}_2} \text{ cm}^{-2}$ as the anode and different water feeding rates: (a) 0.2, (b) 2.0, (c) 5.0 and (d) 10.0 ml min^{-1} . $T = 80 \text{ }^\circ\text{C}$ and atmospheric pressure.

According to Fig. 4.37, the cell voltages at each current density when using $\text{IrO}_2/3\text{Nb-TNT}$ as anodes are slightly better than those obtained using IrRuO_x , and significantly better than those obtained for IrO_2 black. A similar behaviour was observed from the results obtained in three-electrode cell in $0.5 \text{ mol dm}^{-3} \text{ H}_2\text{SO}_4$ (section 4.3.2, Table 4.14). After optimization of the electrode loadings and method of MEA preparation, the best results for the V - j relationship for the PEMWE studied here at $80 \text{ }^\circ\text{C}$ were 1.43 V at 0.1 A cm^{-2} and 1.49 V at 0.5 A cm^{-2} , whereas at $90 \text{ }^\circ\text{C}$ they were 1.41 V at 0.1 A cm^{-2} and 1.47 V at 0.5 A cm^{-2} . These values can be compared to certain extent with the values reported in Table 1.7, section 1.3.7. Similar cell composition and the same experimental temperature and membrane were used in [36], [40] and [43]. Most of the cell voltages reported in Table 1.7 at 100 mA cm^{-2} are higher

than those reported in this work, which confirms the relatively good performance of the MEA prepared with the catalysts reported here.

The Tafel slopes were determined in the low current density range 50–150 mA cm⁻², where the $V\text{-log } j$ Tafel plot is approximately linear and the effects of proton and mass transport resistances can be neglected. The Tafel slopes were between 0.046–0.048 V dec⁻¹ at 80 °C (Table 4.15), which is very close to those reported by Bernt *et al.* in [122] of 0.045–0.050 V dec⁻¹ and by Reier *et al.* in [87] of 0.040–0.045 V dec⁻¹ for amorphous iridium oxide on a titanium substrate.

4.1.4.2 Cost estimation

In this section the cost of the MEAs which performance was shown in Fig. 4.41 is estimated and analyzed. Since the cost values are highly dependent on several factors and vary for the different suppliers and amounts, the supplier and the cost per unit volume of weight (ml or g) of the material are reported here. Here should be noted that during the estimations done in this section, the energy cost (e.g. heating, annealing of the samples), any material losses (e. g. losses during spraying the catalyst ink onto the substrates) and any human resources costs were not taken into account. Heating and annealing conditions follow the procedures reported in section 3.1 and were the same for supported and unsupported materials. The estimation considers only materials and the assumption that the synthesis was done at 100% yield and depositions were done without any material or any other type of losses (the synthesis yield of the materials were considered to be stoichiometric). The purpose of this study is to evaluate the cost increase/decrease when the new materials were used as supports in the best MEA configuration (section 4.1.4.1) and doing a comparison to conventional configurations of MEAs.

Supports cost estimation-

Following materials and prices were taken into account:

Material	Price per unit
Titanium (IV) n-butoxide (98%, Alfa Aesar)	0.083 € g ⁻¹
Niobium (V) ethoxide (99,99999%, Alfa Aesar)	11.70 € g ⁻¹
Absolute ethanol (HPLC grade, Scharlau)	0.015 € ml ⁻¹
Hydrochloric acid (37%, Scharlau)	0.009 € ml ⁻¹
Ammonium carbonate (Acros Organics)	0.041 € g ⁻¹
Sodium hydroxide (reagent grade, Scharlau)	0.014 € g ⁻¹

From the procedure of preparation of Nb-TiO₂ and Nb-TNT in section 3.1, the following prices per 1 g were calculated:

$$\text{TiO}_2 - 0.44 \text{ € g}^{-1}$$

$$3\text{Nb-TiO}_2 - 1.81 \text{ € g}^{-1}$$

$$\text{TNT} - 1.40 \text{ € g}^{-1}$$

$$3\text{Nb-TNT} - 3.00 \text{ € g}^{-1}$$

From the cost estimation of the Nb-TiO₂ it can be seen that there is a significant increase in the cost when Nb was added as a dopant (more than four times higher), even when the concentration is as low as 3 at. % to Ti (atomic ratio Nb:Ti equal to 3:97). Comparison between TNT and Nb-TNT shows that the cost of the doped material increases twice when compared to the undoped one. Transformation from TiO₂ to TNT results in three times higher cost and from Nb-TiO₂ to Nb-TNT, 1.65 times.

IrO₂ and IrRuO_x catalysts cost estimation-

Following materials and prices were taken into account:

Material	Price per unit
TNT	1.40 € g ⁻¹
3 at.% Nb-TNT	3.00 € g ⁻¹
IrCl ₃ ·xH ₂ O (99.9%, Alfa Aesar)	83.20 € g ⁻¹
RuCl ₃ ·xH ₂ O (99.9%, Alfa Aesar)	17.90 € ml ⁻¹
HNO ₃ (69%, ultrapure, Scharlau)	0.184 € ml ⁻¹
Sodium hydroxide (reagent grade, Scharlau)	0.014 € g ⁻¹

IrO₂ black homemade – 141.48 € g⁻¹

IrRuOx black homemade – 88.32 € g⁻¹

50 wt. % IrO₂/3NbTNT – 72.24 € g⁻¹

The estimated price per 1.0 g of metal oxides shows that 50 wt. % IrO₂ supported on 3Nb-TNT has the lowest price in comparison to the other two good anode catalysts. IrRuOx has 39 % lower cost in comparison to the conventionally used IrO₂ and was considered as a good option for IrO₂ replacement [224]. The cost of the proposed 50 wt. % IrO₂ on 3Nb-TNT is 18 % lower than IrRuOx and is almost half of the price of IrO₂.

Electrode cost estimation-

Following materials were considered:

Material	Price per unit
IrO ₂ black homemade	141.48 € g ^{-1*}
IrRuOx black homemade	88.32 € g ⁻¹
50 wt. % IrO ₂ /3NbTNT	72.24 € g ⁻¹
Pt black (45-52 m ² g ⁻¹ , Premetek)	90.17 € g ⁻¹
20 wt.% Pt/Vulcan XC72 (Premetek)	27.37 € g ⁻¹
Tetrabutylammonium hydroxide (1 mol dm ⁻³ in methanol, Sigma Aldrich)	1.02 € g ⁻¹
Glycerol (Panreac)	0.029 € g ⁻¹
5 wt. % Nafion [®] dispersion (Sigma Aldrich)	3.84 € g ⁻¹

Nafion 115 [®] membrane (size 5 cm x 5 cm)	3.84 € per 25 cm ²
--	-------------------------------

*in the procedure reported in section 3.4.2 all materials are reported in g, for this reason and here, in the table are expressed in terms of € g⁻¹

The comparison between the commercially available Pt black and 20 wt. % Pt/Vulcan XC72 shows significantly lower cost of 1 g supported Pt in comparison to Pt black. The difference in price is three times lower when Pt is supported.

Anodes:

Anode 1: 2.0 mg_{IrO₂}cm⁻²; IrO₂ black; 30% Nafion

Compound	Mass / g	Price per unit / € g ⁻¹	Price / €	% of the total cost
IrO ₂ black	0.0100	141.48	1.4148	0.8030
5% Nafion	0.0857	3.84	0.3291	0.1867
Glycerine	0.0800	0.029	0.0023	0.0013
TBAOH	0.0040	1.02	0.0041	0.0023
0.3 mg _{Nafion} cm ⁻² (3 mg 5% solution)	0.0030	3.84	0.0115	0.0065
Total cost			1.7618	

Anode 2: 2.0mg_{IrRuO_x}cm⁻²; IrRuO_x black; 30% Nafion

Compound	Mass / g	Price per unit / € g ⁻¹	Price / €	% of the total cost
IrRuO _x black	0.0100	88.32	0.8832	0.7179
5% Nafion	0.0857	3.84	0.3291	0.2675
Glycerine	0.0800	0.029	0.0023	0.0019

TBAOH	0.0040	1.02	0.0041	0.0033
0.3 mg Nafioncm ⁻² (3 mg 5% solution)	0.0030	3.84	0.0115	0.0093
Total cost			1.2302	

Anode 3: 2.0 mg_{IrO₂}cm⁻²; 50% IrO₂/3NbTNT; 30% Nafion

Compound	Mass / g	Price per unit / € g ⁻¹	Price / €	% of the total cost
50% IrO ₂ /3NbTNT	0.0200	72.24	1.4448	0.6792
5% Nafion	0.1714	3.84	0.6582	0.3094
Glycerine	0.1600	0.029	0.0046	0.0022
TBAOH	0.0080	1.02	0.0082	0.0038
0.3 mg Nafioncm ⁻² (3 mg 5% solution)	0.0030	3.84	0.0115	0.0054
Total cost			2.1273	

A comparison between Anode 1 and Anode 3 shows that IrO₂ black contribution to the total cost is 80 % in comparison to the 72 % of IrRuOx and 68 % of 50 wt. % IrO₂/3Nb-TNT. 98 % of the electrode cost is contribution of the anode catalyst and the 30 wt. % Nafion content in the electrode, which is directly related to the amount of anode catalyst.

Final comparison shows that when IrO₂ is replaced by 50 wt. % IrO₂/3Nb-TNT the increase in the final anode cost is 17 %. When it was replaced by IrRuOx, there was a decrease of 30 %.

Cathodes:Cathode 1: 0.5mg_{Pt}cm⁻²; 20% Pt/Vulcan XC72; 30% Nafion

Compound	Mass / g	Price per unit / € g⁻¹	Price / €	% of the total cost
20% Pt/Vulcan XC72	0.0125	27.37	0.3421	0.4426
5% Nafion	0.1071	3.84	0.4113	0.5321
Glycerine	0.1000	0.029	0.0029	0.0037
TBAOH	0.0050	1.02	0.0051	0.0066
0.3 mg _{Nafion} cm ⁻² (3 mg 5% solution)	0.0030	3.84	0.0115	0.0149
Total cost			0.7729	

Cathode 2: 0.5 mg_{Pt}cm⁻²; Pt-black; 30% Nafion

Compound	Mass / g	Price per unit / € g⁻¹	Price / €	% of the total cost
Pt-black	0.0025	90.17	0.2254	0.7028
5 % Nafion	0.0214	3.84	0.0822	0.2563
Glycerine	0.0200	0.029	0.0006	0.0019
TBAOH	0.0010	1.02	0.0010	0.0031
0.3 mg _{Nafion} cm ⁻² (3 mg 5% solution)	0.0030	3.84	0.0115	0.0358
Total cost			0.3207	

In cathode composition 1 the supported 20 wt. % Pt/Vulcan XC72 contributes up to 44% to the final cost of the electrode in comparison to the unsupported Pt black, which represents 70 % of the electrode cost. As in the case of the anodes, 97 % of the final electrode price is due to the catalyst and Nafion content in the catalyst layer.

Comparison between both cathode compositions shows that when Pt black is replaced by 20 wt. % Pt/Vulcan XC72, the electrode price is increased by 2.5 times.

MEAs:

MEA 1:	Price / €
Anode 1: 2.0 mg _{IrO₂} cm ⁻² ; IrO ₂ black homemade; 30% Nafion 5 cm ²	1.7618
Cathode 1: 0.5mg _{Pt} cm ⁻² ; 20 wt.% Pt/Vulcan XC72; 30% Nafion 5 cm ²	0.7729
Membrane Nafion [®] 115 25 cm ²	3.84
Total	6.3747

MEA 2:	Price / €
Anode 2: 2.0 mg _{IrRuO_x} cm ⁻² ; IrRuO _x black homemade; 30% Nafion 5 cm ²	1.2302
Cathode 1: 0.5mg _{Pt} cm ⁻² ; 20 wt.% Pt/Vulcan XC72; 30% Nafion 5 cm ²	0.7729
Membrane Nafion [®] 115 25 cm ²	3.84
Total	5.8431

MEA 3:	Price / €
Anode 3: 2.0 mg _{IrO₂} cm ⁻² ; 50 wt. % IrO ₂ /3NbTNT; 30% Nafion 5 cm ²	2.1273
Cathode 1: 0.5mg _{Pt} cm ⁻² ; 20 wt.% Pt/Vulcan XC72; 30% Nafion 5 cm ²	0.7729
Membrane Nafion [®] 115 25 cm ²	3.84
Total	6.7402

Comparing the cost of the different parts of MEA1, MEA2 and MEA3 shows that the anode contributes 21 to 31 % of the final MEA price, while the cathode loaded with 0.5 mg_{Pt} cm⁻² of 20 wt. % Pt/Vulcan XC72 represents 11-13 % of it. It was found that the Nafion[®]115 membrane provides the highest cost contribution with 57 to 66 % of the final MEA price.

Comparison of the total price of MEAs 1-3 can provide information about the cost changes when IrO₂ is replaced by another, cheaper and more effective, catalysts. When IrO₂ is replaced by 50 wt. % IrO₂/3Nb-TNT, the increase in the final MEA cost is 5.7 % and when it was replaced by IrRuO_x, there is a decrease of 8.4 %.

MEA 4:	Price / €
Anode 1: 2.0 mg _{IrO₂} cm ⁻² ; IrO ₂ black homemade; 30% Nafion 5 cm ²	1.7618
Cathode 2: 0.5mg _{Pt} cm ⁻² ; Pt black; 30% Nafion 5 cm ²	0.3207
Membrane Nafion® 115 25 cm ²	3.84
Total	5.9225

MEA 5:	Price / €
Anode 2: 2.0 mg _{IrRuO_x} cm ⁻² ; IrRuO _x black homemade; 30% Nafion 5 cm ²	1.2302
Cathode 2: 0.5mg _{Pt} cm ⁻² ; Pt black; 30% Nafion 5 cm ²	0.3207
Membrane Nafion® 115 25 cm ²	3.84
Total	5.3909

MEA 6:	
Anode 3: 2.0 mg _{IrO₂} cm ⁻² ; 50 wt. % IrO ₂ /3NbTNT; 30% Nafion 5 cm ²	2.1273€
Cathode 2: 0.5mg _{Pt} cm ⁻² ; Pt black; 30% Nafion 5 cm ²	0.3207 €
Membrane Nafion® 115 25 cm ²	3.84 €
Total cost	6.2880 €

Comparing the cost contribution of the different parts of MEA4, MEA5 and MEA6 shows that the anode contributes 22 to 33 % to the final MEA price, while the cathode loaded with 0.5 mg_{Pt} cm⁻² of Pt black represents only 5-6 % of it. It was found

that the Nafion[®] 115 membrane provides the highest cost contribution with 61 to 71 % of the final MEA cost.

Comparing the total price of MEAs 4-6 can provide additional information about the cost changes when IrO₂ is replaced by another, cheaper and more effective, catalysts. When IrO₂ is replaced by 50 wt. % IrO₂/3Nb-TNT the increase in the final MEA cost is 5.9 %, When it was replaced by IrRuOx, there was a decrease of 9 %. These values are similar to those calculated above for MEAs 1-3.

Additional comparison between MEA1 and MEA4, MEA2 and MEA5 and MEA3 and MEA6 provides information about the cost changes due to the supporting Pt on Vulcan XC72. It can be seen that when Pt black is replaced by 20 wt. % Pt/Vulcan XC72 (under equal MEA compositions), there is an increase of the final MEA cost of 6.7-7.7 %.

It appeared that when IrO₂ is replaced by IrRuOx and 50 wt. % IrO₂/3Nb-TNT, the difference in the anode cost is significant and when IrRuOx is used, there is a decrease of 30 %. When the supported 50 wt. % IrO₂/3Nb-TNT was used as the anodic catalyst, the increase in the anode cost is 17 %.

When the MEAs were prepared, these differences were significantly reduced and the increase in the final MEA cost caused by the utilization of 50 wt.% IrO₂/3Nb-TNT in comparison to the same MEA with IrO₂ black on the anode is only 5.7-5.9 %. This cost reduction is attributed to the price of the Nafion[®] 115, which provides the highest cost contribution with 57 to 71 % of the final cost of the MEA.

Additionally it can be concluded that the cost increase of the final MEA due to supporting IrO₂ onto 3Nb-TNT (increase of 5.7-5.9 %) is slightly lower than the MEA cost increase caused by the deposition of Pt onto Vulcan XC72 (increase of 6.7-7.7 %.).

This difference can be attributed to the difference in the Nafion[®] content in the catalyst layer (30 wt. % Nafion) which corresponds to the total amount of support and catalyst.

4.2 DMFC

4.2.1 Methanol oxidation reaction electrocatalysts

4.2.1.1. Physico-chemical characterization

XRD patterns of PtRu and Pt black commercial catalysts are shown in Fig. 4.40. This figure clearly shows the crystalline structure of the PtRu and the Pt catalysts nanoparticles. Both XRD spectra display the (111), (200), (220), (311), and (222) diffraction peaks corresponding to the *fcc* crystal structure of Pt. Ru appears to be incorporated into the *fcc* structure of Pt because the diffraction peaks in PtRu are slightly shifted to higher 2θ values with respect to the same peaks in Pt. The diffraction peaks corresponding to (100), (101), (110), (103), and (201) planes of the Ru hexagonal close-packed crystal structure are not observed, thus indicating that if there is some Ru segregation from the PtRu nanocrystals, it is only present as amorphous material or it is

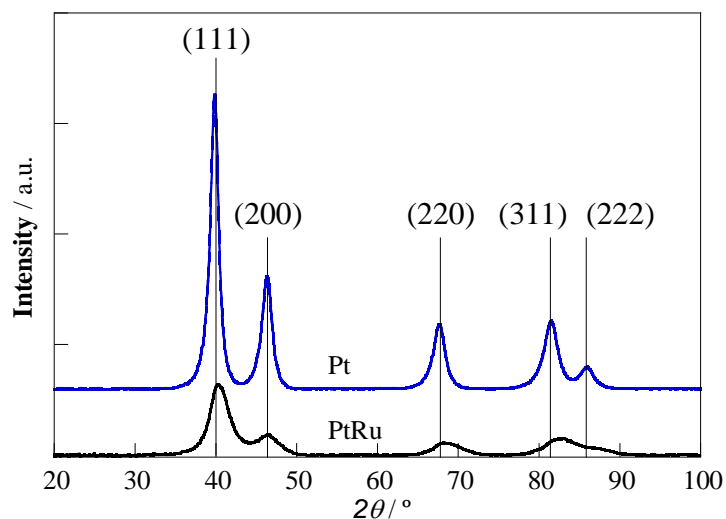


Figure 4.40 X-ray diffraction patterns of PtRu and Pt black catalysts (in parenthesis, planes corresponding to characteristic diffraction signals of *fcc* Pt).

in a very limited amount. The lattice parameters were calculated from the XRD patterns in Fig. 4.40, considering the diffraction peak positions of the Pt signals. The value for

the PtRu black catalyst (3.877 Å) is lower than that of Pt black (3.918 Å), which indicates a contraction of the lattice due to the PtRu alloying to some extent [225]. Mean crystallite sizes, calculated from Scherrer's equation, were 2.3 ± 0.3 and 6.1 ± 0.7 nm for PtRu and Pt blacks, respectively. Then, the maximum theoretical metal surface areas were calculated assuming that such nanoparticles had a spherical shape, using the following equation:

$$SA = 6 \times 10^3 / \rho d \quad (4.2)$$

where SA is the surface area of the metallic nanoparticles ($\text{m}^2 \text{g}^{-1}$); d is the mean crystallite size (nm), and ρ (g cm^{-3}) is the density of Pt or PtRu alloy ($\rho = \rho_{\text{Pt}} X_{\text{Pt}} + \rho_{\text{Ru}} X_{\text{Ru}}$, where $\rho_{\text{Pt}} = 21.45 \text{ g cm}^{-3}$, $\rho_{\text{Ru}} = 12.45 \text{ g cm}^{-3}$, and $X_{\text{Pt(Ru)}}$ are the weight percent of Pt and Ru in the catalyst) [226]. According to Eq. (4.2), the SA (Pt) is $45.8 \text{ m}^2 \text{g}^{-1}$, which is in good agreement with the value reported by the manufacturer (45–52 $\text{m}^2 \text{g}^{-1}$). From EDX measurements, the Pt and Ru contents in PtRu black were 67.2 and 32.8 wt. %, respectively. Then, the maximum SA (PtRu) is $141 \text{ m}^2 \text{g}^{-1}$, which is also in agreement with the value calculated from the analysis provided by the manufacturer ($129 \text{ m}^2 \text{g}^{-1}$).

To assess the influence of catalyst ink composition, specifically the organic solvents used in its formulation, on the morphology and textural properties of catalyst layers, first of all inks were characterized by light scattering experiments. Fig. 4.41 shows the size distribution of agglomerates in the PtRu catalyst inks containing NBA or IPA as organic solvents (see Table 4.16). Two main peaks centred at around 1 μm and 10 μm were observed in both inks. Lim et al. [227] reported a similar

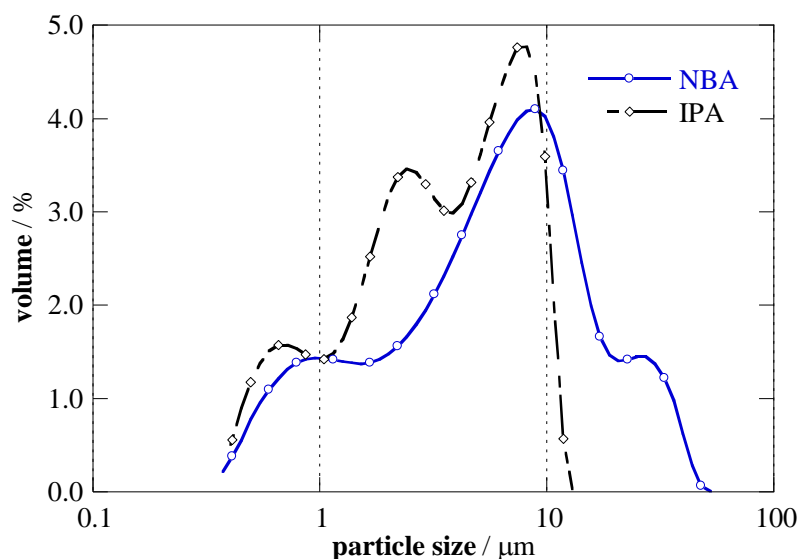


Figure 4.41 Particle size distribution for the PtRu catalyst inks formulated with different organic solvents: (○) NBA and (◇) IPA.

result suggesting that peaks in the region below 1 μm were due to distributed sizes of Nafion[®] ionomer agglomerates in the dispersion solvents. This was further confirmed by studies of Nafion[®] aggregation, which depends on the dielectric constant and the solubility of solvents in water [228]. The Nafion[®] ionomer has polar parts and tends to aggregation when the polarity of the solvent decreases. This explains why the peak

Table 4.16 Physical properties of the solvents used for the catalyst inks.

Solvent	ϵ^a	P_v^b / hPa	T_b^c / °C
n-butyl acetate (NBA)	5.01	13.0	126.5
2-propanol (IPA)	18.0	43.0	82.4

^aDielectric constant at 25 °C

^bVapour pressure at 20 °C

^cBoiling temperature

under 1 μm is centred at smaller size for IPA than for NBA, *i.e.* because the latter solvent has lower polarity than the former. On the other hand, peaks above 1 μm can be

assigned to size distributions of agglomerates of the catalyst nanoparticles and Nafion[®]. It is clear from this figure that these agglomerates are larger when using NBA (note the peak centred at 26 μm). This can also be explained by the lower polarity of NBA, which favours larger-sized catalyst nanoparticles-Nafion[®] agglomerates.

It is expected that the size and compactness of the agglomerates will influence the morphology of the anode catalyst layer once the ink has been applied onto the substrate. Thus, the macroscopic changes in the morphology of the PtRu catalyst layers were examined by SEM. Fig. 4.42 shows the SEM images corresponding to the CLs prepared using NBA and IPA, respectively. It is shown in this figure that both CLs have granular-shape morphology, but it appears that the CL prepared using IPA is more compact and

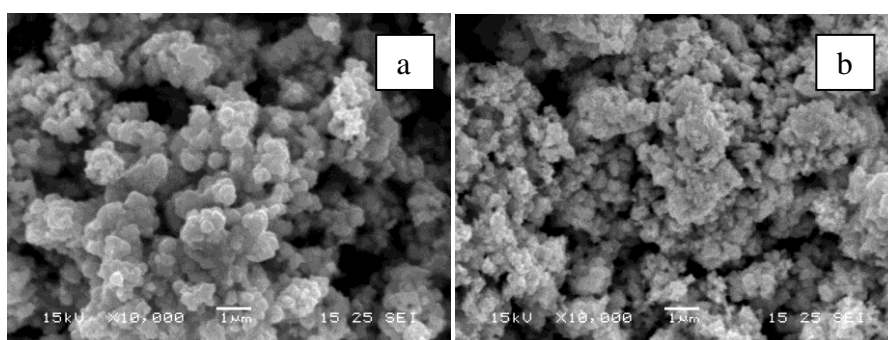


Figure 4.42 SEM images of selected PtRu catalyst layers prepared using (a) NBA and (b) IPA as organic solvents.

less porous than that prepared using NBA. Similar results were reported in the literature for catalyst layers made of supported catalysts [164, 189]. In addition, a significant effect of the size of the catalyst agglomerates on the catalyst layer microstructure is expected. Consequently, to gain a better understanding on the microstructure of the anode catalyst layers in quantitative terms, pore size distributions were determined. Fig. 4.43 shows the pore size distributions corresponding to the PtRu catalyst layers

prepared using NBA and IPA. Both curves show similar shape. However, in the region between 0.1-10 μm ,

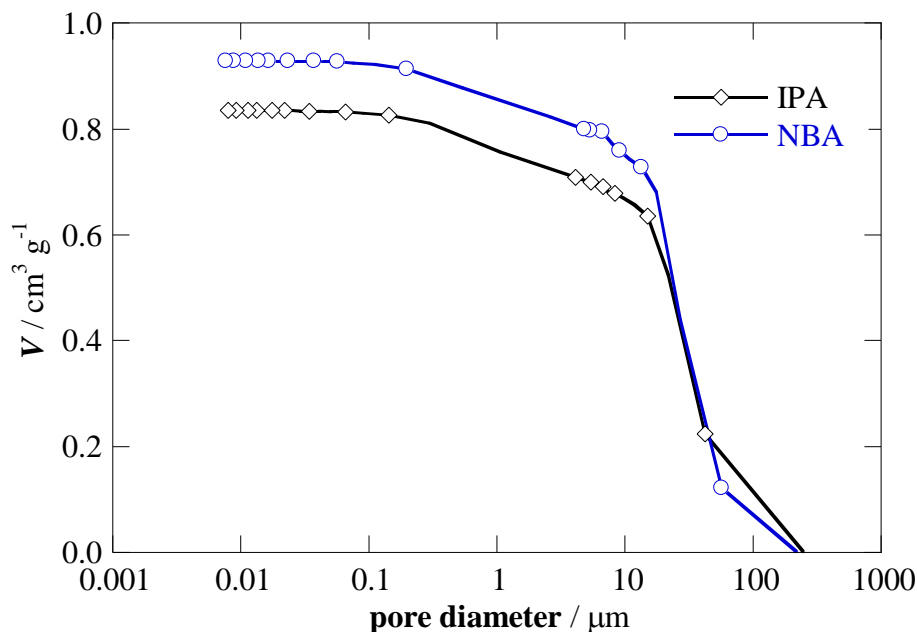


Figure 4.43 Cumulative pore volume (V) vs. pore diameter curves for anode catalyst layers prepared from PtRu catalyst inks containing either (○) NBA or (◇) IPA as organic solvent.

the specific volume of the pores was higher for NBA than for IPA. It has been previously reported in the literature [164,167,168] that this region corresponds to the secondary pores, that is, the space existing between the agglomerates formed by the catalyst nanoparticles and Nafion[®]. Therefore, the secondary pore volume is larger by about 12% when NBA is used as organic solvent, in agreement with the morphology of the catalyst layers observed in Fig. 4.42.

4.2.1.2 Electrochemical characterization

The activity of PtRu porous diffusion electrodes towards methanol oxidation was studied in three-electrode cell filled with $0.5 \text{ mol dm}^{-3} \text{ H}_2\text{SO}_4 + 2.0 \text{ mol dm}^{-3} \text{ CH}_3\text{OH}$ aqueous electrolyte. Fig. 4.44 shows the linear sweep voltammograms corresponding to

methanol oxidation on catalyst layers in contact with the liquid electrolyte, by sweeping the potential from 0.075 to 0.750 V. The oxidation current given by the CL formulated

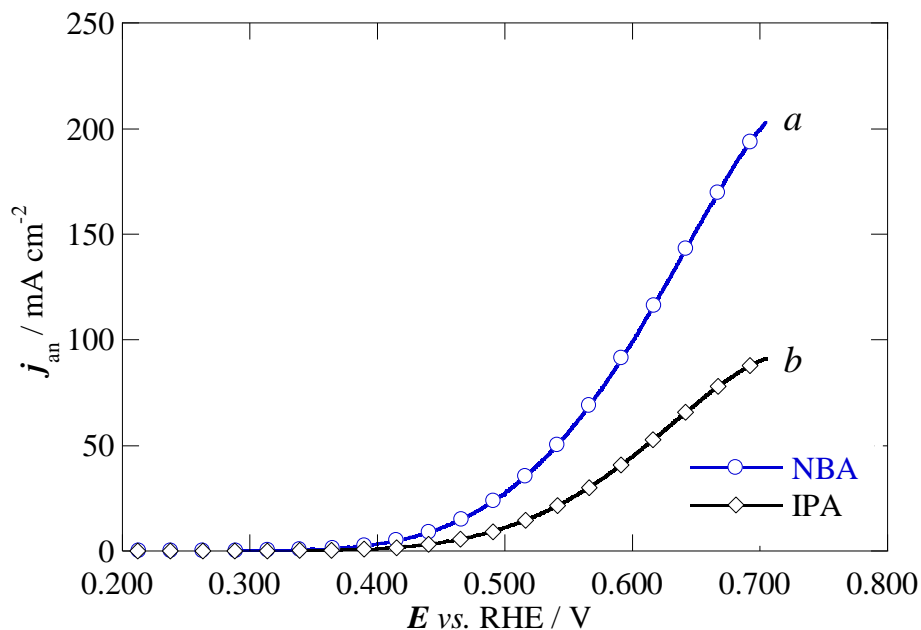


Figure 4.44 j - E curves corresponding to the electrooxidation of methanol on PtRu black electrodes manufactured using (a) NBA and (b) IPA. $2.0 \text{ mol dm}^{-3} \text{ CH}_3\text{OH} + 0.5 \text{ mol dm}^{-3} \text{ H}_2\text{SO}_4$. $T = 20 \text{ }^\circ\text{C}$. Sweep rate of 0.5 mV s^{-1} .

with NBA as solvent was larger than that corresponding to the CL formulated with IPA. At low current densities, where no significant effect of mass transport and ohmic drop is expected, this can be at least partially explained by the different active surface areas of both catalyst layers. The ECSAs for CO stripping were determined to be 52.4 and $47.3 \text{ m}^2 \text{ g}^{-1}$ (using the conversion factor of $420 \text{ } \mu\text{C cm}^{-2}$ [229]), for the CLs made with NBA and IPA, respectively, *i.e.* by about 11% greater in the former. Note, however, that the current densities for NBA are much higher than this percentage when compared to IPA in the high current density part. This difference and the deviation from the exponential form in the potential range $0.55\text{--}0.70 \text{ V}$ strongly suggest that there are transport limitation effects. This transport limitation is more apparent for IPA and could be

explained considering the size and porosity of the agglomerates formed by the ionomer and the catalyst nanoparticles in both solvents, which are smaller in IPA (Fig. 4.41). The smaller porosity can limit the mass transport through the catalyst layer and therefore, the rate of the diffusion of the reactants to the catalyst sites and the rate of the removal of the reaction products from these points can be slowed down.

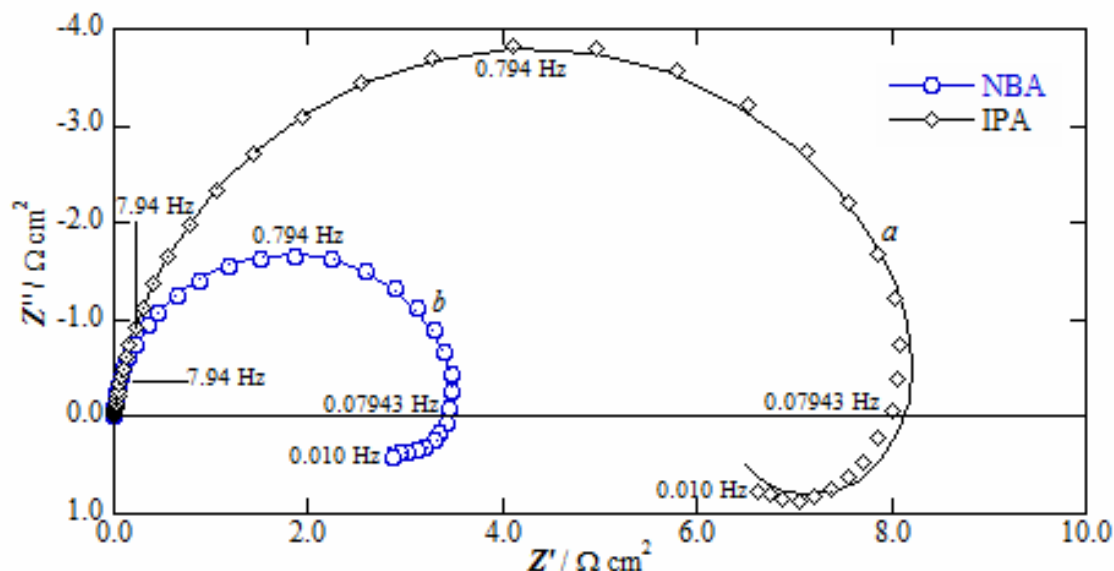
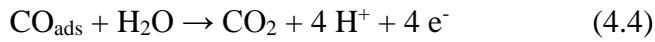
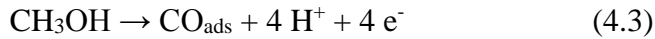


Figure 4.45 Nyquist diagrams corresponding to methanol electrooxidation at 0.500 V on PtRu black electrodes manufactured using (○) NBA and (◇) IPA. 2.0 mol dm⁻³ CH₃OH + 0.5 mol dm⁻³ H₂SO₄. T = 20 °C. The uncompensated resistance has been removed from the Nyquist diagrams. Solid lines correspond to fitting using the equivalent circuit shown in Fig. 4.46.

To obtain more insight into the properties of the catalyst layers, the PtRu catalysed surfaces were studied using the EIS technique, since the resistances associated with the methanol electrooxidation are included in impedance data and could be separated with the help of an appropriate equivalent circuit. Fig. 4.45 depicts the Nyquist plots corresponding to the PtRu catalysed anodes prepared using NBA and IPA. The impedance diagrams obtained at constant potential of 0.500 V showed similar features in both cases. They have the form of slightly depressed semicircles in the region of high and intermediate frequencies (1000-0.07 Hz), ending with an inductive

loop at low frequencies. As shown in Fig. 4.45, the impedance values of the Nyquist plots corresponding to the CL formulated with NBA are smaller than those of the CL formulated with IPA. To gain more insight about this behaviour and its influence on the charge transfer of the methanol electrooxidation reaction, the impedance data have been interpreted by means of an equivalent circuit, assuming that this reaction proceeds via a two-step bifunctional mechanism [144]:



at which methanol is adsorbed mainly on Pt sites, while OH comes from the water dissociation on Ru sites, CO being the main kinetically significant adsorbed intermediate on the catalyst. According to the kinetic theory derived by Armstrong and Henderson [230] and extended by Harrington, Conway [231] and Cao [232], for reactions involving one adsorbed intermediate, in which diffusion of participating species is not rate-limiting, different equivalent circuits can be used to interpret impedance data depending on the potential regions [233, 234]. In the present context, considering that the mass transport effects are not relatively significant at 0.5 V,

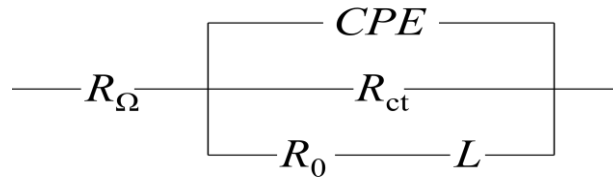


Figure 4.46 Equivalent circuit used to interpret the impedance diagrams for the methanol electrooxidation on PtRu black catalysed diffusion anodes.

the most suitable equivalent circuit to interpret our EIS results is depicted in Fig. 4.46, where R_{Ω} is the external ohmic resistance, which includes the uncompensated

electrolyte resistance between the working and reference electrodes, the electronic resistance of the lead, and any contact resistance that may exist between the external surface of the electrode and the electrolyte; *CPE* is a constant phase element defined as [235]:

$$Z_{\text{CPE}} = 1/Y_0(i\omega)^m \quad (4.5)$$

where Y_0 is the admittance and m is the CPE exponent, represents the double layer capacitance, although porous surfaces can suffer a deviation from the ideal capacitive behaviour, indicated by the value of the frequency power; R_{ct} is the charge transfer of the electrode reaction, that is, how fast the rate of charge transfer changes with the change of the electrode potential which occurs without change in coverage; R_0 serves to modify the phase-delay according to reactions 4.3 and 4.4, and the inductance L means that the current signal follows a voltage perturbation with a phase delay, due to the slowness of CO_{ads} coverage relaxation [236]. The impedance diagrams can be fitted to the equivalent circuit shown in Fig. 4.46. The corresponding results are summarized in Table 4.17 and plotted together with the experimental data as solid lines in Fig. 4.45.

Table 4.17 Fitting parameters obtained using the equivalent circuit of Fig. 4.46 for the methanol oxidation on the PtRu catalyst in the three-electrode cell.

solvent	R_Ω	Y_0	n	R_{ct}	R_0	L	C_{dl}
	/ $\Omega \text{ cm}^2$	/ $\Omega^{-1} \text{ s}^n \text{ cm}^{-2}$		/ $\Omega \text{ cm}^2$	/ $\Omega \text{ cm}^2$	/ H cm^2	/ F cm^{-2}
NBA	0.251	0.05677	0.956	3.600	9.892	62.64	0.05277
IPA	0.378	0.02802	0.922	8.589	24.06	148.4	0.02484

A comparison between the fitting data of Table 4.17 for both solvents points out to the physicochemical properties of the interphase related with the R_{ct} , R_0 and L elements as the main cause of the respective catalyst layer performances. The R_{ct} for methanol

electrooxidation taking place at the catalyst-ionomer interface is smaller for the CL formulated with NBA than that formulated with IPA. This could be related to a higher electroactive surface area of the former. The relative active areas on both CLs can be estimated from impedance measurements through the determination of the double layer capacitance (C_{dl}), because the capacitance values are proportional to such active areas [237]. The values of C_{dl} estimated by Eq. (4.6) [238] are also shown in Table 4.16.

$$C_{dl} = Y_0 (Y_0 R_{ct})^{(1-n)/n} \quad (4.6)$$

The C_{dl} results indicate that the ECSA of the CL formulated with NBA is higher than that formulated with IPA, in good agreement with the results obtained from the CO stripping measurements. This clearly indicates that the secondary pores in the catalyst formulated with NBA make accessible a greater surface area of the catalyst. Furthermore, the anode reaction resistance ARR, which can be calculated from the expression [189]:

$$ARR = R_{ct} \times R_0 / (R_{ct} + R_0) \quad (4.7)$$

is $2.64 \square \text{ cm}^2$ for the CL formulated with NBA, but $6.33 \square \text{ cm}^2$ for CL formulated with IPA, showing that methanol electrooxidation is enhanced in the former. On the other hand, R_0 and L are attributed to the adsorbed intermediates. The lower values corresponding to the CL formulated with NBA can be explained either by its higher number of reaction sites with respect to the CL formulated with IPA and/or by a faster oxidation rate of the intermediates on the former. To test the latter possibility, it is useful to determine the parameter τ^{-1} , the inverse of the coverage relaxation time, which is equivalent to the first order rate constant for the oxidative desorption of the intermediates [239]:

$$\tau^{-1} = R_0 / L \quad (4.8)$$

This calculation gives τ^{-1} values of 0.158 and 0.162 s⁻¹ for CLs formulated with NBA and IPA, respectively. This result suggests that the oxidation rate of the intermediates is similar in both CLs. Therefore, the different performance of the CLs prepared using NBA and IPA is due to the greater availability of the reaction sites in the former.

4.2.2 Membrane electrode assemblies (MEAs)

Fig. 4.47 shows the polarization curves of MEAs in which the anode catalyst layers were formulated with NBA and IPA, denoted as MEA_{NBA} and MEA_{IPA}, respectively, the single DMFCs operating with 2 mol dm⁻³ CH₃OH aqueous solutions at 60 °C. The cathode feed was dry synthetic air at atmospheric pressure. It can be observed that the differences between current densities delivered by MEAs increase as the cell voltage decreases (thus delivering more current). The curvature tending to a limiting current density for the MEA_{IPA} shows mass transport limitation for currents much smaller than those obtained for MEA_{NBA}.

The current densities delivered by the MEAs prepared with NBA and IPA at the technically interesting voltage of 0.400 V were 148 and 85 mA cm⁻², equivalent to a power density of 59 and 34 mW cm⁻², respectively. The power density given by MEA prepared with NBA corresponds to an enhancement of approximately 74 % compared with the MEA prepared with IPA. This suggests that the difference in DMFC performance is due solely to the anode catalyst layer in MEAs, because the composition of the anode GDL, the membrane and the cathode was the same in both types of MEAs. A comparison between the MEA performances obtained in single DMFC (see Fig. 4.47) with those found in the literature for active DMFCs [240-243] revealed that, in spite of the difference in the operating conditions and the MEA composition, the results

presented in Table 4.18 are indicative of the good performance delivered by the MEA made of the anode prepared using NBA.

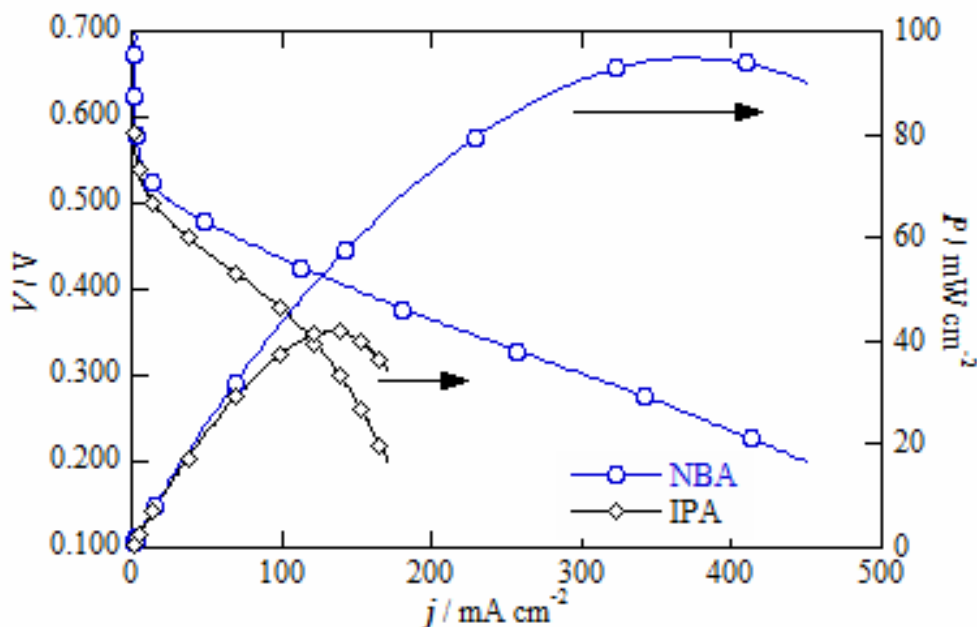


Figure 4.47 V - j polarization and P - j curves for DMFCs with PtRu black catalysed anodes formulated with different inks containing: (\circ) NBA and (\diamond) IPA. Cathodes catalysed with Pt black. $T = 60\text{ }^{\circ}\text{C}$. $[\text{CH}_3\text{OH}] = 2.0\text{ mol dm}^{-3}$, fuel flow rate = 2 mL min^{-1} . Air flow rate = 100 mL min^{-1} .

The corresponding CO electrooxidation curves for the PtRu black catalysed anodes prepared using NBA and IPA are depicted in Fig. 4.48. It can be seen that both curves show the same profile; the CO oxidation peak potentials appeared at 0.510 and 0.517 V, for PtRu-IPA and PtRu-NBA, respectively, and the onset potentials for CO oxidation showed a little difference of 0.059 V, which are values comparable to those previously reported in the literature [244].

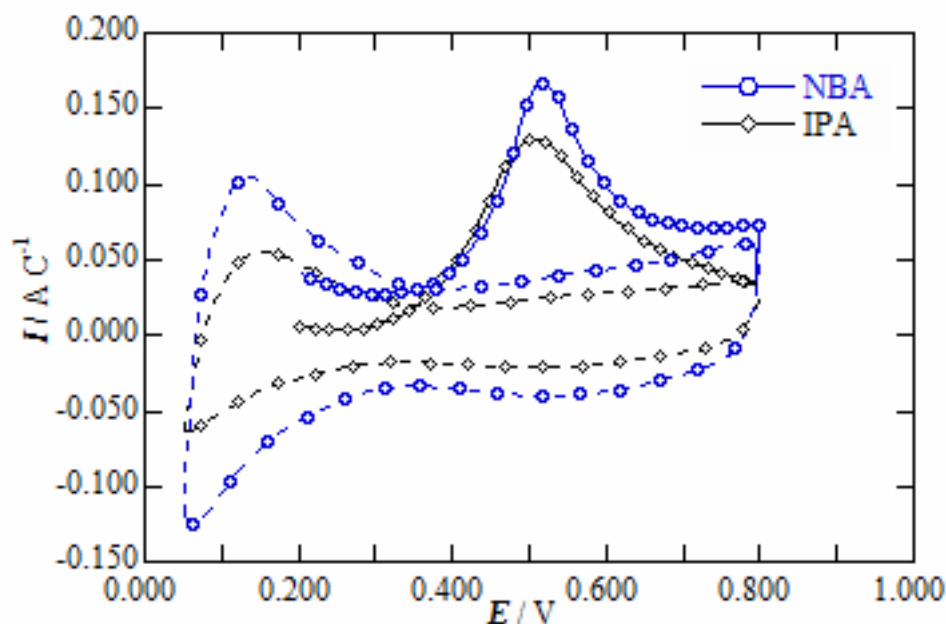


Figure 4.48 CO stripping voltammograms for PtRu black catalysed anodes formulated with different inks containing: (○) NBA and (◇) IPA after adsorption at 0.100 V vs. DHE. $T = 25\text{ }^{\circ}\text{C}$. Anode fed with N_2 ; cathode with H_2 . Both gases humidified with water at T_{cell} . Dashed lines are second scans (currents normalized by the CO_{ads} charge for better comparison).

In order to see whether the catalyst crystallite size could contribute to the dramatic difference observed in the fuel cell performance, XRD spectra of PtRu catalysed anodes with catalyst layer prepared using NBA or IPA, PtRu-NBA and PtRu-IPA, respectively, were registered. Both diffractograms are shown in Fig. 4.49, together with that corresponding to PtRu black catalyst. The calculated mean crystallite sizes were 2.6 ± 0.7 , 2.7 ± 0.6 and 2.3 ± 0.3 nm, for PtRu-NBA, PtRu-IPA and PtRu black catalyst. Therefore, there is no significant difference between crystallite sizes in the three specimens, thus indicating that sintering during catalyst ink after formation or MEA preparation can be excluded.

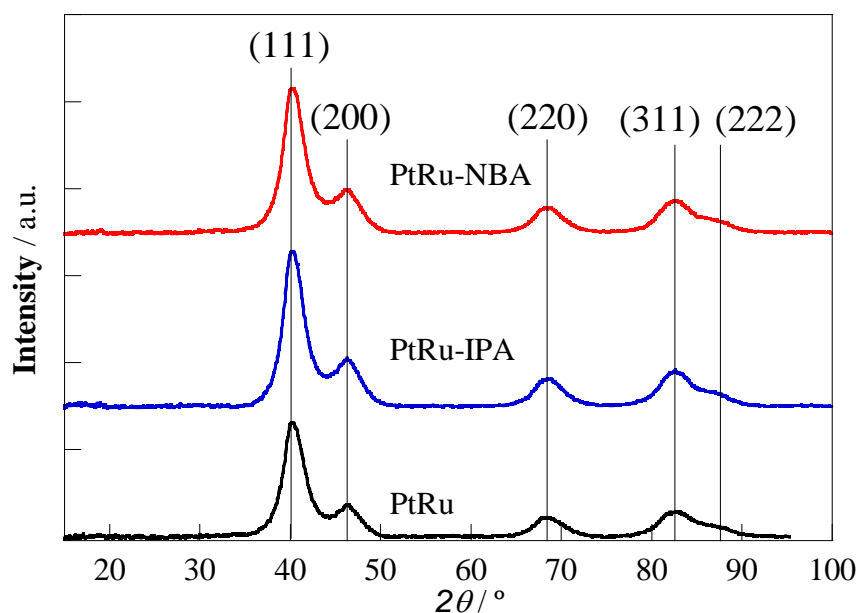


Figure 4.49 X-ray diffraction patterns of PtRu black catalyst (in black), anode prepared with PtRu and IPA (in blue), and anode prepared with PtRu and NBA (in red) (in parenthesis, planes corresponding to characteristic diffraction signals of *fcc* Pt).

Furthermore, to get more insight about the influence of the anode catalyst layer on the MEA performance, we carried out an in situ EIS analysis. Fig. 4.50 depicts the Nyquist plots corresponding to the PtRu black catalyzed anodes, formulated using NBA and IPA, corresponding to MEAs in Fig. 4.47 at the technically interesting potential of 0.400 V *vs.* DHE. The features of both diagrams show essentially a kinetic control, being the methanol electrooxidation more favoured on the anode prepared using NBA. In addition, no mass-transport limitations due to methanol inlet feed are identified and the loops reflecting the inductive behaviour appear at the low frequency end of the impedance plots. The uncompensated resistances, R_{Ω} , were 0.200 and 0.212 $\Omega \text{ cm}^2$, respectively. Furthermore, the anodes used in DMFC usually have a high PtRu content. Consequently, the electrodes are thick and proton conductivity limitations in the catalyst layer could affect the MEA performance. Then, we estimated the proton resistance, R_p , from EIS measurements in the anode catalyst layers in presence of methanol, to reflect the value close to the real operating conditions of the DMFC. To do this, we used the

procedure described by Havránek and Wipperman [245], who adapted the transmission line equivalent circuit of a PEMFC cathode catalyst layer, for a DMFC anode catalyst layer. Briefly, Nyquist diagrams corresponding to methanol oxidation should feature a linear slope at frequencies, ω , much higher than a “characteristic frequency”, ω_c , defined as:

$$\omega_c = 1 / (R_{\text{MeOH}} C_{\text{pdl}}) \quad (4.9)$$

where R_{MeOH} is the resistance of methanol oxidation, which considers the rate determining steps of methanol electrooxidation (the adsorption/dissociation of CH_3OH and the oxidation of adsorbed intermediates, like CO and COH), and C_{pdl} is a pseudo-double layer capacitance, which takes into account the importance of adsorbed intermediates ($\text{CH}_3\text{OH}_{\text{ad}}$, CO_{ad} , COH_{ad} , OH_{ad} , etc.) for the kinetics of methanol electrooxidation with a catalyst surface highly covered by adsorbed intermediates. The pseudo-layer capacitance can be obtained from the capacitive charging current of cyclic voltammograms of the methanol electrooxidation, according to:

$$C_{\text{pdl}} = j_{\text{pdl}} \times \nu^{-1} \quad (4.10)$$

where j_{pdl} is the pseudo-capacitive charging current density and ν is the scan rate. The linear slope, K , can be determined according to:

$$|Z| = K \omega^{-1/2} = \left(\sqrt{R_p / C_{\text{pdl}}} \right) \omega^{-1/2} \quad (4.11)$$

where $|Z|$ is the impedance modulus and ω is the frequency of the harmonic signal. From the linear slope, the proton resistance of the catalyst, R_p , can be determined using the pseudo-double layer capacitance:

$$R_p = K^2 \times C_{\text{pdl}} \quad (4.12)$$

The specific proton conductivity of the catalyst layer is calculated from:

$$\sigma_p = d / AR_p \quad (4.13)$$

where d is the average thickness of the catalyst layer and A is the geometric area of the catalyst layer.

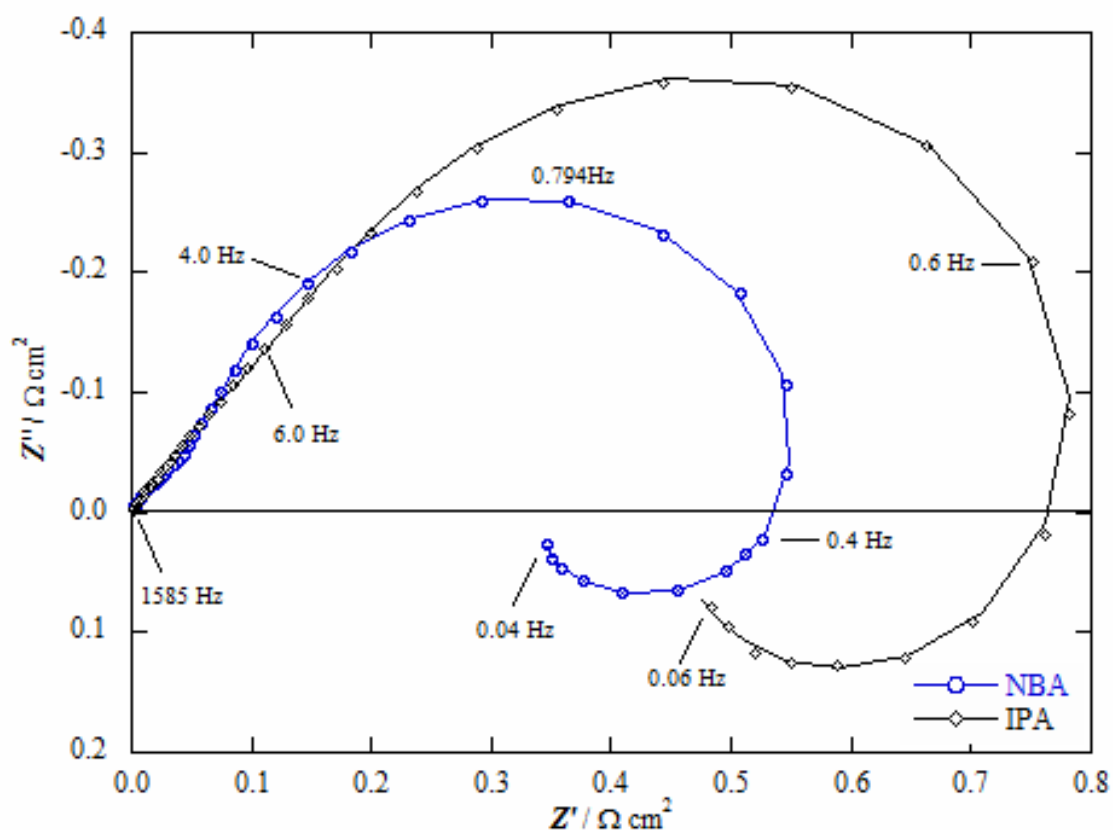


Figure 4.50 Nyquist diagrams corresponding to the methanol electrooxidation in the anode of the DMFC. The PtRu anodes, fed with $2.0 \text{ mol dm}^{-3} \text{ CH}_3\text{OH}$ at 1.5 mL min^{-1} , were manufactured using (\circ) NBA and (\diamond) IPA solvents at $60 \text{ }^\circ\text{C}$. The Pt cathode, fed with H_2 , served as the counter and the reference electrode. $E = 0.400 \text{ V}$ vs. DHE. The uncompensated resistance has been removed from the Nyquist diagrams.

Table 4.18 Performances of single DMFCs using PtRu anode and Pt cathode unsupported catalysts at 0.400 V .

Methanol conc.	Oxidant (P / atm)	T_{cell} / $^\circ\text{C}$	Anode loading / $\text{mg}_{\text{PtRu}} \text{ cm}^{-2}$	Cathode loading / $\text{mg}_{\text{Pt}} \text{ cm}^{-2}$	j / mA cm^{-2}	P / mW cm^{-2}	P_m / $\text{mW mg}_{(\text{PtRu} + \text{Pt})}^{-1}$	Reference
0.5	Air (1.76)	60	8	6	155	62.0	4.40	[246]
1	Air (1)	64	3.9	2.3	76	30.4	4.90	[240]
1	Air (1.05)	55	10	8	141	56.5	3.11	[241]
1	Air (1)	80	3	2	200	80.0	16.0	[242]
2	Air (1)	60	4	4	148	59.0	7.40	This work

To determine the pseudo-double layer capacitances, C_{pdl} , cyclic voltammograms corresponding to the methanol electrooxidation on anodes prepared with different organic solvents, were registered in MEA environment at 0.002, 0.005, 0.010, and 0.020 V s^{-1} . The charging current density, j_{pdl} , was taken at an electrode potential of 0.200 V, at which the current density increased linearly with the scan rate. Values of C_{pdl} were

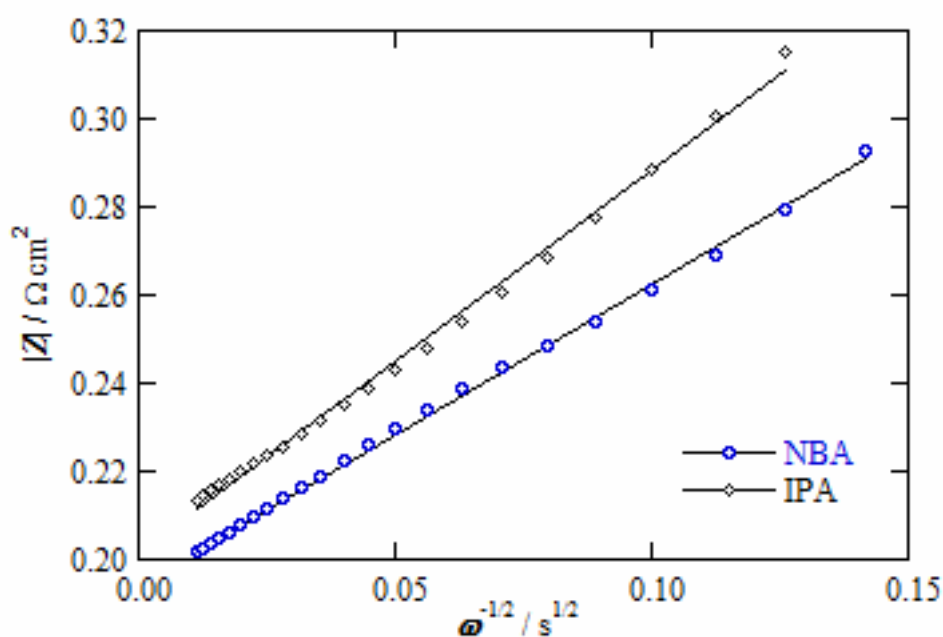


Figure 4.51 $|Z|$ vs. $\omega^{-1/2}$ plots from impedance data taken from Fig. 4.48, corresponding to the PtRu black anodes manufactured using (○) NBA and (◇) IPA solvents.

calculated according to Eq. (4.10) and summarized in Table 4.19. Fig. 4.51 shows the modulus of the impedance, $|Z|$, vs. $\omega^{-1/2}$ of Nyquist diagrams in Fig. 4.50. Good straight lines with linear regression coefficient $r \geq 0.999$ were always found in the region of frequencies from 1258.92 to 7.94 Hz. This frequency range was chosen to minimize the influence of the faradaic process on $|Z|$. Linear slopes K and R_p values have been determined from Eqs. (4.11) and (4.12), respectively, and are also shown in Table 4.19. According to these results, the proton resistance in the anode catalyst layer formulated

Table 4.19 Fitting parameters obtained from the transmission line equivalent circuit for the methanol oxidation on a DMFC anode catalyst layer in the fuel cell [229].

solvent	C_{pdl} / F cm ⁻²	K / cm ² F ^{-1/2}	R_p / Ω cm ²
NBA	0.388	0.680	0.179
IPA	0.423	0.864	0.316

with NBA is approx. 43.4 % lower than that in the anode catalyst layer formulated with IPA. This indicates that the accessible active sites, in a greater amount for NBA than for IPA, are well connected with the ionomers, so that the protons produced during the methanol oxidation with NBA can be easier transported from the active sites to the membrane.

5. Conclusions

5.1 TiO₂ based supports

1. Nb-doped TiO₂ (Nb-TiO₂) and Nb-doped TiO₂ nanotubes (Nb-TNT) with different Nb-concentrations (0, 3, 6 and 10 at. % Nb vs. Ti) were synthesized and characterized as of electrocatalysts for hydrogen evolution reaction (HER), and oxygen evolution reaction (OER) in polymer electrolyte membrane (PEM) water electrolyzers (PEMWE).

2. Textural properties of TiO₂ based supports were suitable for Pt deposition. The specific surface areas of the TNT and Nb-TNT supports were in the range 150-300 m² g⁻¹, and those obtained for TiO₂ and Nb-TiO₂ were in the range 80-100 m² g⁻¹.

3. The conductivity of TiO₂ based materials at room temperature was in the range of 0.6 to 41 μS cm⁻¹ for the different Nb concentrations. However, in this investigation no correlation between the Nb concentration and the conductivity was found.

5.2 Hydrogen evolution catalyst development

4. Pt was deposited onto TiO₂ and Nb-TiO₂ and TNT and Nb-TNT supports as catalyst for the HER. X-ray photoelectron spectroscopy confirmed the existence of strong metal-support interactions (SMSI).

5. The electrochemical performance of the supported Pt catalysts was evaluated for the HER in 0.50 mol dm⁻³ H₂SO₄. Catalysts showed good activity towards HER compared with the state of the art. The highest activity was found to correspond to the Pt/3Nb-TNT catalyst.

5.3 Oxygen evolution catalyst development

6. IrO₂ and IrRuO_x were supported onto TNTs and Nb-TNTs. The resulting materials were tested toward OER in 0.50 mol dm⁻³ H₂SO₄. It was found that the available sites for the crystallite nucleation influenced the crystallite size of the supported catalysts.

7. The deposition of IrO₂ and IrRuO_x onto the supports led to an increase in the total amount of active sites on the catalyst surface, thus resulting in a better OER performance.

8. The presence of Nb increased the sensitivity to oxygen in terms of better onset potential toward oxygen evolution.

5.4 MEA preparation and performance for PEMWE

9. A new low temperature decal method was developed to manufacture CCM type MEAs. Complete transfer of the catalyst layer from decal substrate onto the membrane (Nafion[®] 115) was achieved at 80 bar and 135 °C. Pt loading on the cathode was optimized to 0.5 mg_{Pt} cm⁻² and anode catalyst loading was optimized to 2 mg_{oxide} cm⁻².

10. 50 wt. % IrO₂/Nb-TNT catalyst showed better performance when compared to IrRuO_x and IrO₂, using the same MEA composition and operating conditions. The best performance of the MEA for the low temperature electrolyser corresponded to cell voltages at 100 and 500 mA cm⁻² of: 1.430 and 1.494 V at 80 °C; and 1.407 and 1.468 V at 90 °C.

11. Cost estimation revealed that the cost of 50 wt.% IrO₂/3Nb-TNT was 49% lower in comparison to IrO₂ black.

5.5 Electrode preparation and methanol electrooxidation

reaction

12. The catalyst inks prepared with n-butyl acetate (NBA) were composed of PtRu-Nafion[®] agglomerates, which were greater in size than in the inks with IPA. This influences the textural properties of catalyst layers, having them higher porosity.

13. From linear sweep voltammetry experiments in three-electrode cell it can be concluded that CLs prepared with NBA show higher performance towards methanol oxidation than those prepared with IPA, due to facilitated mass transport and high surface active area.

5.6 MEAs preparation and DMFC performance

14. The solvent used in the anode CLs affects the MEA performance, because mass transport limitations and catalyst utilization. Thus, the current densities of Pt and PtRu catalysts prepared with NBA were about twice the current densities of the same MEAs with catalyst layers prepared with IPA. Peak power densities of 95 and 40 mW cm⁻² were obtained at current densities of 370 and 150 mA cm⁻² for NBA and IPA, respectively.

15. The proton resistance in the anode catalyst layer formulated with NBA was about 43% lower than that formulated with IPA, thus indicating that the accessible active sites, in a greater amount for NBA, were well connected to Nafion[®] and easier transported from the active sites to the membrane.

6. References

- [1] D. Stolten (Ed.). Hydrogen and Fuel Cells. Fundamentals, Technologies and Applications. WILEY-VCH Verlag GmbH 2010.
- [2] G. A. Olah, A. Goepfert, G. K. S. Prakash. Beyond oil and gas: The methanol economy. WILEY-VCH Verlag GmbH 2006.
- [3] P. Nikolaidis, A. Poullikkas. A comparative overview of hydrogen production processes. *Renew Sust Energ Rev* 67 (2017) 597–611.
- [4] M. Carmo, D. L. Fritz, J. Mergel, D. Stolten. A comprehensive review on PEM water electrolysis. *Int J Hydrogen energy* 38 (2013) 4901-4934.
- [5] S. P. S. Badwal, S. Giddey, F. T. Ciacchi. Hydrogen and oxygen generation with polymer electrolyte membrane (PEM)-based electrolytic technology. *Ionics* 12 (2006) 7–14.
- [6] P. Barbaro, C. Bianchini (Ed.). Catalysis for Sustainable Energy Production. WILEY-VCH Verlag GmbH 2009.
- [7] S. A. Grigoriev, V. I. Poremsky, V.N. Fateev. Pure hydrogen production by PEM electrolysis for hydrogen energy. *Int J Hydrogen Energy* 31 (2006) 171-175.
- [8] S. A. Grigoriev, P. Millet, V. N. Fateev. Evaluation of carbon-supported Pt and Pd nanoparticles for the hydrogen evolution reaction in PEM water electrolyzers. *J Power Sources* 177 (2008) 281-285.
- [9] S. A. Grigoriev, P. Millet, S. V. Korobtsev, V. I. Poremskiy, M. Pepic, C. Etiévant, C. Puyenchet, V. N. Fateev. Hydrogen safety aspects related to high-pressure polymer electrolyte membrane water electrolysis. *Int J Hydrogen Energy* 34 (2009) 5986-5991.
- [10] D. Bessarabov, H. Wang, H. Li, N. Zhao. PEM Electrolysis for Hydrogen Production: Principles and Applications, CRC press 2017, p. 14.

- [11] F. J. Salzano, G. Skaperdas, A. Mezzina. Water vapor electrolysis at high temperature: Systems considerations and benefits. *Int J Hydrogen Energy* 10 (1985) 801-809.
- [12] R. L. LeRoy, C. T. Bowen, D. J. Leroy. The Thermodynamics Of Aqueous Water Electrolysis. *J Electrochem Soc* 127 (1980) 1954-1962.
- [13] P. Millet, R. Ngameni, S. A. Grigoriev, N. Mbemba, F. Brisset, A. Ranjbari, C. Etiévant. PEM water electrolyzers: From electrocatalysis to stack development. *Int J Hydrogen Energy* 35 (2010) 5043-5052.
- [14] J. R. Elliott, M. Gleiser. *Thermochemistry for Steel-making*. Addison-Wesley, Reading, Massachusetts, 1: p. 176. 1960
- [15] I. Barin. *Thermochemical data of pure substances*. VCH, New York, 3rd edition, 1995.
- [16] S. Trasatti (Ed.). *Electrodes of conductive metallic oxides. Part B*. Elsevier Scientific, 1980.
- [17] Md M. Rashid, M.K. Al Mesfer, H. Naseem, M. Danish. Hydrogen production by water electrolysis: A review of alkaline water electrolysis, PEM water electrolysis and high temperature water electrolysis. *International Journal of Engineering and Advanced Technology* 4 (2015) 80-93.
- [18] H. Y. Jung, S. Y. Huang, P. Ganesan, B. N. Popov. Performance of gold-coated titanium bipolar plates in unitized regenerative fuel cell operation. *J Power Sources* 194 (2009) 972-975.
- [19] S. A. Grigoriev, P. Millet, S. A. Volobuev, V. N. Fateev. Optimization of porous current collectors for PEM water electrolyzers. *Int J Hydrogen Energy* 34 (2009) 4968-4973.

- [20] P. Millet, F. Andolfatto, R. Durand. Design and performance of a solid polymer electrolyte water electrolyzer. *Int J Hydrogen Energy* 21 (1996) 87-93.
- [21] P. Millet, A. Ranjbari, F. de Guglielmo, S. A. Grigoriev, F. Auprêtre. Cell failure mechanisms in PEM water electrolyzers. *Int J Hydrogen Energy* 37 (2012) 17478-17487.
- [22] V. Mehta, J. S. Cooper. Review and analysis of PEM fuel cell design and manufacturing. *J Power Sources* 114 (2003) 32-53.
- [23] A. Hermann, T. Chaudhuri, P. Spagnol. Bipolar plates for PEM fuel cells: A review. *Int J Hydrogen Energy* 30 (2005) 1297-1302.
- [24] R. L. Borup, N. E. Vanderborgh. Design and testing criteria for bipolar plate material for PEM fuel cell applications. *Mater Res Soc Symp Proc* 393 (1995) 151-155.
- [25] S. K. Kamarudin, F. Achmad, W. R. W. Daud. Review: Overview on the application of direct methanol fuel cell (DMFC) for portable electronic devices. *Int J Hydrogen Energy* 34 (2009) 6902–6916.
- [26] Y. M. Ferng, A. Su. A three-dimensional full-cell CFD model used to investigate the effects of different flow channel designs on PEMFC performance. *Int. J. Hydrogen Energy* 32 (2007) 4466–4476.
- [27] T. Swamy, E.C. Kumbur, M.M. Mench. Investigation of bipolar plate and diffusion media interfacial structure in PEFCs: a fractal geometry approach. *Electrochim Acta* 56 (2011) 3060-3070.
- [28] J. Nie, Y. Chen. Numerical modeling of three-dimensional two-phase gas-liquid flow in the flow field plate of a PEM electrolysis cells. *Int J Hydrogen Energy* 35 (2010) 3183-3197.
- [29] K. Darowicki, J. Orlikowski. Impedance Investigations of the Mechanism of Oxygen Evolution on Composite Electrodes. *J. Electrochem. Soc* 146 (1999) 663-668.

- [30] F. Marangio, M. Pagani, M. Santarelli, M. Cali, Concept of a high pressure PEM electrolyser prototype. *Int. J. Hydrogen Energy* 36 (2011) 7807-7815.
- [31] L. A. Da Silva, V. A. Alves, M. A. P. Da Silva, S. Trasatti, J. F. C. Boodts. Oxygen evolution in acid solution on IrO₂ + TiO₂ ceramic films. A study by impedance, voltammetry and SEM. *Electrochim Acta* 42 (1997) 271-281.
- [32] E. Rasten, G. Hagen, R. Tunold. Electrocatalysis in water electrolysis with solid polymer electrolyte. *Electrochim Acta* 48 (2003) 3945-3952.
- [33] A. T. Marshall, R.G. Haverkamp. Production of hydrogen by the electrochemical reforming of glycerol–water solutions in a PEM electrolysis cell. *Int J Hydrogen Energy* 33 (2008) 4649-4654.
- [34] P. Millet, N. Mbemba, S. A. Grigoriev, V. N. Fateev, A. Aukauloo, C. Etiévant. Electrochemical performances of PEM water electrolysis cells and perspectives. *Int J Hydrogen Energy* 36 (2011) 4134-4142.
- [35] C-. H. Kim, K-. S. Sim, K-. B. Park. Hydrogen Production from Water using Polymer Electrolyte Membrane Conference Proceedings.
- [36] A. T. Marshall, S. Sunde, M. Tsykin, R. Tunold. Performance of a PEM water electrolysis cell using Ir_xRu_yTa_zO₂ electrocatalysts for the oxygen evolution electrode. *Int J Hydrogen Energy* 32 (2007) 2320-2324.
- [37] T. Audichon, E. Mayousse, S. Morisset, C. Morais, C. Comminges, T. W. Napporn, K. B. Kokoh. Electroactivity of RuO₂-IrO₂ mixed nanocatalysts toward the oxygen evolution reaction in a water electrolyzer supplied by a solar profile. *Int J Hydrogen Energy* 39 (2014) 16785-16796.
- [38] S. Siracusano, N. Van Dijk, E. Payne-Johnson, V. Baglio, A. S. Aricò. Nanosized IrO_x and IrRuO_x electrocatalysts for the O₂ evolution reaction in PEM water electrolyzers. *Appl Catal B: Environmental* 164 (2015) 488–495.

[39] G. Wei, Y. Wang, Ch. Huang, Q. Gao, Z. Wang, L. Xu. The stability of MEA in SPE water electrolysis for hydrogen production. *Int J Hydrogen Energy* 35 (2010) 3951-3957.

[40] S. Siracusano, V. Baglio, A. Di Blasi, N. Briguglio, A. Stassi, R. Ornelas, E. Trifoni, V. Antonucci, A. S. Aricò. Electrochemical characterization of single cell and short stack PEM electrolyzers based on a nanosized IrO₂ anode electrocatalyst. *Int J Hydrogen Energy* 35 (2010) 5558-5568.

[41] V. Baglio, A. D. Blasi, T. Denaro, V. Antonucci, A. S. Aricò, R. Ornelas, F. Matteucci, G. Alonso, L. Morales, G. Orozco, L. G. Arriaga. Synthesis, characterization and evaluation of IrO₂-RuO₂ electrocatalytic powders for oxygen evolution reaction. *J New Mat Electr Sys* 11 (2008) 105-108.

[42] A. Di Blasi, C. D'Urso, V. Baglio, V. Antonucci, R. Ornelas, F. Matteucci, G. Orozco, D. Beltran, Y. Meas, L. G. Arriaga. Preparation and evaluation of RuO₂-IrO₂, IrO₂-Pt and IrO₂-Ta₂O₅ catalysts for the oxygen evolution reaction in an SPE electrolyzer. *J Appl Electrochem* 39 (2009) 191-196.

[43] J. C. Cruz, V. Baglio, S. Siracusano, R. Ornelas, L. Ortiz-Frade, L. G. Arriaga, V. Antonucci, A. S. Aricò. Nanosized IrO₂ electrocatalysts for oxygen evolution reaction in an SPE electrolyzer. *J Nanopart Res* 13 (2011)1639-1646.

[44] L. Ma, S. Sui, Y. Zhai. Investigations on high performance proton exchange membrane water electrolyzer. *Int J Hydrogen Energy* 34 (2009) 678-684.

[45] D. Labou, E. Slavcheva, U. Schnakenberg, S. Neophytides. Performance of laboratory polymer electrolyte membrane hydrogen generator with sputtered iridium oxide anode. *J Power Sources* 185 (2008) 1073-1078.

[46] G. Wei, L. Xu, C. Huang, Y. Wang. SPE water electrolysis with SPEEK/PES blend membrane. *Int J Hydrogen Energy* 35 (2010) 7778-7783.

- [47] H. Ito, T. Maeda, A. Nakano, H. Takenaka. Properties of Nafion membranes under PEM water electrolysis conditions. *Int J Hydrogen Energy* 36 (2011) 10527-10540.
- [48] M. Bass, V. Freger. Hydration of Nafion and Dowex in liquid and vapor environment: Schroeder's paradox and microstructure. *Polymer* 49 (2008) 497-506.
- [49] L. Onishi, J. Prausnitz, J. Newman. Water-Nafion equilibria. Absence of Schroeder's paradox. *J Phys Chem* 111 (2007) 10166-10173.
- [50] K. T. Park, U. H. Jung, D. W. Choi, K. Chun, H.M. Lee, S. H. Kim. ZrO₂-SiO₂/Nafion (R) composite membrane for polymer electrolyte membrane fuel cells operation at high temperature and low humidity. *J Power Sources* 177 (2008) 247-253.
- [51] H. L. Lin, S. H. Yeh, T. L. Yu, L. C. Chen. Silicate and zirconium phosphate modified Nafion/PTFE composite membranes for high temperature PEMFC. *J Polym Res* 16 (2009) 519-527.
- [52] N. H. Jalani, K. Dunn, R. Datta. Synthesis and characterization of Nafion (R)-MO₂ (M = Zr, Si, Ti) nanocomposite membranes for higher temperature PEM fuel cells. *Electrochim Acta* 51 (2005) 553-560.
- [53] V. Antonucci, A. Di Blasi, V. Baglio, R. Ornelas, F. Matteucci, J. Ledesma-Garcia, L.G. Arriaga, A.S. Aricò. High temperature operation of a composite membrane-based solid polymer electrolyte water electrolyser. *Electrochim Acta* 53 (2008) 7350-7356.
- [54] V. Baglio, R. Ornelas, F. Matteucci, F. Martina, G. Ciccarella, I. Zama, L. G. Arriaga, V. Antonucci, A. S. Aricò. Solid Polymer Electrolyte Water Electrolyser Based on Nafion-TiO₂ Composite Membrane for High Temperature Operation. *Fuel Cells* 9 (2009) 247-252.

[55] A. Sacca, I. Gatto, A. Carbone, R. Pedicini, E. Passalacqua. ZrO₂-Nafion composite membranes for polymer electrolyte fuel cells (PEFCs) at intermediate temperature. *J Power Sources* 163 (2006) 47-51.

[56] K. Li, G. Ye, J. Pan, H. Zhang, M. Pan. Self-assembled Nafion[®]/metal oxide nanoparticles hybrid proton exchange membranes. *J Membr Sci* 347 (2010) 26-31.

[57] Z. Wang, H. Tang, H. Zhang, M. Lei, R. Chen, P. Xiao, M. Pan. Synthesis of Nafion/CeO₂ hybrid for chemically durable proton exchange membrane of fuel cell. *J Membr Sci* 421–422 (2012) 201-210.

[58] G. Qian, D. W. Smith Jr, B. C. Benicewicz. Synthesis and characterization of high molecular weight perfluorocyclobutyl-containing polybenzimidazoles (PFCB-PBI) for high temperature polymer electrolyte membrane fuel cells. *Polymer* 50 (2009) 3911-3916.

[59] J. S. Wainright, J. -T. Wang, D. Weng, R. F. Savinell, M. Litt. Acid-Doped Polybenzimidazoles: A New Polymer Electrolyte. *J Electrochem Soc* 142 (1995) L121-L123.

[60] R. Bouchet, E. Siebert. Proton conduction in acid doped polybenzimidazole. *Solid State Ionics* 118 (1999) 287-299.

[61] J. T. Wang, R. F. Savinell, J. Wainright, M. Litt, H. Yu. A H₂/O₂ fuel cell using acid doped polybenzimidazole as polymer electrolyte. *Electrochim Acta* 41 (1996) 193-197.

[62] S. J. Paddison, K. D. Kreuer, J. Maier. About the choice of the protogenic group in polymer electrolyte membranes: Ab initio modelling of sulfonic acid, phosphonic acid, and imidazole functionalized alkanes. *Phys Chem* 8 (2006) 4530-4542.

[63] E. K. Pefkianakis, V. Deimede, M. K. Daletou, N. Gourdoupi, J. K. Kallitsis. Novel polymer electrolyte membrane, based on pyridine containing poly(ether sulfone), for application in high-temperature fuel cells. *Macromol Rapid Commun* 26 (2005) 1724-1728.

[64] J. P. Shin, B. J. Chang, J. H. Kim, S. B. Lee, D. H. Suh. Sulfonated polystyrene/PTFE composite membranes. *J Membr Sci* 251 (2005) 247-254.

[65] S. Trasatti. Work function, electronegativity, and electrochemical behaviour of metals: III. Electrolytic hydrogen evolution in acid solutions. *J Electroanal Chem Interfacial Electrochem* 39 (1972) 163–184.

[66] B. E. Conway, G. Jerkiewicz. Relation of energies and coverages of underpotential and overpotential deposited H at Pt and other metals to the 'vulcano curve' for cathodic H₂ evolution kinetics. *Electrochim Acta* 45 (2000) 4075–4083

[67] H. D. Nguyen, T. T. L. Nguyen, K. M. Nguyen, T. H. Ha, Q. H. Nguyen. Preparation of the Vulcan XC-72R-supported Pt nanoparticles for the hydrogen evolution reaction in PEM water electrolyzers. *Adv Nat Sci Nanosci Nanotechnol* 6 (2015) 025012-025017.

[68] S. A. Grigoriev, V. N. Fateev, H. Middleton, T. O. Saetre, P. Millet. A comparative evaluation of palladium and platinum nanoparticles as catalysts in proton exchange membrane electrochemical cells. *Int J Nuclear Hydrogen Production and Application* 1 (2008) 343-354.

[69] S. A. Grigoriev, M. S. Mamat, K. A. Dzhus, G. S. Walker, P. Millet. Platinum and palladium nano-particles supported by graphitic nano-fibers as catalysts for PEM water electrolysis. *Int J Hydrogen Energy* 36 (2011) 4143-4147.

[70] O. Pantani, E. Anxolabéhère-Mallart, A. Aukauloo, P. Millet. Electroactivity of cobalt and nickel glyoximes with regard to the electro-reduction of protons into molecular hydrogen in acidic media. *Electrochem Commun* 9 (2007) 54-58.

[71] B. Hinnemann, P. G. Moses, J. Bonde, K. P. Jørgensen, J. H. Nielsen, S. Horch, I. Chorkendorff, J. K. Nørskov. Biomimetic hydrogen evolution: MoS₂ nanoparticles as catalyst for hydrogen evolution. *J Am Chem Soc* 127 (2005) 5308-5309.

[72] Y. G. Li, H. L. Wang, L. M. Xie, Y. Y. Liang, G. S. Hong, H. J. Dai. MoS₂ nanoparticles grown on graphene: An advanced catalyst for the hydrogen evolution reaction. *J Am Chem Soc* 133 (2011) 7296-7299.

[73] A. Phuruangrat, D. J. Ham, S. Thongtem, J. S. Lee. Electrochemical hydrogen evolution over MoO₃ nanowires produced by microwave-assisted hydrothermal reaction. *Electrochem Commun* 11 (2009) 1740-1743.

[74] R. K. Selvan, A. Gedanken. The sonochemical synthesis and characterization of Cu(1-x)Ni(x)WO₄ nanoparticles/nanorods and their application in electrocatalytic hydrogen evolution. *Nanotech* 20 (2009) 105602.

[75] W. L. Xu, C. P. Liu, W. Xing, T. H. Lu. A novel hybrid based on carbon nanotubes and heteropolyanions as effective catalyst for hydrogen evolution. *Electrochem Commun* 9 (2007) 180-184.

[76] J. Rajeswari, P. S. Kishore, B. Viswanathan, T. K. Varadarajan. Facile hydrogen evolution reaction on WO₃ nanorods. *Nanoscale Res Lett* 2 (2007) 496-503.

[77] H. T. Zheng, M. Mathe. Hydrogen evolution reaction on single crystal WO₃/C nanoparticles supported on carbon in acid and alkaline solution. *Int J Hydrogen Energy* 36 (2011) 1960-1964.

[78] N. Yousfi-Steiner, Ph. Moçotéguy, D. Candusso, D. Hissel. A review on polymer electrolyte membrane fuel cell catalyst degradation and starvation issues Causes, consequences and diagnostic for mitigation. *J Power Sources* 194 (2009) 130–145.

[79] S. Zhang, X.-Z. Yuan, J. Ng Cheng Hin, H. Wang, K. Andreas Friedrich, M. Schulze. A review of platinum-based catalyst layer degradation in proton exchange membrane fuel cells. *J Power Sources* 194 (2009) 588–600.

[80] H. Wendt, V. Plzak. Electrocatalysis and electrocatalysts for cathodic evolution and anodic oxidation of hydrogen. H. Wendt (Ed), *Electrochemical hydrogen technologies*. Elsevier, 1990, p.15

[81] S. Trasatti. Electrocatalysis in the anodic evolution of oxygen and chlorine. *Electrochim Acta* 29 (1984) 1503-1512.

[82] J. O'M. Bockris. Kinetics of activation controlled consecutive electrochemical reactions: anodic evolution of oxygen. *J Chem Phys* 24 (1956) 817.

[83] L. A. DeFaria, J. F. C. Boodts, S. Trasatti. Electrocatalytic properties of ternary oxide mixtures of composition $\text{Ru}_{0.3}\text{Ti}_{(0.7-x)}\text{Ce}_x\text{O}_2$: oxygen evolution from acidic solution. *J Appl Electrochem* 26 (1996) 1195-1199.

[84] E. Tsuji, A. Imanishi, F. Ken-ichi, Y. Nakato. Electrocatalytic activity of amorphous RuO_2 electrode for oxygen evolution in an aqueous solution. *Electrochim Acta* 56 (2011) 2009-2016.

[85] S. Siracusano, V. Baglio, C. D'Urso, V. Antonucci, A. S. Aricò. Preparation and characterization of titanium suboxides as conductive supports of IrO_2 electrocatalysts for application in SPE electrolyzers. *Electrochim Acta* 54 (2009) 6292–6299.

[86] J.-M. Hu, J.-Q. Zhang, C.-N. Cao. Oxygen evolution reaction on IrO₂-based DSA[®] type electrodes: kinetics analysis of Tafel lines and EIS. *Int J Hydrogen Energy* 29 (2004) 791-797.

[87] T. Reier, D. Teschner, T. Lunkenbein, A. Bergmann, S. Selve, R. Kraehnert, R. Schlögl, P. Strasser. Electrocatalytic Oxygen Evolution on Iridium Oxide: Uncovering Catalyst-Substrate Interactions and Active Iridium Oxide Species. *J Electrochem Soc* 161 (2014) F876-F882.

[88] L. Ouattara, S. Fierro, O. Frey, M. Koudelka, C. Comninellis. Electrochemical comparison of IrO₂ prepared by anodic oxidation of pure iridium and IrO₂ prepared by thermal decomposition of H₂IrCl₆ precursor solution. *J Appl Electrochem* 39 (2009) 1361–1367.

[89] S. Song, H. Zhang, X. Ma, Z. Shao, R. T. Baker, B. Yi. Electrochemical investigation of electrocatalysts for the oxygen evolution reaction in PEM water electrolyzers. *Int J Hydrogen Energy* 33 (2008) 4955-4961.

[90] J. Xu, Q. Li, M. K. Hansen, E. Christensen, A. L. T. García, G. Liu, X. Wang, N. J. Bjerrum. Antimony doped tin oxides and their composites with tin pyrophosphates as catalyst supports for oxygen evolution reaction in proton exchange membrane water electrolysis. *Int J Hydrogen Energy* 37 (2012) 18629-18640.

[91] A. Marshall, B. Børrensen, G. Hagen, M. Tsytkin, R. Tunold. Electrochemical characterization of Ir_xSn_{1-x}O₂ powders as oxygen evolution electrocatalysts. *Electrochim Acta* 51 (2006) 3161-3167.

[92] J. L. Corona-Guinto, L. Cardeño-García, D. C. Martínez-Casillas, J. M. Sandoval-Pineda, P. Tamayo-Meza, R. Silva-Casarin, R. G. González-Huerta. Performance of a PEM electrolyzer using RuIrCoO_x electrocatalysts for the oxygen evolution electrode. *Int J Hydrogen Energy* 38 (2013) 12667-12673.

[93] V. K. Puthiyapura, S. Pasupathi, S. Basu, X. Wua, H. Su, N Varagunapandiyam, B Pollet, K Scott. Ru_xNb_{1-x}O₂ catalyst for the oxygen evolution reaction in proton exchange membrane water electrolyzers. *Int J Hydrogen Energy* 38 (2013) 8605-8616.

[94] A. Zlotorowicz, F. Seland, S. Sunde. Composite Thin Film Iridium- Niobium Oxide Electrocatalysts for the Oxygen Evolution Electrode. *ECS Trans* 50 (2013)71-84

[95] V. K. Puthiyapura, S. Pasupathi, H. Su, X. Liu, B. Pollet, K. Scott. Investigation of supported IrO₂ as electrocatalyst for the oxygen evolution reaction in proton exchange membrane water electrolyser. *Int J Hydrogen Energy* 39 (2014) 1905-1913.

[96] P. Mazúr, J. Polonský, M. Paidar, K. Bouzek. Non-conductive TiO₂ as the anode catalyst support for PEM water electrolysis. *Int J Hydrogen Energy* 37 (2012) 12081-12088.

[97] W. Hu, S. Chen, Q. Xia. IrO₂/Nb-TiO₂ electrocatalyst for oxygen evolution reaction in acidic medium. *Int J Hydrogen Energy* 39 (2014) 6967-6976.

[98] S. Sharma, B. G. Pollet. Support materials for PEMFC and DMFC electrocatalysts – A review. *J Power Sources* 208 (2012) 96 – 112.

[99] Y-. C. Nah, I. Paramasivam, P. Schmuki. Doped TiO₂ and TiO₂ nanotubes: Synthesis and applications. *Chem Phys Chem* 11(2010) 2698-2713.

[100] H. Chhina, S. Campbell, O. Kesler. Ex Situ and In Situ stability of Platinum supported on Niobium–doped titania for PEMFCs. *J Electrochem Soc* 156 (2009) B1232-B1237.

[101] A. Trenczek-Zajac, M. Rekas. Electrical Properties of Nb-doped titanium dioxide TiO₂ at room temperature. *Mater Sci–Poland* 24 (2006) 53-60.

[102] O. K. Varghese, D. Gong, M. Paulode, K. G. Ong, E. C. Dickey, C. A. Grimes. Extreme changes in the electrical resistance of titania nanotubes with hydrogen exposure. *Adv Mater* 15 (2003) 624-627.

[103] E. Sotter, X. Vilanova, E. Llobet, M. Stankova, X. Correig. Niobium-doped titania nanopowders for gas sensor applications. *J Optoelectron Adv M* 7 (2005) 1395-1398.

[104] N. R. Elezović, B. M. Babić, L. Gajić-Krstajić, V. Radmilović, N. V. Krstajić, L. J. Vračar. Synthesis, characterization and electrocatalytical behavior of Nb-TiO₂/Pt nanocatalyst for oxygen reduction reaction. *J Power Sources* 195 (2010) 3961-3968.

[105] S. L. Gojković, B. M. Babić, V. R. Radmilović, V. N. Krstajić. Nb-doped TiO₂ as a support of Pt and Pt-Ru anode catalyst for PEMFCs. *J Electroanal Chem* 639 (2010) 161-166.

[106] C. L. Wong, Y. N. Tan, A. R. Mohamed. A Review on the formation of titania nanotube photocatalysts by hydrothermal treatment. *J Environ Manage* 92 (2011) 1669-1680.

[107] G. Chen, S. R. Bare, T. E. Mallouk. Development of supported bifunctional electrocatalysts for unitized regenerative fuel cells. *J Electrochem Soc* 149 (2002) A1092-A1099.

[108] R. Asmatulu, A. Karthikeyan, D. C. Bell, S. Ramanathan, M. J. Aziz. Synthesis and variable temperatures electrical conductivity studies of highly ordered TiO₂ nanotubes. *J Mater Sci* 44 (2009) 4613-4616.

[109] Y. Fu, Z. D. Wei, S. G. Chen, L. Li, Y. C. Feng, Y. Q. Wang, X. L. Ma, M. J. Liao, P. K. Shen, S. P. Jiang. Synthesis of Pd/TiO₂ nanotubes/Ti foil for oxygen reduction reaction in acidic solution. *J Power Sources* 189 (2009) 982-987.

[110] T. Kasuga, M. Hiramatsu, A. Hoson, T. Sekino, K. Niihara. Formation of titanium oxide nanotube. *Langmuir* 14 (1998) 3160-3163.

[111] T. Kasuga. Formation of titanium oxide nanotubes using treatments and their characteristic properties. *Thin Solid Films* 496 (2006) 141-145.

[112] C. K. Lee, S. S. Liu, H. C. Chen. Applications of hydrothermal method derived titanate nanotubes as adsorbents. *Recent Pat Nanotechnol* 3 (2009) 203-212.

[113] B. Poudel, W. Z. Wang, C. Dames, J. Y. Huang, S. Kunwar, D. Z. Wang, D. Banerjee, G. Chen, Z. F. Ren. Formation of crystallized titania nanotubes and their transformation into nanowires. *Nanotechnology* 16 (2005) 1935-1940.

[114] A. Tighineanu, T. Ruff, S. Albu, R. Hahn, P. Schmuki. Conductivity of TiO₂ nanotubes: Influence of annealing time and temperature. *Chem Phys Lett* 494 (2010) 260-263.

[115] J. Shim, C. R. Lee, H. K. Lee, J. S. Lee, E. J. Cairns. Electrochemical characteristics of Pt-WO₃/C and Pt-TiO₂/C electrocatalysts in a polymer electrolyte fuel cell, *J Power Sources* 102 (2001) 172-177.

[116] L. Xiong, A. Manthiram. Synthesis and characterization of methanol tolerant Pt/TiO_x/C nanocomposites for oxygen reduction in direct methanol fuel cells. *Electrochim Acta* 49 (2004) 4163-4170.

[117] M. Gustavsson, H. Ekström, P. Hanarp, L. Eurenus, G. Lindbergh, E. Olsson, B. Kasemo. Thin film Pt/TiO₂ catalysts for the polymer electrolyte fuel cell. *J Power Sources* 163 (2007) 671-678.

[118] A. Lewera, L. Timperman, A. Roguska, N. Alonso-Vante. Metal support interactions between nanosized Pt and metal oxides (WO₃ and TiO₂) studied using X-ray photoelectron spectroscopy. *J Phys Chem C* 115 (2011) 20153-20159.

- [119] J. H. Cho, J. M. Kim, J. Prabhuram, S. Y. Hwang, D. J. Ahn, H. Y. Ha, S.-K. Kim. Fabrication and evaluation of membrane electrode assemblies by low-temperature decal methods for direct methanol fuel cells. *J Power Sources* 187 (2009) 378-386.
- [120] N. N. Krishnan, J. Prabhuram, Y. T. Hong, H. J. Kim, K. Yoon, H. Y. Ha, T. H. Lim, S. K. Kim. Fabrication of MEA with hydrocarbon based membranes using low temperature decal method for DMFC. *Int J Hydrogen Energy* 35 (2010) 5647-5655.
- [121] H. Su, B. J. Bladergroen, S. Pasupathi, V. Linkov, S. Ji. Performance Investigation of Membrane Electrode Assemblies for Hydrogen Production by Solid Polymer Electrolyte Water Electrolysis. *Int J Electrochem Sci* 7 (2012) 4223 – 4234.
- [122] M. Bernt, H. A. Gasteiger. Influence of Ionomer Content in IrO₂/TiO₂ Electrodes on PEM Water Electrolyzer Performance. *J The Electrochem Soc* 163 (2016) F3179-F3189.
- [123] W. Xu, K. Scott. The effect of ionomer content on PEM water electrolyser membrane electrode assembly performance. *Int J Hydrogen Energy* 35 (2010) 12029-12037.
- [124] I. Parsons. Fuel cell handbook. United States of America, NY: EGG services, 2000.
- [125] K. Kordesch and G. Simader. Fuel cells and their applications. VCH Publishers, (1996).
- [126] P. W. Atkins. Physical chemistry. VCH Publishers (1990).
- [127] A. J. Joseph, A. S. Abdulkareem, A. Jimoh, A. S. Afolabi. Theoretical Energy and Exergy Analyses of Direct Methanol Fuel Cell. *Adv Mater Sci Appl* 4 (2015) 63-75.

[128] M. Sajgure, B. Kachare, P. Gawhale, S. Waghmare, G. Jagadale. Direct Methanol Fuel Cell: A Review. *International Journal of Current Engineering and Technology Special Issue-6* (Oct 2016) 8-11.

[129] P. Joghee, J. N. Malik, S. Pylypenko, R. O'Hayre. A review on direct methanol fuel cells – In the perspective of energy and sustainability. *MRS Energy & Sustainability* 2 (2015) doi:10.1557/mre.2015.4

[130] M. F. Garcia, J. M. Sieben, A. S. Pilla, M. M. E. Duarte, C. E. Mayer. Methanol/air fuel cells: catalytic aspects and experimental diagnostics. *Int J Hydrogen Energy* 33 (2008) 3517-3521.

[131] W. Z. Li, Q. Xin, Y. S Yan. Nanostructured Pt-Fe/C cathode catalysts for direct methanol fuel cell: The effect of catalyst composition. *Int J Hydrogen Energy* 35 (2010) 2530-2538.

[132] J. B. Xu, T. S. Zhao, W. W. Yang, S. Y. Shen. Effect of surface composition of Pt-Au alloy cathode catalyst on the performance of direct methanol fuel cells. *Int J Hydrogen Energy* 35 (2010) 8699-8706.

[133] E. Antolini, J. R. C. Salgado, L. G. R. A. Santos, G. Garcia, E. A. Ticianelli, E. Pastor, E. R. Gonzalez. Carbon supported Pt-Cr alloys as oxygen reduction catalysts for direct methanol fuel cells. *J Appl Electrochem* 36 (2006) 355-362.

[134] K. G. Nishanth, P. Sridhar, S. Pitchumani, A. K. Shukla. A DMFC with methanol-tolerant-carbon-supported-Pt-Pd-alloy cathode. *J Electrochem Soc* 158 (2011) B871-B876.

[135] H. Meng, P. K. Shen, Z. D. Wei, S. P. Jiang. Improved performance of direct methanol fuel cells with tungsten carbide promoted Pt/C composite cathode electrocatalyst. *Electrochem Solid-State Lett* 9 (2006) A368-A372.

[136] K.-W. Park, D.-S. Han, Y.-E. Sung. PtRh alloy nanoparticle electrocatalysts for oxygen reduction for use in direct methanol fuel cells. *J Power Sources* 163 (2006) 82–86.

[137] E. Antolini, J. R. C. Salgado, E. R. Gonzalez. The stability of Pt-m (M = first row transition metal) alloy catalysts and its effect on the activity in low temperature fuel cells: A literature review and tests on a Pt-Co catalyst. *J Power Sources* 160 (2006) 957-968.

[138] L. Xiong, A. Manthiram. Effect of atomic ordering on the catalytic activity of carbon supported PtM (M = Fe, Co, Ni, and Cu) alloys for oxygen reduction in PEMFCs. *J Electrochem Soc* 152 (2005) A697-A703.

[139] T. R. Ralph, M. P. Hogarth. Catalysis for low temperature fuel cells part I: The cathode challenges. *Platinum Met Rev* 46 (2002) 117-135.

[140] R. W. Reeve, P. A. Christensen, A. Hamnett, S. A. Haydock, S. C. Roy. Methanol tolerant oxygen reduction catalysts based on transition metal sulfides and their application to the study of methanol permeation. *Electrochim Acta* 45 (2000) 4237-4250.

[141] G. Q. Sun, J. T. Wang, R. F. Savinell. Iron(III) tetramethoxyphenylporphyrin (FeTMPP) as methanol tolerant electrocatalyst for oxygen reduction in direct methanol fuel cells. *J Appl Electrochem* 28 (1998) 1087-1093.

[142] J. Wang, R. Savinell. Simulations studies on the fuel electrode of a methanol air polymer electrolyte fuel cell. in: S. Srinivasan, D. D. Macdonald, A. C. Khandkar (Eds.). *Proceedings of the symposium on Electrode material for Energy Conversion and Storage* PV 94-23. The Electrochemical Society Proceedings Series, Pennington, NJ, 1994, p. 326.

[143] J. Guo, G. Sun, S. Sun, S. Yan, W. Yang, J. Qi, Y. Yan, Q. Xin. Polyol-synthesized PtRu/C and PtRu black for direct methanol fuel cells. *J Power Sources* 168 (2007) 299-306.

[144] M. Watanabe, S. Motoo. Electrocatalysis by ad-atoms: Part II. Enhancement of the oxidation of methanol on platinum by ruthenium ad-atoms. *J Electroanal Chem* 60 (1975) 267-273.

[145] S. Goto, N. N. Y. Li, T. Senoo, K. Noda, Y. Kudo, A. Maesaka, T. Hatazawa. PtRu nanoparticles catalytic activity enhanced by the ligand effect . *MRS Proc* 1127 (2008) DOI10.1557/PROC-1127-T07-01.

[146] Y. S. Kim, S. H. Nama, H.-S. Shim, H.-J. Ahn, M. Anand, W. B. Kim. Electrospun bimetallic nanowires of PtRh and PtRu with compositional variation for methanol electrooxidation. *Electrochem Commun* 10 (2008) 1016–1019

[147] J.- H. Choi, K.- W. Park, I.- S. Park, W.-. H. Nam, Y.-. E. Sung. Methanol electro-oxidation and direct methanol fuel cell using Pt/Rh and Pt/Ru/Rh alloy catalysts. *Electrochim Acta* 50 (2004) 787–790

[148] M. S. Ureta-Zañartu, M. Montenegro, J. H. Zagal. Methanol electro-oxidation on Pt-Rh alloy in acid medium. *Bol Soc Chil Quím* 46 (2001) 209-216.

[149] M. Götz, H. Wendt. Binary and ternary anode catalyst formulations including the elements W, Sn and Mo for PEMFCs operated on methanol or reformat gas. *Electrochim Acta* 43(1998) 3637-3644.

[150] F. Alcaide, G. Álvarez, P. L. Cabot, H.- J. Grande, O. Miguel, A. Querejeta. Testing of carbon supported Pd-Pt electrocatalysts for methanol electrooxidation in direct methanol fuel cells. *Int J Hydrogen Energy* 36(2011)4432-4439.

[151] C. Lamy, A. Lima, V. LeRhun, F. Delime, C. Coutanceau, J.- M. Léger. Recent advances in the development of direct alcohol fuel cells (DAFC). *J Power Sources* 105 (2002) 283-296.

[152] N. Yousfi-Steiner, Ph. Moçotéguy, D. Candusso, D. Hissel. A review on polymer electrolyte membrane fuel cell catalyst degradation and starvation issues: Causes, consequences and diagnostic for mitigation. *J Power Sources* 194 (2009) 130–145.

[153] Y. K. Zhou, K. Neyerlin, T. S. Olson, S. Pylypenko, J. Bult, H. N. Dinh, T. Gennett, Z. P. Shao, R. O'Hayre. Enhancement of Pt and Pt-alloy fuel cell catalyst activity and durability via nitrogen-modified carbon supports. *Energy Environ Sci* 3(2010)1437-1446.

[154] K. N. Wood, S. Pylypenko, T. S. Olson, A. A. Dameron, K. O'Neill, S. T. Christensen, H. N. Dinh, T. Gennett, R. O'Hayre. Effect of halide-modified model carbon supports on catalyst stability. *ACS Appl Mater Interfaces* 4(2012) 6727-6734.

[155] S. Pylypenko, A. Queen, T. S. Olson, A. Dameron, K. O'Neill, K. C. Neyerlin, B. Pivovar, H. N. Dinh, D. S. Ginley, T. Gennett, R. O'Hayre. Tuning carbon-based fuel cell catalyst support structures via nitrogen functionalization. II. Investigation of durability of Pt-Ru nanoparticles supported on highly oriented pyrolytic graphite model catalyst supports as a function of nitrogen implantation dose. *J Phys Chem C* 115(2011) 13667-13675.

[156] P. Kolla, K. Kerce, Y. Normah, H. Fong, A. Smirnova. Metal oxides modified mesoporous carbon supports as anode catalysts in DMFC. *ECS Trans* 45(2013)35-45.

[157] J. Prabhuram, T. S. Zhao, Z. K. Tang, R. Chen, Z. X. Liang. Multiwalled carbon nanotube supported PtRu for the anode of direct methanol fuel cells . J Phys Chem B 110(2006)5245-5252.

[158] S. Bong, Y. R. Kim, I. Kim, S. Woo, S. Uhm, J. Lee, H . Kim. Preparation and electrochemical performance of Pt/graphene nanocomposites. Electrochem Commun 11(2009)846-849.

[159] S. Kang, S. Lim, D.H. Peck, S.K. Kim, D.H. Jung, S.H. Hong, H.G. Jung, Y. Shul: Stability and durability of PtRu catalysts supported on carbon nanofibers for direct methanol fuel cells. Int J Hydrogen Energy 37(2012)4685-4693.

[160] H. Y. Lee, W. Vogel, P. P. Chu. Polyaniline Coated Active Carbon as Binary Catalysts Support for Direct Methanol Fuel Cell. ECS Transactions 19(2009)127-142.

[161] J. -F. Drillet, R. Dittmeyer, K. Jüttner. Activity and long-term stability of PEDOT as Pt catalyst support for the DMFC anode. J Appl Electrochem 37 (2007) 1219-1226.

[162] Y. -M. Tsou, L. Cao, M. Young, J. Morse. Approaches to improve durability & special applications of FC MEAs. ECS Trans 19 (31) (2009) 47-55.

[163] A. Mehmood, M. A. Scibioh, J. Prabhuram, M. -G. An, H. Y. Ha. A review on durability issues and restoration techniques in long-term operations of direct methanol fuel cells. J Power Sources 297 (2015) 224-241.

[164] S. -J. Shin, J. -K. Lee, H. -Y. Ha, S. -A. Hong, H. -S. Chun, I. -H. Oh. Effect of the catalytic ink preparation method on the performance of polymer electrolyte membrane fuel cells. J Power Sources, 106 (2002) 146-152.

[165] M. Uchida, Y. Fukuoka, Y. Sugawara, H. Ohara, A. Ohta. Improved preparation process of very-low-platinum-loading electrodes for polymer electrolyte fuel cells. *J Electrochem Soc* 145 (1998) 3708-3713.

[166] M. Chisaka, H. Daiguji. Effect of glycerol on micro nano structures of catalyst layers in polymer electrolyte membrane fuel cells. *Electrochim Acta* 51 (2006) 4828-4833.

[167] M. Uchida, Y. Aoyama, N. Eda, A. Ohta. New preparation method for polymer-electrolyte fuel cells. *J Electrochem Soc* 142 (1995) 463-468.

[168] J. Lobato, M. A. Rodrigo, J. J. Linares, K. Scott. Effect of the catalytic ink preparation method on the performance of high temperature polymer electrolyte membrane fuel cells. *J Power Sources* 157 (2006) 284-292.

[169] R. N. Bonifácio, J. O. A. Paschoal, M. Linardi, R. Cuenca. Catalyst layer optimization by surface tension control during ink formulation of membrane electrode assemblies in proton exchange membrane fuel cell. *J Power Sources* 196 (2011) 4680-4685.

[170] M. Chisaka, H. Daiguji. Effect of organic solvents on catalyst layer structure in polymer electrolyte membrane fuel cells. *J Electrochem Soc* 156 (2009) B22-B26.

[171] M. Chisaka, E. Matsuoka, H. Daiguji. Effect of organic solvents on the pore structure of catalyst layers in polymer electrolyte membrane fuel cells. *J Electrochem Soc* 157 (2010) B1218-B1221.

[172] T. -H. Yang, Y. -G. Yoon, G. -G. Park, W. -Y. Lee, C. -S. Kim. Fabrication of a thin catalyst layer using organic solvents. *J Power Sources* 127 (2004) 230-233.

[173] T. T. Ngo, T. L. Yu, H. -L. Lin. Influence of the composition of isopropyl alcohol/water mixture solvents in catalyst ink solutions on proton exchange membrane fuel cell performance. *J Power Sources* 225 (2013) 293-303.

[174] M. Uchida, Y. Aoyama, N. Eda, A. Ohta. Investigation on the microstructure in the catalyst layer and effects of both perfluorosulfonate ionomer and PTFE-loaded carbon on the catalyst layer of polymer electrolyte fuel cells. *J Electrochem Soc* 142 (1995) 4143-4149.

[175] M. Schonert, K. Jakoby, C. Schlumbohm, A. Gülsen, J. Mergel, D. Stolten. Manufacture of robust catalyst layers for the DMFC. *Fuel Cells* 4 (2004) 175-179.

[176] T. T. Ngo, T. L. Yu, H. -L. Lin. Nafion-based membrane electrode assemblies prepared from catalyst inks containing alcohol-water solvent mixtures. *J Power Sources* 238 (2013) 1-10.

[177] Y. Zhu, J. Liang, C. Liu, T. Ma, L. Wang. Development of a passive direct methanol fuel cell (DMFC) twin-stack for long-term operation. *J Power Sources* 193 (2009) 649-655.

[178] V. Baglio, A. Stassi, E. Modica, V. Antonucci, A. S. Aricò, P. Caracino, O. Ballabio, M. Colombo, E. Kopnin. Performance comparison of portable direct methanol fuel cell mini-stacks based on low-cost fluorine-free polymer electrolyte and Nafion membrane. *Electrochim Acta* 55 (2010) 6022-6027.

[179] T. Tsujiguchi, M. A. Abdelkareem, T. Kudo, N. Nakagawa, T. Shimizu, M. Matsuda. Development of a passive direct methanol fuel cell stack for high methanol concentration. *J Power Sources* 195 (2010) 5975-5979.

[180] Y. Kim, D. Shin, J. Seo, N. Chang, H. Cho, Y. Kim, S. Yon. System integration of a portable direct methanol fuel cell and a battery hybrid. *Int J Hydrogen Energy* 35 (2010) 5621-5637.

- [181] Y. Na, J. Suh, I. Song, K. -H. Choi, H. Choi, K. B. Kim, J. -Y. Park. Stable operation of air-blowing direct methanol fuel cell stacks through uniform oxidant supply by varying fluid flow fixtures and developing the flow sensor. *Int J Hydrogen Energy* 36 (2011) 9205-9215.
- [182] N. K. Shrivastav, S. B. Thombre, R. B. Chadge. Liquid feed passive direct methanol fuel cell: challenges and recent advances. *Ionics* 22 (2016) 1-22.
- [183] X. M. Ren, M. S. Wilson, S. Gottesfeld. High performance direct methanol polymer electrolyte fuel cells. *J Electrochem Soc* 143(1996)L12–L15.
- [184] A. K. Shukla, P. A. Christensen, A. Hamnett, M. P. Hogarth. A vaporfeed direct-methanol fuel-cell with proton-exchange membrane electrolyte. *J Power Sources* 55(1995)87-91.
- [185] J. G. Liu, Z. H. Zhou, X. X. Zhao, Q. Xin, G. Q. Sun, B. L. Yi. Studies on performance degradation of a direct methanol fuel cell (DMFC) in life test. *Phys Chem Chem Phys* 6(2004)134-167.
- [186] Z. -B. Wang, H. Rivera, X. -P. Wang, H. -X. Zhang, P. -X. Feng, E. A. Lewis, E. S. Smotkin. Catalyst failure analysis of a direct methanol fuel cell membrane electrode assembly. *J Power Sources* 177(2008)386 -392.
- [187] A. Bauer, E. L. Gyenge, C. W. Oloman. Direct methanol fuel cell with extended reaction zone anode: PtRu and PtRuMo supported on graphite felt. *J Power Sources* 167 (2007) 281–287.
- [188] L. Zou, J. Guo, J. Liu, Z. Zou, D. L. Akins, H. Yang. Highly alloyed PtRu black electrocatalysts for methanol oxidation prepared using magnesia nanoparticles as sacrificial templates. *J Power Sources* 248 (2014) 356-362.

[189] J. -H. Kim, H. -Y. Ha, I. -H. Oh, S. -A. Hong, H. I. Lee. Influence of the solvent in anode catalyst ink on the performance of a direct methanol fuel cell. *J Power Sources* 135 (2004) 29-35.

[190] Y. Ma, Y. Lin, X. Xiao, X. Zhou, X. Li. Sonication–hydrothermal combination technique for the synthesis of titanate nanotubes from commercially available precursors. *Mater Res Bull* 41 (2006) 237-243.

[191] H. H. Ou, S. L. Lo. Review of titania nanotubes synthesized via the hydrothermal treatment: Fabrication, modification and application. *Sep Purif Technol* 58 (2007) 179-191.

[192] Y. Xu, X. Xie, J. Guo, S. Wang, Y. Wang, V. K. Mathur. Effects of annealing treatment and pH on preparation of citrate-stabilized PtRu/C catalyst. *J Power Sources* 162 (2006) 132-140.

[193] J. C. Cruz, A. Ramos Hernández, M. Guerra –Balcazar, A. U. Chávez-Ramirez , J. Ledesma-García, L. G. Arriaga. Electrochemical Evaluation of a Ir-Ru Binary Oxide for Oxygen Evolution Reaction. *Int J Electrochem Sci* 7 (2012) 7866 – 7876.

[194] L. J. van der Pauw. A method of measuring specific resistivity and Hall effect of discs of arbitrary shape. *Philips Research Reports* 13 (1958) 1–9.

[195] F. C. Nart, W. Vielstich. Normalization of porous active surfaces. in: W. Vielstich, A. Lamm, H. A. Gasteiger (Eds.). *Handbook of fuel cells. Fundamentals; technology and applications*, vol. 2, John Wiley & Sons, Chichester, 2003, pp. 302–315.

[196] S. Ardizzone, G. Fregonara, S. Trasatti. “Inner” and “outer” active surface of RuO₂ electrodes. *Electrochim Acta* 35 (1990) 263-267.

- [197] A. T. Marshall, S. Sunde, M. Tsypkin, R. Tunold. Performance of a PEM water electrolysis cell using image electrocatalysts for the oxygen evolution electrode. *Int J Hydrogen Energy* 32 (2007) 2320-2324.
- [198] F. Alcaide, G. Álvarez, O. Miguel, M. J. Lázaro, R. Moliner, A. López-Cudero, J. Solla-Gullón, E. Herrero, A. Aldaz. Pt supported on carbon nanofibers as electrocatalyst for low temperature polymer electrolyte membrane fuel cells. *Electrochem Comm* 11 (2009) 1081-1084.
- [199] F. Alcaide, G. Álvarez, N. Tsiouvaras, M. A. Peña, J. L. G. Fierro, M. V. Martínez-Huerta. Electrooxidation of H₂/CO on carbon-supported PtRu-MoO_x nanoparticles for polymer electrolyte fuel cells. *Int J Hydrogen Energy* 36 (2011) 14590-14598.
- [200] T. Kasuga, M. Hiramatsu, A. Hoson, T. Sekino, K. Niihara. Titania nanotubes prepared by chemical processing. *Adv Mater* 11 (1999) 1307-1311.
- [201] X. B. Chen, S. S. Mao. Titanium dioxide nanomaterials: synthesis, properties, modifications and applications. *Chem Rev* 107 (2007) 2891-2959.
- [202] Q. Chen, W. Z. Zhou, G. H. Du, L. M. Peng.. Trititanate nanotubes made via a single alkali treatment. *Adv Mater* 14 (2002) 1208-1211.
- [203] Z. Y. Yuan, B. L. Su. Titanium oxide nanotubes, nanofibers and nanowires. *Colloids Surf A* 241 (2004) 173-183.
- [204] S-. Y. Chu, T-. Y. Chen, I-. T. Tsai, W. Water. Dopping effects of Nb additives on the piezoelectric and dielectric properties of PZT ceramics and its application on SAW device. *Sensor Actuator A* 113 (2004) 198-203.
- [205] H. Chhina, S. Campbell, O. Kesler. Characterization of Nb and W doped titania as catalyst supports for Proton Exchange Membrane Fuel Cells. *J New Mat Elect Sys* 12 (2009) 177-185.

[206] D. V. Bavykin, V. N. Parmon, A. A. Lapkin, F. C. Walsh. The effect of hydrothermal conditions on the mesoporous structure of TiO₂ nanotubes. *J Mater Chem* 14 (2004) 3370-3377.

[207] S. Rau, J. Colom Tomás, T. Smolinka, R. E. Fuentes, J. W. Weidner. PEM Electrolyzer with Nano-structured Electrodes for High Efficient Hydrogen Production. 18th World Hydrogen Energy Conference 2010 - WHEC 2010, Essen, Germany, May 16-21.

[208] L. Chevallier, A. Bauer, S. Cavaliere, R. Hui, J. Rozière, D. J. Jones. Mesoporous Nanostructured Nb-Doped Titanium Dioxide Microsphere Catalyst Supports for PEM Fuel Cell Electrodes. *Appl Mater Interfaces* 4 (2012) 1752–1759.

[209] J. F. Moulder, W. F. Stickle, P. E. Sobol, K. D. Bomben. Handbook of X-ray Photoelectron Spectroscopy. A reference book of standard spectra for identification and interpretation of xps data. Physical Electronics, Eden Prairie, MN, 1995.

[210] H. Angerstein-Kozłowska, in: E. Yeager, J. O'M. Bockris, B. E. Conway, S. Sarangapani (Eds.). *Comprehensive Treatise of Electrochemistry*, vol. 9, Plenum Press, New York, 1984. pp. 15–61.

[211] T. Bhowmik, M. K. Kundu, S. Barman. Palladium nanoparticle–graphitic carbon nitride porous synergistic catalyst for hydrogen evolution/oxidation reactions over a broad range of pH and correlation of its catalytic activity with measured hydrogen binding energy. *ACS Catal* 6 (2016) 1929–1941.

[212] J. Wang, F. Xu, H. Jin, Y. Chen, Y. Wang. Non-Noble Metal-based Carbon Composites in Hydrogen Evolution Reaction: Fundamentals to Applications. *Adv Mater* 29 (2017) 1605838.

[213] S. Anantharaj, S. R. Ede, K. Sakthikumar, K. Karthick, S. Mishra, S. Kundu, *Recent Trends and Perspectives in Electrochemical Water Splitting with an*

Emphasis on Sulfide, Selenide, and Phosphide Catalysts of Fe, Co, and Ni: A Review. *ACS Catal* 6 (2016) 8069–8097.

[214] Y. Zhang, J. Yan, X. Ren, L. Pang, H. Chen, S. (F.) Liu. 2D WS₂ nanosheet supported Pt nanoparticles for enhanced hydrogen evolution reaction. *Int J Hydrogen Energy* 42 (2017) 5472–5477.

[215] X. Wang, X. Yuan, X. Liu, W. Dong, C. Dong, M. Lou, J. Li, T. Lin, F. Huang. Monodisperse Pt nanoparticles anchored on N-doped black TiO₂ as high performance bifunctional electrocatalyst. *J Alloy Compd* 701 (2017) 689–675.

[216] T. Yang, H. Zhu, M. Wan, L. Dong, M. Zhang, M. Du. Highly efficient and durable PtCo alloy nanoparticles encapsulated in carbon nanofibers for electrochemical hydrogen generation. *Chem Commun* 52 (2016) 990–993.

[217] J. Cheng, H. Zhang, G. Chen, Y. Zhang. Study of Ir_xRu_{1-x}O₂ oxides as anodic electrocatalysts for solid polymer electrolyte water electrolysis. *Electrochim Acta* 54 (2009) 6250-6256.

[218] C. P. DePauli, S. Trasatti. Electrochemical surface characterization of IrO₂ + SnO₂ mixed oxide electrocatalysts. *J Electroanal Chem* 396 (1995) 161-168.

[219] E. Kuznetsova, V. Petrykin, S. Sunde, P. Krtil. Selectivity of Nanocrystalline IrO₂-Based Catalysts in Parallel Chlorine and Oxygen Evolution. *Electrocatalysis* 6 (2015) 198-210.

[220] S. Ardizzzone, C. L. Bianchi, L. Borgese, G. Cappelletti, C. Locatelli, A. Minguzzi, S. Rondinini, A. Vertova, P. C. Ricci, C. Cannas, A. Musinu. Physico-chemical characterization of IrO₂-SnO₂ sol-gel nanopowders for electrochemical applications. *J Appl Electrochem* 39 (2009) 2093–2105.

[221] A. T. Marshall, R. G. Haverkamp. Electrocatalytic activity of IrO₂-RuO₂ supported on Sb-doped SnO₂ nanoparticles. *Electrochim Acta* 55 (2010) 1978–1984.

[222] A. Marshall, B. Børresen, G. Hagen, M. Tsykin, R. Tunold. Hydrogen production by advanced proton exchange membrane (PEM) water electrolyzers—Reduced energy consumption by improved electrocatalysis. *Energy* 32 (2007) 431-436.

[223] M. Lira-Cantu, M. K. Siddiki, D. Muñoz-Rojas, R. Amade, N. I. González-Pech. Nb-TiO₂/polymer hybrid solar cells with photovoltaic response under inert atmosphere conditions. *Sol Energ Mat Sol C* 94 (2010) 1227-1234.

[224] E. Brightman, J. Dodwell, N. van Dijk, G. Hinds. In situ characterisation of PEM water electrolyzers using a novel reference electrode. *Electrochem Commun* 52 (2015) 1-4.

[225] D. Chu, S. Gilman. Methanol electrooxidation on unsupported Pt-Ru alloys at different temperatures. *J Electrochem Soc* 143 (1996) 1685-1690.

[226] A. S. Aricò, P. L. Antonucci, E. Modica, V. Baglio, H. Kim, V. Antonucci. Effect of Pt-Ru alloy composition on high-temperature methanol electro-oxidation. *Electrochim Acta* 47 (2002) 3723-3732.

[227] C. Lim, R. G. Allen, K. Scott. Effect of dispersion methods of an unsupported Pt-Ru black anode catalyst on the power performance of a direct methanol fuel cell. *J Power Sources* 161 (2006) 11-18.

[228] S. Wang, G. Sun, Z. Wu, Q. Xin. Effect of Nafion[®] ionomer aggregation on the structure of the cathode catalyst layer of a DMFC. *J Power Sources* 165 (2007) 128-133.

[229] T. Vidaković, M. Christov, K. Sundmacher. The use of CO stripping for in situ fuel cell catalyst characterization. *Electrochim Acta* 52 (2007) 5606-5613.

[230] R. D. Armstrong, M. Henderson. Impedance plane display of a reaction with an adsorbed intermediate. *J Electroanal Chem* 39 (1972) 81-90.

[231] D. A. Harrington, B. E. Conway. AC Impedance of Faradaic reactions involving electrosorbed intermediates-I. Kinetic theory. *Electrochim Acta* 32 (1987) 1703-1712.

[232] C. -N. Cao. On the impedance plane displays for irreversible electrode reactions based on the stability conditions of the steady-state-I. One state variable besides electrode potential. *Electrochim Acta* 35 (1990) 831-836.

[233] G. Wu, L. Li, B. -Q. Yu. Effect of electrochemical polarization of PtRu/C catalysts on methanol electrooxidation. *Electrochim Acta* 50 (2004) 1-10.

[234] F. Seland, R. Tunold, D. A. Harrington. Impedance study of methanol oxidation on platinum electrodes. *Electrochim Acta* 51 (2006) 3827-3840.

[235] A. Lasia. Electrochemical impedance spectroscopy and its applications in: B.E. Conway, R.E. White, J.O'M. Bockris (Eds.), *Modern Aspects of Electrochemistry*, no. 32, Kluwer Academic/Plenum Publishers, New York, NY, 1999, p. 143.

[236] J. T. Müller, P. M. Urban, W. F. Hölderich. Impedance studies on direct methanol fuel cell anodes. *J Power Sources* 84 (1999) 157-160.

[237] D. Chakraborty, I. Chorkendorff, T. Johannessen. Electrochemical impedance spectroscopy study of methanol oxidation on nanoparticulate PtRu direct methanol fuel cell anodes: Kinetics and performance evaluation. *J Power Sources* 162 (2006) 1010-1022.

[238] J. Brug, A. L. G. Van den Eeden, M. Sluyters-Rehbach, J. H. Sluyters. The analysis of electrode impedances complicated by the presence of constant phase element. *J Electroanal Chem Interfacial Electrochem* 176 (1984) 275-295.

[239] R. E. Melnick, G. T. R. Palmore. Impedance spectroscopy of the electro-oxidation of methanol on polished polycrystalline platinum. *J Phys Chem B* 105 (2001) 1012-1025.

[240] H. Dohle, H. Schmitz, T. Bewer, J. Mergel. Development of a compact 500 W class direct methanol fuel cell stack. *J Power Sources* 106 (2002) 313-322.

[241] C. Xie, J. Bostaph, J. Pavío. Development of a 2 W direct methanol fuel cell power source. *J Power Sources* 136 (2004) 55-65.

[242] J. Prabhuram, N. N. Krishnan, B. Choi, T. -H. Lim, H. Y. Ha, S. -K. Kim. Long-term durability test for direct methanol fuel cell made of hydrocarbon membrane. *Int J Hydrogen Energy* 35 (2010) 6924-6933.

[243] W. F. Lin, M. S. Zei, M. Eiswirth, G. Ertl, T. Iwasita, W. Vielstich. Electrocatalytic activity of Ru-modified Pt(111) electrodes toward CO oxidation. *J Phys Chem B* 103 (1999) 6968-6977.

[244] H. N. Dinh, X. Ren, F. H. Garzon, P. Zelenay, S. Gottesfeld. Electrocatalysis in direct methanol fuel cells: in-situ probing of PtRu anode catalyst surfaces. *J Electroanal Chem* 491 (2000) 222-233.

[245] A. Havránek, K. Wippermann. Determination of proton conductivity in anode catalyst layers of the direct methanol fuel cell (DMFC). *J Electroanal Chem* 57 (2004) 305-315.

[246] X. Ren. Performance of direct methanol fuel cells for portable power applications, in: *Catalysis for sustainable energy production*. P. Barbaro and C. Bianchini (Eds.), Wiley-VCH Verlag GmbH & Co. KGaA, Weinheim (Germany), 2009, Ch. 2, pp. 47-69.

APPENDIX

List of symbols

Symbol	Explanation
α_a / α_c	Anodic / Cathodic transfer coefficients
a_{H_2O} / a_{CH_3OH}	Activity of water/methanol
b_a / b_c	Anodic / Cathodic Tafel slopes (V dec ⁻¹)
B (FWHM)	Full width at half maximum
C_{dl}	Double layer capacitance (F cm ⁻²)
C_{pdl}	Pseudo-double layer capacitance (F cm ⁻²)
d	Interplanar spacing (nm)
E_{cell}	Cell voltage (V)
E_{real}	Real cell voltage (V)
E_{rev} (E^0_{rev})	Reversible cell potential (standard reversible cell potential) (V)
E_{th} (E^0_{th})	Thermoneutral cell potential (standard thermoneutral cell potential) (V)
ϵ	Dielectric constant
$\epsilon_{\Delta H}$	Thermal energy efficiency (%)
$\epsilon_{\Delta G}$	Energy efficiency in terms of Gibbs energy (%)
η	Overpotential (V)
θ	Glancing angle (degree)
F	Faraday constant (96485 C cm ⁻¹)
ΔG (ΔG^0)	Gibbs energy (standard Gibbs energy) of the reaction (kJ mol ⁻¹)
ΔH (ΔH^0)	Enthalpy of the reaction (standard enthalpy) of the reaction (J mol ⁻¹)
hkl	Miller indices
j	Current density (A cm ⁻²)
j_0	Exchange current density (A cm ⁻²)
j_{pdl}	Charging current density (A cm ⁻²)
L	Crystallite size (nm)
λ	Wave length (nm)
μ_i	Chemical potential (kJ mol ⁻¹)
n	Number of electrons
v	Scan rate (mV s ⁻¹)
P	Power density (mW cm ⁻²)
p_{H_2}	Hydrogen pressure (atm)

p_{O_2}	Oxygen pressure (atm)
P_v	Vapour pressure (hPa)
ρ	Density (g cm^{-3})
q^*_{A}/q^*_{C}	Anodic total charge/Cathodic total charge (mC)
$q^*_{dl} (q^*_{outer})$	Double-layer (Outer) charge (mC)
Q_H	Charge for hydrogen desorption (mC)
$q^*_{redox} (q^*_{inner})$	Redox (inner) charge (mC)
R	Gas constant ($8.314 \text{ JK}^{-1}\text{mol}^{-1}$)
R_{total}	Overall ohmic resistance (Ω)
$\Delta S (\Delta S^0)$	Entropy of the reaction (standard entropy) of the reaction (J mol^{-1})
σ	Specific conductivity (S g^{-1})
T	Temperature (K, $^{\circ}\text{C}$)
T_b	Boiling temperature ($^{\circ}\text{C}$)
τ	Coverage relaxation time (s)
Y_0	Admittance ($\Omega^{-1} \text{ s}^n \text{ cm}^{-2}$)
$ Z $	Impedance modulus
ω	Frequency (Hz)

List of acronyms

Acronym	Explanation
AFC	Alkaline Fuel Cell
APU	Automotive power unit
ARR	Anode reaction resistance ($\Omega \text{ cm}^2$)
ATR	Autothermal steam reforming
ATO	Sb-doped tin oxide
<i>B</i> (FWHM)	Full width at half maximum
BET	Brunauer-Emmett-Teller
BJH	Barrett-Joyner-Halenda
CCM	Catalyst-coated membrane
CCS	Catalyst-coated substrate
CHs pyrolysis	Hydrocarbon pyrolysis
CL	Catalyst layer
CNFs	Carbon nanofibers
CNTs	Carbon nanotubes
CPE	Constant phase element
CV	Cyclic voltammetry
DHE	Dynamic hydrogen electrode
DMFC	Direct methanol fuel cell
ECSA	Electrochemical active surface area
EDX	Energy dispersive X-ray spectroscopy
EIS	Electrochemical impedance spectroscopy
<i>fcc</i>	Face-centred cubic lattice
FRA	Frequency response analyzer
GC	Glassy carbon electrode
GDE	Gas diffusion electrode
GDL	Gas diffusion layer
HER	Hydrogen evolution reaction
HHV	High heating values

IPA	Isopropanol
LHV	Low heating values
LSV	Linear sweep voltammetry
MCFC	Molten Carbonate Fuel Cell
MEA	Membrane electrode assembly
MOR	Methanol oxidation reaction
MSE	Mercurous sulfate electrode ($\text{Hg} \text{Hg}_2\text{SO}_4, \text{K}_2\text{SO}_4(\text{sat})$)
NBA	n-butyl acetate
NWs	Nanowires
OCP/OCV	Open circuit potential/Open circuit voltage
OER	Oxygen evolution reaction
ORR	Oxygen reduction reaction
RAFC	Phosphoric Acid Fuel Cell
PANI	Polyaniline
PEDOT	Poly (3,4-ethylenedioxythiophene)
POX	Partial oxidation
PEM	Polymer-electrolyte membrane (Proton exchange membrane)
PE(M)FC	Polymer-electrolyte (membrane) fuel cell
PEMWE	Polymer-electrolyte membrane water electrolyser
PFSA	Perfluorosulfonic acid polymers
PBI	Poly[2,2'-(m-phenylene)-5,5'-bibenzimidazole]
PTFE	Polytetrafluoroethylene
PEMFC	Proton exchange membrane fuel cells
PWA	Tungstophosphoric acid
rds	Rate determining step
RG	Research grade purity
rGO	Reduced graphene oxide
RH	Relative humidity
RHE	Reversible hydrogen electrode
SA	Surface area ($\text{m}^2 \text{g}^{-1}$)

SEM	Scanning electron microscopy
SOEC	Solid oxide electrolyte cell
SOFC	Solid oxide fuel cell
(S)MSI	(Strong) metal-support interaction
SPE	Solid-polymer electrolyte
SPEEK	Sulfonated polyetherketone
SR	Steam reforming
STP	Standard temperature pressure
TBAOH	Tetrabutylammonium hydroxide
TEM	Transmission electron microscopy
TNTs	Titanium dioxide (titania) nanotubes
UHV	Ultra high vacuum
UPD	Underpotential deposition
UPS	Uninterruptible power supplies
XPS	X-ray photoelectron spectroscopy
XRD	X-ray diffraction

Curriculum Vitae

Personal Details

Name: Radostina Vasileva Genova-Koleva
Date of birth: 15/01/1982
Nationality: Bulgarian
Email: genova.radostina@gmail.com

Education

2012 – 2017 PhD in the Department of Materials Science and Physical Chemistry, Faculty of Chemistry, University of Barcelona, Spain

2004 – 2006 MSc in the Department of General and Inorganic Chemistry, Faculty of Chemistry, University of Sofia, Bulgaria
Master's programme "Inorganic substances and materials for high technologies"

2000 – 2004 BSc in the Department of General and Inorganic Chemistry, Faculty of Chemistry, University of Sofia, Bulgaria

1995 – 2000 Secondary education – chemistry, National High School of Mathematics and Science, Sofia, Bulgaria

Research Experience

Jul 2010 – Aug 2013 FP7 Marie Curie Early Stage Researcher, CIDETEC-IK4, San Sebastian (Donostia), Spain
Synthesis, development, physicochemical and electrochemical characterization of variety of catalysts and catalyst supports for PEM Fuel Cells and PEM Water Electrolysis. PEM electrolyzer performance at low and middle temperatures. MEA preparation, optimization and characterization. Development testing protocols for MEAs and catalysts for PEM electrolysis.

Jul 2012 – Jul 2012 FP7 Marie Curie Early Stage Researcher (Visiting researcher), ICGM-UMR5253-Equipe AIME, Université Montpellier II, Montpellier, France.
Physicochemical tests of electrocatalyst supports TiO₂, Nb-TiO₂, TNT and Nb-TNT.

Mar 2008 – Dec 2009 FP6 Marie Curie Early Stage Researcher, LTNFM (Laboratory of Technology of Novel Functional Materials), ICM, University of Warsaw, Warsaw, Poland
Synthesis and characterization of new materials for hydrogen storage. Testing transition metal hydrides as potential lightweight stores of hydrogen. Synthesis of yttrium and

ytterbium hydride and yttrium amidoborane, investigation of the thermal stability, structure and properties as a potential new materials for hydrogen store.

- Aug 2009 – Sep 2009** FP6 Marie Curie Early Stage Researcher (Visiting researcher), Chemical Physics Group, Department of Applied Physics, Chalmers University of Technology, Gothenburg, Sweden
Characterization of ytterbium hydride as a hydrogen storage material at low pressures with quartz crystal microbalance (QCM).
- Nov 2004 – Jul 2006** MSc Inorganic Chemistry, Department of General and Inorganic chemistry, University of Sofia.
Master's programme "Inorganic substances and materials for high technologies"; Master's thesis "Influence of Magnetic field on Crystal Growth of Monocrystals of TGS from water solutions".

Teaching Experience

- 2005 – 2008** Practical course in general and inorganic chemistry for graduates (Lab Assistant, Department of General and Inorganic chemistry, University of Sofia)
- 2010 – 2010** Practical course in general and inorganic chemistry for graduates (Lab Assistant, Department of General and Inorganic chemistry, University of Sofia)

Awards / Fellowships

- 2010 – 2013** FP7 Marie Curie ESR, ITN "SUSHGEN" (research fellow, CIDETEC-IK4, Spain)
- 2008 – 2009** FP6 Marie Curie ESR, RTN "Hydrogen" (research fellow, University of Warsaw, Poland)

Additional Skills

- Chemistry** Gas adsorption analysis, Organic/Inorganic standard techniques (NMR, UV/Vis, IR, TGA, DSC, MS, XRD, XPS, SEM, EDX), mechanochemical and wet synthesis, working with air and moisture sensitive compounds in glovebox. Electrochemical techniques –CV, LSV, EIS, CO-stripping.
- Computer Skills** OS Windows; Microsoft Office; Origin; KaleidaGraph; Powder Cell; Material Studio, Corr Ware and CView, Power Suite.
- Languages** English (fluent), Bulgarian (native), Spanish (intermediate), Polish (beginner).

Projects

Name	Sustainable Hydrogen Generation (SUSHGEN)
Funding organisation	EU
Participants	CIDETEC (Centro de Tecnologías Electroquímicas), UNEW, CNRS, NTNU, IEES, FORTH/ICE-HT, Advent Technologies
Duration	2010 – 2013
Responsible investigator	Dr. Francisco Alcaide Monterrubio (Spanish group) (involved 2 researchers)
Name	Automotive PEMFC Range Extender with High Temperature Improved MEAs and Stacks (ARTEMIS)
Funding organisation	EU
Participants	CIDETEC (Centro de Tecnologías Electroquímicas), CNRS, CEA, POLITO, NEDSTACK, CR FIAT.
Duration	2012 – 2015
Responsible investigator	Dr. Francisco Alcaide Monterrubio (Spanish group) (involved 4 researchers)
Name	Understanding the Degradation Mechanisms of a High Temperature PEMFC Stack and Optimization of the Individual Components (DeMStack)
Funding organisation	EU
Participants	CIDETEC (Centro de Tecnologías Electroquímicas), FORTH, ICTP, ADVENT, JRC-IET, HELBIO, PROTOTECH.
Duration	2013 – 2016
Responsible investigator	Dr. Francisco Alcaide Monterrubio (Spanish group) (involved 4 researchers)
Name	Production and storage of hydrogen (Hydrogen)
Funding organisation	EU

Participants	University of Warsaw, Chalmers University of Technology, EPFL, EMPA, Leiden University, University of Oxford, DTU, Shell BV, Global Solutions International (SHL), University of Iceland
Duration	2007-2009
Responsible investigator	Prof. Wojciech Grochala (Polish group)

Conference participations

- European Materials Research Society 2016 Fall Meeting (E-MRS 2016 Fall Meeting), 19-22 September 2016, Warsaw, Poland.
 Autors: F. Alcaide, G. Álvarez, R. V. Genova-Koleva, H.-J. Grande, O. Miguel, A. Querejeta
 Title: Non-precious metal/chalcogen carbon supported catalysts for oxygen reduction in PEMFCs (poster)
- XXXIV Reunión del Grupo de Electroquímica de la RSEQ, XV Encontro Ibérico de Electroquímica, July 2013, Valencia, Spain
 Autors: F. Alcaide, G. Álvarez, R. Genova-Koleva, H.-J. Grande, O. Miguel
 Title: Electrocatalizadores para cátodos de pilas de combustible PEMFC basados en grafeno (poster)
- 4th European PEFC & H₂ Forum, 2-5.07.2013, Lucerne, Switzerland
 Autors: R. Genova-Koleva, F. Alcaide, H.-J. Grande, O. Miguel
 Title: Titanium dioxide nanotubes based catalyst supports for hydrogen evolution in PEM water electrolyser (poster)
- The 4th RTN Meeting Nano and Surface Science Approaches to Production and Storage of Hydrogen, 14-19.11.2010, Noordwijkerhout, Leiden, The Netherlands
 Autors: Radostina Genova, Wojciech Grochala
 Title: Probing hydrogen storage properties of selected bulk light metal amidoboranes and of thin yttrium films (oral presentation)
- The 3rd RTN Meeting Hydrogen for the Future (MCR TN Hydrogen), 21-25.10.2009, University of Warsaw (Warsaw, Poland)
 Autors: Radostina Genova, Wojciech Grochala
 Title: Probing hydrogen storage properties of materials based on yttrium and ytterbium (oral presentation)

- Reactivity of nanoparticles for more efficient and sustainable energy production (summer school), 22-27.08.2009, CINF, Sandbjerg, Denmark
Autors: Radostina V. Genova, Karol J. Fijałkowski, Wojciech Grochala
Title: Probing hydrogen storage properties of YX_3/MNH_2BH_3 composites (X = H, F, Cl ;M = Li, Na) (poster)
- Hydrogen-Metal Systems, GRC, 12-17.07.2009, Lucca, Italy
Autors: Radostina V. Genova, Karol J. Fijałkowski, Wojciech Grochala
Title: Probing hydrogen storage properties of YX_3/MNH_2BH_3 composites (X = H, F, Cl ;M = Li, Na) (poster)
- Hydrogen and Hydrogen Storage, Methods and Materials 3-6.01.2009, IISc, Bangalore (Bangalore, India)
Autors: R. V. Genova, K. J. Fijałkowski, W. Grochala
Title: Synthesis, properties and decomposition of $Y(NH_2BH_3)_3$ (poster)

Publications

1. F. Alcaide, G. Álvarez, P. L. Cabot, R. Genova-Koleva, H-. J. Grande, O. Miguel. Effect of the solvent in the catalyst ink preparation on the properties and performance of unsupported PtRu catalyst layers in direct methanol fuel cells. *Electrochim Acta* 231 (2017) 529-538.
2. R. V. Genova, F. Alcaide, P. L. Cabot, G. Álvarez, H-. J. Grande, O. Miguel. Platinum supported on Nb-doped TiO_2 and Nb-doped TiO_2 nanotubes as high performance cathodes for proton exchange membrane water electrolyzers. Under review
3. R. V. Genova, F. Alcaide, P. L. Cabot, G. Álvarez, A. Querejeta, H-. J. Grande, O. Miguel. Titanium Dioxide Nanotubes as Supports for IrOx and IrRuOx Electrocatalysts for Oxygen Evolution in PEM Water Electrolysis. In preparation
4. R. V. Genova, K. Fijałkowski, A. Budzianowski, W. Grochala. Towards $Y(NH_2BH_3)_3$: Probing hydrogen storage properties of YX_3/MNH_2BH_3 (X = H, F, Cl) (M = Li, Na). *J Alloys Comp* 499 (2010) 144-148.
5. K. J. Fijałkowski, R. V. Genova, Y. Filinchuk, A. Budzianowski, M. Derzsi, T. Jaroń, P. J. Leszczynski, W. Grochala. $Na[Li(NH_2BH_3)_2]$ – the first mixed-cation amidoborane with unusual crystal structure. *DALTON TRANS* 40 (2011) 4407-4413.
6. A. J. Churchard, E. Banach, A. Borgschulte, R. Caputo, Jian-Cheng Chen, D. Clary, K. J. Fijałkowski, H. Geerlings, R. V. Genova, W. Grochala, T. Jaroń, J. C. Juanes-Marcos, B. Kasemo, G. J. Kroes, I. Ljubić, N. Naujoks, J. K. Nørskov, R. A. Olsen, F. Pendolino, A. Remhof, L. Románszki, A. Tekin, T. Vegge, M. Zäch and A. Züttel. A multifaceted approach to the hydrogen storage problem. *PhysChemChemPhys* 13 (2011) 16955-16972.